MAX–PLANCK–INSTITUTE FÜR RADIOASTRONOMIE

The Transient Radio Sky: Pulsars and Fast Radio Bursts

Dissertation

zur

Erlangung des Doktorgrades (*Dr. rer. nat.*)

der

Rheinischen Friedrich–Wilhelms–Universität Bonn

der

Mathematisch-Naturwissenschaftlichen Fakultät

vorgelegt von

Marilyn Cruces

aus

Concepción, Chile

Bonn 2020

Angefertigt mit Genehmigung der Mathematisch-Naturwissenschaftlichen Fakultät
der Rheinischen Friedrich–Wilhelms–Universität Bonn

1. Referent: Prof. Dr Michael Kramer
2. Referent: Prof. Dr Norbert Langer
3. Referent: Prof. Dr Simon Stellmer
4. Referent: Prof. Dr Volkmar Gieselmann
Tag der Promotion: 09.04.2021
Erscheinungsjahr: 2021

RHEINISCHE FRIEDRICH–WILHELMS–UNIVERSITÄT BONN

Abstract

by Marilyn (Mary) Cruces

for the degree of

Doctor rerum naturalium

This thesis focuses on targeted searches of two radio transients associated with neutron stars (NS): Pulsars and Fast Radio Bursts (FRBs), and the study of their properties over different timescales. Pulsars emit beams of electromagnetic radiation along their magnetic axis, which is detected mainly as pulses at radio frequencies. They are means to study stellar evolution, to place limits on the equation of state for ultra-dense matter, to map the free electron distribution of our Galaxy and are superb natural laboratories in which to test theories of gravity in the strong-field regime. FRBs are an observational phenomena consisting of bright flashes of millisecond duration, detected so-far exclusively at radio frequencies. Although their astrophysical origin remains a mystery, it is proposed that their narrow and coherent pulses probe the large distance they travelled through; thus, FRBs could become powerful cosmological tools to probe the epoch of reionization, to test the homogeneity and isotropy of the Universe, and to constrain the weak equivalence principle, to name a few.

Chapter 5 presents the ongoing drift-scan pulsar survey using the world largest single-dish radio telescope, the *Five-hundred-meter Aperture Spherical radio Telescope* (FAST). It reports the follow-up campaign of 10 pulsars discovered in the early commissioning phase of FAST with the use of the 100-m Effelsberg radio telescope. Highlights are PSR J1951+4724, a young and energetic pulsar with nearly 100% of linearly polarized flux and visible up to an observing frequency of 8 GHz, and PSR J2338+4824, a pulsar in a 95.2-day binary with a Carbon-Oxygen White dwarf (WD). Given the orbital parameters, the companion is estimated to have a minimum mass of 1.029 $M_\odot$, placing it as the widest known binary system with a massive WD. Additionally, PSR J2338+4824 seems to be a long-term nulling pulsar given the high non-detection rate, which is not consistent with the diffractive scintillation timescale. With the full set of pulsars in addition to the 11 FAST pulsars followed-up by the Parkes radio telescope, a population analysis is performed. It is shown that FAST seems to be discovering an old population of pulsars.

Chapter 6 studies the long-term evolution of the magnetic field of millisecond pulsars (MSPs) to understand their lower values when compared to the normal pulsar population. According to the standard scenario, they are formed from pulsars in binary systems, where the millisecond rotation is caused by the accre-

tion of matter and angular momentum from their companion. However, how the magnetic field decays through accretion is not well understood. An alternative hypothesis is explored, in which the decay is due to *ambipolar diffusion* before the accretion process. The observed binary systems are used to constrain the time available for the decay based on the current pulsar companion: a Helium WD, a Carbon-Oxygen WD, or another NS. With a simplified model without baryon pairing, it is shown that the process agrees with the general distribution of observed magnetic field strengths in binary systems.

Chapter 7 presents an extensive multi-wavelength campaign on the first discovered repeating FRB, FRB 121102. Three radio telescopes: Effelsberg, Green Bank, and the Arecibo Observatory, were used to shadow higher energy experiments with the Gran Telescope Canaria (optical), NuSTAR (X-ray) and INTEGRAL (gamma-ray). From the 36 bursts detected with Effelsberg, one has a pulse width of 39 ms, which is the widest burst ever detected from FRB 121102. With one burst detected during simultaneous NuSTAR observations, a 5-σ upper limit of 5×10^{47} erg on the 3–79 keV energy of an X-ray burst counterpart is placed. With the roughly four years of data with Effelsberg, it is found a periodicity of 161±5 days, confirming the potential periodicity reported recently in the literature. Comparing the wait times between consecutive bursts within a single observation to Weibull and Poisson distributions, it is shown that if the few events with millisecond separation are excluded, the arrival times are Poisson distributed. It is proposed that such closely spaced burst may be the components of one broad burst. Finally, it is found that the bursts' cumulative energy distribution with energies from $\sim 10^{38}$–10^{39} erg is well described by a power-law with a slope of $\gamma = -1.1 \pm 0.2$. It is proposed that a single power-law might be a poor descriptor of the data over many orders of magnitude.

To my brothers Luis and Marcelo...

"What is this? a crossover episode?."

Mr. Peanut Butter

Acknowledgements

The last four years have been full of adventures, learning, fun and science!. This thesis would have not been possible without each of these factors and the following people from whom I am deeply thankful:

Michael Kramer – for building such a friendly group and working atmosphere, and giving me a possibility to be a part of and contribute to it. It is inspiring to be part of a group where science, fun, friendship and support converge. You manage (somehow) to dedicate time to all of us to share some anecdote, wisdom and motivation – particularly appreciated during the crazy Covid-19 times. As my supervisor, your questions – at first sight simple – always provided a different perspective. Thanks for trusting me with tasks that made me grow as a scientist and as a person...Danke!

$\infty + 1$ thanks to David Champion – for being a great day-to-day advisor. For being there whenever I had a question, for the support, cheering me up when things were not working, and for being all-round a caring and thoughtful advisor, and a fun person to work with...Thanks!.

To Laura Spitler – for the patience and guidance through the FRB mysteries. You were not formally my advisor but your support felt like. It has been so much fun to work with you...Thanks!.

Di Li, Weiwei Zhu and their team – for the scientific guidance, for welcoming me in China and showing me around. Every trip to China was full of surprises and learning about your culture... Xièxiè.

Ewan Barr, Gemma Hansen and Norbert Langer – for being members of my TAC, for accompanying and guiding me through the PhD.

The *Fundis* group – as a whole – for the fun, help and good vibes. Special mention to Paulo Freire, Hans Kloeckner, the Roberts Main and Wharton, Ramesh Karuppusamy, Aris Noutsos and John Antoniadis.

Alex Kraus – for coordinating each of the observations with Effelsberg that were involved in this thesis and for sneaking in some observations on short notice. I extend my thanks to the Effelsberg operators team, with special mention to Ralph, Willy and Thomas.

Henning (El gringo loco) Hilmarsson, my PhD twin – for being the greatest office mate for the PhD adventure...Takk!.

Jose (Joey) Martinez – for the friendship and good humour, and the tons of cumbias we played at the *office amigos*... Muchos thank yous!.

Eleni Graikou – for helping me out with pulsar timing, for being a great friend and supporting me on the power-lifting adventure.

Natalya (Babushka) Porayko – for helping me out with statistics-related questions, for always surprising me with a new crazy idea, and for the endless discussions about communism... Spasibo!.

Ann-Sofie Bak Nielsen – whom I wish I had met before in my trips to Leiden – for the company and discussions about Nordic countries and socialism... Tak!.

Mariya Halvadzhieva – whom in a short time became a good friend – for being a loving and caring person, and a good listener.

Tilemachos (Nevermind) Athanasiadis – for entertaining Bouzouki sessions and deep discussions about random things. Efharisto!.

To Joscha Jahns – for being a good listener and the interesting discussions about CO2 emissions... Danke!.

To Jonah Wagenveld – for showing me how to dance your name... Dankjewel!.

The pulsar searching team: Tasha Gautam (Dhanyawad!), Vishnu Balakrishnan, Prawjal Voraganti (Dhanyavaada!), Jompoj Wongphecauxson (Kob khun krub!) and Marina Berezina (Spasibo!) for discussions about non-detections and the infinite ways pulsar scripts could crash.

My Aifa buddies: Kevin (thanks!), David and Ana (gracias!), and Toma (Mulţumesc!), for the company and the beers at Fiddlers.

Kira Kühn and Le Tran – for your kindness and guidance through the tons of German bureaucracy. You are the best!. Danke!.

Rainer and Simone, for supporting my crazy ideas when I was the IMPRS representative. Danke!.

Ralph and Charlie – for proofreading this thesis. Thanks!.

Elizabeta Fotina and Zlata Fedorova – for the friendship, fun, parties, and showing me music which I would have never listened otherwise. From Russia with love... Spasibo!

My *Astro PUC in Europe* team: Sofia Gallego, Yasna Ordenes, Pedro Salas and Rodrigo Leiva. Travelling across Europe to visit each other made Chile feel closer. Gracias totales!.

Olemma, Susi, Felipe and Luis – for constantly reminding me that friendship is independent of distance. Gracias totales!.

Thanks to my sweet Karla Diaz – for her unconditional friendship. Gracias totales!.

Matriarchs of my family: Mom, tía Pili, tía Sandra, tía Ingrid, Ingrid Gomez, Karen Reese and Carla Gomez – for the support, which was key to follow my dreams. Gracias totales!.

Lastly but not least, to my brothers, Luis and Marcelo – for the love, (∼)patience and inspiring me to become a better version of myself. Gracias totales!.

Contents

List of Figures

List of Tables

Nomenclature

Recurring acronyms

AGN	Active galactic nucleus	AXP	Anomalous X-ray pulsar
BH	Black hole	DEC	Declination
DM	Dispersion measure	EM	Electromagnetic waves
FRB	Fast radio burst	FoV	Field of View
GC	Galactic center	GRB	Gamma-ray burst
IGM	Intergalactic medium	ISM	Interstellar medium
LoS	Line of sight	NS	Neutron star
PA	Position angle	PSR	Pulsar
RA	Right ascension	RF	Radio frequency
RFI	Radio frequency interference	RM	Rotation measure
RRAT	Radio rotational transient	SEFD	System equivalent flux density
SGR	Soft gamma repeater	SNR	Supernova remnant
S/N	Signal to noise ratio		

Telescope acronyms

AO	Arecibo observatory 305-m William E. Gordon radio telescope
ASKAP	Australian square kilometer array pathfinder
CHIME	Canadian hydrogen intensity mapping experiment
EFF	Effelsberg 100-m radio telescope
EVN	European VLBI network
FAST	Five-hundred-metre aperture spherical radio telescope
GBT	Robert C. Byrd Green Bank Telescope
LOFAR	The low frequency array
Parkes	Parkes 64-m radio telescope
UTMOST	Upgraded Molongolo observatory synthesis telescope
VLA	Karl G. Jansky very large array
WSRT	Westerbork synthesis radio telescope

Numerical Constants

π	$= 3.14156$
$1\,\mathrm{rad}$	$= 57.296\,\mathrm{degrees}$
e	$= 2.7183$
$\log e$	$= 0.4343 = \ln(10)^{-1}$

Physical Constants

Speed of light	$c = 2.9979 \times 10^{10}\,\mathrm{cm\,sec^{-1}}$
Gravitational constant	$G = 6.670 \times 10^{-8}\,\mathrm{dynes\,cm^2\,gr{-}1}$
Planck's constant	$h = 6.626 \times 10^{-27}\,\mathrm{erg\,sec}$
Coulomb's constant	$k = 1$
Boltzmann's constant	$k_\mathrm{B} = 1.381 \times 10^{-16}\,\mathrm{erg\,deg^{-1}}$
Stefan–Boltzmann constant	$\sigma = 5.6704 \times 10^{-5}\,\mathrm{erg\,cm^{-2}\,s^{-1}\,K^{-4}}$
Electron mass	$m_\mathrm{e} = 9.110 \times 10^{-28}\,\mathrm{gr}$
Proton mass	$m_\mathrm{p} = 1.673 \times 10^{-24}\,\mathrm{gr}$

Astronomical Constants

Astronomical unit (1 AU)	$= 1.496 \times 10^{13}\,\mathrm{cm}$
Parcec (1 pc)	$= 3.086 \times 10^{18}\,\mathrm{cm}$
Solar mass ($1\,\mathrm{M_\odot}$)	$= 1.989 \times 10^{27}\,\mathrm{gr}$
Solar radius ($1\,\mathrm{R_\odot}$)	$= 6.960 \times 10^{10}\,\mathrm{cm}$
Solar luminosity ($1\,\mathrm{L_\odot}$)	$= 3.9 \times 10^{33}\,\mathrm{erg\,s^{-1}}$
Absolute magnitude of the Sun (M_V)	$= 4.8$
Apparent magnitude of the Sun (m_V)	$= -26.7$
Effective temperature of the Sun (T_eff)	$= 5770\,\mathrm{K}$

Chapter 1

Introduction

1.1 The transient radio sky

One may assume that all astrophysical events occur on timescales which are much longer than a human lifespan. However, there are transient phenomena in the sky which occur on the order of a few milliseconds to a few weeks. The first such transient events ever noticed were from supernova explosions[1] within the Milky Way. If these explosions are at distances of the order of a kiloparsec, they can be visible with the naked eye – as bright as the stars in the night sky. There are several transient phenomena in the sky when observed at radio frequencies also. Solar flares are sudden eruptions of electromagnetic radiation lasting tens of minutes to hours, detected also at radio frequencies (Dellinger, 1937), and if strong enough, may affect the communications near the 30 MHz producing a blackout[2]. Additional radio transient events are millisecond bursts from Jupiter also near the 30 MHz (Franklin & Burke, 1956), and the magnetically peculiar CU Virginis star, whose radio emission lasting hours is modulated by its rotational phase (Trigilio et al., 2000).

The birth of radio astronomy was in the 1930's, with Karl Jansky's search for the source of the noise interfering in radio transatlantic voice communications. The disturbances were soon found to be radio emission from the Milky way (Jansky, 1933). By the 1950's, radio detections included stars and other galaxies. By the 1960's, bright point sources with no optical counterpart were found, they were called *Quasars*[3]. In 1967, the *Mullard Radio Astronomy observatory* was built, an array consisting of dipole antennas observing at a radio frequency of 81.5 MHz. This radio telescope was used to study the angular size of distant radio sources through interplanetary scintillation[4]. While studying quasars a periodic 1.33-second signal was discovered (Hewish et al., 1968). At first, the source was assumed to be to terrestrial interference; however, it was soon confirmed to be astrophysical as the sky position and its parallax placed the source outside the solar system. Moreover, based on its flux density of $10^{17}\,\mathrm{erg\,s^{-1}}$ and periodicity, it was estimated that the source must not exceed a size of 4.8×10^3 km (Hewish et al., 1968).

[1] Extremely bright and powerful explosions of stars at the end of their lifetimes.

[2] Space weather prediction center: https://www.swpc.noaa.gov/phenomena/solar-flares-radio-blackouts

[3] Quasars are galaxies powered by a central supermassive black-hole actively accreting matter at high rate ($>10^3 M_\odot yr^{-1}$). Refer to Alexander & Hickox (2012) and references therein.

[4] Modulations of the flux density caused by the scattering from the solar wind leading (Narayan, 1992).

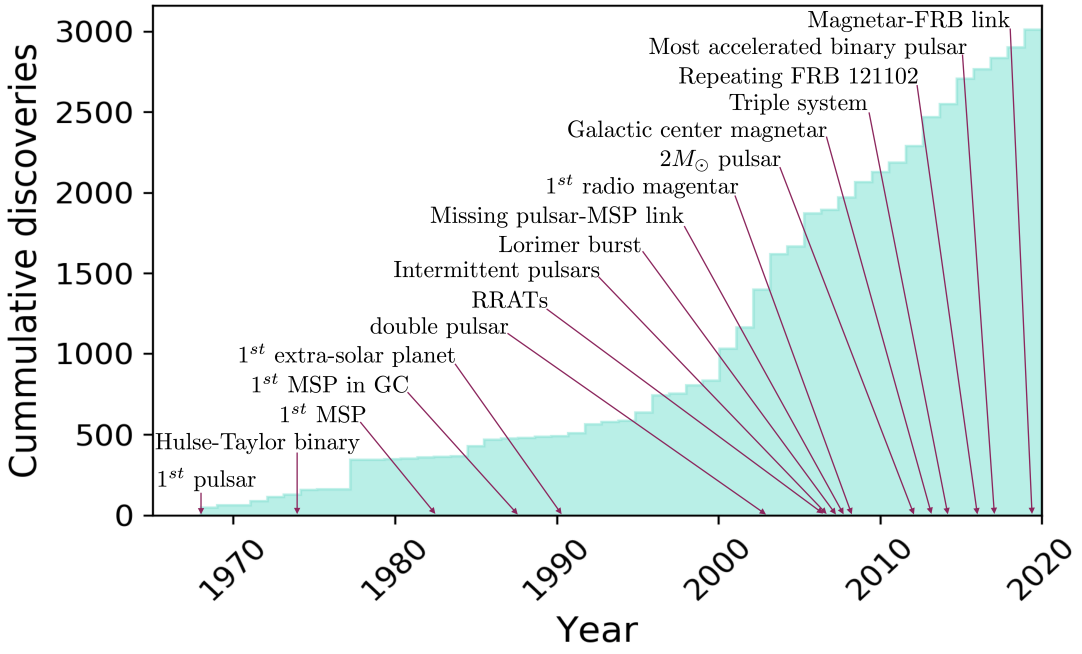

Figure 1.1: The cumulative number of pulsars discovered across time and discovery highlights. The year of discovery of the milestones is shown with arrows. The data was obtained from the ATNF pulsar catalog (see Footnote 6). Image adapted from Kramer & Stappers (2015).

Because of its compactness, the event was associated with stable oscillations of white dwarf (WD) and neutron stars (NSs). Interestingly, until then NSs were only hypothesised. Baade & Zwicky (1934) had proposed that the core collapse of a supernova explosion could leave behind a compact star composed mostly of neutrons. Later Tolman (1939) and Oppenheimer & Volkoff (1939) worked on the formalism to describe the hydrostatic equilibrium of NSs. The source reported by Hewish et al. (1968) was consistent with the NS prediction; however, the WD scenario was favoured. The strong evidence came along with the discovery of the Crab pulsar and its short spin period of 33.09 ms and association to a supernova remnant (SNR) (Staelin & Reifenstein, 1968; Lovelace & Tyler, 2012). Because of the apparent radio pulsations, such sources where named pulsars. In 1974, the Nobel prize in physics was awarded for the discovery of pulsars[5]. The interest for pulsars proliferated, and a new field in radio astronomy emerged.

Soon after the Mullard Radio observatory had announced the discovery of more pulsars, radio telescopes around the world had joined the pulsar hunt. Figure 1.1 shows the cumulative number of pulsar discoveries across time and highlights milestones in

[5] https://www.nobelprize.org/prizes/physics/1974/summary/

pulsar astronomy. Within the first two years, the number of known pulsars increased to above 40, thanks to telescopes such as the Molonglo in Australia (Vaughan et al., 1969; Turtle & Vaughan, 1968), Arecibo observatory in Puerto Rico (Craft et al., 1968), Jodrell bank telescope in UK (Davies & Large, 1970), the National Radio Astronomy Observatory in Green bank in US (Taylor & Huguenin, 1969; Reifenstein et al., 1969) and the Nançay Radio Observatory in France (Bourgois et al., 1969). During early stages, most of the advances in pulsar astronomy were due to the discovery of new sources. However, early on, it was proposed that they could be used as a tool for testing relativity and mapping the interstellar electron density (Counselman & Shapiro, 1968).

The steep increase in discoveries near the year 2000 (see Figure 1.1) was due to the start of a major large-scale pulsar survey using the 64-m Parkes radio telescope in Australia. The survey called *Parkes Multi-beam Pulsar Survey* (PMPS; Manchester et al. 2001), stands as the most successful survey to date. PMPS made use of a 13-beam receiver observing at a central frequency of 1.4 GHz. It was focused on surveying the Galactic plane between Galactic latitudes $|b| < 5°$ and longitude $50° < l < 260°$; thus, having excellent access to the inner Galaxy center. PMPS alone has discovered roughly one-third of the pulsars currently known, marking an era of big pulsar surveys. Additional large-scale surveys are the 1.4 GHz PALFA survey, which made use of the most sensitive radio telescope available at the time: the 305-m Arecibo observatory (Cordes et al., 2006). Additionally, the *High Time Resolution Universe* at 1.4 GHz, the first all-sky survey for pulsars using the 64-m Parkes for the southern sky search (Keith et al., 2010) and the 100-m Effelsberg as the northern counterpart (Barr et al., 2013).

Today, over 3000 NSs are known[6]. As seen in Figure 1.1, highlights are the Hulse-Taylor pulsar, the first pulsar in a binary system which led to the first evidence of the existence of gravitational waves (Taylor et al., 1974); the first exoplanets discovered, which were orbiting pulsar PSR B1257+12 (Wolszczan & Frail, 1992); the double pulsar, which is the best test of general relativity in the strong field regime (Kramer et al., 2006; Wex, 2014); new populations of pulsars: millisecond pulsars, RRATs (McLaughlin et al., 2006), Intermittent pulsars (Kramer et al., 2006) and magnetars (Camilo et al., 2006); and the newest radio transient, Fast radio bursts (FRBs). FRBs are millisecond duration radio flashes originated at cosmological distances, whose origin remains unknown (Lorimer et al., 2007).

From the detected population of NSs, pulsars are the fastest spinning and most abundant type known. The search for single pulses from pulsars led to the discovery of FRBs. They are also thought to be linked to NSs, due to the high energy involved in the bursts emission at cosmological distances (Lorimer et al., 2007; Spitler et al., 2016; Chatterjee et al., 2017). I discuss in the following Sections the properties of NSs, the basics of the pulsar model, the currently known population and their use as a tool to test fundamental physics. I continue with FRBs, and their connection to pulsars, what we currently know about them and their use as cosmological tools.

[6]Pulsar catalog: https://www.atnf.csiro.au/people/pulsar/psrcat/

1.2 Neutron stars

During most of a star's life, thermal and photon pressure balance the gravitational force (Gamow, 1939). A chain of conversions fuel energy production through nuclear fusion (e.g. Hydrogen to Helium, Helium to Carbon, etc.) until, eventually, no more energy can be obtained through fusion as the fuel runs out. At this point, thermal pressure alone is not sufficient to maintain the equilibrium, and the star collapses. Following the contraction, the density increases and electrons become a degenerate Fermi gas. If electrons produce enough pressure against the compression, then a *white dwarf* (WD) star is formed. However, if the star is massive ($M >\sim 10\mathrm{M}_\odot$), electron pressure is not enough to prevent the collapse and the star will continue to contract. Protons and electrons begin to combine to form neutrons through inverse β-decays[7], and the compactness will lead to a degenerate Fermi gas of neutrons. If neutron degeneracy pressure is enough to prevent further gravitational collapse, a NS is born. Due to the rapid transformation of electrons and protons into neutrons, an enormous amount o energy is released, and the outer layers of the star are expelled in a supernova explosion (Baade & Zwicky, 1934). However, if the star is too massive ($M >\sim 25\mathrm{M}_\odot$), the full collapse can not be stopped. The end product will be a *black hole* (BH).

As the star shrinks, due to the conservation of magnetic flux and angular momentum, the NS reaches extreme densities, high magnetic fields strengths and fast rotation. Inside the NS the matter is highly compressed. The typical density of $1.4\mathrm{M}_\odot$ in a sphere of 10 km radius leads to values above supra-nuclear densities in the NS core. Above nuclear densities, the state of matter is unknown (Arponen, 1972; Alpar & Sauls, 1988). At such high densities, superfluid neutrons, superconducting protons and exotic particles such as free hyperons or quarks may also exist in the core. As will be discussed in Section 1.6, the measurement of the NS mass for binary systems can constrain the matter expected to be found in the core (Antoniadis et al., 2013).

With magnetic fields as high as 10^{15} G, NSs are the strongest magnets in the Universe. The origin of such strong magnetic fields is not well understood; however, the accepted scenarios include dynamo effect or seed magnetic field from the progenitor star (Spruit, 2008).

Regarding rotation, a NS can spin as fast as a couple of milliseconds. The highest possible rotational frequency is given by Kepler frequency, above which centrifugal force leads to mass shedding (Burgio et al., 2003). Its value depends on the mass and radii of the NS.

1.3 Dipole model

The conventional model used to describe pulsars is the dipole in the vacuum. This is shown in Figure 1.2. In this model, the rotating NS has a dipolar magnetic field where the last field line that co-rotates with the NS, defines the radius of the *light cylinder*.

[7] Inverse β-decay reaction: $\nu_e + p \rightarrow e^+ + n$, where ν_e is the electron antineutrino, p is the proton, e^+ is a positron and n the neutron.

Inside the light cylinder, the field lines are closed (inner acceleration gap). Beyond the light cylinder the field lines are open, as the co-rotating speed is higher than the speed of light (outer acceleration gap) (Sturrock, 1971). At the magnetosphere, the highly collimated radio beam is produced. The charged particles are pulled out from the NS surface and accelerated to relativistic speeds along the open field lines, emitting photons through curvature radiation. This emission mechanism leads to a high degree of polarization. The electron-positron pairs formed through curvature radiation can be further accelerated, leading to emission at higher frequencies (Sturrock, 1971). Although pulsars seem to be pulsating, the radiation formed at the magnetic poles is continuous. The pulsating effect is a consequence of the misalignment between the rotation and magnetic axis, leading to beams sweep. If the beam crosses our line of sight, as the NS rotates, a series of pulses is detected at Earth. This is known as the *lighthouse effect*.

In the following, I provide a simplified view of the derivation of the main parameters of the dipole model based on concepts of electromagnetism described in Jackson (1975).

The radiated power from a rotating magnetic dipole is

$$P_{\rm rad} = \frac{2}{3}\frac{\ddot{m}^2}{c^3}, \tag{1.1}$$

where m is the magnetic dipole moment. If the magnetic dipole rotates with an angular velocity Ω, then the magnetic dipole moment is written as

$$m = m_{\rm o} e^{-i\Omega t} \tag{1.2}$$

$$\implies \ddot{m} = \Omega^2 m_{\rm o} e^{-i\Omega t}, \tag{1.3}$$

at time t=0

$$\ddot{m} = \Omega^2 m_{\rm o}. \tag{1.4}$$

Substituting into Equation 1.1

$$P_{\rm rad} = \frac{2}{3c^3}\left(m_{\rm o}\Omega^2\right)^2. \tag{1.5}$$

For an uniformly magnetized sphere of radius R and surface magnetic field strength B

$$m_{\rm o} = BR^3 \sin(\alpha), \tag{1.6}$$

where α is the magnetic inclination axis. Substituting into Equation 1.5, the magnitude of magnetic dipole moment is

$$P_{\rm rad} = \frac{2}{3c^3}\Omega^4\left(BR^3\sin(\alpha)\right)^2. \tag{1.7}$$

The angular speed can be re-written in terms of the spin period P as

$$\Omega = \frac{2\pi}{P}, \tag{1.8}$$

$$\implies \dot{\Omega} = -2\pi P^{-2}\dot{P}, \tag{1.9}$$

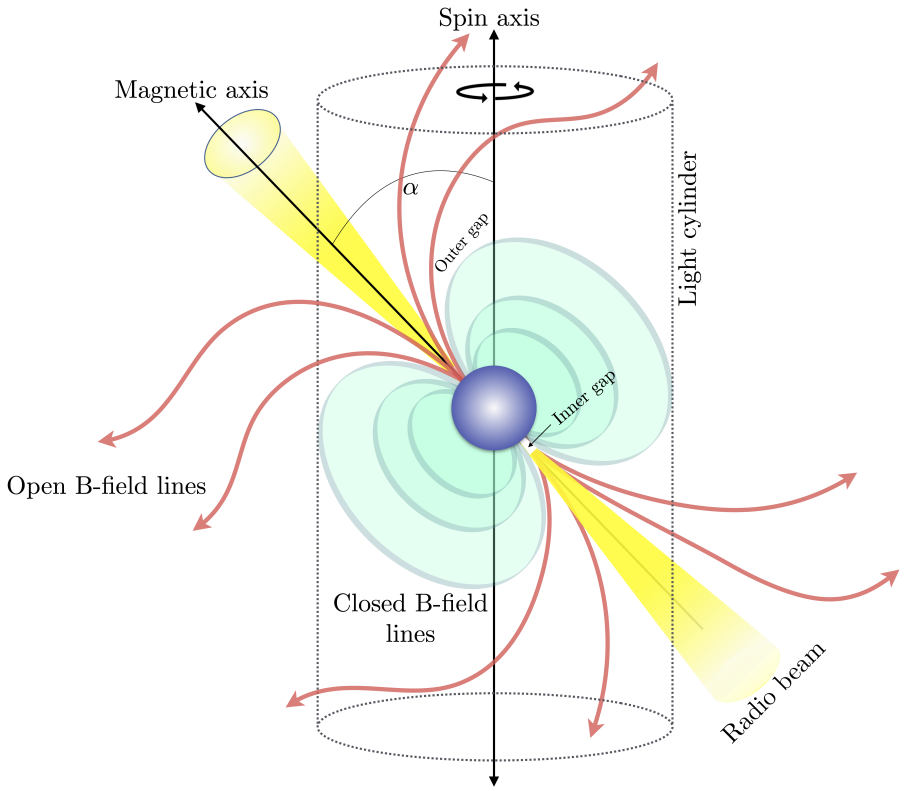

Figure 1.2: Schematic view of the dipole model for pulsars. The light cylinder is the imaginary surface at which the corotation speed equals the speed of light. Inside the cylinder the magnetic (B) field lines are closed, while outside the cylinder are open. The particles accelerated along the open B-field lines emit through curvature radiation. The electron-positron pairs generated are accelerated further and emit a collimated radio beam. The inclination angle α is the angle between the spin axis and the magnetic axis.

thus Equation 1.7 becomes

$$P_{\text{rad}} = \frac{2}{3c^3}\left(\frac{2\pi}{P}\right)^4 \left(BR^3\sin(\alpha)\right)^2. \tag{1.10}$$

For a pulsar the radiation comes from the loss of angular kinetic energy. The rotation energy is

$$E_{\text{rot}} = \frac{1}{2}I\Omega^2, \tag{1.11}$$

$$= \frac{1}{2}I\left(\frac{2\pi}{P}\right)^2, \tag{1.12}$$

hence the instantaneous power of the angularly accelerating pulsar is

$$\frac{dE_{\text{rot}}}{dt} = \frac{1}{2}I\frac{d}{dt}(\Omega^2), \tag{1.13}$$

$$= I\Omega\dot{\Omega}, \tag{1.14}$$

$$\implies \boxed{\frac{dE_{\text{rot}}}{dt} = -4\pi^2 I\frac{\dot{P}}{P^3}}. \tag{1.15}$$

If rotation is the main source of energy, then

$$P_{\text{rad}} = -\frac{dE_{\text{rot}}}{dt}, \tag{1.16}$$

thus we can equate Equation 1.10 to the negative of Equation 1.16 and obtain B as

$$B = \left(\frac{3c^3 I}{8\pi^2 R^6\sin^2(\alpha)}\right)^{\frac{1}{2}} (P\dot{P})^{\frac{1}{2}}. \tag{1.17}$$

We can estimate the moment of inertia for a canonical NS of 10 km radius and a mass of $1.4M_\odot$ under the assumption of uniform density

$$I = \frac{2}{5}MR^2, \tag{1.18}$$

thus B is composed of known constants plus P and $\dot{P}$. Replacing Equation 1.18 and re-writing in convenient units

$$B = 3.2\times10^{19}\left(\frac{P\dot{P}}{[s]}\right)^{\frac{1}{2}} \times \frac{1}{\sin(\alpha)}[G]. \tag{1.19}$$

The surface magnetic field strength has minimum value when $\alpha = 90°$, thus

$$\boxed{B > 3.2\times10^{19}\left(\frac{P\dot{P}}{[s]}\right)^{\frac{1}{2}}[G]}. \tag{1.20}$$

Normally, when referring to the surface B-field strength, it is implicit it is the minimum B and that the dipole radiation is only due to rotational energy loss. An additional useful quantity from the dipole model is the estimation of the dipole's age, referred to as *characteristic age*. To do so we re-write the identity

$$P\dot{P} = P\frac{dP}{dt}, \tag{1.21}$$

$$\implies \int_0^\tau P\dot{P}dt = \int_{P_o}^{P} PdP, \tag{1.22}$$

assuming there is no magnetic field decay, $P\dot{P}$ is constant[8]

$$P\dot{P}\int_0^\tau dt = \int_{P_o}^{P} PdP, \tag{1.23}$$

$$\implies P\dot{P}\tau = \frac{1}{2}(P - P_o)^2, \tag{1.24}$$

assuming that the observed spin period is much smaller than the initial $P_o^2 << P^2$, then Equation 1.24 becomes

$$\boxed{\tau = \frac{P}{2\dot{P}}}. \tag{1.25}$$

The pulsar's spin frequency ν is not constant as it looses energy with every rotation. As discussed in Lorimer & Kramer (2012), the slow-down of the pulsar over time can be written as

$$\dot{\nu} = -\alpha\nu^n, \tag{1.26}$$

where α is a constant and n is the so called *braking index*. n is expressed in terms of the frequency and it first and second derivative as

$$\boxed{n = \frac{\nu\ddot{\nu}}{\dot{\nu}^2}} \tag{1.27}$$

If the energy loss is purely through dipolar emission, then $n = 3$. However, other sources of energy loss, such as particle wind can also contribute to the spin-down (Harding et al., 1999). Measuring the braking index is challenging because it depends on the second time derivative, which is usually very small, with values below $10^{-20}\,\mathrm{Hz\,s^{-2}}$ (Espinoza, 2018). The older the pulsar, the smaller $\ddot{\nu}$ and the harder to measure it. For young pulsars where it has been possible to measure n, the values range from -1.2 to 3 (Espinoza et al., 2017), clearly indicating that spin evolution due to dipolar radiation is not the full picture. This is also proven by intermittent pulsars, where additional mechanisms (such as magnetospheric particle outflows) are required to explain the

[8] This should be taken with caution as the magnetic field is thought to decay (Goldreich & Reisenegger, 1992a). However, on short timescales the assumption is reasonable.

larger spin down rate in the on state than that in the off state (e.g. Kramer et al. 2006; Lorimer et al. 2012).

Equations 1.15, 1.20, 1.25 and 1.27 are the core equations of the dipole model, which despite its simplicity provides an insightful first order approximation of the pulsar's parameters based on the observables P and $\dot{P}$. The $P-\dot{P}$ *diagram* for pulsars is constructed from such dipole model, and in an analogy to the *Hertzsprung-Russell diagram*[9] for stars, it allows the different populations of pulsars to be identified. This will be further discussed in Section 1.5.

1.4 Propagation effects

The space between stars in the Galaxy is filled with a dilute medium rather than being empty. This diffuse medium is called *interstellar medium* (ISM), and makes up to 5% of the total mass of the Galaxy (Snell, 2011). The ISM is mainly composed of matter in the form of gas – which corresponds to 99% of its mass (Herbst, 1995) – but it has additional components such as dust and cosmic rays. The ISM is not static, the gas moves and therefore fluctuations are observed in density and temperature in different regions. New stars are born from those density/temperature fluctuations, and as they reach the end of their life, they return the material, for instance, through supernova explosions, which in turn provide feedback to new star formation.

As radio waves propagate to Earth, they interact with the ionized turbulent ISM. The beamed radio signals are primarily affected by *dispersion*, the frequency-dependent delay due to different group velocities; *scattering*, the delay due to multiple path propagation; *scintillation*, intensity variations due to constructive and destructive interference; and *Faraday rotation*, changes in the observed polarization by the magnetized plasma (Cordes, 2002). I discuss now each of these effects.

1.4.1 Dispersion delay

In vacuum, an electromagnetic (EM) wave of frequency f emitted at a distance d from Earth will propagate at the speed of light; thus, the travelling time is $t = d/c$. However, in the ISM the propagation time of the signal is increased due to the dispersion by the plasma along the path by a factor μ, also known as the *refractive index*. The group velocity (v_g) of the EM signal through the plasma is described to the first order by

$$v_{\rm g}(f) = c\sqrt{1-\left(\frac{f_{\rm p}}{f}\right)^2}. \tag{1.28}$$

[9]Example of the Hertzsprung-Russell Diagram: https://astronomy.swin.edu.au/cosmos/H/Hertzsprung-Russell+Diagram

For a low-density, non-relativistic, cold plasma composed mostly of free electrons, the plasma frequency is

$$f_{\rm p} = \sqrt{\frac{e^2 n_e}{\pi m_e}} \tag{1.29}$$

$$\simeq 8.5 \left(\frac{n_e}{\rm cm^{-3}}\right) \rm kHz, \tag{1.30}$$

where n_e is the electron density, e and m_e are the electron's charge and rest mass respectively. When $f < f_{\rm p}$ the signal does not propagate, and if $f >> f_{\rm p}$ the wave travels at roughly c. It is also inferred that higher frequencies are less affected by dispersion. This is one of the reasons why several pulsar/FRB searches are carried out at gigahertz frequencies.

The time delay introduced by the dispersion is

$$t_d = \int_0^d \frac{dl}{v_{\rm g}} - \frac{d}{c} \tag{1.31}$$

$$= \frac{1}{c}\int_0^d \left[1 - \left(\frac{f_{\rm p}}{f}\right)^2\right]^{-\frac{1}{2}} dl - \frac{d}{c}. \tag{1.32}$$

Using the binomial theorem for fractional exponent and keeping the first order of the expansion, we obtain

$$t_d = \frac{1}{c}\int_0^d \left[1 + \frac{1}{2}\frac{f_{\rm p}^2}{f^2}\right] dl - \frac{d}{c}. \tag{1.33}$$

We recall the expression for $f_{\rm p}$ in Equation 1.29 and finally obtain

$$t_d = \frac{e^2}{2\pi m_e c}\frac{\int_0^d n_e\, dl}{f^2}. \tag{1.34}$$

The *Dispersion Measure* is defined as the integrated free-electron density along the path between the source and the observer

$$\rm DM \equiv \int_0^d n_e\, dl. \tag{1.35}$$

Therefore the expression of the dispersive delay can be re-written as

$$t_d = \frac{e^2}{2\pi m_e c}\frac{\rm DM}{f^2}. \tag{1.36}$$

Re-writing it to convenient units we find

$$t_d = 4.15 \times 10^6 \left(\frac{\rm DM}{\rm pc\,cm^{-3}}\right)\left(\frac{f}{\rm MHz}\right)^{-2} \rm ms. \tag{1.37}$$

The DM is measured by comparing the pulse arrival time at different frequencies. In combination with an electron density model of the Galaxy, the pulsar distance can be estimated. Moreover, given an independent distance measurement, for instance, through parallax (Gullahorn & Rankin, 1978) or source association with supernova remnants or globular clusters (GC), the electron density along the line of sight can be mapped (Cordes & Lazio, 2002; Yao et al., 2017).

Worth noting that the dispersion delay can be corrected, so the different observed frequencies can be combined to create an integrated pulse profile. This will be further discussed in Section 3.2.2.

1.4.2 Faraday Rotation

Faraday rotation is the result of the interaction between EM wave and the magnetic field in a ionized medium, leading to the rotation of the linear polarization plane. As pulsar/FRB signals propagate to Earth, they encounter the magneto-ionized component of the ISM. The Lorentz force exerted on the free electrons force them to move in a plane perpendicular to the magnetic field direction. This results in a delay produced by the difference of the refractive index of the right and left-handed polarization.

The difference in phase for the right (+) and left polarization (−) for an EM pulse emitted at a distance d at a frequency f is:

$$\Delta\Psi_{\rm F} = \int_0^d (k_r - k_l) dl, \tag{1.38}$$

where k is the wavenumber ($k = 2\pi/\lambda$). We use the refractive index μ to the second order and re-write k as

$$k(f) = \frac{2\pi}{c} f\mu \tag{1.39}$$

$$= \frac{2\pi}{c}\sqrt{1 - \frac{f_{\rm p}^2}{f^2} \pm \frac{f_B f_{\rm p}}{f^3}}, \tag{1.40}$$

The cyclotron frequency f_B is

$$f_B = \frac{eB_{||}}{2\pi m_e c}, \tag{1.41}$$

with $B_{||}$ as the magnetic field parallel to the line of sight. Substituting Equation 1.41 into 1.40, and afterwards introducing it in Equation 1.38 we obtain a difference in phase given by

$$\Delta\Psi_{\rm F} = \frac{e^3}{\pi m_e^2 c^2 f^2} \int_0^d \left(n_e B_{||}\right) dl. \tag{1.42}$$

In analogy to dispersion measure, the *rotation measure* is defined as

$$\mathrm{RM} = \frac{e^3}{2\pi m_e^2 c^4} \int_0^d \left(n_e B_{||}\right) dl, \tag{1.43}$$

thus Equation 1.42 becomes

$$\Delta\Psi_{\rm F} = 2\lambda^2 \times {\rm RM}. \tag{1.44}$$

The observed polarisation position angle (PPA), which defines the orientation of polarisation plane with respect to the line of sight is (Radhakrishnan & Cooke, 1969)

$$\Delta\Psi_{\rm PPA} = \lambda^2 \times {\rm RM}. \tag{1.45}$$

The DM and the RM are used to estimate the average magnetic field strength along the traveled path with

$$\overline{B}_{||} = \frac{\int_0^d \left(n_e B_{||}\right) dl}{\int_0^d n_e dl}, \tag{1.46}$$

recalling the expression for the DM and RM in Equations 1.35 and 1.43, and re-writing in convenient units

$$\overline{B}_{||} = 1.23\,\mu{\rm G} \left(\frac{\rm RM}{\rm rad\,m^{-2}}\right) \left(\frac{\rm DM}{\rm pc\,cm^{-3}}\right). \tag{1.47}$$

DM and RM are key values to describe the propagation of radio waves and will be extensively used across this thesis.

1.4.3 Scattering

The fluctuations in the electron density along the line of sight, lead to a non-constant refractive index μ. As a result, an EM pulse undergoes multi-path propagation. In order to derive the expressions for the EM pulse broadening and the intensity variations, the so-called thin-screen model is used. It is a simplified model that assumes the material causing the pulse scattering is in a thin-screen of width a, located halfway between the source and the observer (Williamson, 1972). As seen in Figure 1.3, the initially coherent emitted EM waves are randomly distorted by the electron density perturbations (Δn) at the screen. This broadening effect is due to the direction changed by an effective angle θ. While most of the radiation arrives simultaneously, a fraction of it will arrive later, forming an asymmetric broadening of the pulse. The asymmetry is modelled with a one-side exponential convolved with the intrinsic pulse shape.

The observed intensity of a pulse as a function of time is (Lorimer & Kramer, 2012)

$$I(t) \propto e^{\frac{-\Delta t}{\tau_s}}, \tag{1.48}$$

where Δt is the geometric time delay due to a longer optical path

$$\Delta t = \frac{\theta^2 d}{c}, \tag{1.49}$$

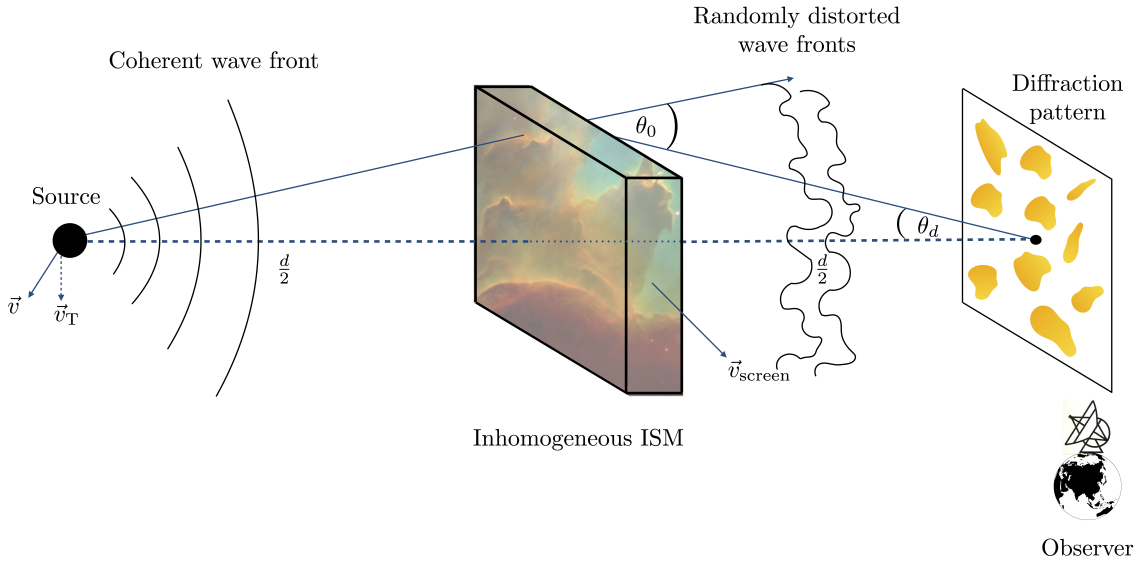

Figure 1.3: Schematic view of the thin-screen scattering model. It assumes that the material causing the pulse scattering is in a thin screen of width a, located between the observer and the source. The coherently emitted waves are distorted due to the scattering by the inhomogeneities in the screen, leading delays in the time of arrival and a diffraction pattern at the observer's position. Adapted from Lorimer & Kramer (2012).

and τ_s is the *scattering timescale*

$$\tau_s = \frac{\theta_d d}{c} \tag{1.50}$$

$$= \frac{e^2}{4\pi^2 m_e^2} \frac{\Delta n_e^2}{a} d^2 f^{-4}. \tag{1.51}$$

As seen in Equation 1.51, the pulse shape broadening is more pronounced at low observing frequencies, due to the strong dependence of the scattering time with the frequency. Contrary to the effect of dispersion and Faraday rotation, scattering can only be partially corrected (for example) through multi-frequency observations, where the strong frequency dependence of scattering allows the ISM effects and other achromatic to be distinguished (Palliyaguru et al., 2015). Scattering makes challenging to detect sources with pulse widths narrower than the scattering time, as they are broadened, becoming weaker and in some cases undetectable. The scattering effect limits the sensitivity to pulses at large distances, such as FRBs, or sources located in environments with high plasma density, such as pulsars in the Galactic center (Macquart & Kanekar, 2015).

1.4.4 Scintillation

Closely connected to scattering is *scintillation*, the phase shifts due to the density fluctuations previously discussed, that give rise to constructive and destructive diffraction patterns (see Figure 1.3). Scintillation occurs when the phase of the waves differ by less than one radian (Lorimer & Kramer, 2012)

$$2\pi \Delta f \tau_s \sim 1, \tag{1.52}$$

thus, it is a modulation of intensity as a function of time and frequency. The bandwidth Δf is the frequency width of the regions of enhanced or reduced intensity, and is known as *scintillation bandwidth* or *decorrelation bandwidth*. *Scintillation timescale* is the time modulation of the intensity fluctuations. The regions with enhanced intensity are referred to as *scintills*. The interference intensity patterns and its time modulation depend on the properties of the scattering screen, such as scattering material sizes, the relative velocity between the source and observer, and the distance.

When the distance of the scattering screen to the observer is small – near field approximation – scintillation occurs in the *weak regime*. Examples of near turbulent screens are the solar wind and Earth's ionosphere. The Fresnel diffraction equations are used to describe weak scintillation. On the other hand, if the screen is in the far-field, then scintillation is in the *strong regime*, and Frauhnofer's diffraction formalism is used (Narayan, 1992). For strong scintillation, diffractive and refractive effects are taken into account. Diffractive scintillation has a timescale of minutes to hours, and arises from the small inhomogeneities in the electron density (Galt & Lyne, 1972). On the contrary, refractive scintillation is caused by the large scale inhomogeneities, leading to scintillation timescales of the order of days to weeks (Rickett et al., 1984).

Interestingly, pulsars are the only known radio sources sufficiently compact to show diffractive scintillation (Dai et al., 2016).

As the intensity modulations depend on the relative motion of the pulsar and the screen, its velocity component transversal to the line of sight can be calculated as (Lorimer & Kramer, 2012)

$$V_{\rm ISS} = \frac{A}{\rm kms^{-1}} \left(\frac{d}{\rm kpc}\right)^{\frac{1}{2}} \left(\frac{\Delta f_{\rm DISS}}{\rm MHz}\right)^{\frac{1}{2}} \left(\frac{f}{\rm GHz}\right)^{-1} \left(\frac{\Delta t_{\rm DISS}}{\rm s}\right)^{-1} \tag{1.53}$$

where A is a constant that depends on the distribution of the inhomogeneities along the line of sight and the screen geometry.

For distant pulsars, the scintillation effect is negligible as the decorrelation bandwidth is too large to be observed within a standard observation bandwidth of a few hundreds of MHz. Therefore scintillation is better observed in nearby pulsars with low DM.

1.5 The radio pulsar population

As of now, we have described pulsars in a neutral manner, reducing them to a NS that emits a collimated radio beam. However, there are several populations of pulsars with particular emission features. Here we discuss the most abundant populations observed at radio frequencies. A $P - \dot{P}$ diagram of the known radio pulsars reported in the ATNF catalogue (as of October 2020) is shown in Figure 1.4. The $P - \dot{P}$ is constructed based on the dipole model presented in Section 1.3. Alongside are displayed lines of constant surface B-field strength (Equation 1.20), lines of constant rotational energy loss (Equation 1.15) and characteristic age (Equation 1.25). Four populations are identified: normal pulsars, millisecond pulsars, radio rotational transients and radio magnetars.

1.5.1 Normal pulsars

Normal pulsars correspond to the big island in the center of the $P - \dot{P}$ diagram and are by far the most abundant known radio pulsar population. As discussed in Section 1.3, they are rotating NSs that emit beams of electromagnetic radiation along their magnetic axis as result of the spin-down. This is the reason why they are known as rotation-powered pulsars (hereafter referred as "pulsars" unless otherwise specified).

The slowest spinning pulsar to date is PSR J0250+5854 with a spin period of 23.5 seconds (Tan et al., 2018). As seen in the $P - \dot{P}$ diagram, most of the normal pulsars have B-field strengths ranging from 10^{11}– 10^{13} G. Iconic pulsars in this population are PSRs B1919+21, the first pulsar ever detected; B0531+21, also known as the Crab Pulsar, the first pulsar to be associated with its SNR (the Crab Nebula); B0833-45, known as the Vela pulsar due to its association with the Vela SNR, the brightest pulsar at radio frequencies.

From the $P - \dot{P}$ diagram it is observed that pulsars span a wide range of ages, from thousands of years to Gigayears. It is also observed that young pulsars have spin

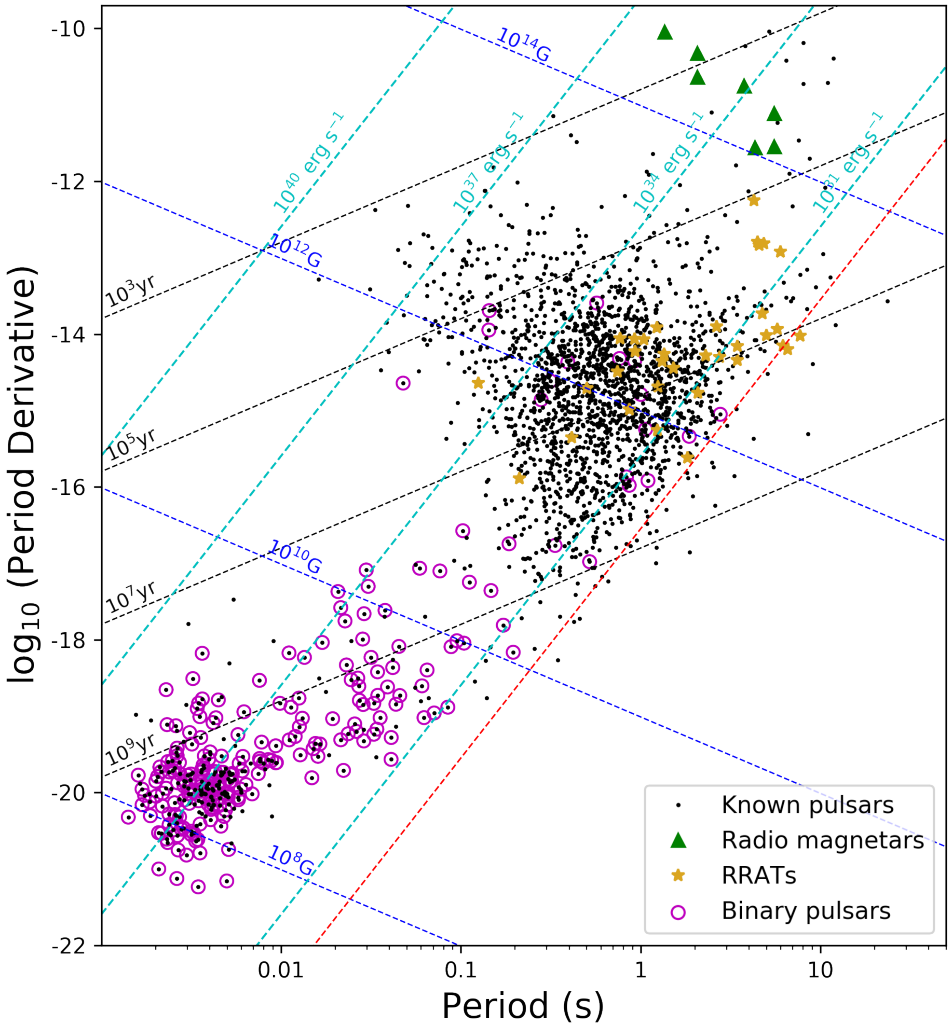

Figure 1.4: $P - \dot{P}$ *diagram.* Known pulsars are shown with *black dots*, pulsar in binary systems with *magenta circles*, radio rotational transients (RRATs) with *yellow stars* and radio magnetars with *green triangles*. Alongside are drawn lines of constant magnetic field strength (*blue dashed-lines*), lines of constant characteristic age (*black dashed-lines*) and lines of constant rotational energy loss (*cyan dashed-lines*) as derived from the rotating dipole model. The death line shown corresponds to Bhattacharya et al. (1992) classic polar gap model (*red dashed-line*) and represents the point where pulsar's radio emission is expected to cease.

periods that are much shorter than the old pulsars[10]. They are of particular interest as they probe the properties of pulsars at birth such as their spin periods (e.g. Igoshev & Popov 2013), B-field strengths (e.g. Muslimov & Page 1996), thermal cooling (e.g. Potekhin et al. 2015) and velocities (e.g. Noutsos et al. 2012). Pulsars are born with short spin periods of the order of milliseconds (e.g. Perna et al. 2008) and mean velocity of $450 \pm 90\,\mathrm{km/s}$ (Lyne & Lorimer, 1994). Because the typical velocity of stars in the Milky Way is near $30\,\mathrm{km/s}$, pulsar must have acquired such high birth velocities from kicks due to asymmetries during the SN explosion (Lai et al., 1995; Spruit & Phinney, 1998). We further discuss in Chapter 6 the properties at birth and how they evolve during the life of a pulsar.

Despite being rotation powered, young and old pulsars usually have distinctive behaviours. Several young pulsars have been seen to show sudden spin-ups, a phenomenon known as *pulsar glitches*. Glitches are believed to be the result of a rapid transfer of angular momentum from the superfluid core of the NS to its crust (Anderson & Itoh, 1975). There are 58 pulsars in the ATNF catalogue known to have glitched at least once; one of the most remarkable glitching pulsars is the Crab pulsar with over 26 Glitches detected to 2015 (Lyne et al., 2015). Regarding the population of older pulsars (age $> 1\,\mathrm{Myr}$), a fraction of them shows an abrupt cessation of their emission, either during several spin periods or for longer timescales (minutes, hours, days). The short-term behaviour of the radiation is called *pulsar nulling* (Backer, 1970), while the long-term one is called *pulsar intermittency* (Lyne, 2009).

1.5.2 Millisecond pulsars

Millisecond pulsars (MSPs) are old and fast-rotating pulsars, with spin periods typically below 30 ms and ages of the order of gigayears. They correspond to the cluster in the bottom-right part of the $P - \dot{P}$ diagram. MSPs are a different population of radio pulsars as their evolution underwent binary evolution. MSPs are believed to be formed from normal pulsars in binary systems, where they have attained their fast rotation from the accretion of matter and angular momentum from a companion star at the cost of the orbital angular momentum (e.g. Alpar et al. 1982; Bhattacharya & van den Heuvel 1991a). This is called the *recycling scenario* and is supported (among other) by the high fraction of MSPs in binary systems (*purple-circles* in the $P - \dot{P}$ diagram). Besides the rapid spin, MSPs have significantly smaller surface B-field strengths 10^8–$10^9\,\mathrm{G}$, raising the question of whether the B-field decay is a consequence of the accretion process or the old age of the pulsar. Chapter 6 dives into both scenarios and models a B-field evolution occurring before the accretion process.

MSPs can have a constant energy loss rate. Upon correcting their spin period by the steady spin-down, they are extremely stable rotators, whose precision approaches that of atomic clocks over timescales of a few years (Davis et al., 1985). Their time-keeping feature is the key for most of the use of pulsars as tools for fundamental physics, which will be discussed in Section 1.6. Out of the roughly 300 known MSPs, 70% are in

[10]Excluding MSPs, which are a different population of pulsars which were spun up to millisecond periods through accretion from the companion star.

binary systems, where the predominant companions are helium white-dwarfs (∼45%), carbon-oxygen white-dwarfs (∼15%), and other neutron star companions (∼2%). The study of MSPs and their companions is crucial to understand stellar binary evolution (Tauris et al., 2011a, 2012a).

1.5.3 Radio rotational transients

Rotating radio transients are sources with a sporadic emission of radio pulses; thus, they are generally not detected in standard pulsar periodicity searches (see Section 3.2.1.1 for search methods). The reprocessing of the PMPS survey led to one-quarter of the previously detected pulsars, to be also seen through single pulses. However, additional 17 sources had no corresponding periodic pulsar counterpart. The study of the time intervals between pulses, by calculating the greatest common denominator, revealed in many RRATs its underlying periodicity and showed they were indeed rotating objects (McLaughlin et al., 2009).

As it is seen in the $P - \dot{P}$ diagram, RRATs have a wide range of spin periods, from hundreds of milliseconds to several minutes. RRATs are thought to be extreme pulsar nullers which remain off most of the time; thus, not all of the regularly-spaced pulses are detected. Over 100 RRATs have been discovered, 75% of them with an identified spin period (ANTF catalogue, see Footnote 6).

1.5.4 Magnetars

Magnetars are young and highly magnetized neutron stars, with magnetic field strengths as high as 10^{15} G and spin periods from hundreds of milliseconds to tens of seconds[11]. They were detected first as soft gamma repeaters (SGRs) and anomalous X-ray pulsars (AXPs), due to the bursts detected in γ-rays and flare activity in X-rays (Mazets et al., 1979). Although their connection to NSs was established early on, their spin periods of seconds and the young age of kiloyears was inconsistent with the short spin periods expected for young pulsars. For a long time, they were not seen in radio frequencies. The probe of their link came years later with the discovery of radio pulsations from magnetar XTE J1810-197 (Camilo et al., 2006) and afterwards 1E 1547.0-5408 (Camilo et al., 2007). To date, seven magnetars are known to emit in radio frequencies (see Magnetar Catalogue Footnote 11).

Perhaps the most remarkable feature of magnetars is that contrary to normal radio pulsars, where the rotation powers their emission, magnetars are powered by the dissipation of their strong magnetic field on short timescales of thousands of years (Thompson & Duncan, 1996a). This is supported by the persistent X-ray luminosities of $10^{35}\,\mathrm{erg\,s^{-1}}$ seen in SGRs, which is up to two orders of magnitude above the luminosities expected from rotational energy loss (Thompson & Duncan, 1995).

[11] http://www.physics.mcgill.ca/~pulsar/magnetar/main.html

1.6 Laboratories for fundamental physics

Pulsars have a wide variety of science applications; however, here, I will focus on those which aim to address questions in fundamental physics.

1.6.1 Testing theories of gravity

Compact objects such as NSs are superb tools to test theories of gravity in the strong-field regime, where the largest deviation from a flat space-time is found. As mentioned before, they are incredibly stable rotators, where the emission time of each pulse is precisely known. Any small[12] deviations from the expected time of arrival on Earth is a fingerprint of a physical phenomenon. Pulsars in close binary systems are of particular interest, as they provide large deviations from a Keplerian orbit. As the binary loses energy due to gravitational wave emission, they spiral-in and the orbital distance decreases. The changes in the orbital parameters are thus measured through long-term timing.

The first binary neutron star system PSR B1913+16, also known as the Hulse-Taylor binary, consist of two neutron stars, where one is observed as a pulsar (Taylor, 1975). The system is in a very tight orbit of 7.75-hr with a high eccentricity of 0.61, and where the NS observed as a pulsar has a spin period of roughly 59 ms. Upon its discovery, Taylor (1975) immediately recognised the potential to test the deviation from Newton's gravitational physics. This is the reason why its discovery was awarded in 1993 with the Nobel prize in physics *"For opening up new possibilities for the study of gravitation"*[13]. The decrease in the orbital distance is in precise agreement with the orbit shrinking due to the loss of gravitational waves predicted by GR to the 99.8% level (Weisberg & Taylor, 2005; Weisberg & Huang, 2016). The Hulse-Taylor binary led to the first indirect evidence for the existence of gravitational waves. Later, Kramer et al. (2006) using the binary pulsar (both NSs emit as pulsars) PSR J0737-3039A/B, showed an agreement to the 99.95% level, which is up to date the most stringent test of GR in the strong field regime.

PSR J1757-1854 is a newly discovered relativistic binary: a 21.5-ms pulsar in a highly eccentric ($e \sim 0.6$) 4.4-h orbit with an NS (Cameron et al., 2018). PSR J1757-1854 stands as a tighter version of the Hulse-Taylor pulsar. As it has the most accelerated pulsar known, it has great potential to provide further constraints and to allow us to explore a new relativistic parameter space. Worth nothing, binary pulsars can be used for tests not only of GR but, also of alternative theories such as the scalar tensor theory of gravity.

1.6.2 Gravitational wave detector

Pulsars can be used to detect GW passing over Earth, through changes in the measured spin frequency due to the quadrupolar perturbations of space-time. GW signals will

[12] The most stable MSPs have fractional frequency instabilities $< 10^{-14}$ above one-year timescale. Example of this are PSRs B1937+21 and B1855+09 (Lorimer, 1998).

[13] https://www.nobelprize.org/prizes/physics/1993/press-release/

appear as an anomalous residual in the pulse arrival time (Detweiler, 1979). MSPs are preferred over young or normal pulsars as they have a more stable spin frequency over long timescales. Nevertheless, even MSPs are subject to intrinsic and extrinsic red-noise[14] variations, for instance, due to propagation effects. An optimal approach is to use a set of MSPs, whose residuals can be correlated to search for signatures in the pulse arrival times. This set of pulsars is referred to as *Pulsar timing array* (PTA), and provide an observing window into the extremely low-frequency GWs ($\sim 10^{-9} - 10^{-7}$ Hz) complementing LIGO/Virgo, LISA, and Cosmic microwave background (CMB) experiments. In this frequency range, GWs are primarily expected to be originated from individual massive nearby systems, or a stochastic GW background.

There are several PTA experiments around the world: the Parkes PTA (PPTA; Hobbs 2005), the European PTA (EPTA; Kramer & Champion 2013), the North American Nanohertz Observatory for Gravitational Waves (NANOgrav, Jenet et al. 2009a), all joining efforts under the International PTA (IPTA; Hobbs et al. 2010) experiment, to name a few. Although, as of now, no event has been detected with PTAs, stringent limits have been placed to the amplitude of the gravitational wave background (A_{GW}) from supermassive black hole binaries at the reference frequency of 1 yr^{-1}. PPTA constrained $A_{GW} < 1.0 \times 10^{-15}$ based on 4 pulsars (Shannon et al., 2013), EPTA constrained $A_{GW} < 3.0 \times 10^{-15}$ based on a 18-year dataset of six pulsar (Lentati et al., 2015), NanoGrav placed $A_{GW} < 1.37 \times 10^{-15}$ based on their latest 12.5-year dataset of 47 pulsars (Arzoumanian et al., 2020), and finally IPTA data release 1, found $A_{GW} < 1.7 \times 10^{-15}$ (Verbiest et al., 2016).

1.6.3 Constraining the equation of state of super-dense matter

The *Equation of State* (EoS) describes the relation between thermodynamic variables such as the density, pressure and radius. As we saw before, the composition of the NS core is poorly understood due to the largely unknown behaviour of matter at supranuclear densities. The possible components of the NS cores can be addressed by independently measuring macroscopic observables such as the NS mass, spin period and its radius. While the mass and the spin period can be accurately measured through pulsar timing, an independent measure of the radius is hard. The *X-ray Neutron star Interior Composition Explorer* (NICER) plans to measure the radii of neutron stars to a precision better than 5% (Gendreau et al., 2012). Riley et al. (2019) reports a mass of $1.34^{+0.15}_{-0.16} M_\odot$ and a radius of $12.71^{+1.14}_{-1.19}$ km for the first time for PSR J0030+0451 based on NICER data, through a pulse-profile modelling technique (Bogdanov et al., 2019).

Stringent constraints to the EoS have already been placed with mass measurements through the relativistic Shapiro delay in MSPs in binary systems with highly inclined orbits (Özel & Freire, 2016). This effect describes the delay in pulse arrival times as the pulsar passes behind its companion, due to the curvature of the space-time induced

[14] The color of noise refers to the frequency power spectrum. White-noise has flat frequency spectrum, i.e., is a linear function of the frequency (f). Red-noise (also called Brownian noise) has a power which scales proportional to $1/f^2$.

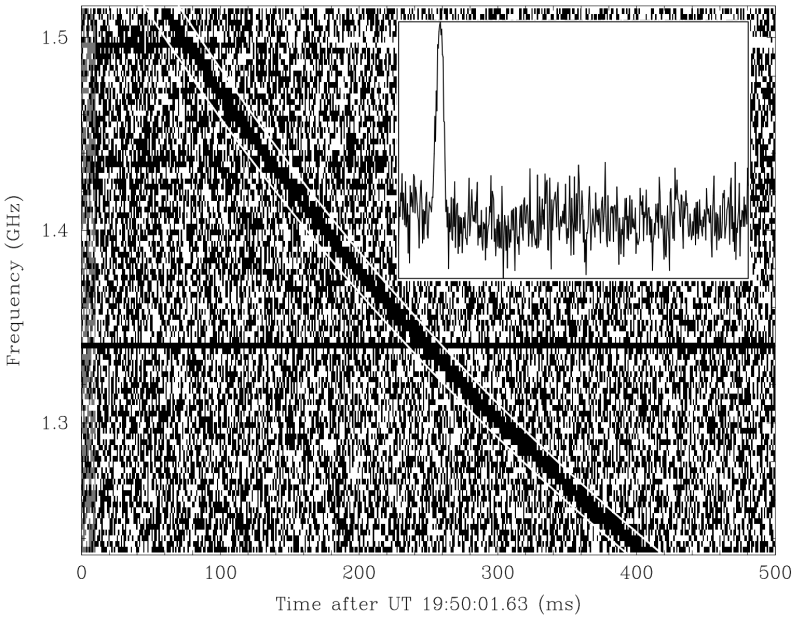

Figure 1.5: The Lorimer burst, first fast radio bursts detected. The plot shows the dynamic spectrum of the burst before correcting by dispersion delay. The smaller plot (*top-right*) shows the integrated pulse profile after the dispersion correction. Image from Lorimer et al. (2007).

by it (Kaspi et al., 1994). The Shapiro delay[15] can provide the mass of both, the MSP and its companion. Each EoS predicts a relation for the radius and the mass of the NS, particularly each EoS predicts a mass above which the NS collapses into a BH. If an EoS predicts a mass smaller than the measured mass of an MSP, then the EoS is excluded.

The mass measurements of $1.66 \pm 0.2 M_\odot$ for PSR J1903+0327 (Freire et al., 2011), $1.9 \pm 0.4 M_\odot$ for PSR J1614-2230 (Demorest et al., 2010), $2.01 \pm 0.04 M_\odot$ for PSR J0348+0432 (Antoniadis et al., 2013), and $2.14^{+0.1}_{-0.09} M_\odot$ for PSR J0740+6620 (Cromartie et al., 2020) excluded several EoS, and ruled out the presence of hyperons, bosons and free quarks in the NS core (Demorest et al., 2010). They also probed that NSs can be stable at masses well above the Chandrasekhar mass limit[16].

1.7 Fast radio bursts

In addition to pulsars, FRBs are the focus of this thesis project. As it was earlier mentioned, FRBs are a relatively new observational phenomena consisting of bright

[15] In combination with rate of advance in periastron ($\dot{\Omega}$) and assuming GR.

[16] The Chandrasekhar mass limit is nearly $1.4 M_\odot$. Below this mass the gravitational collapse is supported by electron degeneracy pressure. Above, electron degeneracy pressure is not enough to prevent gravity from further collapsing into a NS or BH.

radio flashes of millisecond duration. The first FRB ever discovered, known as the Lorimer burst (FRB 010724), was found over a decade ago during the reprocessing of the archival data of the Parkes radio telescope, while searching for single pulses of RRATs (Lorimer et al., 2007); then a new discovery in the pulsar field. As seen in Figure 1.5, the Lorimer burst displayed a quadratic frequency-dependent delay corresponding to a DM of 375 $\mathrm{pc\,cm^{-3}}$. This indicated a propagation through a column density, beyond the Milky Way's contribution. The subsequent radio follow-up of over 90-hr led to no new detections and no association to events at other wavelengths. The short duration suggested a stellar-size engine, and in combination with the one-off nature, apparently connected FRBs to cataclysmic events such as merging neutron stars or evaporating black-holes (Lorimer et al., 2007).

As more Parkes archival data were searched for single pulses, additional FRBs were detected (Keane et al., 2012a; Thornton et al., 2013; Burke-Spolaor & Bannister, 2014; Champion et al., 2016). All of them were single bursts (i.e. non-repeating) and – Except for the Keane et al. (2012a) burst – had DM excess beyond the contribution of the Galaxy, consistently placing FRBs at cosmological distances. However, they were only detected with Parkes, which at the time had yet another unknown phenomenon, called *Perytons*. They had similar characteristics to FRBs: broad-band, millisecond duration, and high DM. However, Perytons were found to be clustered around lunchtime, with very similar DM and coming from a specific direction. Further investigation of the signal revealed they corresponded to the microwave in the kitchen area (Petroff et al., 2015). They were originated by the sudden powering down of the magnetron, whenever the microwave's door was open before it finished the cycle.

FRB 121102, discovered in Arecibo's PALFA survey (Spitler et al., 2014), was the first FRB discovery from a telescope other than Parkes. Interestingly, FRB 121102 has three times the maximum DM contribution expected from the Galaxy along its line-of-sight. The picture of FRB as single events changed with the detection of 10 additional bursts from FRB 121102 (Spitler et al., 2016). The repetition rejected cataclysmic events as the origin for repeating FRBs.

During the first years, the observations were mostly carried out with single-dish telescopes. However, their small field-of-view (FoV) (see Section 2.3 for further discussion) was not optimal for carrying out surveys over a wide sky area. Adaptations of transit telescopes to perform Pulsar/FRB observation, such as *The Canadian Hydrogen Intensity Mapping Experiment* (CHIME), the upgraded *Molonglo Observatory Synthesis Telescope* (UTMOST), plus the *Australian Square Kilometre Array Pathfinder* (ASKAP) became a game-changer in the FRB field. The large FoV (200 $\mathrm{deg^2}$ for CHIME, 7.8 $\mathrm{deg^2}$ for UTMOST) of these telescopes increased the number of FRBs from a couple of tens to over thousands[17]. With the use of interferometers such as ASKAP, single-pulse FRBs can be localized to few arcseconds upon discovery. ASKAP alone has localized nine non-repeating FRBs (Macquart et al., 2020; Heintz et al., 2020) and one repeater (Kumar et al., 2019).

Up to now, over 20 repeaters have been reported (Spitler et al., 2016; CHIME/FRB

[17] https://chime-experiment.ca/en

Collaboration et al., 2019; Kumar et al., 2019; Fonseca et al., 2020). Interestingly, many of them have a much lower DM excess, implying that they are closer than FRB 121102. However, radio telescopes such as Arecibo and FAST are expected to find distant FRBs due to their higher sensitivity.

1.7.1 Repeating FRBs

FRB 121102 was for several years the only known repeating FRB, while more and more non-repeating FRBs were being detected. This started the discussion about whether FRBs stem from a single population of sources or two (or more) different populations. Despite the dichotomy, FRB 121102 opened a window in the study of FRBs, as its repetitions allow for the collection of many bursts to study their energy distribution, underlying repetition pattern, frequency structure and time evolution.

Bursts from FRB 121102 have shown complex time-frequency structure (Hessels et al., 2019) with multiple components and a downward drifting pattern, 100% linearly polarized emission, a flat polarization position angle, and a highly variable rotation measure (Michilli et al., 2018; Hilmarsson et al., 2020). For most non-repeating FRBs the localization is poorly constrained to several arcminutes, corresponding to the FoV of single-dish radio telescopes. On the contrary, the repeating nature of FRB 121102 allowed planned observations to pinpoint its position. Chatterjee et al. (2017) used interferometry with the VLA to localize FRB 121102, and Tendulkar et al. (2017) identified its host galaxy, a low-metallicity dwarf galaxy at a redshift of z=0.1. Marcote et al. (2017), with the use of the European VLBI Network (EVN) and Arecibo, pinpointed its position to milliarcsecond resolution and established the connection to a persistent radio source.

The repeating nature of FRB 121102 and its association to a persistent radio source placed young magnetars embedded in an SNR as the preferred scenario. Magnetars can explain the repeating behaviour, the persistent emission and the bursts, the high linear polarization fraction and flat polarization angle. The model of magnetars predicts emission at high energy, such as X-ray and $\gamma-$rays. Multi-wavelength follow-up campaign of non-repeating FRBs is challenging due to their one-off nature and poor localization. However, with the precise localization of FRB 121102, multi-wavelength observations became feasible (Scholz et al., 2017). As of now, no simultaneous radio/X-ray detection has been made; thus, placing only upper limits on the energy of a potential X-ray counterpart.

Lately, with the increasing number of new FRBs, so did the number of repeating sources. Transit instruments like CHIME and UTMOST are ideal for identifying repeaters due to daily coverage of their visible sky. During its commissioning, CHIME detected eight new repeating FRBs (CHIME/FRB Collaboration et al., 2019). One of those repeaters, FRB 180916, was localized soon after to its host, a massive spiral galaxy at redshift z=0.0337 (Marcote et al., 2020). Despite different host galaxy types, FRBs 121102 and 180916 are both located in a star-forming region within their host.

1.7.2 Progenitor scenarios

Whether FRBs belong to one or several source populations is still open to debate. Like neutron stars, FRBs could have several manifestations based on their age, environment, magnetic field strength. Naturally, models accounting for cataclysmic or non-cataclysmic events should be able to explain the observational characteristic of FRBs.

1.7.2.1 Cataclysmic progenitors

Most of the one-off cataclysmic events are based on a pulse generated by the merger between compact objects such as NSs, WDs and BHs. The merging binary NSs model argues that after the coalescence, the magnetic braking mechanism yields coherent radio emission (Totani, 2013a). Furthermore, the B-field strengths found in pulsars are sufficient to explain the observed FRB fluxes. The event rate of mergers of NS-NS system is also consistent with the FRB rates. For merging BH binaries, where at least one is a rotating BH, during the inspiral phase, the rapid magnetic flux change in the system leads to a magnetospheric outflow with an increasing wind power that results in the emission of coherent curvature radiation (Zhang, 2016). The BH-BH merger could produce an FRB and a short GRB accompanied by EM counterpart in X-rays and GWs. FRBs have also been hypothesized to be formed from binary WD-WD mergers, where the twisted magnetic field of the resultant massive WD triggers coherent emission from magnetic reconnection (Kashiyama et al., 2013). The model agrees with the rates of FRBs and predicts that some FRBs can be accompanied by type Ia supernovae explosions or X-ray debris disks.

Exotic models that could produce a millisecond radio pulse are the blitzar model, where a supermassive NS produces an FRB as it collapses to form a BH due to magnetic braking (Falcke & Rezzolla, 2014), NSs collapsing to a quark star resulting in a quark nova explosion (Shand et al., 2016), and white holes produced from primordial BHs exploding back (Barrau et al., 2014).

1.7.2.2 Non-cataclysmic progenitors

Non-cataclysmic models tend to involve neutron stars due to their strong magnetic fields, coherent emission mechanisms and strong gravitational fields. The large amount of energy emitted over millisecond durations requires a coherent emission process from a compact region of stellar size. Michilli et al. (2018) reported narrow temporal structure below $30\mu s$ implying an emission size of $<$10 km.

Models involving magnetars embedded in supernova remnants (Lyutikov, 2014; Beloborodov & Li, 2016; Metzger et al., 2017a), such as superluminous supernovae (SLSNe), propose that the burst originates from the interaction of the magnetar and its surrounding SNR. This can account for the changing DM seen in FRBs like FRB 121102 (Law et al., 2017), and agrees with the localizations of some FRBs to star-forming regions, which are typical magnetar environments. However, until recently, none of the known magnetars in the Galaxy showed an energetic FRB-like event that could support

the model. Moreover, none of the known radio magnetars showed bursts of similar characteristics in term of high energy. The missing connection appeared with the known Galactic magnetar SGR 1935+2154 in late April 2020, when X-ray bursts detected by INTEGRAL (Mereghetti et al., 2020) were followed by a very bright millisecond radio burst detected by CHIME (The CHIME/FRB Collaboration et al., 2020) and STARE2 (Bochenek et al., 2020). The radio burst with energy above 10^{34} erg is several orders of magnitude above the single pulses detected for any radio magnetar or pulsars thus far (The CHIME/FRB Collaboration et al., 2020); however, it is still a couple of orders of magnitude below the energetics of known FRBs.

The CHIME/FRB Collaboration et al. (2020) discovered an activity cycle with a periodicity of 16.3 ± 0.1 days in the repetition of FRB 180916. The periodicity clearly disfavours models invoking sporadic processes, such as NS and Asteroids/Comets interactions (Bagchi, 2017), and favours instead an orbital system, a precessing object (The CHIME/FRB Collaboration et al., 2020), or lensing of the NS emission by stellar winds (Cordes et al., 2017). Recently, a potential 157 day periodicity for FRB 121102 was suggested (Rajwade et al., 2020). We tested the periodicity hypothesis of FRB 121102 with data taken independently with Effelsberg at L-band (1.36 GHz). We present the analysis and results in Chapter 7.

1.7.3 Constraining progenitor scenarios

The growing number of detected FRBs have led to inferred event rate densities of FRBs between 10^3–10^4 over the whole sky every day (Champion et al., 2016; Bhandari et al., 2018). The statistical analysis of the FRB population and the event rates are used to compare the rate of potential progenitor sources. FRB repeaters are of particular interest, as it can be investigated how the isotropic energy of a collection of events is distributed. One commonly assumed distribution is a power-law with index γ

$$R(E > E_{\rm min}) \propto E^{\gamma} \tag{1.54}$$

where R is the rate of events above a given energy E. Note the energy ranges are so far restricted to radio frequencies from 0.3–8 GHz (Pilia et al., 2020; Chawla et al., 2020). We discuss in Chapter 7 the energy distribution of FRB 121102 with the use of bursts detected by Effelsberg.

Event rates for a survey or telescope – calculated with the number of events detected in a total observing time – is used to make predictions on the rate for other telescopes, following

$$R = R_{\rm ref} \left(\frac{F_{\rm min}}{F_{\rm ref}} \right)^{\gamma} \tag{1.55}$$

where $R_{\rm ref}$ is the reference rate at a a given telescope for a minimum detectable fluence of $F_{\rm min}$. Fluence (F) is the flux density of an event multiplied by its duration. It is emphasized that the deduced event rates among telescopes should not be compared without scaling the rates due to the difference in telescope sensitivities. Equation 1.55 is the most simple form of event rate scaling, additional methods include the luminosity

function (Luo et al., 2020). Knowing γ can also provide insights into the mechanisms responsible for FRBs. X-ray binaries and Active galactic nuclei (AGNs) show an energy distribution following a log-normal relation (Kunjaya et al., 2011), high-energy bursts of magnetars (Göğüş et al., 2000) and flares from Sgr A* (Li et al., 2015) show a power-law behaviour γ =-0.6 – -0.7. Giant pulses from pulsars like the Crab pulsar show also a power law γ =-2 (Karuppusamy et al., 2010), while for PSR J1823-3021A γ =-2.63 (Abbate et al., 2020).

For either one-off cataclysmic events or repeating sources, their progenitors must be abundant enough to explain the high rates of thousands or more events per day over the full sky. As discussed in Petroff et al. (2019), FRB rates are two orders of magnitude below the estimations for core-collapse supernova (CCSN), although the rates change considerably depending on the Ib or Ic supernova type. When compared with superluminous supernovas, the FRB rates are at least one order of magnitude larger. Transient events, such as GRB, are as well an order of magnitude below the estimated FRB rates. However, these estimations have not always considered FRB beaming fraction[18], which could significantly change the event rates (Connor et al., 2020).

Since the discovery of the repetition of FRB 121102, it has been clear that its burst detections are clustered. Oppermann et al. (2018) suggested that a Weibull distribution with shape parameter $k = 0.34$ is a good descriptor of the waiting time between consecutive detections. For Weibull statistics $k < 1$ means clustering of the events, $k = 1$ recovers the Poissonian case, and $k >> 1$ represents a constant separation of the events. We investigate in Chapter 7 whether the strong event clustering was a consequence of the unknown periodic activity.

1.7.4 Cosmological tools

Although the progenitors of FRBs remain unknown, the information encoded in their narrow and coherent pulses probe the medium they travel through. While pulsars probe the ISM, FRBs have travelled cosmological distances; thus, probing as well the inter galactic medium (IGM) and the ISM in their host galaxies. However, most of the cosmological applications require event numbers one or two orders of magnitude higher than the currently known, and most importantly, localizations to host galaxies. Thanks to telescopes such as CHIME, ASKAP and UTMOST the numbers are growing rapidly. Moreover, the use of telescope arrays enables them to act as an interferometer capable of a localization down to tens to a couple of hundreds of milliarcseconds.

Some of the applications of FRBs as cosmological tools discussed in the literature are:

- **Constraints on the Photon Mass:** If light propagates in the vacuum at the speed of light, the photon rest mass should be zero. If it is different than zero, then the speed of light in the vacuum is frequency dependent. Using FRBs, the time delay between the arrival of the different pulse frequencies is used to place a

[18] Describes the fraction of the sky covered by the radiation beam.

stringent upper limit on the rest mass of the photon (Wu et al., 2016). However, this frequency dependence is indistinguishable from the dispersion delay (see Section 1.4.1). Localized FRBs can overcome this problem if the DM contribution from the IGM, ISM and host galaxy is modelled. The limits place so far the photon mass below 5×10^{-50} kg (Wu et al., 2016; Bonetti et al., 2017).

- **Equation of state of dark energy:** FRBs can be used as standard candles to measure distances in the Universe at higher redshift ($z > 1$) than what is currently achievable with SNe type Ia. Liao et al. (2020) proposed a relation between the standardized luminosity and duration relation of FRBs that can be used to constrain the time variability of dark energy.

- **Epoch of reionization:** The evolution of the electron density in the IGM and its inhomogeneity during the epoch of reionization – phase transition where the gas in the Universe went from neutral to ionized – can be probed with the differential DM measurements of thousand of FRBs at high redshifts ($z > 6$; Zheng et al. 2014).

- **Cosmic anisotropy:** FRBs can be used to test the homogeneity and isotropy of the Universe on cosmological scales, by studying the fluctuations of the DM variance for FRBs across different lines of sight. If the fluctuations are due to noise, then there is no preferred direction in the Universe. However, thousands of FRBs with known redshifts are needed to find the cosmic anisotropy with a dipole amplitude of 0.01 (Qiang et al., 2020).

- **Constraining Weak Equivalence Principle:** One of the main foundations of Einstein's theory of general relativity is that two objects in the same gravitational field should fall with the same acceleration. If photons have non-zero mass, their speed depends on frequency, thus on the energy and their rest masses, yielding different accelerations. Upon modelling the propagation effects discussed in Section 1.4, the difference in the arrival time of two different frequencies is used to test the precision of the weak equivalence principle (Wei et al., 2015; Wang et al., 2020).

- **IGM magnetic fields:** Analogous to mapping the magnetic field in the ISM with pulsars through DM and RM measurements and Equation 1.47, FRBs can be used to map the magnetic field of the IGM. However, due to their cosmological distances, the DM and RM should be corrected by redshift (Zheng et al., 2014).

1.8 Thesis outline

On this Chapter I have discussed the current picture of pulsars and FRBs: how they were discovered, their connection to NSs, the propagation effects their radio emission is subject to, the sub-classes of pulsars and FRBs, and how they can be used as tools for fundamental physics.

- In Chapter 2, I discuss the data acquisition chain and what makes FAST and Effelsberg suitable telescopes to observe such radio transients.
- In Chapter 3, I show the most commonly used algorithms to search for such transients in timeseries and how to mitigate the effect of radiofrequency interference.
- In Chapter 4, I discuss the technique to extract the science of the pulsar discoveries, *pulsar timing*. I show the procedures to develop a timing model describing the time of emission of radio pulses and how it is improved through the regular monitoring of the sources until each rotation of the pulsar is precisely accounted for.
- In Chapter 5 reports the follow-up with Effelsberg of 10 new pulsars from the early FAST pulsar survey.
- In Chapter 6, I study the magnetic field evolution of pulsars to understand the transition between classical radio pulsar and recycled millisecond pulsar.
- In Chapter 7 I present the results of an extensive multi-wavelength campaign of FRB 121102 with the Effelsberg Telescope, the Green Bank Telescope and the Arecibo Observatory to shadow the Gran Telescope Canaria (optical), NuSTAR (X-ray) and INTEGRAL (gamma-ray).
- In Chapter 8 I discuss the implications of this thesis and present future prospects.

Chapter 2

Data acquisition

A radio wave detector consists of a conductor – such as a wire – connected to an electronic RC circuit. The incoming standing electromagnetic waves resonate and induce a current in the circuit, thus inducing voltages. The frequency of the resonance signal can be fine-tuned through the capacitor (C) and its intensity with the resistor (R). While the principle is simple, the complexity in a radio telescope arises from the low flux density of the astrophysical waves, the procedure to amplify the signal, and the fact that we are interested in a frequency range instead of a single frequency.

Contents

2.1 Components of a radio telescope

The main components of a radio telescope are a reflecting surface, the frontend and the backend. Figure 2.1 illustrates the data flow from the last two components. In the following, I will discuss their role in the data collection chain.

2.1.1 Reflector

The antenna is the reflecting surface responsible for collecting and focusing the incoming radio frequencies (RF). The spacial point where the RF focuses is where the feedhorn is placed.

Although the standard image of a radio telescope is a parabolic steerable dish, they exist in many shapes and can be classified based on their reflector's geometry (parabolic, spherical, cylindrical), focal plane position (Axial, Offset, Cassegrain, Gregorian) and if they are used as a stand-alone instrument or as part of an array in interferometric mode. Table 2.1 lists twelve radio telescopes around the world equipped to perform Pulsar/FRB observation and their geometry. For this thesis, I primarily used the 100-m Effelsberg (EFF) radio telescope, a parabolic fully steerable radio telescope; and the *Five-hundred-meter Aperture Spherical radio telescope* (henceforth FAST), a spherical radio telescope with fixed primary reflector. We discuss in more detail their specifications in Section 2.5 and 2.6. Additional facilities used to complement the observations were the 64-m *Parkes radio telescope* (fully steerable parabolic dish) for the pulsar science in Chapter 5; the 100-m *Green Bank Telescope* (GBT; parabolic fully steerable dish), and the Arecibo observatory (AO; fixed primary aperture) for the FRB science presented in Chapter 7.

Several reasons can lead to the preference of observations with one telescope over another. The *Low Frequency Array* (LOFAR), performs better at low frequencies, from tens to couple hundreds of MHz; while dishes, such as VLA, EFF, and PKS, are suited to high frequencies (>1 GHz). Transit telescopes, such as the *Canadian Hydrogen Intensity Mapping Experiment* (CHIME), offer all-visible-sky FoV at the cost of poor localization (tens of arcminutes to degrees). Regarding the sub-reflector types, the prime focus is of use for the full frequency range of the antenna, but blocks part of the incoming RF. Offset feeds can mitigate this issue as they reduce the blockage problem considerably, but introduce polarization artefacts (Uson & Cotton, 2008). What is the most suitable radio telescope depends on the science case. The information from a set of radio telescopes can be combined to boost the benefits of each type. If we take as example FRB science; while transit instruments like CHIME are the most effective telescopes at detecting new sources given their large FoV, interferometers, such as VLA are better at pinpointing accurate positions (as high as milliarcsecond resolution).

The wavelengths or frequency range that a radio telescope is sensitive to will greatly depend on the surface accuracy of the reflector. For instance, to be sensitive to radio waves with a length of 21 centimetres, the surface needs to be accurate to a fraction of the wavelength – otherwise, the RF loose coherence by the imperfections. The minimum flux density detectable by a radio telescope is defined by its collecting area and the efficiency of the dish, the ability of the receiver to amplify the RF, the observation's bandwidth, and ultimately the integration time of the observation.

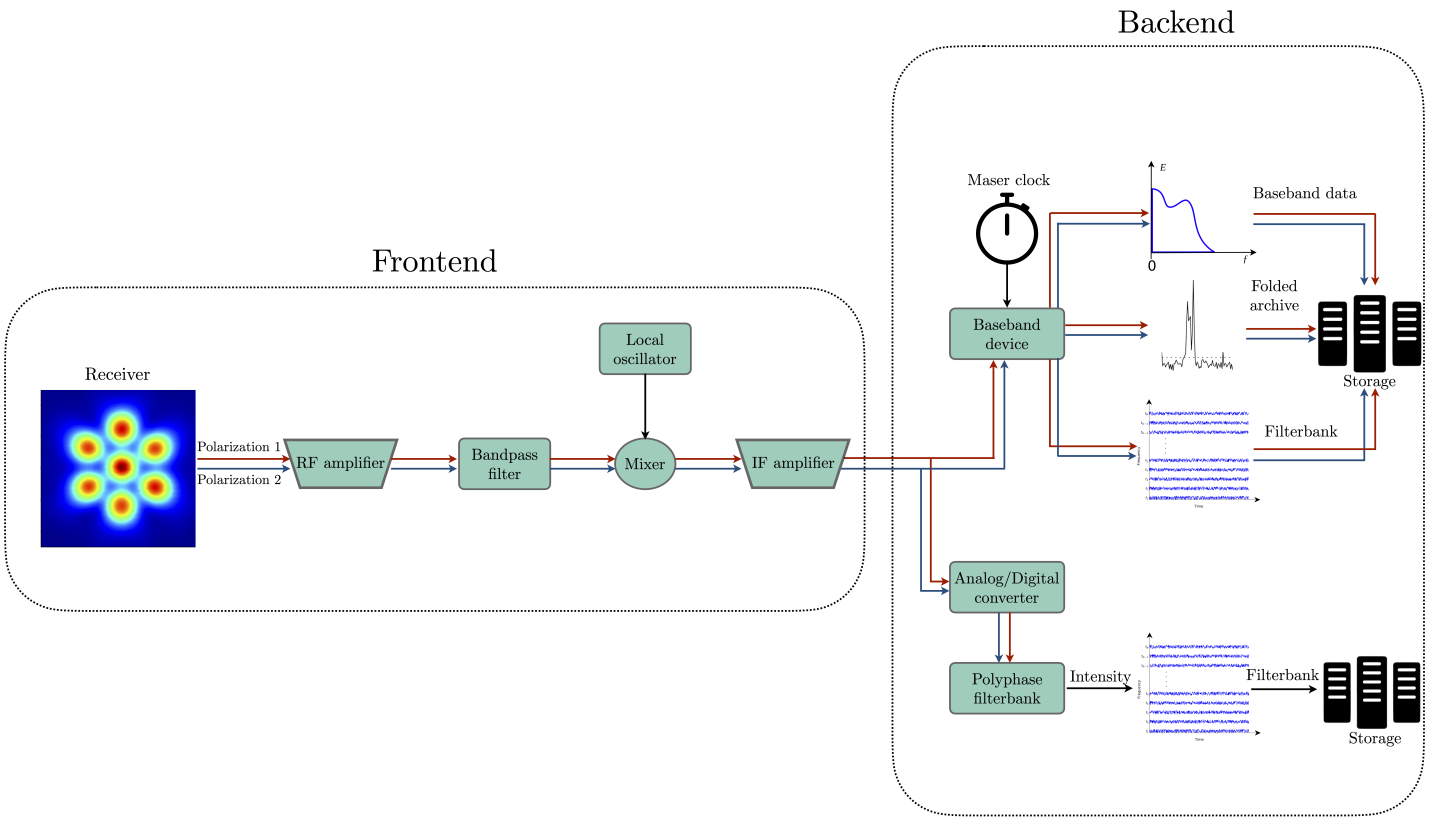

Figure 2.1: Pulsar data acquisition process for the 100-m Effelsberg radio telescope with the 7-beam receiver. The polyphase filterbank backend is used for the *search mode* observations, and the baseband backend for the *timing mode* observations. Abbreviations: RF=Radio frequency, IF=Intermediate frequency.

Name	Reflector	Focal plane	Mode	Size (m)	Frequency (GHz)
VLA	parabolic	offset Cassegrain	Interferometer	28×25	1.0–12.0
GMRT	parabolic	prime focus	Interferometer	30×45	300–1.4
Parkes	parabolic	prime focus	fully steerable	64	0.7–4.0
Lovell	parabolic	prime focus	fully steerable	76.2	0.4–1.4
EFF	parabolic	prime focus	fully steerable	100	1.2– 43.0
GBT	parabolic	offset Gregorian	fully steerable	100	0.3–15.0
AO	spherical	Gregorian	filled aperture	305	0.302–10.0
FAST	spherical	deformable	filled aperture	500	0.25–1.9
Nançay	Kraus-type	cross-antenna	transit	94	1.2– 3.5
LOFAR	dipoles	-	transit	1000	0.02–0.27
CHIME	cylindrical	north-south	transit	4×20×100	0.4–0.8
MeerKAT	parabolic	off-axis	Interferometer	64×13.5	0.856–3.0

Table 2.1: Example of radio telescopes around the world equipped to perform Pulsar/FRBs observations in the frequency range described in the sixth column. Abreviations: VLA=Very Large Array, GMRT=Giant Metrewave Radio Telescope, EFF=Effelesberg,GBT=Robert C. Byrd Green Bank Telescope, AO=Arecibo Observatory, FAST=Five-hundred-meter Aperture Spherical radio Telescope, Nançay=Nançay Radio Observatory, LOFAR=Low-Frequency Array, CHIME=Canadian Hydrogen Intensity Mapping Experiment.

2.1.2 Frontend

Frontend refers to the processing of the incoming RF entering feedhorn, to the first stage of amplification. The feedhorn is responsible for conveying the RF even further to a narrower beam, and for rejecting off-axis RF and frequencies outside the desired range. Most of the telescopes are equipped with two channels (n_p), where the RF is split into two orthogonal polarizations. Because the treatment of each channel is similar, in the following, I will focus on the description of one channel.

As shown in Figure 2.1, as the RF enters the receiver, it is amplified by the *low noise amplifier* (LNA). The amplifier is cooled cryogenically to a temperature of typically a few tens of Kelvin to limit the production of thermal noise. However, as this process amplifies all sorts of frequencies (not only the desired astrophysical ones) the signal is filtered by removing known frequencies from terrestrial transmitters (see Section 2.4) and is restricted to a preferred frequency range. This can be done before or after the LNA. The frequency response is known as bandpass. Its shape is a function of the LO, and often is made to resemble a boxcar function. However, in practice, the signal response is much more complex, and parts of the band are more sensitive to the receiver than others. An example of a bandpass response is shown in Figure 2.2. It was obtained by averaging the power at different frequencies over the observation. In the example, we see that the bandpass does not resemble a boxcar function. The most sensitive part of the bandpass shown in Figure 2.2 is the range from 1300 MHz to 1425 MHz, and from 1440 MHz to 1490 MHz, where the baseline is roughly flat. As it will be discussed in Section 3.2.4, the largest spike in the bandpass correspond to the 21 cm Hydrogen line.

The next step is the *mixer*, where the RF is mixed with the frequency coming from the *local oscillator* $f_{\rm LO}$, to bring the signal to an intermediate frequency (IF), $f_{\rm IF}$, which is defined by:

$$f_{\rm IF} = f_{\rm RF} - f_{\rm LO} \tag{2.1}$$

where f_{RF} is the frequency of the RF. The IF carries (under certain conditions) the same information as the RF, but with a tunable frequency that is chosen to convenience by modifying the f_{LO}. The mixing process is called *heterodyning*, and intends to reduce the signal loss due to cable transmission. Finally, the output of the frontend are analog voltages from the upper and lower sideband.

2.1.3 Backend

The backend is the final part of the data collection chain and is where the data is digitized and stored. As the IF enters the backend, the analog-to-digital converter (ADC) maps the incoming signal of the voltages at a given sampling rate (nanoseconds to microseconds order) to a digital number representing its magnitude. Such a number is an n-bit value, with 2^n. For example, for 8-bits the value ranges from 0 to 255 when unsigned, or from -128 to +127 when signed.

The two most common pulsar backends are *Fast Fourier transform (FFT) spectrometers* (Price, 2016) and *baseband backend* (Hankins & Rickett, 1975; Stairs et al.,

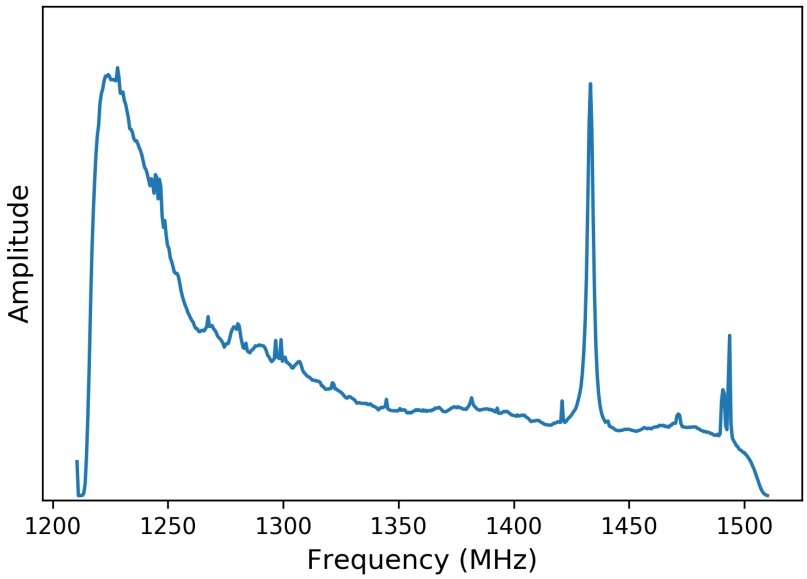

Figure 2.2: Bandpass response of the central beam of Effelsberg's 7-beam feed array at 1.36 GHz. The large spike correspond to the 21 cm hydrogen line and the less pronounced spikes to RFI.

2000). FFT spectrometers were among the first pulsar timing and searching backend used. They are multi-channel spectrometers which stream the data into narrow frequency bands after the ADC converter has digitized the data. To reduce the effect of spectral leakage[1] most backend use a *polyphase filterbank* system[2]. Nowadays, polyphase FFT spectrometers are the most common pulsar search backend. Because of this, both polarizations are summed as it is not needed for searching. Baseband backends became popular for pulsar timing as they preserve the signal phase, coherently correct the dispersion delay (see below), and provide high-precision timing and polarimetric information (Stokes parameters U, Q, V, I). Baseband backends imprint accurate timestamps to the samples through a maser clock. As polyphase FFT spectrometers are used mostly for pulsar search, they may or may not make use of a maser clock to synchronize.

After the signal is digitized, is formatted according to the scientific requirements, and sent to the disk storage to be collected whenever is needed for processing.

[1]Spectral leakage is when signals at specific frequencies distribute their power to adjacent Fourier bins. For strong signals such as radio frequency interference, the leakage can hinder astrophysical signals.

[2]Technique description: https://casper.ssl.berkeley.edu/wiki/The_Polyphase_Filter_Bank_Technique

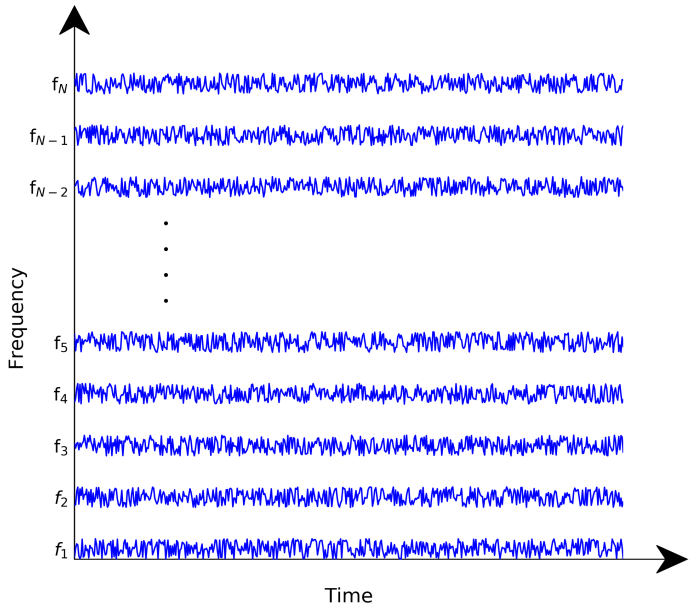

Figure 2.3: Illustration of the data product of an observation with a radio telescope after frequency channelisation. Each of the N-frequency channels contains the powers of the signal at each time sample (sorted in time from start to the end of the observation). Each channel has a finite bandwidth $\Delta f_{\rm ch}$, where the total bandwidth is $\Delta f = N \times \Delta f_{\rm ch}$

2.2 Data Formats

When the data is directed to the backend, one common practice is to split the observing band into smaller parts or frequency channels, each with finite bandwidth. This is necessary, as processing the full bandwidth leads to large data rates, which is computationally expensive. For a faster data flow, each sub-band is sent in parallel to a separate computer. Figure 2.3 illustrates the new structure of the data as it is split in N frequency bands, where each channel from f_1 to f_N is a timeseries.

When the source is known, and so it is its dispersion measure, the delay correction to each frequency can be applied in real-time to the incoming raw voltages (Shrauner, 1997), i.e., before the data is split into frequency channels. This is known as *coherent dedispersion* and it has the benefit of boosting the S/N. If on the other hand, the observation is made with no knowledge of the source – for instance, when carrying out a blind search – we are left with a delay correction possible to each frequency channel only. Coherent dedispersion is preferred to distinguish narrow emission signatures of pulsars and FRBs, such as multiple components in the pulse profile. This is shown in Figure 2.4 with an observation of PSR B0329+54 recorded with both modes. The difference between coherent (right) and incoherent (left) dedispersion is evident: the pulse is narrower, its features better defined and the S/N enhanced by the coherent dedispersion.

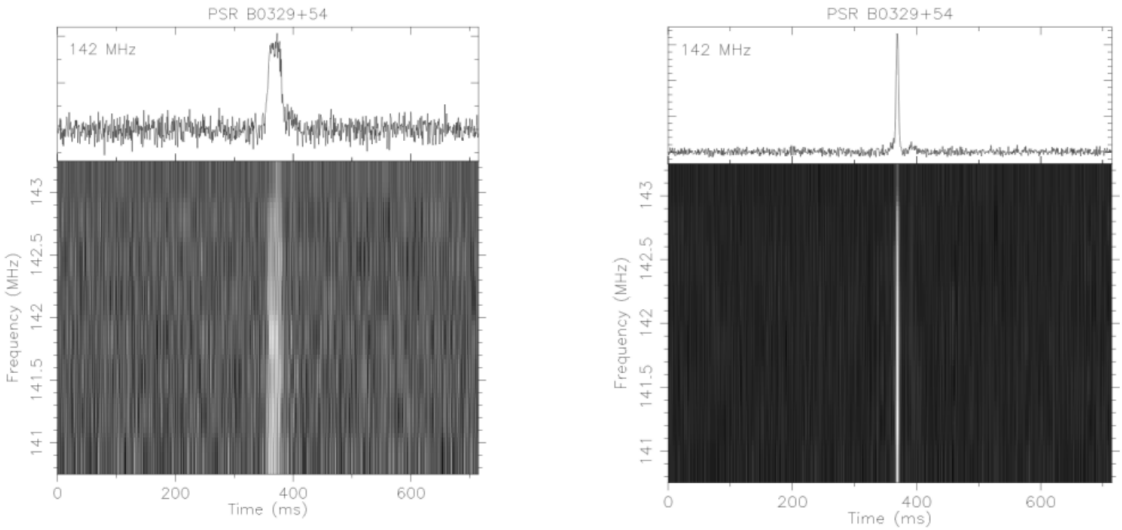

Figure 2.4: Incoherent (*left*) vs. coherent (*right*) dedispersion for a 12 minutes observation of PSR B0329+54 taken with the LFFE Receiver at the Westerbork Synthesis Radio Telescope (WSRT). The top plot displays the pulse profiles obtained when integrating in frequency the dynamic spectra in the lower panel. Image credit: Fundamental Physics in Radio Astronomy and Digital Laboratory at MPIfR.

Combining all frequency channels for each time sample results in a timeseries, where the S/N of a pulse is enhanced by a factor of $\sqrt{N}$, with N as the number of frequency channels added. This timeseries is the basis for Pulsar and FRB science and is discussed in more detail in Chapter 3. The sampling rate of the backend determines the resolution of the timeseries. Typical sampling rates for Pulsar/FRB observations are tens of microseconds. Naturally, higher sampling rates are preferred as it leads to higher resolution; however, this means larger files and more disk space needed for their storage. For pulsar searches, as a rule of thumb, the sampling rate should be at least such that it allows the pulse profile of the fastest known pulsar to be sampled. If we take the fastest known pulsar – as of now – PSR J1748-2446ad with a spin period of 1.39 ms (Hessels et al., 2006), a sampling time of $\sim 400\mu$s or higher provides enough samples across the pulse period.

In the following section, I discuss three relevant data formats for this thesis: baseband data, timing data, and search data.

2.2.1 Baseband data

After the signal leaves the frontend, the IF is in the frequency range $[f_{lo}, f_{lo} + \Delta f]$, where f_{lo} is the frequency at the lower edge of the observing band, and Δf is the bandwidth of the bandpass filter (300 MHz in the example case of Figure 2.2). The IF can be brought back to its base-band frequency – i.e., to the interval $[0, \Delta f]$ – by mixing the signal with a second LO. Because they retain all the information of the original signal

(phase and amplitude), the dispersive effect of the ISM can be removed by multiplying the base-band voltages with an inverse function, whose dispersion characteristic is the inverse of the delay produced by the ISM (Lorimer & Kramer, 2012). As this correction varies from source to source, the correction is only feasible when the DM of the source is known.

By its nature as nyquist sampled data, these files are large and can quickly fill up the disk storage, one of the reasons why pulsar surveys – due to their extensive data collection and no prior knowledge of the source – do not record baseband data. However, it is particularly beneficial to use baseband data for timing as the higher S/N allows high precision (due to the sharper pulse profile), and for scintillation studies of known pulsars, as baseband leads to the higher resolution of the scintills.

2.2.2 Search data

As the name points out, search data is the format preferred when searching for a source from which we have little to no knowledge of. The data are generally produced for radio transient surveys, where the main focus is to detect the signal rather than analyzing its properties, which is why a time clock maser is not mandatory, nor is polarization information required. Once a source has been discovered in the data, and the parameters such as the period and dispersion pinpointed through S/N optimization (see section 3.1), it is common practice to shift afterwards to record timing data.

Search mode data is often saved in *filterbank* or *PSRFITS*[3] format. It contains a header listing the relevant information of the observation – date, receiver name, sampling rate, and observing frequency – concatenated to an array of n-bit values. The structure of a filterbank can be understood from Figure 2.3. The array of values is composed of the timeseries of each frequency channel (from f_1, f_2,...,f_N), appended one after another. We refer hereafter to search data and filterbanks indistinctly.

2.2.3 Timing data

If, in addition to the DM, the spin period of the pulsar is known (among other relevant parameters that characterize its rotation; see Section 4), the data can be stored as folded data. Folding an observation means that given the spin period of the source, the data stream will be added every one rotation. This procedure is illustrated in Figure 2.5, by taking an example of a pulsar with a spin period of 1 second. By adding several rotations, we create an integrated pulse, whose S/N is the coherent combination of the S/N of the individual pulses. This is of particular interest, because often the single pulses of pulsars are buried in the noise and are not detected in the timeseries unless folding is performed.

Often, if folding is performed during the observation in real-time or from the base-band data offline, the data is corrected through coherent dedispersion. If the data is instead folded from an undedispersed filterbank file (with no correction of the DM delay), then only incoherent correction is applied. The files created from the folding

[3] https://www.atnf.csiro.au/research/pulsar/psrfits_definition/Psrfits.html

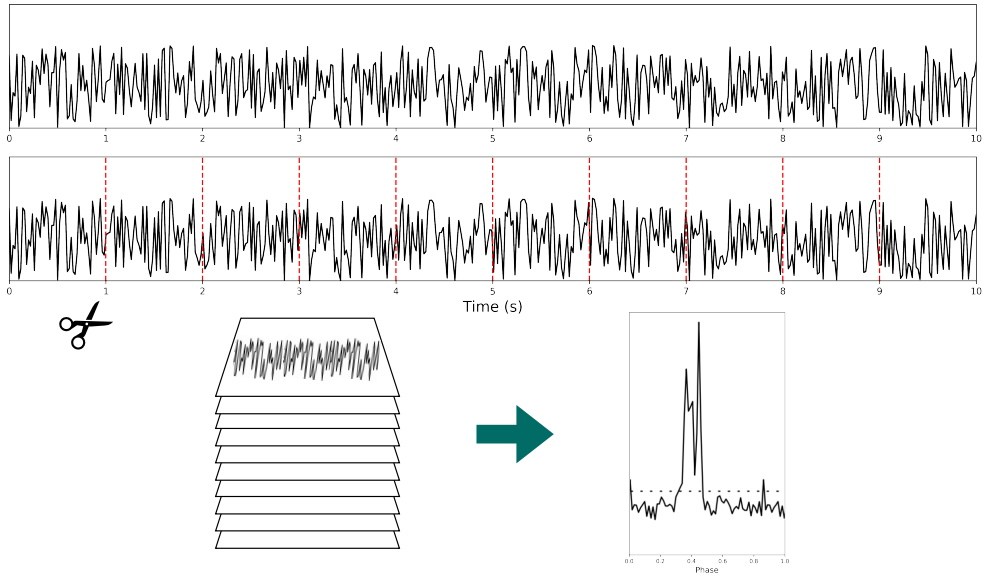

Figure 2.5: Schematic view of the pulsar data folding technique. The upper timeseries is folded at the spin period of the pulsar, yielding an integrated pulse profile where the pulsar is now visible (*bottom-right*).

procedure are referred to as archive files or folded archives indistinctly. Worthy of note is that to coherently combine observations taken across different epochs and from different telescopes, the observations must have accurate time stamps. This is achieved with the use of maser clocks linked to the terrestrial time standard.

2.3 Radio telescope performance

The aperture of a parabolic reflector has an angular power response as shown in Figure 2.6, which is modelled with a Bessel function of order zero. This is often referred to as *beam pattern*, and it is composed of the main beam and surrounding side lobes. The antenna is most sensitive when the radiation enters from the center of the main beam and becomes less sensitive with higher angular offsets until it meets the side lobes, where a localised increase in sensitivity is present. However, each successive side lobe is less sensitive than the previous. The full-width at half-maximum (FWHM) scales inversely with the effective diameter (D) of the reflector as follows

$$\text{FWHM} \simeq 58.4^{\text{o}} \frac{\lambda}{\mathcal{A}D} \tag{2.2}$$

$$\simeq 58.4^{\text{o}} \times 300 \frac{1}{\mathcal{A}D} \left[\frac{\text{MHz}}{f}\right], \tag{2.3}$$

where $\mathcal{A}$ is the aperture efficiency and λ is the observing wavelength. The aperture efficiency is the ratio between the effective area that reflects radiation into the receiver

(A_e) and the geometric area (A_o) of the reflector. Thus its value has a maximum $\mathcal{A} = 1$ when the aperture is uniformly illuminated and $\mathcal{A} < 1$ otherwise. We notice that for fixed values, the beam size – thus the FoV – is reduced for higher frequencies. However, this issue can be compensated for with the inclusion of multi-beam receivers.

The sensitivity of a radio telescope is given by its *Gain*, which is the power transmitted per unit of solid angle relative to an antenna with uniform gain at all the directions. It is expressed in terms of the diameter and aperture efficiency as (Lorimer & Kramer, 2012)

$$G = \frac{\pi D^2}{8k_{\mathrm{B}}}\mathcal{A}, \tag{2.4}$$

where k_B is the Boltzmann constant. To measure the true sensitivity of the observation, the receiver should be taken into account too. Thus, an alternative measure of the sensitivity is through the *system equivalent flux density* (SEFD), which is calculated as (Lorimer & Kramer, 2012):

$$\mathrm{SEFD} = \frac{2k_{\mathrm{B}}\,T_{\mathrm{sys}}}{\mathcal{A}}. \tag{2.5}$$

Because the SEFD takes into account the geometry and the receiver, it is a good way to compare the sensitivity across telescopes.

The minimum detectable flux density for a radio telescope is calculated from the radiometer equation as (Lorimer & Kramer, 2012)

$$S_{\mathrm{min}} = \frac{\mathrm{S/N_{min}} \cdot \mathrm{SEFD}}{\sqrt{n_{\mathrm{p}} \cdot t \cdot \Delta\nu}}, \tag{2.6}$$

where $\mathrm{S/N_{min}}$ is the minimum detectable signal-to-noise, t is the integration time, n_p is the number of polarisation channels and $\Delta\nu$ is the observation bandwidth. However, if instead of a pulsar observation, a single pulse is considered (such as an FRB), then the pulse width replaces t. Another benefit of Equation 2.6, is that if the source is known, along with its flux density, the relation offers an easy mean to calculate the integration time needed to have a detection with a given S/N.

2.4 Radio Frequency Interference

The universe might be very empty, but our near sky, up to ∼35000 kilometres, is not. Satellites, airport radars, mobile networks, Wi-fi, and transmission towers emit in the radio frequency band and can be confused with astrophysical signals. These unwanted signals are commonly referred to as *radio frequency interference* (RFI) and are one of the most significant challenges in modern radio astronomy. RFI introduce thousands-to-millions of (false) candidates to be inspected when carrying out a search; it alters the noise baseline of an observation, thus affecting the actual S/N of a pulse; and in the most extreme case leads to non-linear effects, such as receiver saturation, making the observation unusable.

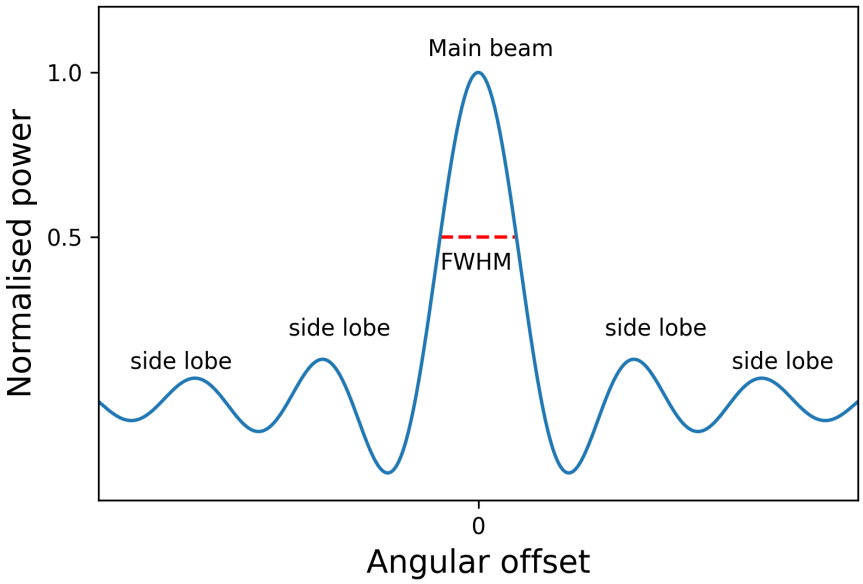

Figure 2.6: Representation of the cross-section of a beam pattern at an arbitrary frequency. Abbreviation: FWHM=Full-width at half maximum.

In Figure 2.7 the radio spectrum allocations in Germany is shown. Although only the frequency range from 500 MHz to 3 GHz is displayed, it exposes how crowded the band is by industrial and military telecommunication, and the small portion ($< 5\%$) that is allocated to radio astronomy (*green-dashed-bars*). More importantly, the power from such RFI is many orders of magnitude stronger than the signal we receive from pulsars and FRBs (millions of times stronger, or more), thus observing in the band where their main power emits would hinder any detection. Nevertheless, the harmonics of the transmitters are still strong enough to affect the observation. This is why, preferentially, radio telescopes are located in areas far from large human settlements and transmission towers from broadcasting systems. However, not all the interference comes from kilometres away. A portion of the RFI is generated at the telescope itself by its components (receivers, backends) and electronics of common use, such as the computers needed to operate the telescope.

Even if the telescope is built far from transmission towers, the backends are placed inside a Faraday room, and wireless networks are banned, not all the RFI are removed. Further data cleaning at several processing stages is required to obtain a clear and unambiguous signal. Furthermore, because the narrow frequency bands allocated to radio astronomy, often observations go outside the protected band, meaning that techniques need to be explored to coexist with the terrestrial signals. We discuss in detail the most common techniques and algorithms to mitigate the effects of RFI in the data in Section 3.2.4.

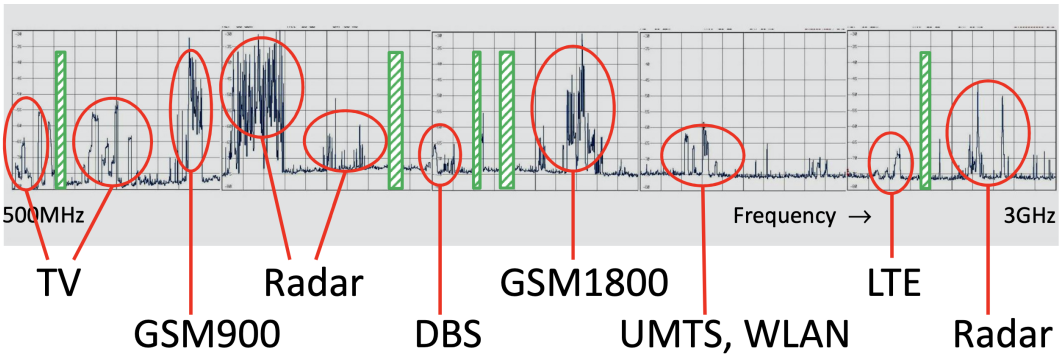

Figure 2.7: Primary frequency allocations for radio astronomy in Germany. The *green-dashed bands* correspond to the frequency ranges reserved for astronomy. In red it is highlighted the prevalent sources of RFI. Abbreviations: TV=Television, GSM=Global System for Mobile communication, DBS=Radio station, UMTS=Universal Mobile Telecommunications, WLAN=Wireless Local Area Network, LTE=Long-Term Evolution (communication for mobile devices). Image Credit: R. Keller and K. Grypstra (MPIfR).

2.5 The 100-meter Effelsberg radio telescope

The Effelsberg radiotelescope started operation in August 1972 and was until the year 2000 the largest fully steerable radio telescope, after being surpassed by the 100×110-meter GBT. One of the biggest challenges when operating such a large dish is how to keep its parabolic shape, due to the telescope deformation by gravity as it moves in elevation. Any small deviation from a perfect parabola changes the focal point of the radio waves. This technical issue was corrected by allowing an additional controlled deformation of the dish that leads to a slightly different focal point, covered afterwards by slightly moving the feedhorn (Kraus et al., 2015). This novel technique allows Effelsberg to reach a dish accuracy below 0.5 mm, which is significantly below the 1 mm accuracy expected initially. GBT and Effelsberg sizes are around the largest dish sizes achievable for a fully steerable radio telescope. Larger dishes can be only achieved with fixed primary reflectors such as the 305-m Arecibo and the 500-m FAST (see Table 2.1).

One of the most surprising aspects of the Effelsberg is that despite its size and weight of over 3000 tons, it can rotate with a speed of up to 30^o/min to point a source. This means that it only takes 12 minutes to give a full turn, thus making it the fastest positioning large fully-steerable radio telescope in the world.

Effelsberg's visible sky extends from declination 90° down to -20^o; thus, the Galactic center is visible daily for up to ∼4 hours. It operates mainly as a stand-alone instrument but is also part of a network of radio telescopes around the world such as the European Pulsar Timing Array (Kramer & Champion, 2013), the Large European Array for Pulsars (Bassa et al., 2016) and Very Long Baseline Interferometry (Schuh

Sensitivity	1.37 K/Jy
Number of Polarization	2 (LCP + RCP)
System temperature	23 K
SEFD	17 Jy
Aperture efficiency	48%
Beam efficiency	63%
Beam size	10’

Table 2.2: Specifications of Effelsberg’s 7-beam receiver at 1.36 GHz. Abbreviations: LCP=Left circular polarization, RCP=Right circular polarization, SEFD=System effective flux density.

& Behrend, 2012) networks. The frequency range covered by Effelsberg goes from 408 MHz (73 cm) up to 86 GHz (3.5 mm), making it ideal for continuum as well as spectral lines observations. However, the pulsar backends are equipped to observe from 1.2 GHz (21 cm) to 43 GHz (7 mm; Kramer et al. 1997).

The primary receiver used for this thesis work was the 7-beam receiver, in combination with the PFFTS and Automatix backends.

2.5.1 7-beam receiver

Our observations are split into *searching mode* and *timing mode*. For both, we made use of the 7-beam receiver at a central observing frequency of 1.36 GHz. The 7-beam is arranged in a hexagonal pattern whose geometry is displayed in Figure 2.8. The image shows the full pattern of the receiver on the sky, including the side lobes of each beam (top). Each beam of the array has a fixed position with respect to the other beams; however, the receiver can be rotated as a whole with an angle measured anti-clockwise. The main parameters of the 7-beam receiver at L-band are shown in Table 2.2. Each observation of a sky position defined by the central beam is referred to as *pointing*.

2.5.2 Pulsar mode backends

For the search observations, we made use of the Pulsar Fast Fourier Transform Spectrometer (PFFTS) (Barr et al., 2013). The PFFTS records data with a time resolution of 54 μs and a 300 MHz bandwidth split into 512 frequency channels. In this mode, all the seven beams of the feed array record data simultaneously. Their combination allows the more extensive sky coverage for blind surveys, and in the case of a targeted search, where only the main beam is required, the outer beams can be used for RFI mitigation purposes (see Section 3.2.4.3). The output of the PFFTS observations are 32-bit filterbank files; however, by subtracting the bandpass after identifying the bad frequency channels (see Section 3.2.4.1), the dynamic range is reduced to 8-bit filterbank files. Those require less disk space and are easier to transfer to the computer clusters for processing. For the PFFTS data, it is only possible to apply incoherent dedispersion when folding.

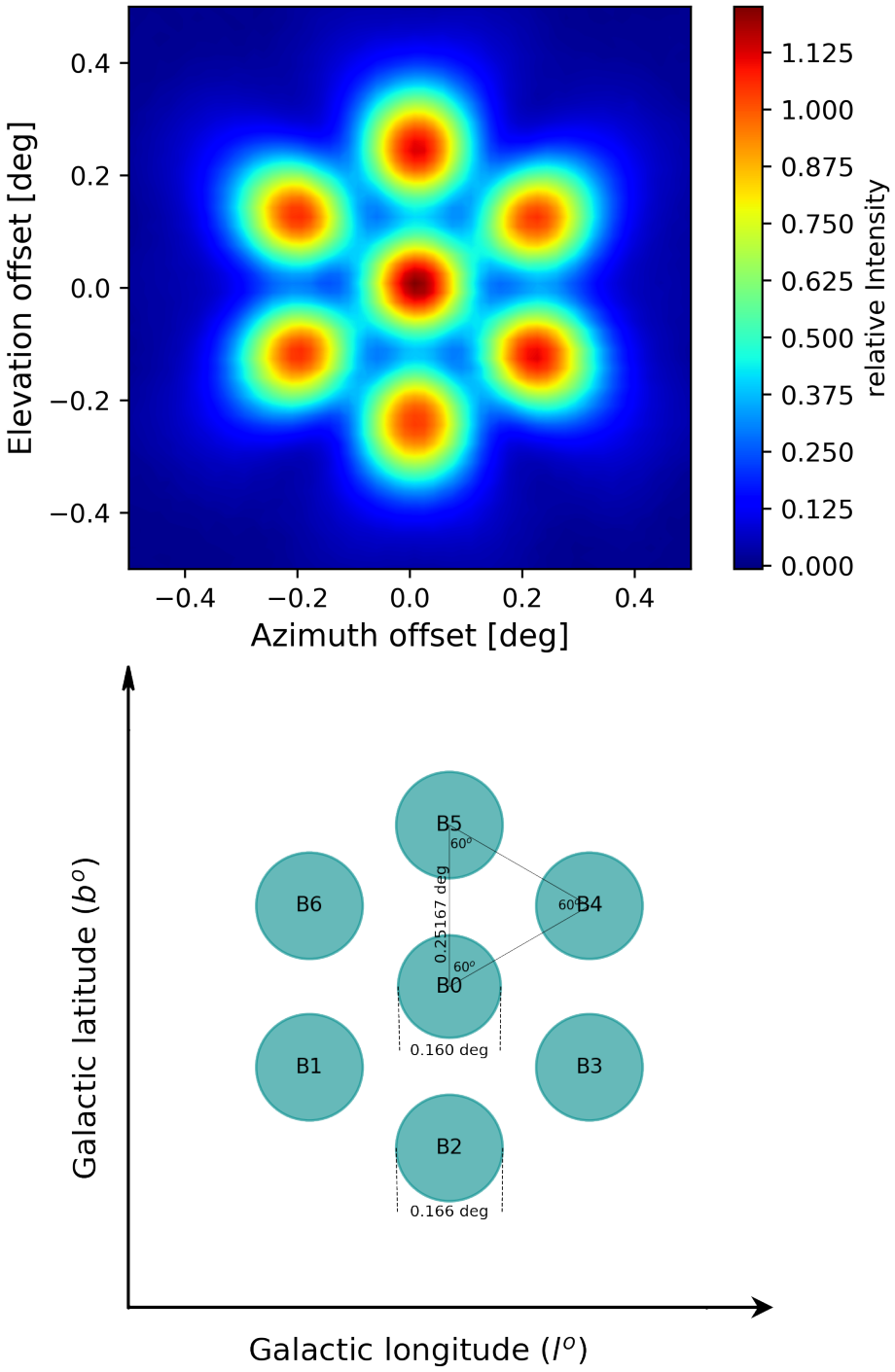

Figure 2.8: Effelsberg's 7-beam receiver beam pattern at 1.36 GHz (*top*) and beam arrangement and geometry (*bottom*). B_o is the central beam, B_i is the i^{th} beam. Credit for the data used in the upper plot: E. Fuerst and A. Kraus.

For timing, only data from the central beam is recorded. The data digitisation is performed with the use of the high precision pulsar timing backend PSRIX (Lazarus et al., 2016). PSRIX has a bandwidth of 250 MHz, which is split into 256 frequency channels. The time resolution will vary depending on the pulsar's spin period, and the sampling needed to create 1024 bins of phase resolution. PSRIX data retains time stamps, and the circular and linear polarisation information. Besides folded archives, PSRIX can produce baseband data and filterbank files (like the PFFTS). For the PSRIX filterbanks, the time resolution is 51.2 μs. Contrary to the PFFTS, PSRIX records accurate time stamps (nano-second level) with a maser clock. However, because it only records data with the central beam, it is unpractical for FRB or pulsar surveys. For data recorded in baseband or folded archives, the dispersion correction is applied coherently.

Despite the fact that the PFFTS and PSRIX operate separately, their use is not exclusive. It is possible to use the central beam to record data with the PFFTS and PSRIX simultaneously. This setup is of use for targeted searches of FRBs and Pulsars: PFFTS data allows to search for the source, and PSRIX data provides accurate TOAs. Example of this use case is presented in Chapter 7.

2.6 The Five-hundred-meter Aperture Spherical radio Telescope

The world's largest single-dish radio telescope, the Five-Hundred Aperture Spherical radio Telescope (FAST), was first proposed as a prototype for SKA. However, as SKA opted for many smaller single dishes in an array-mode instead of one single large dish, FAST was developed as a stand-alone project. It is inspired by Arecibo's spherical design, but it has some key differences:

- It has more than twice the collecting area of AO – 196,000 m^2 and 73,000 m^2, respectively.
- The spherically shaped reflector has over 2000 small elements called actuators, which in combination to a system of cables the otherwise static spherical dish is deformed to track sources longer than otherwise possible (up to 6 hours).
- It has a light-weight cabin. There is no rigid connection between the reflector and the feed cabin. Instead, the cabin is suspended by cables connected to six towers around the dish (see Figure 2.9).

The last characteristic is essential, as to adopt AO's design for the feed cabin, would lead to over 10,000 tons of steel placed on top of the dish, which is impractical. On the contrary, FAST's suspended cabin design only weighs 50 tons. Worth noting is that to compensate the position offsets due to wind, a secondary system in the cabin adjusts its location through laser tracking.

FAST was built in a karst depression located in the Guizhou province in China, one of the few places on the planet to have these types of depression to build a gigantic

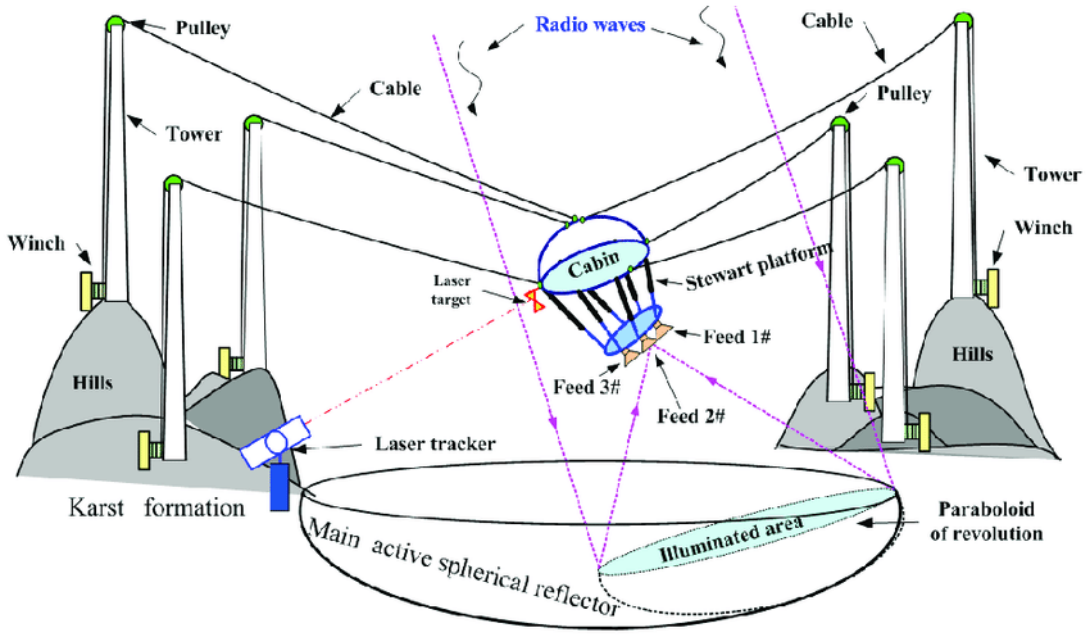

Figure 2.9: Schematic overview of FAST. Image credit Duan et al. (2016).

Aperture (m)	500
Illuminated aperture (m)	300
Opening angle (°)	112.8
Focal ratio	0.4665
Resolution (')	2.9
Pointing accuracy (")	8
Slewing time (min.)	<10
Declination range (°)	-15 – 65

Table 2.3: FAST characteristics overview

500-m dish; hence, lowering the cost of its construction significantly. The site gives FAST a zenith angle of 40°, and is surrounded by mountains, thus providing a natural blockage of RFI. A radio-quiet zone is essential for a telescope as sensitive as FAST.

The construction of FAST was completed in September 2016, in only five years. Its main characteristics are displayed in Table 2.3 and a schematic overview of its structure is presented in Figure 2.9.

2.6.1 Commissioning phase

FAST saw first light with the first pulsar ever detected, PSR B1919+21. The commissioning phase started with a testing instrument, the single-beam ultra-wide-band receiver (UWB) with a gain of 10.1 K/Jy. The primary goal during the commissioning stage was to calibrate FAST's complex positioning system, and to work on data ac-

	UWB	19-beam
Number of beams	1	19
System temperature (K)	60-70	24
Gain (K/Jy)	10.1	18.2
Sampling rate (μs)	200	100
Frequency range (MHz)	270 – 1620	1050–1450
Number of polarization	2	2

Table 2.4: FAST's UWB and 19-beam receiver comparison.

quisition and processing (see more details of the UWB receiver in Chapter 5). In May 2018, FAST was upgraded with its primary receiver, the 19-beam L-band Array with a gain of 18.2 K/Jy (Jiang et al., 2020). Figure 2.10 shows the combined response of the beams (top) and the beam center arrangement and geometry (bottom).

FAST is equipped with a pulsar timing/searching backend, a baseband backend, a VLBI backend and the SETI backend. However, it was not until the upgrade to the 19-beam receiver that multiple observation modes could be carried out simultaneously. The pulsar backend is a Polyphase filterbank based system where a maser clock imprints the timestamps.

The comparison between the UWB instrument and FAST's primary 19-beam receiver is shown in Table 2.4. The most noticeable difference regards the relative gain of the receivers, with the 19-beam almost twice as sensitive. This is caused by the roughly three times lower system temperature than the UWB. The UWB is a *Quad-Ridge Flared Horn* of physical size of 1.45 m×1.2 m, size needed to operate as low as 270 MHz. The large size, however, prevents it from being placed within a Dewar to be cooled down to temperatures of 24 K, as it is the case of the 19-beam receiver (Jiang et al., 2019).

During the commission phase, a large part of the telescope time was used in pulsar search in drift-scan mode, where the receiver is fixed to a position, and the sky passes through the beam. For the UWB, the time taken for a source to drift through the beam at the lower end of the band was roughly 50 seconds. For the 19-beam receiver the drift time is ∼20 seconds.

Telescopes such as Effelsberg and Parkes had a key role during FAST's commissioning phase. Candidate confirmation allowed FAST's pointing system to be refined, and the timing observations led to clock stability comparisons. Chapter 5 discusses the Effelsberg follow-up of some of the pulsars discovered by FAST during its early commission phase with the UWB. After FAST was upgraded with the 19-beam receiver and the source positioning and data acquisition challenges were managed and tested, shared-risk Observing Proposals led to a broader range of science cases to be covered. This improved its performance and prepared FAST for normal operation.

Finally, FAST left the commissioning phase in January 2020 and is now fully operational. With 18.2 K/Jy of gain, FAST positions itself as the world's most sensitive radio telescope with the potential to produce significant scientific results.

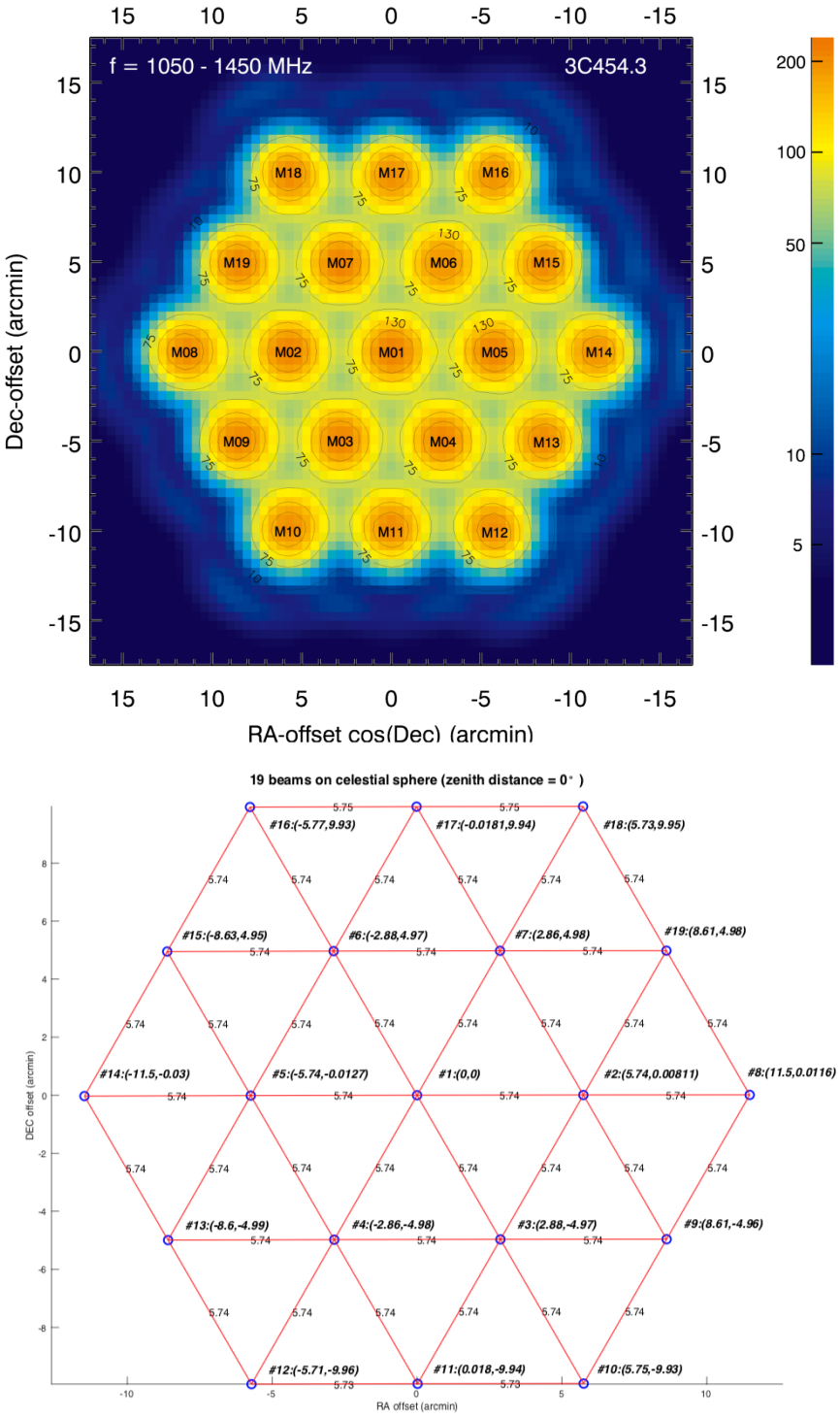

Figure 2.10: FAST's 19-beam L-band receiver. Top: beam pattern on the sky (Jiang et al., 2020). Bottom: arrangement of the beams. The blue dots represent the beam center of each of the 19 beams. Bottom image credit: P. Wang.

2.6.2 Science with the largest dish

The pulsar survey using FAST is one of the key science projects at the telescope. FAST's unrivalled collecting area has two major benefits. The first is raw sensitivity, allowing the dimmest pulsars to be detected; the second is the new parameter space for pulsars in binary systems. The short integration times needed to achieve certain sensitivity, have the potential to detect extremely accelerated systems and potentially pulsar-black hole binaries[4]. These detections are of special interest for testing gravity, as discussed in Section 1.6. Pulsar search with FAST is discussed in detail in Chapter 5.

Simulations based on pulsar population models estimate 4000 pulsars could be discovered by FAST in the Galactic plane, where 10% of them will be MSPs (Smits et al., 2009). FAST's most stable MSPs can be included in pulsar timing arrays, to substantially improve their sensitivity to GWs – which currently comprises 49 sources for the IPTA experiment – and substantially improving the S/N required for high-precision timing (Hobbs et al., 2019).

FAST is one of the most effective telescopes for detecting FRBs at the highest redshifts. Such sources can help to constrain the high-end of the FRB luminosity function (Zhu et al., 2020). Li et al. (2017) estimate that 5 ± 2 events per 1000 hours can be detected by FAST with the L-band 19-beam receiver for a fluence threshold of 0.03 Jy ms, and assuming all-sky event rates of 3×10^4 day^{-1}. An increase in FRBs at high redshifts is crucial to understand their origin, in addition to their use as cosmological tools (see discussion in Section 1.7.4).

Additional key science projects at FAST are HI surveys to map the neutral hydrogen in the Milky Way and other galaxies through the 21 cm line; radio continuum and recombination lines; the evolution of stellar sources with its inclusion in VLBI network; and search signals from extraterrestrial intelligence (SETI) from distant galaxies (Nan et al., 2011).

[4]To date, no binaries containing a BH and a pulsar has been detected.

Chapter 3

Pulsar and FRB Searches

While timing is the key to extract the science from pulsars, they first need to be discovered. Although pulsars are known to emit across the full spectrum, the vast majority were detected first in radio; thus surveys in this frequency regime are preferred. Once a pulsar has been discovered, it can be observed at other wavelengths to investigate the extent of its emission. In this chapter, the key techniques to search for pulsars and FRBs are discussed.

Contents

3.1 Radio searches

Radio searches can be *blind*, where a large region of the sky is uniformly mapped; or *targeted*, where specific regions are observed when events are expected to be present. Common targets include globular clusters (GCs), γ-ray point sources, SNR, and WDs. For FRBs, targets include persistent radio sources (Ofek, 2017), γ-ray bursts (Palliyaguru et al., 2020), and superluminous supernovae (Hilmarsson et al., 2020). Depending on the science case, one type of survey may be preferred. As discussed in Section 1.6, in order to best detect the stochastic GW background, PTAs should sample a population of MSPs which is widely distributed in the sky. Large scale blind surveys are therefore of interest, as they are more likely to reveal a wider population of sources and a sky distribution with different characteristics. A well-sampled sky distribution is also preferred to map the electron density of the Galaxy (Cordes & Lazio, 2002; Yao et al., 2017).

For targeted pulsar surveys, GCs have a higher probability of finding MSPs than anywhere else in the sky, even when compared to the Galactic plane. The high stellar densities in GC cause significant dynamical interaction, which leads to close binary systems undergoing mass-transfer, thus higher formation rates of MSPs (Bahramian et al., 2013). Regarding γ-ray point sources as targets, gamma-ray pulsations in pulsars

have been detected (e.g. Abdo et al. 2009). The fact that 40% of the Fermi Large Area Telescope (LAT) sources are unassociated, suggests that a large fraction could be identified with pulsars. Out of the 389 known MSPs, 133 are in GCs and 97 are γ-ray sources, demonstrating the impact of targeted searches.

Often for targeted searches, there is a-priory information of the source which is used to reduce the parameter range to be searched, such as the distance and orbital periods. On the contrary, for blind searches, each pointing of the sky is searched in wider parameter space to account for a potentially high DM contribution due to due to larger distances.

3.2 Search methods

This thesis is based on targeted pulsar searches of FAST pulsar candidates described in Chapter 5, and the follow-up of FRB 121102, which is presented in Chapter 7. For the pulsar targets, period and DM estimation already exists. For the FRB 121102 follow-up the DM is already known. However, I discuss here the general structure of a search algorithm.

The common steps of the data processing algorithms are:

1. RFI mitigation: removal of bad frequency channels
2. Dedispersion: removal of the dispersive delay
3. RFI mitigation: removal of bad time samples
4. Search: identify candidates
5. Candidate inspection: identify promising candidates

Because the search algorithm is the core of the data processing pipelines, I discuss first the broadly employed techniques. I continue with the discussion on how to address the DM range to search over optimal DM steps. Finally, we explore the diagnostic plots to identify candidates and how the number of false candidates is reduced through RFI mitigation techniques applied at several stages of data processing.

3.2.1 Search algorithms

Searching for pulsars, particularly in blind searches, is computationally expensive. With the continued improvement in the sensitivity of radio telescopes, novel techniques can be used to account for extremely relativistic systems. However, the parameter space explored is often the result of a trade-off between the subject of interest and the computing power available to a researcher. In the following Subsections, I discuss the commonly used algorithms to search for pulsars and FRBs.

3.2.1.1 FFT search

The periodic nature of pulsars allows their signal to rise above the noise level by transforming the timeseries into its frequency domain components. As the data correspond to a discretely and evenly sampled timeseries, the method used is the *Discrete Fourier Transform* (DFT), where the k^{th} element of the DFT ($\mathcal{F}_k$) is defined as

$$\mathcal{F}_k = \sum_{n=0}^{N} x_n \, e^{-2\pi i n k/N}, \tag{3.1}$$

where x is the series of N elements to convert, and $i^2 = -1$. The frequency spacing for an observation (Δbin) of length T is thus $\Delta bin = 1/T$. Computing the DFT requires $\mathcal{O}(N^2)$ operations, which results in long computing times given the combination of a large number of trials and a large number of samples for long observations (minutes-to-hours) or high sampling rates. However, the use of the *Fast Fourier Transform* (FFT) algorithm for efficient computation of the DFT brings the operations down to $\mathcal{O}(NlogN)$.

Worth noting is that Equation 3.1 yields a set of complex numbers, as the timeseries was changed to a new basis (sine and cosine) represented by a phase and amplitude. However, for search, we are only interested in achieving a detection, thus the amplitude of the signals. The *Fourier power spectrum* is calculated as

$$\mathcal{P}_k = \mathrm{Re}(\mathcal{F}_j)^2 + \mathrm{Im}(\mathcal{F}_j)^2, \tag{3.2}$$

and the *Fourier amplitude spectrum* is defined as

$$\mathcal{A}_k = \sqrt{\mathcal{P}_k}\,. \tag{3.3}$$

An important consideration when searching in the FFT is the presence of RFI and fluctuations in the electronics of the receiver (such as amplifiers) which introduce red-noise (see Footnote 14) in the observation. Contrary to white-noise (which are random Gaussian variations), red-noise alters the rms of the timeseries and therefore the S/N levels. Red noise affects low frequencies (slow pulsars) more strongly as it scales with the inverse of the square of the frequency. Furthermore, long observations are particularly affected by red-noise, as it builds cumulatively with the observation length. Subtracting the running median is one of the standard methods used to normalize a power spectrum.

Pulsars have narrow pulses, where the fraction where the pulse is "on" relative to the pulse period is referred to as *duty cycle*

$$\delta = \frac{W}{P}, \tag{3.4}$$

where W is the pulse width, and P is the pulsar's spin period. For a sharp pulse profile profile, the power is distributed over many harmonics, contrary to pure sinusoidal signals, where all the power is at the fundamental frequency. The harmonics

of a pulsar, with fundamental frequency 1/P, are located in the Fourier spectra at 2/P (second harmonic), 3/P (third harmonic), etc. To boost the S/N, the method of *harmonic summing* (Taylor & Huguenin, 1969) is used, whereby several harmonics are added together. Subsequently, the statistical significance is evaluated by the sum of its normalized harmonic powers. To perform harmonic summing, the power spectrum is added to a version of itself stretched by a factor of two. The result is frequency bins summed with its second harmonics, thus enhancing the S/N. The procedure can be repeated many times, up to a given number of harmonics. However, there is an optimal number of harmonics that boost the S/N before adding mostly noise. Standard searches sum up to the 16^{th} or 32^{th} harmonics.

After harmonic summing, the false-alarm-rate of a bin exceeding an S/N threshold by chance is given by (Lorimer & Kramer, 2012)

$$p_{\text{false}}\left(\text{S/N} > \text{S/N}_{\text{thres}}\right) = e^{-(\sigma_l\,\text{S/N}_{\text{thres}}+\sigma_t)^2}, \tag{3.5}$$

where σ_t is the mean value of the Fourier amplitudes (see Equation 3.3) and σ_l is the local root mean square. The equation is derived from the probability density function (PDF) of a normalized Fourier power spectrum that follows a χ^2 distribution. Setting the number of events above the power threshold to be equal to one per trial, Lorimer & Kramer (2012) present a simplified relation to estimating the $\text{S/N}_{\text{thres}}$

$$\text{S/N}_{\text{thres}} \sim \frac{\sqrt{\ln\left(n_{\text{trials}}\right) - 0.89}}{0.46}, \tag{3.6}$$

where n_{trials} is the number of trials during the search. For a standard 30 minutes long observation with Effelsberg at a sampling rate of 54μs and DM $\in [0, 2000]$ pc cm^{-3} covered by roughly 1000 trials, the S/N threshold for a search range is

$$\begin{aligned} n_{\text{trials}} &= 18518[\text{samples/s}] \times 1800[\text{s}] \times \frac{1}{2} \times 1000\,[\text{DM trials}] \times 4\,[\text{harmonics}] \\ &\simeq 6.7 \times 10^{11} \\ &\implies \text{S/N}_{\text{thres}} \simeq 10. \end{aligned}$$

However, the derivation in Equation 3.5 assumes the presence of purely Gaussian noise in the data. The RFI situation associated with the observation could necessitate considering higher thresholds.

3.2.1.2 Acceleration search

In the presence of a binary system, the orbital motion of the pulsar will produce a frequency shift in the power of the signal (Doppler shift). The apparent change in the spin period (P_{obs}) of the pulsar and its derivative ($\dot{P}_{\text{obs}}$) is (Lorimer & Kramer, 2012)

$$P_{\text{obs}}(t) = P_{\text{i}}\left[1 + \frac{v_{\text{l}}(t)}{c}\right], \tag{3.7}$$

$$\dot{P}_{\text{obs}}(t) = P_{\text{i}}\frac{a_{\text{l}}(t)}{c}, \tag{3.8}$$

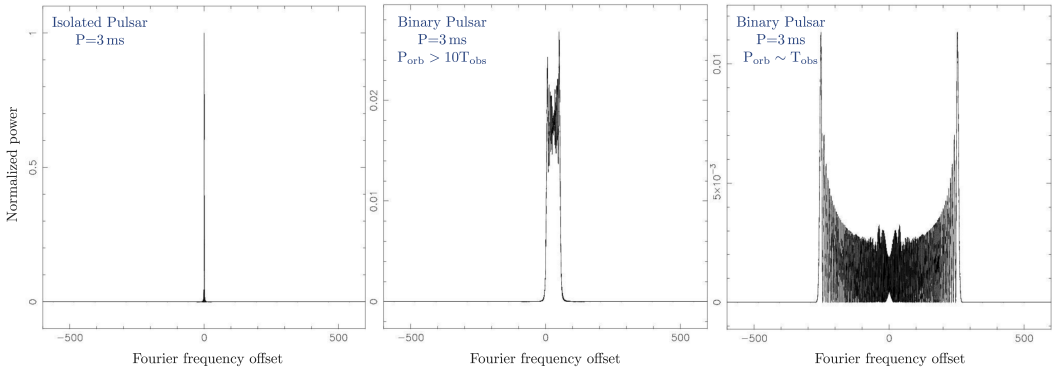

Figure 3.1: Distribution of the power in the Fourier power spectrum of a pulsar with a spin period of 3 ms when is isolated (*left*), in a binary where the length of the observation is 10% or less of the orbit (*center*), or when is in a short period binary of a similar observation length (*right*). Credit for the original plot: S. Ransom.

where P_i is the intrinsic period, v_l is the velocity along the line-of-sight and a_l its derivative, and c is the speed of light. As the pulsar's orbital parameters are not known at the search stage, the approximation of constant acceleration ($v_{\rm l}(t) = a_{\rm l} \cdot t$) is often used. However, this only applies if the length of the observation is shorter than 10% of the orbital period (hereon referred to as 10% rule, see Ransom et al. 2002; Ng et al. 2015). The time-dependent change spreads the power of the signal across a maximum of $z_{\rm max}$ adjacent frequency bins

$$z_{\rm max} = \frac{a_{\rm l}}{cP} T^2, \tag{3.9}$$

with T being the integration length across which a_l is measured. The power spreading is shown in Figure 3.1 for a simulated 3-ms period MSP. It is seen that in comparison with the isolated case (left) when the observation time is 10% of the binary period (center), the Fourier power is spread on neighbouring bins reducing the S/N significantly. When the observation time and binary orbit are of the same order, then the power is spread over a broader range of Fourier bins and the S/N further decreased. The correction (or resampling) to account for the signal spread of a pulsar can be carried out either in the Fourier or time domain.

With *frequency domain corrections*, the i^{th} frequency in the Fourier spectrum will be combined with the bins in the interval $[f_i - z_{\rm max}\Delta bin,\ f_i + z_{\rm max}\Delta bin]$. PRESTO searches such as `accelsearch` (Ransom, 2011) are based on the resampling of the Fourier spectrum.

With *time corrections*, several acceleration trials are used to correct the timeseries for the earlier or delayed arrival of the signal respectively. Eatough et al. (2013) derived

an optimized acceleration step-size

$$\Delta a = 64c\frac{t_{\rm samp}}{T^2}, \tag{3.10}$$

where t_{samp} is the sampling interval. Such relation was obtained by fixing the maximum smearing over the length of the observation to be four times the sampling interval for signals that lie exactly in between two acceleration trials. With this relation, 50% of pulses are smeared by less than one-time sample. SIGPROC's `seek` routine utilizes the time-domain correction.

Whether acceleration searches correct for the effect of orbital acceleration of a pulsar with frequency resampling and z_{max}, or time correction with a_l, this procedure is always the most computationally expensive part of the pipeline. Blind searches of long observations can take up to days to fully process the data. However, with the current advance of computing techniques, such as GPU-based processing, the computation time can be significantly reduced to a few minutes or to a couple of hours. For the work involved in this thesis, I made extensive use of both SIPROC's and PRESTO's approaches to acceleration search. For the parameters described in Equation 3.7 a standard running time for the CPU-based pipeline was ∼12 hours.

3.2.1.3 Fast Folding Algorithm

As FFT based searches strongly depend on the number of pulses within one observation to reconstruct the S/N of the periodic signal, they are less sensitive to slow pulsars. An alternative approach to sampling the parameter space where FFT is less sensitive is the *Fast Folding Algorithm* (FFA). This technique consists of the direct folding (see Section 2.2.3) of the dedispersed timeseries at a range of trial spin periods. Each resulting profile is evaluated based on the significance of the pulse. Contrary to FFT and acceleration searches, the *Fast Folding Algorithm* (FFA) is less affected by red-noise, thus is more sensitive to slow pulsars with periods >1 s (Cameron et al., 2017). Figure 3.2 shows a sensitivity comparison between a standard FFT search with harmonic summing, and an FFA algorithm (Morello et al., 2020). It shows that FFA is more efficient than a standard FFT search, regardless of the pulsar's spin period and duty cycle.

Although the implementation of the *Fast Folding Algorithm* optimizes the number of computations by reducing redundant operations, it is still too computationally expensive to carry out blind surveys for a wide range of trial periods. To fold over short periods ($P < 0.5$ s) leads particularly to long computing times as the number of operations scales with $\mathcal{O}(Nlog(N/P))$, where N is the number of samples is the data (Cameron et al., 2017). Because I carried out targeted searches to confirm the nature of pulsar candidates detected by FAST (see Chapter 5), I made use of the `RIPTIDE`[1] FFA implementation by Morello et al. (2020). For this purpose, I explored a reduced DM range near the candidate and explored trial periods $P \in [0.1\,s, 10\,s]$.

[1] https://github.com/v-morello/riptide

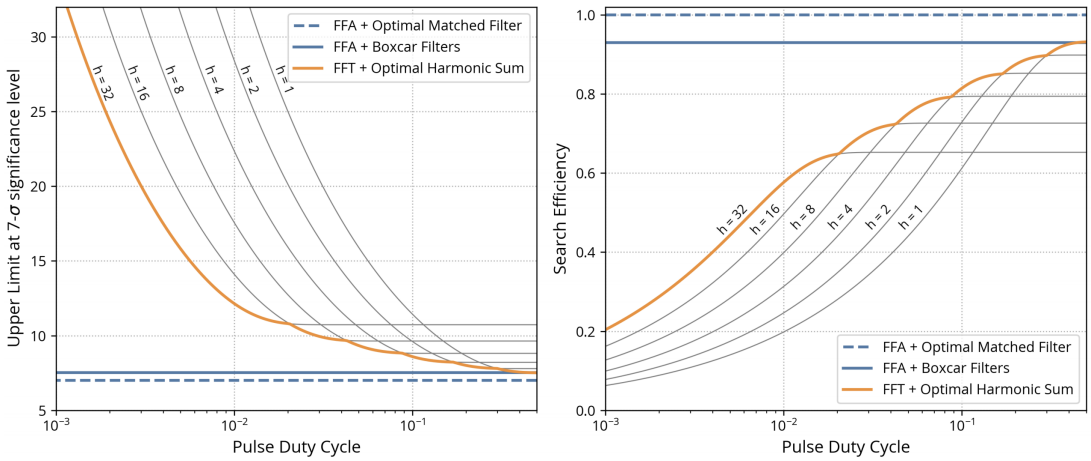

Figure 3.2: Sensitivity comparison between an FFA search and an FFT search with incoherent harmonic summing (h=1,2,4,8,16,32). FFA is tested with a boxcar-shaped filter (*blue line*) and a filter that reproduces the known pulse shape (*blue dashed-line*). *Left:* minimum signal amplitude that can be detected with 50% probability as a function of the pulse duty cycle. *Right:* ratio between the theoretical amplitude and the result of the search procedure (search efficiency) as a function of the duty cycle. Image from Morello et al. (2020).

3.2.1.4 Single pulse search

As mentioned before slow pulsars have fewer pulses per observation length, thus FFA is a better approach than FFT. However, if too few pulses are contained, for instance, in RRATs searches, then the efficiency of FFA is also reduced. A single-pulse (SP) search is a must-do during a survey to sample the parameter space where FFT and FFA based searches are less sensitive to.

Pulsars were discovered first in an analysis of a timeseries. Most of brightest pulsars, such as the Crab Pulsar and the Vela pulsar, can be detected in the dedispersed timeseries as they show strong single pulses. We mentioned in Section 1.5 that the search for single pulses of pulsars led to the discovery of RRATs (see Section 1.5), and the search for RRATs led to FRBs. Currently, SP searches continue to be the standard method to search for FRBs.

SP searches are based on a matched filter technique, where a timeseries is convolved with a filter, usually of a boxcar shape. This technique improves the S/N of a timeseries in the presence of Gaussian noise. Importantly, because the width of the pulse – either an FRB, pulsar or RRAT – is unknown apriori, several filter widths are explored in such way that the width in number of samples equals widths ranging from a couple to hundreds of milliseconds. The choice of the S/N threshold (S/N_{thres}) above which bursts are deemed significantly, should be such that dim bursts are detectable, but not as low to be below the noise level, thus adding too many SP candidates as a result of random fluctuations. The false-alarm-probability of having n samples above

a minimum S/N (S/N_{min}) by chance is (Lorimer & Kramer, 2012)

$$n(S/N > S/N_{min}) \sim 2N_{samp} \int_{S/N_{min}}^{\infty} e^{-x} dx. \tag{3.11}$$

By setting the false-alarm-probability to a couple of accepted false detections per trial, the resultant S/N threshold is roughly 5. However, the previous calculation was made under the assumption of Gaussian noise. In practice, different radio telescopes adjust the threshold estimated with Equation 3.11 based on the RFI situation of the observation. Accepted thresholds are S/N_{thres} of 6 or 7. Chapter 7 lists the minimum detectable S/N for AO, GBT and Effelsberg.

The technique of convolution can also be applied in the Fourier domain. In this case, the timeseries is transformed using an FFT, and the resulting power spectrum is multiplied by the frequency response of the match filter[2]. The signal is then transformed back to the time domain using the inverse FFT. This reduces the computing cost of the search, as multiplication is less computationally expensive than convolution. PRESTO's `single_pulse_search.py` algorithm makes use of this technique, and it was extensively used as part of the FRB 121102 follow-up and to search for the pulsar and RRAT candidates of FAST.

3.2.2 Dedispersion

The algorithms previously discussed need to be iterated over a DM range when the exact DM of the source is unknown. For each DM trial, the timeseries is corrected by the corresponding dispersion. *Dedispersion* refers to the correction of the dispersive delay introduced to signals by plasma along the line of sight. As discussed in Section 1.4.1, dispersion smears a pulse across the frequency channels of the observation, so that signals of higher frequencies arrive earlier than signals of lower frequencies. Each of the N frequency channels in the observing band is shifted with respect to each other by a number of samples. Dedispersing consists of shifting back the samples to align the pulse across all the N frequency channels. Figure 3.3 shows the reconstructed pulse (right panel; referred to hereon as an aligned pulse) with enhanced S/N. Not dedispersing the data, might result in an undetectable signal, as seen in Figure 3.3 (left panel).

We take the data structure shown in Figure 2.3 to illustrate the dispersion delay correction during data processing. Each of the N-frequency channels in the observation band corresponds to a timeseries of $N_{samp} = T/t_{samp}$ samples, where t_{samp} is the sampling rate and T the length of the observation. The set of frequency channels composes the observing bandwidth Δf.

We defined the dispersion delay in Equation 1.37 in terms of the DM and the observing frequency. Taking this equation, we calculate the delay between a reference frequency in the band (f_{ref}) and a channel i ($i \in [1, 2, .., N]$]) with frequency f_i as

[2]Multiplication in the frequency domain corresponds to convolution in the time domain

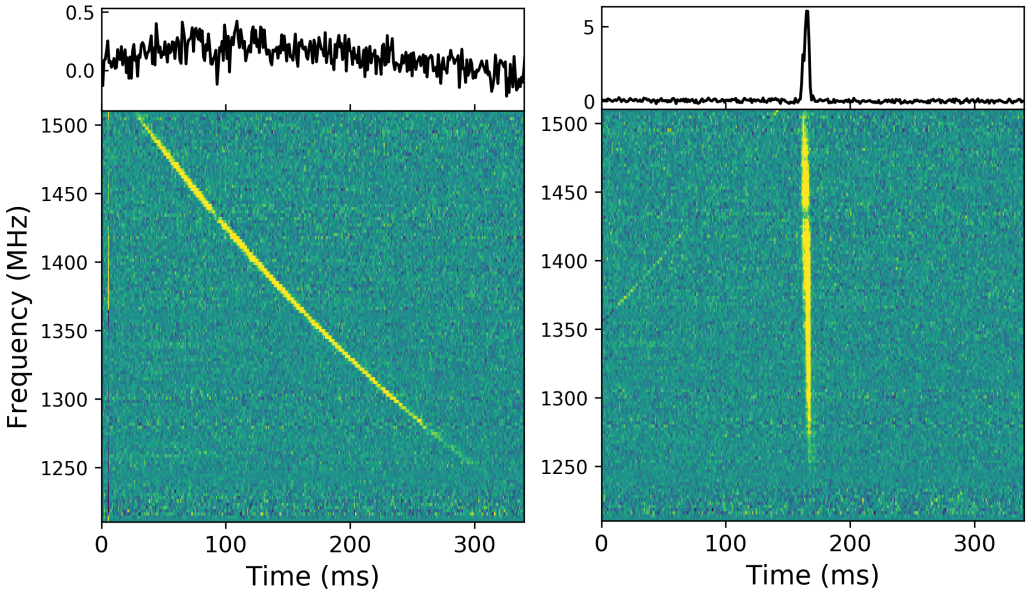

Figure 3.3: Effect of dedispersion. The top plot displays the pulse profiles obtained when integrating in frequency the dynamic spectra in the lower panel. *Left:* no dispersion delay correction. *Right:* incoherent dedispersion at 563.0 $\mathrm{pc\,cm^{-3}}$.

$$t_d = 4.15 \times 10^6 \left(\frac{\mathrm{DM}}{\mathrm{pc\,cm^{-3}}}\right) \left(\frac{\mathrm{MHz^2}}{f_{\mathrm{ref}}^2} - \frac{\mathrm{MHz^2}}{f_i^2}\right) \mathrm{ms}. \tag{3.12}$$

Standard reference frequencies may be the middle, the top, or the bottom frequency of the band. Because of the discrete form of the data, a more useful calculation is the number of time bins to shift the timeseries of the i^{th} channel

$$n_i = \frac{4.15 \times 10^6}{t_{\mathrm{samp}}} \left(\frac{\mathrm{DM}}{\mathrm{pc\,cm^{-3}}}\right) \left(\frac{\mathrm{MHz^2}}{f_{\mathrm{ref}}^2} - \frac{\mathrm{MHz^2}}{f_i^2}\right). \tag{3.13}$$

Naturally, due to the discrete nature of the timeseries, n_i should be taken as the nearest integer. Figure 3.3 shows the effect of applying the corresponding dedispersion. Before the signal correction, the pulse is hidden in the noise due to the delay of roughly 250 milliseconds between the top and bottom of the frequency band. After a delay correction corresponding to a DM of 563 $\mathrm{pc\,cm^{-3}}$, the pulse is aligned across the frequency channels, and the pulse's SNR increased. Worth noting is that for these searches, the dispersion correction is incoherent as the corrections are applied to channelized data.

Since the DM is not known apriori, it is a free parameter that should be sampled with DM trials over a wide range. The optimal range and step size are determined by:

- S/N recovery: The trial DM should be close enough to the true DM of the pulsar/FRB such that the signal can be detected.

- Computing time: The total number of DM trials should be optimized. Small DM steps increase the computational cost of the data processing, without necessarily leading to significant improvement of the S/N. On the other hand, large steps could lead to the true DM lying between two DM trials, thus the pulse is broadened to the point of not being detectable.

- Observing frequency: The smearing time due to dispersion for a bandwidth Δf centered at an observing frequency $f_{\rm o}$ is

$$\tau_d = 1.205 \times 10^{-7} \mathrm{DM} \left(\frac{\Delta f}{f_{\rm o}^3} \right) \mathrm{ms}. \tag{3.14}$$

  The maximum distance to sources that a blind survey is sensitive to depends on the intra-channel dispersion smearing due to a given DM – which depends on observing frequency, and the frequency channel width. Searches at frequencies of a couple of hundreds of MHz are more affected by pulse smearing due to dispersion than searches carried out in the GHz. While frequencies at L-band (near 1 GHz) normally search for a DM range $\in [0, 2000]$ pc cm^{-3}, low frequency surveys (such as with LOFAR) search roughly up to 200 pc cm^{-3}.

If the smearing attributed to pulse broadening due to the difference between the trial DM and the true DM is set equal to the sampling rate, then the DM step is defined as (Lorimer & Kramer, 2012)

$$\Delta \mathrm{DM} = 1.205 \times 10^{-7} \left(\frac{\mathrm{t_{samp}}}{\mathrm{ms}} \right) \left(\frac{f^3}{\Delta f} \right) \mathrm{pc\,cm^{-3}}, \tag{3.15}$$

thus the i^{th} DM trial is

$$\mathrm{DM}_i = 1.205 \times 10^{-7} \, (i-1) \left(\frac{\mathrm{t_{samp}}}{\mathrm{ms}} \right) \left(\frac{f^3}{\Delta f} \right) \mathrm{pc\,cm^{-3}}. \tag{3.16}$$

Equation 3.15 is used to calculate the DM step size until the so-called *diagonal DM* is reached, where the smearing time across the bandwidth of the frequency channel, known as *intra-channel smearing* is equal to the sampling time. Because for incoherent dedispersion corrections cannot be applied within the frequency channel, at this stage, continuing with the full resolution is computationally inefficient. The time resolution can be therefore downsampled by a factor of two, a new DM step is calculated according to Equation 3.15 and dedispersion can proceed once more until diagonal DM is reached again. The resolution can be further downsampled by a factor of 4, then 8, then 16 and so on. Figure 3.4 shows the dedispersion plan I used for Effelsberg data using PRESTO's `DDplan.py` routine.

At each DM trial, after the delay corrections have been applied, all the frequency channels are summed to create a combined timeseries. We obtain the zero-DM timeseries for the trial equal to $i = 0$ in Equation 3.16.

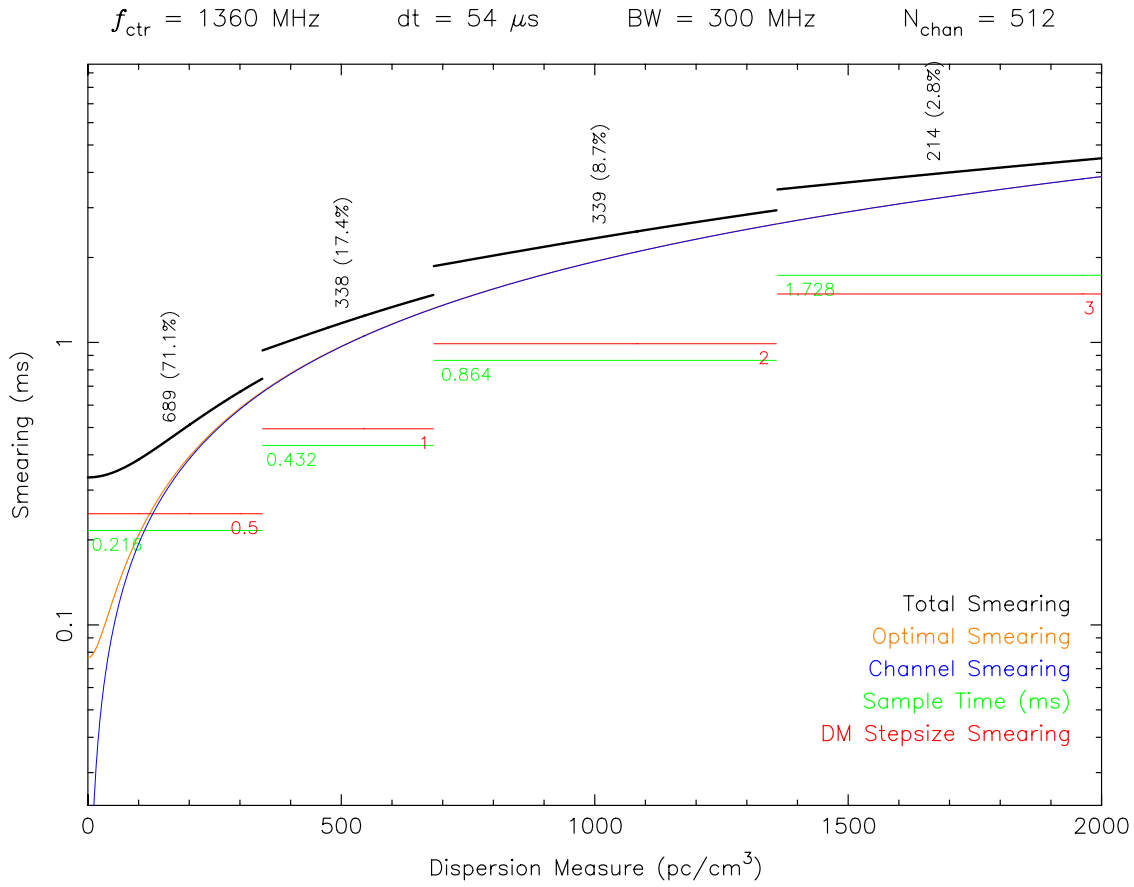

Figure 3.4: Dedispersion plan from `DDplan.py` for an observation carried out with Effelsberg based on the data parameters as described at the top of the figure. The optimal DM stepsize (*red curve*) based on intrachannel smearing is $0.5\,\mathrm{pc\,cm^{-3}}$ for DM $\in [0, 344.5]$, $1.0\,\mathrm{pc\,cm^{-3}}$ for DM $\in [345.5, 682.5]$, $2.0\,\mathrm{pc\,cm^{-3}}$ for DM $\in [682.5, 1360.5]$ and stepsize of $3.0\,\mathrm{pc\,cm^{-3}}$ for DM $\in [1360.5, 2002.5]$. Abbreviations: f_{ctr}=central obsersing frequency, dt=sampling rate, BW=observation bandwidth, N_{chan}=Number of frequency channels.

3.2.3 Candidate folding

Regardless of the type of search, additional filters must be applied before the candidates are manually inspected to reduce duplication. After the search has finished, the outcome is a list of candidates. For Pulsar candidates, the list includes the information such as $P, \dot{P}, DM$. For SP search, the candidate list includes the time of the event and the DM. This information is used to create the diagnostic plots presented in Figures 3.5 and 3.6 for single-pulse (SP) and periodic candidates, respectively.

`prepfold` is the commonly used routine to fold a pulsar candidate. It runs an optimization based on a reduced range near the provided input parameters $(DM, P, \dot{P})$ and it reports several χ^2 tests to estimate the significance of the candidate. A good indicator is the number of σ above the noise level. To limit the manual inspection to the most significant candidates, those with a σ below a certain threshold are filtered out. Further criteria include grouping a single periodicity detected over several DM trials, keeping only the candidate whose DM leads to the highest S/N. Candidates related by integer Harmonics are grouped into a single candidate as well. If the search included acceleration resampling, the candidate whose acceleration or z_{max} gives the highest S/N is kept.

The SP candidates plot is a summary of all the events detected during the search at the different DM trials. Events are shown with concentric circles, whose size represents the S/N; the higher the S/N, the larger the circle. The summary plot is the first inspection of promising candidates. As previously discussed, real candidates should not peak at DM of $0\,\mathrm{pc\,cm^{-3}}$. In Figure 3.6, several events are observed to be clustered at a DM of roughly $57\,\mathrm{pc\,cm^{-3}}$. After the quick overview of the candidates encountered, the next step is to inspect each event with plots such as the one shown in Figure 3.3 and panels *c* and *d* in Figure 3.7. They correspond to an extract of the observation around the event time for each frequency channel. This is known as the *dynamic spectrum* or *waterfaller plot*. By integrating each time sample across the frequency band, the integrated pulse profile is obtained (top). Usually, each candidate is evaluated at DM=$0\,\mathrm{pc\,cm^{-3}}$, and the DM of the event. For SP searches, the key to filtering duplicated candidates is to keep the candidate that returns the highest S/N. Naturally, if the S/N leading to the strongest detection peaks at DM=$0\,\mathrm{pc\,cm^{-3}}$, the candidate is discarded regardless of the search technique used.

In the past decade, the use of Machine learning methods have been widely included to identify the most promising candidates from candidate plots such as the ones shown in Figures 3.3 and 3.5. Eatough et al. (2010) reported the first application of an artificial neuronal network technique to automatically identify pulsar candidates from pulsar surveys. Additional successful applications of pattern recognition methods are PICS (Zhu et al., 2014) and SPINN (Morello et al., 2014), both based on deep neural networks. AI-based methods are of great use in the era of big data, where telescopes such as FAST and SKA will produce high numbers of candidates, which will be unfeasible to inspect entirely by eye.

After the application of all (or some selection of) the methods mentioned above, the remaining numbers of candidates which must be inspected by eye are typically from

tens to hundreds. However, if RFI mitigation or candidate filter is not performed, the number scales up to thousands to millions of candidates.

3.2.4 RFI mitigation techniques

RFI mitigation is implemented at multiple stages. Before the data processing, to ensure good quality of the data entering the search pipelines, and during processing to reduce the number of false candidates. Contrary to white-noise (see Footnote 14), RFI is non-gaussian and comes in different forms. It has a wide range of intensities, are narrow or broad-band, sporadic or periodic. Figure 3.7 shows examples of RFI in candidate plots obtained from pulsar (panel a and b) and FRB search algorithms (panel c and d).

The cumulative effect of RFI over an observation – if not properly mitigated – can hinder a detection of an astrophysical signal, extend the computing time of processing pipelines by increasing the number of candidates to fold, resulting in longer manual inspection time. In the worst-case scenario, when the power of most of the frequency channels or time samples are saturated, it leads to a non-linear response in the LNA. Therefore RFI can mask any useful information in an observation.

I proceed to describe the RFI mitigation techniques used to process the data presented in Chapters 5 and 7. Some of them correspond to broadly used algorithms, while some other techniques were implemented for this thesis.

3.2.4.1 Frequency domain mitigation

The observation's bandpass (see Figure 2.2) is the frequency response of a receiver to the incoming signals. It is obtained by integrating the observation length for each frequency channel. Barr et al. (2013) implemented a bandpass RFI excision algorithm based on spike identification. Through this method, power excesses from narrow-band RFI (spikes) and the associated channels are removed. An example of the technique is shown in Figure 3.8, where the red-shaded regions are the frequency channels of an observation labelled as "bad". The disadvantages of this method are that it is difficult to find low S/N spikes, and that it can lead to the removal of a significant portion of the band although the spike may not be RFI, but instead resonance lines. As S/N scales with the number of frequency channels, this, in turn, decreases sensitivity to dimmer sources.

A bandpass template-based approach was developed as part of this thesis for the Effelsberg's 7-beam receiver data. The bandpasses of the data recorded by each of the seven beams are compared with the corresponding bandpass templates. The algorithm computes the residuals between an observation and the model and flags a channel as "bad" given a threshold deviation (2σ or 3σ). The output from the algorithm is shown in Figure 3.9. The diagnostic plot shows the worst four beams of an observation, where the bad channels are flagged with green crosses. By comparing the bad channel list from each beam, the residual threshold can be set based on the occurrence in several beams. This approach leads to $<5\%$ of flagged frequency channels, in contrast to the spike-detection-based algorithm where as much as 20% is removed.

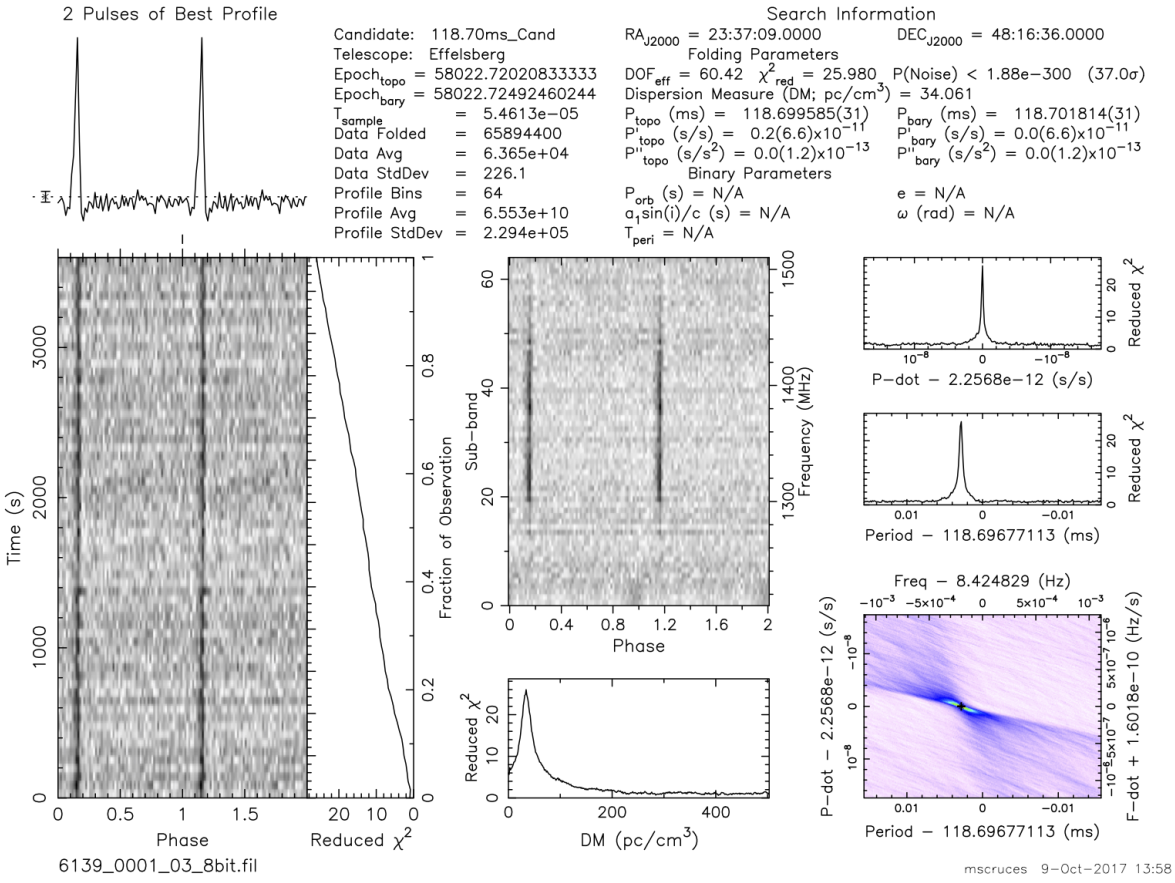

Figure 3.5: PRESTO's `prepfold` candidate plot. *Top-left:* pulse profile for a phase from 0 to 2. *Bottom-left*: persistence of the signal along the observation length. *Top-middle:* persistence of the signal across the frequency band. *Bottom-middle:* strength of the signal in term of χ^2 as a function of the DM trials. *Top-right:* χ^2 as function of the spin period trials. *Middle-right:* χ^2 as function of the trials in spin period derivative. *Bottom-right:* parameter space of the spin period and its derivative. The information in the header of the observation and the best parameters from the folding optimization is shown at the top.

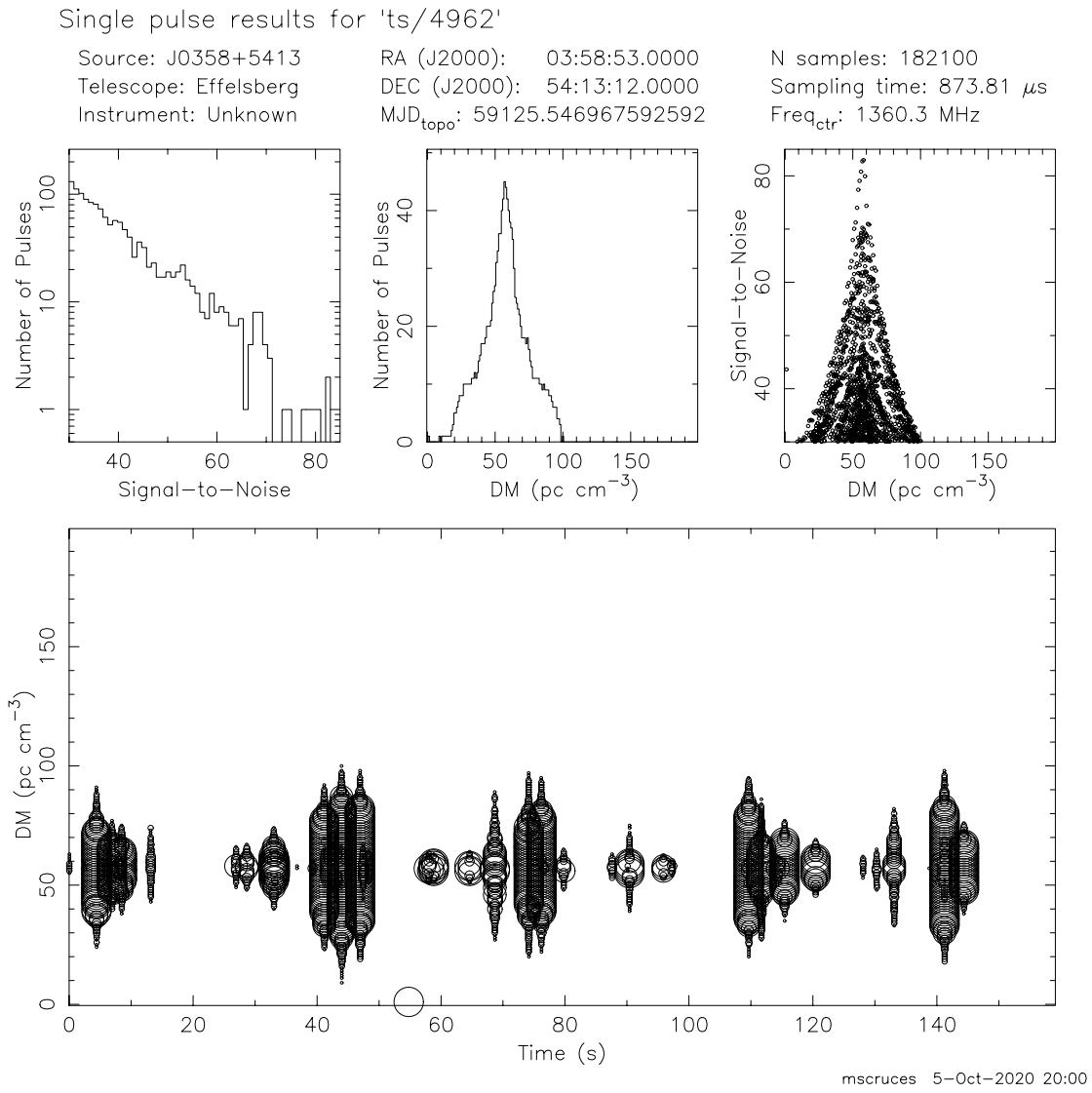

Figure 3.6: PRESTO's `single_pulse_search.py` candidate plot for single-pulse events of PSR J0358+5413. *Top-left:* signal-to-noise distribution of the events. *Top-center*: dispersion measure distribution of the events. *Top-right:* dispersion measure of the single-pulse events against its signal-to-noise. *Bottom:* event time relative to the length of the observation, the size of the circles is proportional to the strength of the signal-to-noise of the event.

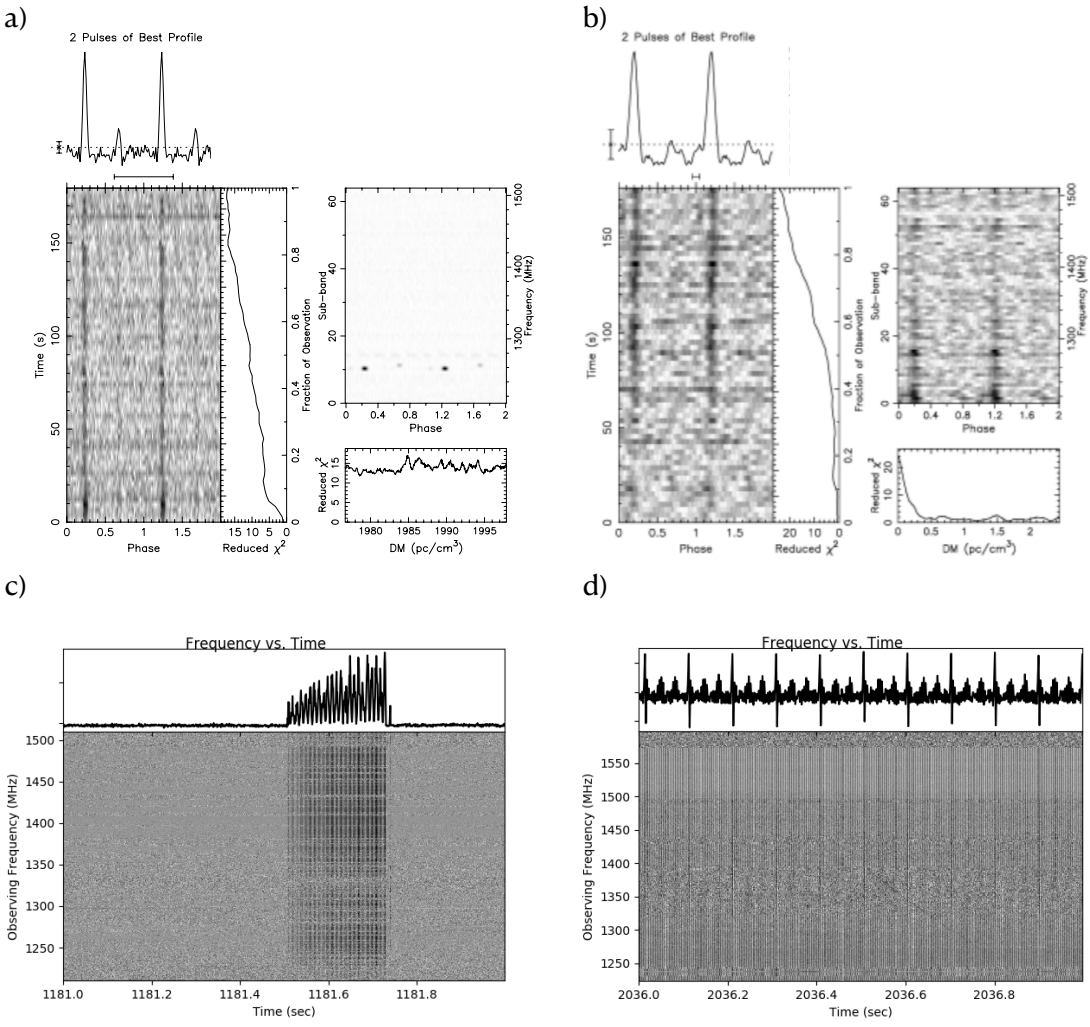

Figure 3.7: Example of radio frequency interference (RFI) in pulsar and FRB searches. *Top*: RFI in pulsar-candidate diagnostic plots. a) is a narrow-band periodic RFI, while b) corresponds to a periodic broad-band RFI. *Bottom*: RFI in FRB-candidate diagnostic plots. c) is a spurious broad-band RFI and d) is a periodic broad band RFI. See Figures 3.5 and 3.3 for plot description.

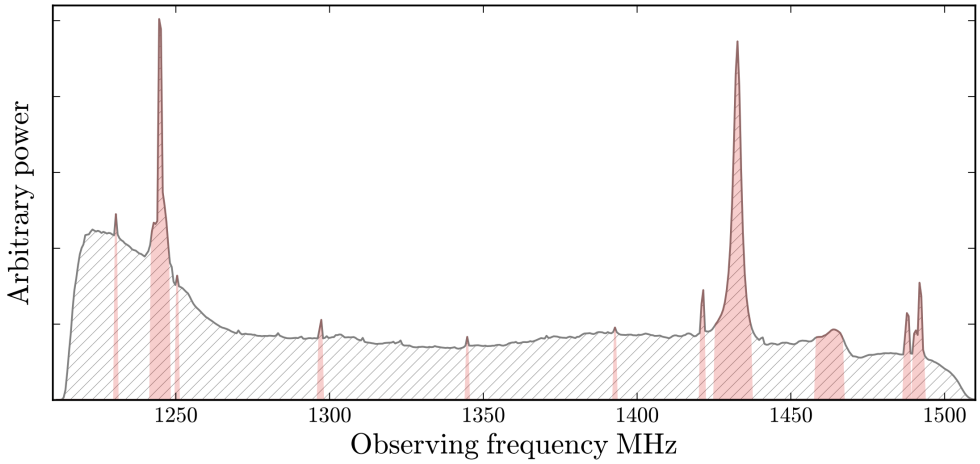

Figure 3.8: Radio frequency interference mitigation technique based on spike identification in a observation's bandpass response. The red-shaded regions are the frequency intervals flagged as RFI affected. Image credit: E. Barr

Before establishing a template for each beam, a statistical analysis was carried out to verify the stability of the bandpass shape across time. We compared the bandpass shape for over 200 randomly selected search mode observations spanning roughly four years. We concluded that the bandpasses had a consistent shape across epochs and that there were frequency ranges where spikes were always present. Such spikes are not RFI induced but instead correspond to resonance lines, such as the hydrogen line at 21 cm. We tested whether the frequency ranges with the always-present spikes were sensitive to pulsar signals. To do so, we used tens of test pulsar observations, where a known bright pulsar is observed at the start of the observation to test the receiver and the data recording flow. It was concluded that those frequency ranges still contributed to the S/N of the known pulsar.

The method of flagging channels from the bandpass analysis reduces strong narrowband false candidates such as those displayed in Figure 3.7 in panel *a*

3.2.4.2 Time domain mitigation

An electromagnetic wave set of terrestrial origin has not travelled through the ISM as it originates either from Earth or from Earth's orbit; thus, it has not interacted with plasma and has no dispersion delay in its time of arrival (DM=0 $\mathrm{pc\,cm^{-3}}$). This is the key to identifying bad samples or intervals in the timeseries while minimizing the risk of flagging an astrophysical pulse. The signals present in the timeseries can be impulsive or periodic. However, periodic RFI is better spotted in the Fourier domain and will be discussed in the next Subsection. The origin of impulsive-broadband RFI are sparks, such as switches, petrol engines and electric fences in the surrounding area of the radio telescope. Impulsive RFI can corrupt data spanning a few time samples

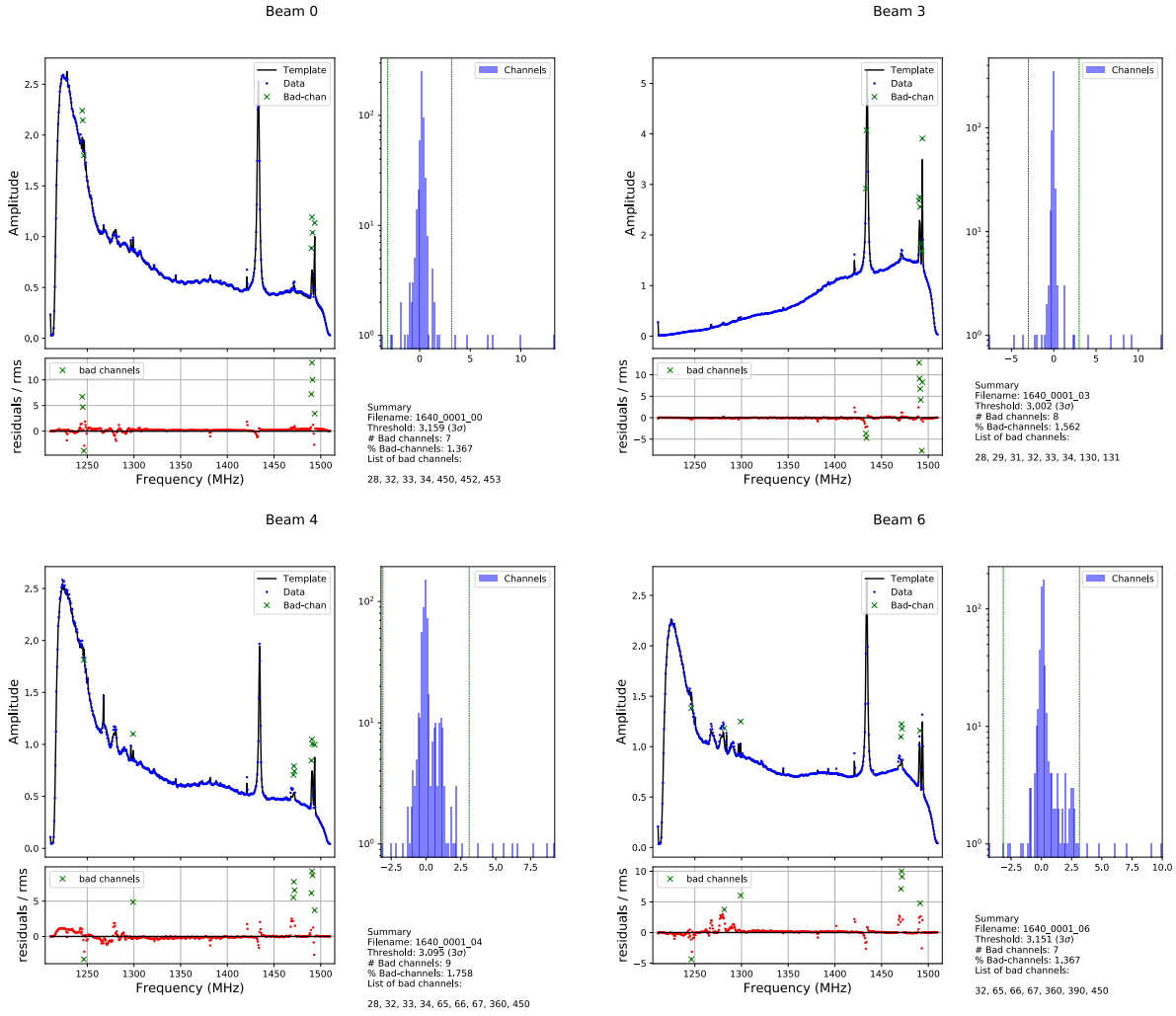

Figure 3.9: Diagnostic plots from the bandpass-template based algorithm to identify bad frequency channels. The plots show the analysis of a 3 minutes long observation with Effelsberg's 7-beam receiver at 1.36 GHz. The plot shows beams 0, 3, 4 and 6. The *green crosses* show the bad channels identified.

to a full observing interval, and if not mitigated, can significantly raise the number of candidates in single-pulse searches by thousands or millions.

A well-tested algorithm to mitigate time-domain RFI is the *zero-DM filter* (Eatough et al., 2009). The algorithm computes the mean power across the frequency channels for each sample in an undedispersed timeseries (DM=0 $\mathrm{pc\,cm^{-3}}$). The mean is subtracted from all the frequency channels of the given time sample. As broadband RFI results in simultaneous power rise across all frequency channels, they are removed using this filter. Figure 3.10 illustrates the effect of the zero DM filter: Panel *a* shows an extract of simulated undedispersed data containing broadband RFI (wide band) and a transient astrophysical signal such as an FRB or a Pulsar (dispersed quadratic curve). After the zero-DM filter application (Panel *b*), it is seen that the RFI was removed while the astrophysical signal remains. Panel *d* shows the Fourier spectrum of the transformed timeseries before zero-DM filtering, while Panel *e* shows the result of the filter application. It is seen that the pulsar's harmonics remain and the periodic RFI has been significantly reduced.

The zero-dm filter is implemented in many sub-routines of the standard pulsar data processing software such as PRESTO (Ransom, 2011) and SIGPROC[3]. However, its drawback is seen in Figure 3.7 Panel *c*. The depressions in power on either side of the pulse profile are a consequence of the subtraction procedure. The lower the DM of the signal and the larger the spin period (for pulsars), the more significant such depressions are. As pointed out by Eatough et al. (2009), this can potentially lead to up to a 50% of signal-loss for the main harmonic of pulsars with spin periods larger than 200 milliseconds and DM$<$ 100 $\mathrm{pc\,cm^{-3}}$. Ultimately, if the DM is low enough, it will remove all the power leading to an undetectable signal.

3.2.4.3 Fourier domain mitigation

As mentioned in Subection 3.2.4.2, periodic RFI signals are best spotted via Fourier transformation of the timeseries. As with zero-DMing, using the undedispersed timeseries prevents the "flagging" of real pulsar signals as RFI. During the FFT analysis, dominant frequencies (peaks) exceeding a power threshold are identified, and their significance explored at a range of DM trials to verify if the power of the signal peaks at DM$=$ 0 $\mathrm{pc\,cm^{-3}}$. Pulsars at low DM or bright enough that they are also detected at zero DM, are therefore left unflagged.

A statistical analysis of recurrent bad periodicities leads to a list often referred to as *birdies*. The birdies list is consulted by processing scripts in order to always ignore such periodicities.

For multi-feed array receivers a more sophisticated approach is possible by combining the information obtained from many beams. This requires that the centre of each beam points to a different sky position, and each beam recording data simultaneously. If a candidate is present in multiple beams, this indicates a terrestrial origin for the source. However, because neighbouring beams can have a spacial overlap, either

[3] http://sigproc.sourceforge.net/

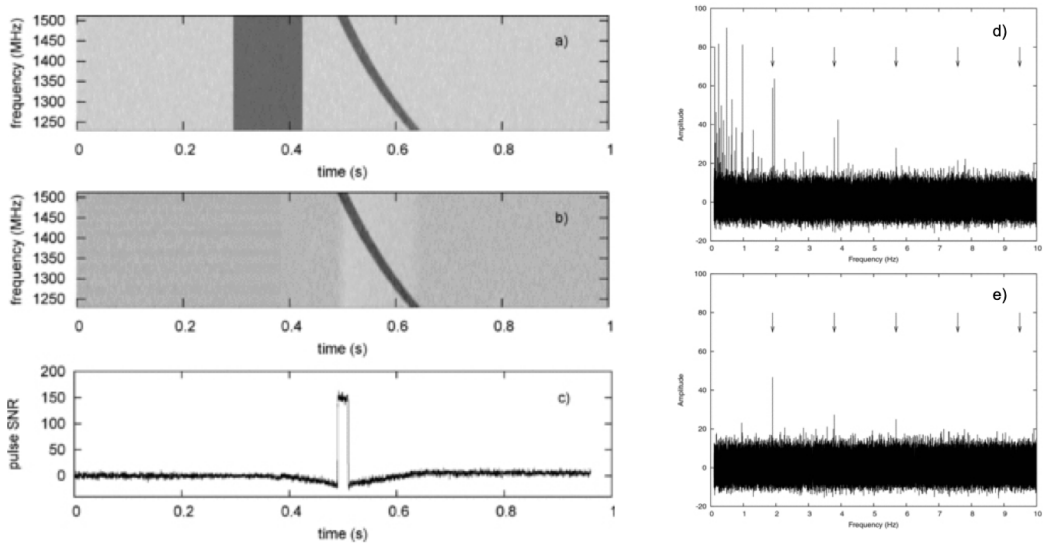

Figure 3.10: *Zero-DM* filter. *Left:* before (*a*) and after (*b*) the method was applied to simulated data. *c* is the the resultant S/N of the pulse profile post filter. *Right:* Fourier spectrum of the data before (*a*) and after (*b*). The arrows indicate the Harmonics of the pulsar. Image credit: Eatough et al. (2009).

between their main beams or their side-lobes (see Figures 2.6 and 2.8), the distance between beams should also be considered, to prevent flagging bright pulsars as RFI.

A multi-beam RFI mitigation algorithm was developed as part of this thesis for Effelsberg's 7-beam receiver data. The use of several independent beams allows a lower S/N threshold to be considered, thus removing more subtle RFI. The multiple-beam, occurrence-based algorithm searches for periodic signals in an FFT with the use of SIGPROC's `seek` script. The signal detections of each of the seven beams are correlated afterwards. Candidates detected in three or more non-neighbouring beams are then flagged as RFI. The outcome of the multi-beam excision algorithm is a list of RFI periodicities to be removed from the candidate list, before creating the candidate plots. This technique has proven to be efficient at identifying periodic RFI such as the ones in Panels *a*, *b*, and *d* of Figure 3.7.

3.2.4.4 PRESTO's rfifind

`rfifind` is a PRESTO routine (Ransom, 2011) designed to mask bad frequency channels and time samples. It is based on a statistical analysis of the observation in small data blocks – typically of a few seconds – for which the power distribution, mean and standard deviation are computed. Any outlier samples are identified and flagged. The outcome of `rfifind` is a mask file where the corrupted frequency channels are replaced with zeros, and bad blocks of data are replaced with the running mean value for

that channel. The mask file is used afterwards in further PRESTO based algorithms such as `prepdata, prepsubband` (for dedispersion), `prepfold` (to fold a candidate), `single_pulse_search.py` (to search for single pulses). `rfifind` is efficient at identifying strong narrow-band and short-duration, broad-band RFI (Figure 3.7, panels *a* and *c* respectively).

3.2.4.5 Manual cleaning

The methods listed above can be implemented as part of data processing scripts to provide an automated RFI excision procedure. This is preferable when processing large amounts of data, for instance, from pulsar or FRB surveys. However, the most promising candidates often undergo a refined manual inspection and removal of bad frequency channels as well as bad time intervals to optimize their S/N. Examples of pulsar software to carry manual cleaning are `paz, pazi` and `psrzap` (van Straten et al., 2012). Figure 3.11 shows the plot of a folded candidate before and after manual cleaning with `pazi` (van Straten et al., 2012). The wobbly baseline in the left panel has been removed, and the S/N has significantly improved, but most importantly, the pulsar is unambiguously detected after the cleaning procedure.

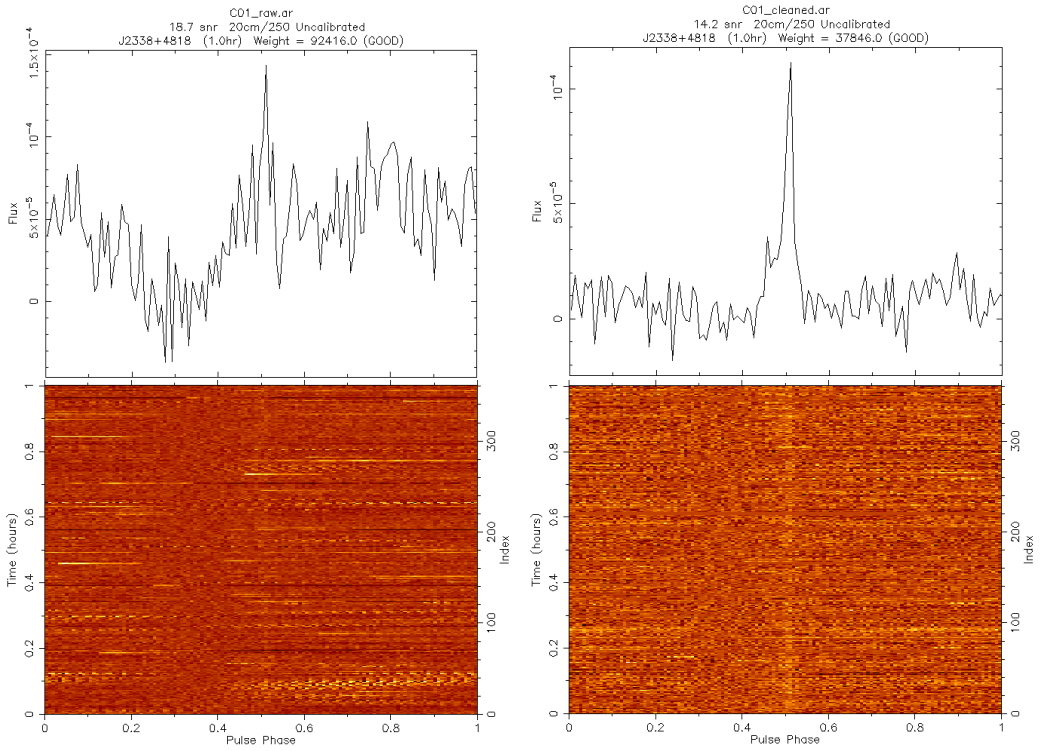

Figure 3.11: Example of manual cleaning of RFI with PSRCHIVE's `pazi` routine (van Straten et al., 2012). *Left*: folded archive file before cleaning. *Right*: folded archive file after manual cleaning with pazi. The data was cleaned in time and frequency.

Chapter 4

Timing a new pulsar

Upon a pulsar's discovery, there is a rough estimation of its parameters such as spin period, DM and position. However, they are not precise enough to predict the spin rotation during the long term; needed for the science applications discussed in Section 1.6. Timing is the method of precisely measuring the times of arrival (TOA) of the pulses at the telescope and comparing them with a model that describes the pulsar rotation within a given time range. With each observation, the model improves, and it becomes reliable over longer timescales. Once the model can account for every rotation, it is said to be a *phase connected/coherent timing solution*. In this section, I discuss the steps required to create a model predicting the pulsar rotation down to an accuracy of a small fraction of its spin period.

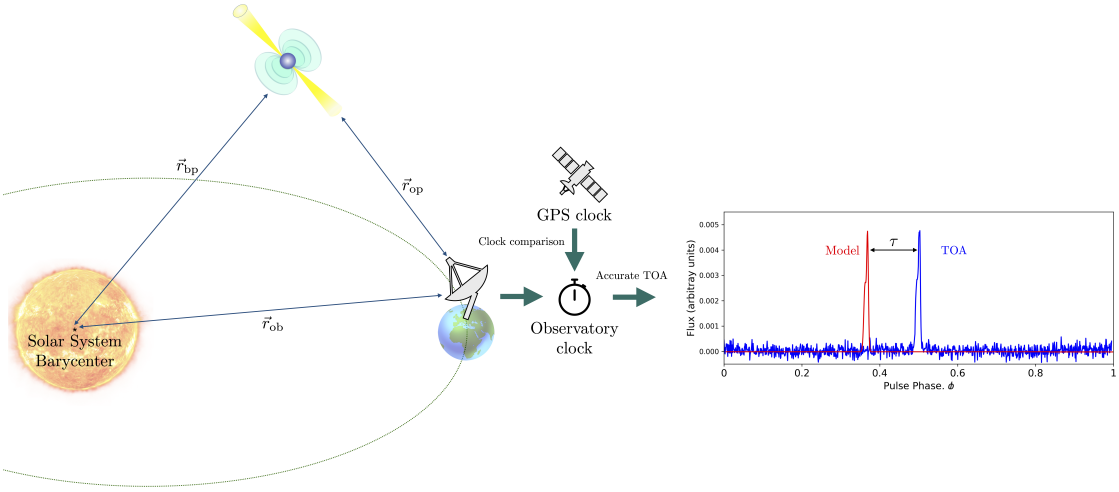

Figure 4.1: Schematic view of timing procedure and geometry involved. See text for explanation.

Contents

4.1 Establishing a folding ephemeris

After a suitable candidate has been obtained from the search procedure discussed in the previous chapter, the spin period of the pulsar is known to a precision that only allows folding within hours of the observation. If we were to shift soon after to carry out real-time folding observations, the imprecision in the spin period would likely lead to a pulse shifted where the integrated pulse profile is broadened or entirely not visible. The more time has passed between the discovery and the confirmation observation, the less likely it is to see the pulsar in the folded archive. Instead, a preferred approach is a series of observations performed in search mode, with short cadence (few hours to a few days apart). A pulsar search is carried out over a reduced parameter space, and the spin period measured at each epoch.

The position can be pinpointed to a better accuracy than the telescope's beam, by applying a grid to the sky position. The S/N of several detections at beam positions are used to determine the location of the pulsar. As is was discussed in Section 2.3, the beam sensitivity decreases toward its border by 50%; thus by locating the pulsar as close as possible from the beam center the S/N is enhanced. However, refining the position is only possible if the pulsar does not scintillates over timescales comparable to the length of the observations. Otherwise, changes in S/N cannot be exclusively attributed to the position of the source within the beam. An example of a close-packed grid for the central beam of Effelsberg's 7-beam receiver is provided in Figure 4.2. The Galactic coordinates needed for each pointing of the grid are with respect to the position of the central beam $(l_c; b_c)$. The source location is narrowed down depending on the overlapping region where the pulsar is detected[1].

As illustrated in Figure 4.1, a template for the pulse profile is needed to obtain TOAs from the observation. In its most basic form, it consists of a Gaussian fit to the profile. Multiple components can be added based on the number of Gaussians needed to reconstruct the profile. This type of template is called *noise-free template*. The most common cross-correlation techniques to obtain precise TOAs are the *Fourier phase gradient* (Taylor, 1992) and the *Fourier Domain Markov Chain Monte Carlo (MCMC)* (Verbiest et al., 2016) algorithms. Matching the template (f) with the observation's averaged pulse profile (g) as a function of the phase offset is done through the cross-correlation

$$(f * g)(\tau) = \int_{-\infty}^{+\infty} f^*(t)\, g(t+\tau) dt, \tag{4.1}$$

where τ is shift. Both methods are Fourier domain-based, thus after converting through FFT, the phase offset is measured as a displacement of the to signal in the Fourier spectrum. The difference between the two approaches relies on the uncertainty estimation. The phase gradient method uses a linear gradient fit, while the other uses a one-dimensional Monte-Carlo fit based on the likelihood as a function of phase-shift. The MCMC based method has shown to perform better in the low-S/N regime as it does not assume noise Gaussianity (Verbiest et al., 2016). For pulsars with high S/N,

[1] In addition to the beam shape should be considered, see Section 2.3

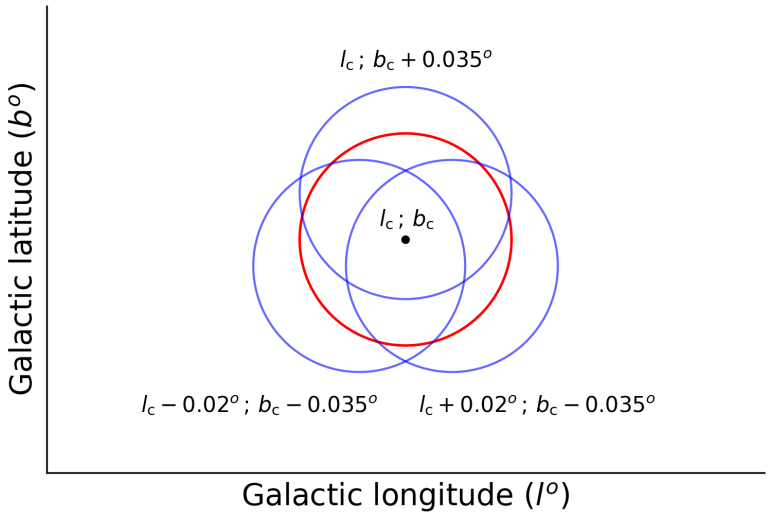

Figure 4.2: Close packed grid geometry for the central beam of Effelsberg's 7-beam receiver. The coordinates are provided in Galactic coordinates: l is the Galactic longitude and b is the Galactic latitude. The central beam (*red circle*) has coordinates l_c ; b_c.

both methods are comparable. After applying the inverse function to the correlation, the signal phase offset is calculated and the corresponding TOA.

The reason the integrated pulse profiles are used to extract TOAs, instead of single pulses, is due to the shape and S/N variability from pulse to pulse. By adding hundreds of pulses coherently, the profile (often) becomes stable (Lorimer & Kramer, 2012) and the S/N higher. This is demonstrated in Figure 4.3 (left) with single pulses from PSR B0950+08. The combination of all of them yields the profile displayed at the bottom. To achieve the highest S/N possible is important, as it relates to the precision at which the TOA is measured

$$\sigma_{\mathrm{TOA}} \sim \frac{W}{S/N}, \tag{4.2}$$

where W is the pulse width. Bright and narrow profiles pulsar allows TOAs to be determined to the nanosecond level (Shannon et al., 2015). An additional note on the integrated pulse profile is its dependence on the observing frequency. In part, this effect is intrinsic to the profile evolution, partially, is due to propagation effects such as scattering (see Section 1.4.3). Thus, the template is only correlated with observations at similar frequencies. Figure 4.3 (right) shows the profile evolution of pulsar PSR J1740-3052. If we were to do timing at 590 MHz using a template obtained at 2.2 GHz, the reference point, also known *fiducial point* at each frequency might erroneously lead to phase shifts. If the observation is carried out with the use of a broadband receiver, it can be split into frequency sub-bands. Each sub-band is compared to the template

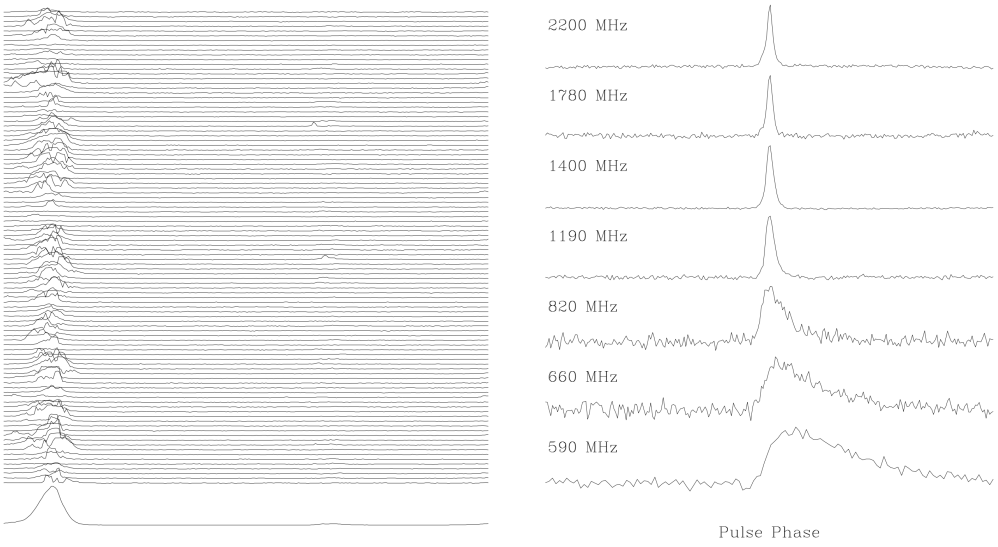

Figure 4.3: Pulse profile variability. *Left*: 100 pulses from PSR B0950+08, demonstrating pulse-to-pulse variability in shape and intensity. *Right*: Pulse profile shape changes for PSR J1740-3052 at multiple frequencies. Images from Stairs (2003).

of the corresponding frequency range.

Depending on the length of the observation, it can be split into time sub-integrations of a given length, each which is combined to obtain one integrated pulse profile. This allows more than one TOA to be extracted per observation.

There are several parameters needed to describe the pulses TOAs. Some of them are intrinsic to the rotation (*spin parameters*), associated to their location (*astrometric parameters*) and connected to the orbital motion (*binary parameters*) when the pulsar is in a binary system. In the following, I describe such parameters and how they are obtained and included in the timing model.

4.1.1 Isolated pulsars

Isolated pulsars are generally the easiest to model. Upon measuring the spin period a few times, usually days to weeks apart, it can be refined to an accuracy that permits the real-time folding. Phase differences between observations, below 0.02, are usually acceptable for timing models. The spin parameters that go in the model are

- **Spin Frequency** (F0): Known initially as a result of the search procedure.
- **Spin Frequency Derivative** (F1): For isolated pulsars, F1 is measured based on the difference in the spin frequency measured at different epochs. Usually, for isolated pulsars, weeks/months are needed to have a measurement of 3σ or more significant.

The astrometric parameters are

- **Sky coordinates** (RA, DEC): Measured in the Equatorial coordinate system[2], with Right Ascension and Declination. As it was mentioned earlier, at discovery, the position is known within the receiver's beam size, which can correspond to several arcminutes. However, it is refined by performing a sky grid like the one presented in Figure 4.2.

- **Dispersion measure** (DM): The value obtained at discovery is optimized to yield the highest S/N, by aligning signal across the frequency channels.

- **Proper motion** (PMRA, PMDEC): it corresponds to the angular velocity across the sky exhibited by the pulsar, which is broken down into the components of right ascension and declination, respectively. As discussed in Section 1.5, young pulsars – especially but not exclusively – exhibit high transverse velocities. This translates into changes in the sky position. At the time of discovery, the proper motion is unknown. Therefore is not included in the initial timing model (hereon referred to as raw ephemeris). As the timing campaign continues, the residuals will show trends indicating unmodeled parameters. This will be discussed in Section 4.3.

It is highlighted that because the parameters change in time, each value reported must be referred to an epoch. The reference epoch is expressed in Modified Julian Days (MJD). An example of a raw ephemeris is

```
PSR          J2129+4115
RA           21:29:18.5
DEC          +41:15:49.9
F0           0.59262181385
F1           0.0
DM           35.4
PEPOCH       58480.610
```

where PSR is the source name, based on the 4-digits of its right ascension, followed by the 4-digits of its declination. PEPOCH refers to the reference epoch of the spin period (or spin frequency). In the example, F1 was set to zero as its value was not above 3σ. This raw ephemeris is used by the backend of the telescope to fold the data in real-time. For systems where the search backend does not imprint accurate TOA with a time maser and/or the filterbank is not coherently dedispersed, to move to timing observations as soon as possible is preferred.

4.1.2 Pulsars in a binary orbit

For pulsars in binary systems, further parameters need to be accounted for, due to the orbital motion of the pulsar and the Doppler shift previously discussed in Section 3.2.1.2. Pulsars in wide binaries, i.e. where the orbital period (P_b) is of several days, can be described with the classic Keplerian orbit parameters. For pulsars in tight

[2]Description: https://astronomy.swin.edu.au/cosmos/E/Equatorial+Coordinate+System

binary orbits (P_b ∼hours), deviations from Newtonian physics must also be considered. Let us discuss first a Keplerian orbit, which is described by the set of parameters

- **Orbital period** (PB)
- **Projected semi-major axis** (OM)
- **Orbital eccentricity** (ECC)
- **Longitude of periastron** (A1)
- **Epoch of passage of periastron** (T0)

The parameters are geometrically connected as shown in Figure 4.4. From Kepler's equation, the position of an object along an elliptical orbit is written in terms of three angular parameters, also known as *anomalies*. Those are the mean anomaly M, the eccentric anomaly E, and the true anomaly A. They are connected through

$$M = E - e\,\mathrm{sinE} \tag{4.3}$$

$$M = \frac{2\pi}{P_\mathrm{b}}(t - T_0) \tag{4.4}$$

$$\tan\left(\frac{\mathrm{A}}{2}\right) = \sqrt{\frac{1+e}{1-e}}\tan\left(\frac{\mathrm{E}}{2}\right) \tag{4.5}$$

$$P_\mathrm{b}^2 = 4\pi^2\frac{a}{\mathrm{G}(m_\mathrm{p} + m_\mathrm{c})} \tag{4.6}$$

where e is the eccentricity, T_0 is the epoch of periastron passage, and a is the sum of the pulsar and companion semi-major axes. m_p and m_c are the pulsar and the companion masses, respectively. These set of equations are solved numerically. The standard method to achieve a solution for the binary orbit involves fitting the parameters to a series of spin period measurements closely spaced in time. However, this is not always possible depending on the availability of the telescope or scintillation effects, which can make the pulsar undetectable. Freire et al. (2001) provides an alternative method based on the *period-acceleration plane*, which does not depend on the observing epochs. In this approach, the apparent spin period of the pulsar is described by

$$P(A) = P_0\left(1 + \frac{v_l(A)}{c}\right) \tag{4.7}$$

$$a_l(A) = -\left(\frac{2\pi}{P_\mathrm{b}}\right)^2\frac{a}{1-e^2}(1 + e\,\mathrm{cos}A)^2\sin(\omega + \mathrm{A}) \tag{4.8}$$

with v_l and a_l the velocity and acceleration of the pulsar along the line of sight, respectively, and ω is the longitude of the periastron. By carrying out a series of observations, the spin period and its derivative are measured at different epochs. The acceleration is thus calculated following Equation 3.8. The measurements are plotted, and the curved of spin period vs acceleration formed is fit with Equations 4.7 and 4.8, which does not depend on time. This allows the orbital parameters to be estimated without solving

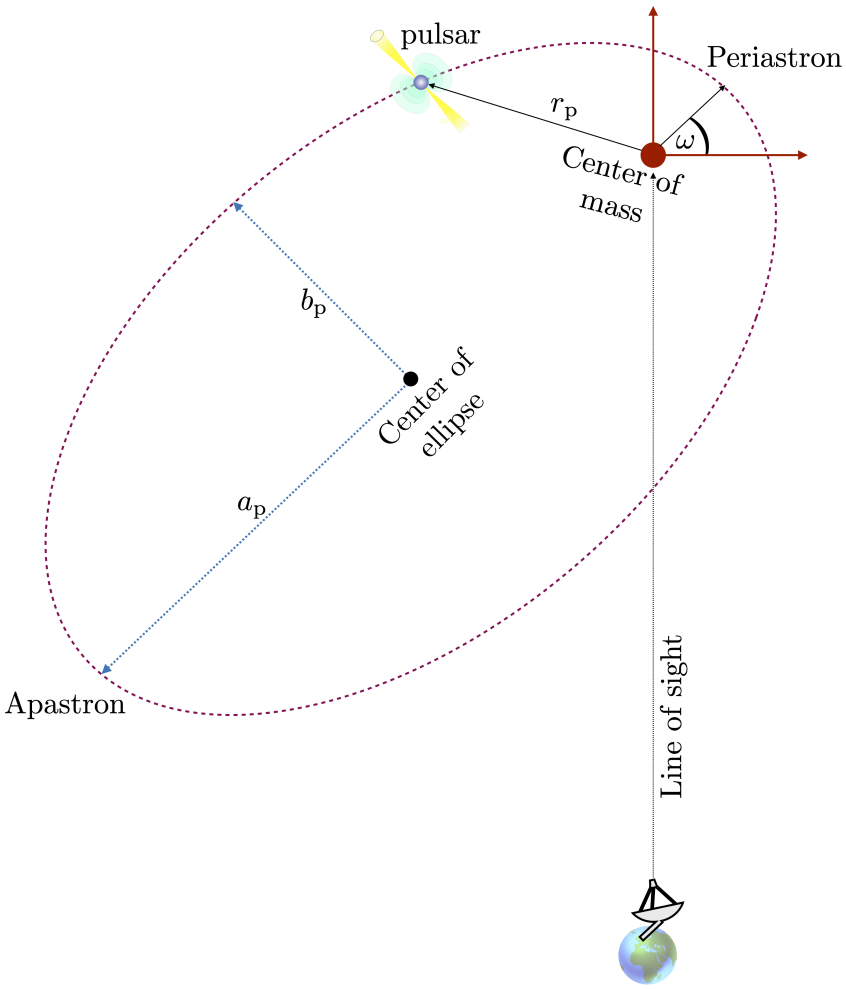

Figure 4.4: Schematic representation of a pulsar in an arbitrary binary orbit. a_p and b_p are the longitude of the semi-major and semi-minor axis, r_p is the distance to the pulsar and ω is the longitude of periastron.

Kepler's equations. Figure 4.5 shows two examples of such a fit. A circular orbit is seen in the period-acceleration plane as an ellipse (left), while eccentric orbits adopt more complex shapes (right).

After the binary parameters are estimated, a raw ephemeris is used to start real-time folding. An example of a folding ephemeris for a binary pulsar is

```
PSR          J2337+4818
RA           23:38:06.2
DEC          +48:18:32.4
F0           8.423872363380
F1           -1.18D-16
PEPOCH       58909.654311
DM           35.8
BINARY        DD
A1           117.5
E            0.0018
T0           58868.435
PB           95.19
OM           99.61
```

When the binary system is in a wide binary (tens of days or more), it is unlikely to be able measure the acceleration within an observation. An alternative approach to solving Kepler's equations is a periodogram search. The classical method is the Lomb-Scargle periodogram. By sufficiently sampling the spin period at different epochs, the modulation of the changes will be due to the orbital period. By fitting a periodic sinusoidal function afterwards, the amplitude of the sinusoid is related to the projected semi-major axis. This is an approximation for nearly circular orbits. This technique was used with PSR J2338+4818, presented Chapter 5. It was estimated that the pulsar is in 95.1 days binary with a projected semi-major axis of 116 light seconds. After the timing follow-up, it was found that the orbit is 95.25536 days, the projected semi-major axis is 117.58572 light seconds, and the eccentricity is 0.0018237; in agreement with the initial guess. It is emphasised, that the raw ephemeris files here presented for an isolated and a binary pulsar, are in its most basic form. A full description of the available parameters is presented in Hobbs (2012). In Chapter 5, timing solutions for ten pulsars are presented, one in a wide binary system and nine isolated pulsars.

When the pulsar is in a very tight binary orbit with a compact companion (NSs, WDs, BHs), relativistic effects are present. Therefore, additional parameters must be included in the model to correct the deviations from a Keplerian orbit. The parameters as measured are theory independent, but they can be related to a theory, in this case GR (Damour & Deruelle, 1985, 1986)

- *Rate of periastron advance* ($\dot{\omega}$): The rate at which the orbit orientation changes,

also known as periastron precession

$$\dot{\omega} = 3T_{\odot}^{\frac{2}{3}} \frac{1}{1-e^2} \left(\frac{P_{\rm b}}{2\pi}\right)^{-\frac{5}{3}} (m_{\rm p}+m_{\rm c})^{\frac{2}{3}} \tag{4.9}$$

where $T_{\odot} = GM_{\odot}/c^3$, with G the gravitational constant.

- *Einstein delay* (γ): Delay caused by the gravitational redshift and time dilation as the pulsar moves along the orbit

$$\gamma = T_{\odot}^{\frac{2}{3}} \left(\frac{P_{\rm b}}{2\pi}\right)^{\frac{1}{3}} \frac{m_{\rm c}(m_{\rm p}+2m_{\rm c})}{(m_{\rm p}+m_{\rm c})^{\frac{4}{3}}} \tag{4.10}$$

- *Orbital decay* ($\dot{P}_{\rm b}$): The rate at which the orbital period decreases, caused by gravitational radiation damping.

$$\dot{P}_{\rm b} = -\frac{192\pi}{5} T_{\odot}^{\frac{5}{3}} \left(\frac{P_{\rm b}}{2\pi}\right)^{-\frac{5}{3}} \frac{m_{\rm p}m_{\rm c}}{(m_{\rm p}+m_{\rm c})^{\frac{1}{3}}} \left(1+\frac{73}{24}e^2+\frac{37}{96}e^4\right)(1-e^2)^{-\frac{7}{2}} \tag{4.11}$$

- *Range parameter* (r)

$$r = T_{\odot} m_{\rm c} \tag{4.12}$$

- *Shape parameter* (s)

$$s := \sin i = x\, T_{\odot}^{-\frac{1}{3}} \left(\frac{P_{\rm b}}{2\pi}\right)^{-\frac{2}{3}} \frac{(m_{\rm p}+m_{\rm c})^{\frac{2}{3}}}{m_{\rm c}} \tag{4.13}$$

where $x = a\sin i$, with i the inclination of the orbit with respect to the line-of-sight.

The last two parameters (r, s) describe the *Shapiro delay*, which is the extra time delay experienced by light as the pulsar moves behind its compact companion with respect to the observer (Shapiro, 1964). The effect is the result of the time dilation and extra path due to a curved space-time induced by the companion's gravitational field. The number of measurable post-Keplerian parameters depend on the timing precision and masses. In circular orbits is harder to measure the longitude of the periastron, thus $\dot{\omega}$ is poorly constrained. For the Shapiro delay, nearly edge-on (highly inclined) orbits yield precise measurements when the pulsar is nearly behind the companion during orbital conjunction.

4.2 Timing model

Thus far, we have discussed the TOAs at the telescope as a reference point. However, Earth-based time reference is not an inertial reference frame, as Earth moves around the Sun. More importantly, TOAs are different at different telescopes, thus combining

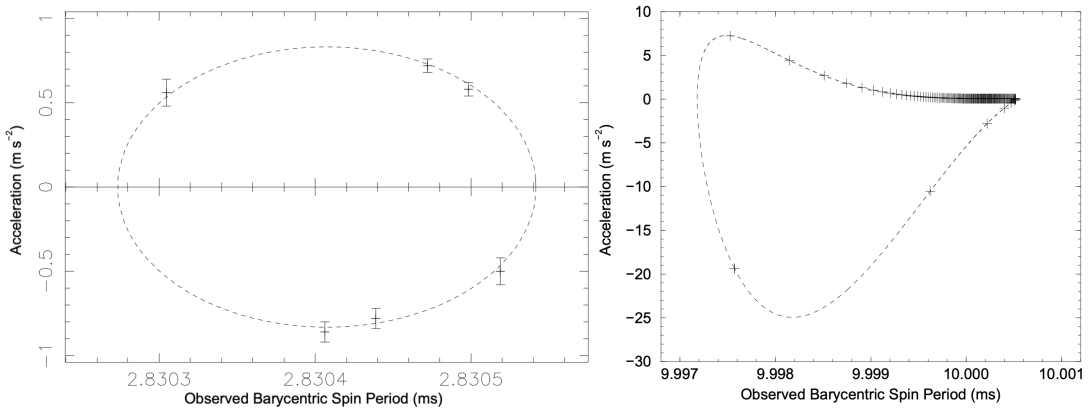

Figure 4.5: Period-acceleration diagram. *Left*: Observed acceleration for millisecond pulsar 47 Tuc S. The best fit is an orbit with $P_\mathrm{b} = 1.24\,\mathrm{days}$; $x = 0.79$; $e = 0$. Simulated binary system with $P_\mathrm{b} = 1.0\,\mathrm{days}$; $x = 1$; $e = 0.9$ and $\omega = 140°$. Images from Freire et al. (2001).

and comparing datasets is not straight forward. A standard reference frame is the Solar System barycenter[3] (SSB), which is the closest to an inertial frame that can be accurately measured[4]. The conversion is done through the equation (Lorimer & Kramer, 2012)

$$t_\mathrm{bary} = t_\mathrm{topo} - \frac{\mathcal{D} \times DM}{f^2} + \Delta_{\mathrm{R}_\odot} + \Delta_{\mathrm{S}_\odot} + \Delta_{\mathrm{E}_\odot}. \tag{4.14}$$

The second term in the equation corrects the dispersive delay discussed in Section 1.4.1, thus referencing to the TOA of a pulse at infinite frequency. $\Delta_{\mathrm{S}_\odot}$ is the light-travel time between the telescope and the SSB, known as the *Römer delay*, $\Delta_{\mathrm{S}_\odot}$ and $\Delta_{\mathrm{E}_\odot}$ are the Shapiro and Einstein delay respectively. The last three terms in Equation 4.14, refer to the effects inside the Solar system. The equation assumes that for pulsars in binary systems, the Einstein and Shapiro delay, and the light-travel time between the pulsar and the binary barycenter, were already corrected. The regularity of a pulsar's rotation is seen when the TOAs are converted from the SSB time to the pulsar emission time (t_psr). To compare the timing data to the model of the pulsar's rotation, the TOAs need to be converted once more, this time to the reference frame of the pulsar. However, if the pulsar is in a binary orbit, first, the SSB time is converted to the barycentric time of the binary, and then to the pulsar emission time.

If the pulsar slow-down is solely due to dipole radiation, then the rotational phase evolution is expressed as (Lorimer & Kramer, 2012)

$$\phi(t) = \nu t + \frac{1}{2}\dot{\nu} t^2 + \frac{1}{6}\ddot{\nu} t_\mathrm{psr}^3 + ..., \tag{4.15}$$

[3]The center of mass of the Solar system.

[4]The Solar system dynamic as e.g. studied by the Jet Propulsion Laboratory: https://www.cv.nrao.edu/course/astr534/Pulsars.html

or in terms of number of rotation between a time t and a reference time t_0 as

$$N(t) = N_0 + \nu(t - t0) + \frac{1}{2}\dot{\nu}(t - t0)^2 + \frac{1}{6}\ddot{\nu}(t - t0)^3 + ..., \tag{4.16}$$

where N_0 is the number of rotations at the reference epoch t_0. This is possible, as with each rotation one pulse is emitted.

4.3 Improving the timing model

After the timing model has been created with the use of the ephemeris, we have a phase predictor, $\phi(t_{\rm mod})$, and the corresponding phases measured at each observation, $\phi(t_{\rm psr})$. The difference between the observations and the timing model of each TOA, called *timing residuals*, is simple defined as

$$r_i = \phi_i(t_{\rm psr}) - \phi_i(t_{\rm mod}). \tag{4.17}$$

The most commonly used estimator for the goodness of the fit is the χ^2 test,

$$\chi^2 = \frac{1}{n}\sum_i \left(\frac{r_i}{\sigma_i}\right)^2, \tag{4.18}$$

with σ_i the uncertainty of the i^{th} TOA, and n the number of degrees of freedom. If the model accurately describes the data, then $\chi^2 \sim 1$ and the residuals are Gaussianly distributed around zero. For $\chi^2 < 1$, the model over predicts the uncertainties. For $\chi^2 >> 1$, the large deviations are likely to show trends in the residuals, due to errors in the timing parameters and/or unmodeled effects. Each of the parameters in the timing model is fit through least-squares minimization. The two most commonly used packages for model fitting are `TEMPO`[5] and `TEMPO2` (Hobbs, 2012).

Panel *a* of Figure 4.6 shows an example of the residuals of a good fit (top left), where no clear trends are distinguishable. On the contrary, the rest of the panels show a high correlation. Panel *b* shows the trend in the presence of an error in the frequency derivative, panel *c* shows an error in the position (RA and DEC) which results in a sinusoidal trends, and unmodeled proper motion will be seen as a sinusoidal residual with increasing amplitude over time as seen in panel *d*.

After the initial timing ephemeris is established according to the procedures described in Section 4.1, the timing observations are carried out on a weekly to monthly cadence. TOAs are collected for typically a year until the position of the pulsar is unambiguously determined. The one year constraint is placed by the Earth's orbit around the Sun, which is the time usually needed to break the degeneracy between a parabolic trend in the residuals caused by an incorrect $\dot{P}$, and the sinusoidal shape from an incorrect position over timescales of months. Once we can unambiguously account for every rotation of the pulsar over the time span of the data, it is said to have reached a *phase-connected timing solution*. At this point, P and $\dot{P}$ are used to infer further parameters based on the dipole model, with the set of equations presented in Section 1.3

[5] `http://tempo.sourceforge.net/`

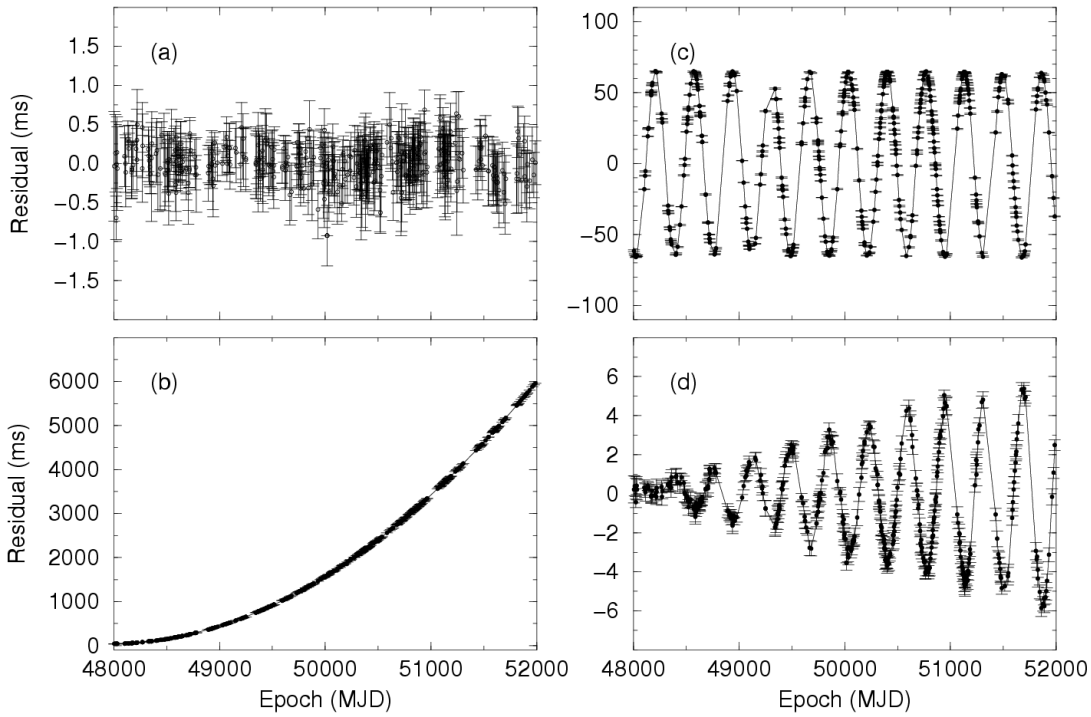

Figure 4.6: Example of timing residuals. Image from Lorimer & Kramer (2012)

(B-field strength, spin-down luminosity, characteristic age, braking index). Moreover, by locating the pulsar in the $P - \dot{P}$ diagram, it can be inferred to which population of pulsars it belongs to based in its location on it (see Section 1.5). Finally, as the sky position is determined (likely) to milliarcsecond resolution, other observing frequencies (optical, X-ray, γ-ray) can be explored to understand the extent of its emission.

Despite having reached a timing solution, the observations can continue to reach higher timing accuracy; for instance, when millisecond pulsars have the potential to be included in PTAs to detect GWs. This means, the pulsar is bright enough to have high S/N within reasonable observing time for a given telescope, and there is no correlated noise. Then the observations continue to reduce the residuals from tens to hundreds of microseconds, to tens to couple hundred of nanoseconds; hence, the time range for the timing solution is extended.

Chapter 5

FAST early discoveries: Effelsberg follow-up

This chapter is based on an article titled *"FAST early discoveries: Effelsberg follow-up"*, which was submitted to Monthly Notices of the Royal Astronomical Society.

As the lead author of this publication, I made use of the Effelsberg radio telescope to confirm the pulsar candidates, to carry out the timing observations, I have reduced and searched the data, performed the analysis, and written the manuscript.

The full author list is **M. Cruces**, D. Champion, M. Kramer, D. Li, W. Zhu, P. Wang, A. D. Cameron, G. Hobbs, P. Freire, E. Graikou, Y. Mao, and the CRAFTS collaboration.

5.1 Abstract

We report the follow-up of 10 pulsars discovered by the Five-hundred-meters Aperture Spherical radio-Telescope (FAST) during its early commissioning phase. The pulsars were discovered in the 500-MHz band through the use of the ultra-wide-band receiver in drift-scan mode. We carried out the timing campaign with the 100-m Effelsberg radio-telescope at a frequency of 1.36 GHz. We analyse their scientific potential based on the obtained timing solutions and their polarimetric properties. A highlight is PSR J2338+4818, a mildly recycled pulsar in a 95.2-d binary with a $1.029 M_{\odot}$ Carbon-Oxygen white dwarf (WD) as derived from the mass function. This makes the system the widest WD binary with the most massive companion.

We conducted a population analysis including 11 FAST pulsars previously reported. We concluded that FAST seems to be uncovering a population of older pulsars, closer to the expected turn off point, where radio emission is no longer detected. Lastly, we analysed the large inconsistencies in the distance estimations between the NE2001 and YMW16 electron density models. While for high Galactic latitudes not-well-constrained DM distances are not surprising, the large differences for pulsars located near the Galactic plane are unexpected. We propose that the combination of artefacts in the models plus the under-representation of pulsars in the sky region between $70^{\circ} < l < 100^{\circ}$ led to the large differences.

5.2 Introduction

Pulsars are a type of rotating neutron star (NS) that emits beams of electromagnetic radiation along their magnetic axis. Such radiation is detected as pulses mainly at radio

frequencies. Pulsars are means to study stellar evolution (Tauris et al., 2017), to place limits on the equation of state for ultra-dense matter (Lattimer & Prakash, 2001; Özel & Freire, 2016), to map the free electron distribution of our Galaxy (Cordes & Lazio, 2002; Yao et al., 2017), and are remarkable natural laboratories in which to test theories of gravity in the strong-field regime (Kramer et al., 2006; Wex, 2014). Furthermore, besides being a source of emission of gravitational waves (GWs; from inspiralling binary systems), such as the ones detected by LIGO/Virgo (Abbott et al., 2017), pulsars can also be used as tools to detect gravitational waves originating from supermassive black holes binaries. This is achieved through pulsar timing arrays (Hobbs et al., 2010; Kramer & Champion, 2013; Jenet et al., 2009b), in which the most rotationally-stable pulsars – whose precision approaches that of atomic clocks on long timescales – are used as a window into the extremely low-frequency ($\sim 10^{-9}$ Hz) GWs, complementing the frequency ranges explored by LIGO/Virgo, LISA, and CMB experiments. To advance our understanding of the underlying fundamental physics above mentioned, finding more pulsars is a priority.

A major pulsar survey has started using the largest single-dish radio telescope, the *Five-hundred-meter Aperture Spherical radio Telescope* (hereafter FAST) (Nan et al., 2011). Pulsar science is one of the key projects at FAST. After its completion in July 2016 and having seen first light in September 2016, FAST underwent testing and commissioning as part of a three-year initial phase. Already at the commissioning stage, FAST was finding new pulsars, revealing its unprecedented sensitivity with the discovery of over 250 new pulsars to date[1][2].

The 100-m Effelsberg radio telescope has been key in confirming and following-up the discoveries from the on-going *Commensal Radio Astronomy FAST Survey* (CRAFTS) drift-scan survey. Although FAST is capable of performing self-confirmations and timing of its own sources, its slewing time of up to 10 minutes and the quickly growing number of good candidates requires additional facilities to follow-up the discoveries. As a counterpart to Effelsberg,the 64-m Parkes radio telescope has been used to confirm and study new pulsars in the southern part of the sky. Figure 5.1 displays the sky observable by FAST and also for Effelsberg (EFF) and Parkes (PKS).

In this paper, we report the follow-up campaign with Effelsberg of 10 pulsars discovered by FAST in the early commissioning phase with the Ultra Wide Band receiver (UWB). We describe the technical characteristics of the survey and the strategy employed for the follow-up observations carried-out by Effelsberg in Section 5.3. In Section 5.4 we describe the methods used to establish a phase-connected timing solution, and how the information of the calibrated pulse profiles is used to constrain the pulsar's geometry. In Section 5.5 we report the timing solutions and discuss the individual features of the newly discovered pulsars. In Section 5.6 we analyse the full sample of the pulsars discovered (as of now) by FAST's UWB survey which were followed-up by both Effelsberg and Parkes (see Cameron et al. 2020 for pulsars studied by Parkes). We also discuss the population of pulsars that these discoveries trace and explore the

[1] http://crafts.bao.ac.cn/
[2] http://zmtt.bao.ac.cn/GPPS/

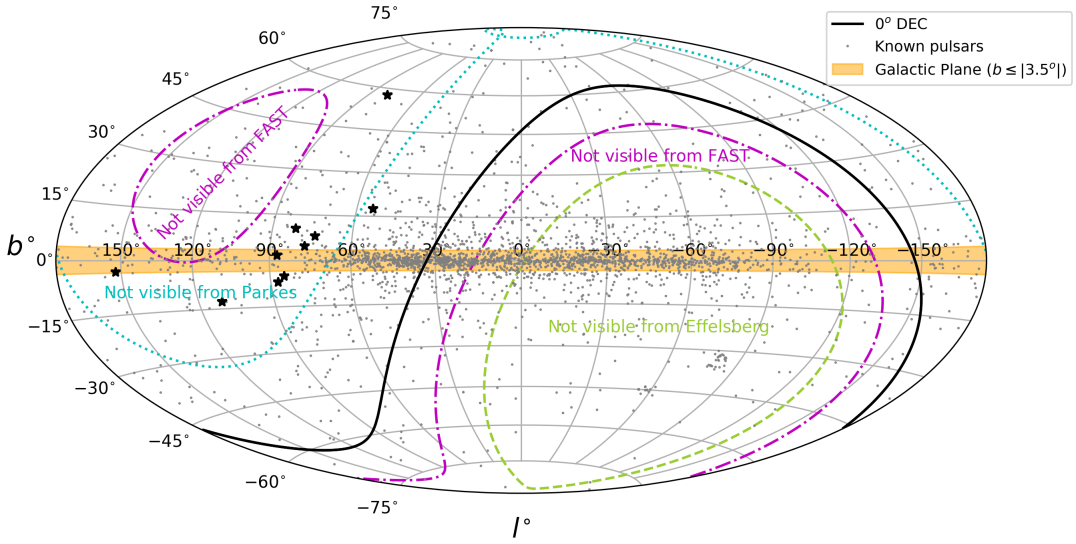

Figure 5.1: Sky coverage in Galactic coordinates of the 500-m FAST (magenta), the 100-m Effelsberg (green) and the 64-m Parkes (cyan) radio telescopes. The *black-stars* show the position of the FAST/EFF pulsars described in Tables 5.1,5.2,5.3 and 5.4. The yellow shaded regions shows the Galactic Plane ($|b| \leq 3.5°$), the black curve shows the line of zero declination and the *grey dots* show the known pulsars reported in the ATNF catalogue.

reasons why these pulsars could have been missed by previous surveys. Our concluding remarks are given in Section 5.7.

5.3 Observations

5.3.1 CRAFTS pulsar survey

The CRAFTS pulsar survey searches the sky in drift-scan mode from declination $-15°$ to $+65°$ (see Figure 5.1). During the first part of the commissioning phase, it made use of a single-beam UWB receiver recording radio frequencies from 270 MHz to 1.62 GHz (Li & Pan, 2016). The UWB was a testing instrument developed only for commissioning purposes: it allowed FAST to work on the data recording, positioning calibration, testing the timing precision as well as to work on the data flow and processing scripts. With the UWB receiver, most of the candidates were found in the 500 MHz band, due to radio frequency interference (RFI) at higher frequencies. At the lower band a source passes through the beam roughly in 50 seconds and the main beam has a size of 12 arcminutes (see Figure 5.2). The UWB led to the discovery of over 70 new pulsars (out of the 118 pulsars discovered as of now in the blind survey, see footnote 1). Currently the data are undergoing reprocessing.

FAST's unrivalled collecting area has two major benefits for pulsar surveys. The

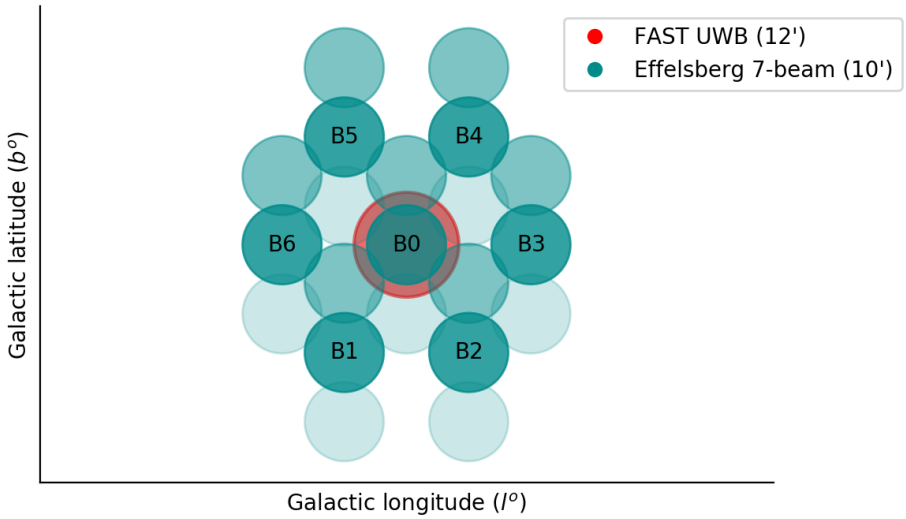

Figure 5.2: Effelsberg's 7-beam receiver setup and comparative size with FAST's UWB receiver beam. The survey grid with the 7-beam receiver is constructed by applying a rotation of 30° to the start positioning angle to each of the 3 pointing needed to fully cover the region. An offset of ±0.14° is applied to the upper and lower pointing respectively.

first is simply raw sensitivity, allowing us to detect pulsars too dim to be seen by earlier, less-sensitive telescopes. The second is the binary parameter space that can be searched. In most pulsar surveys a large number of trial accelerations need to be searched to account for the apparent change in the spin period of pulsars in binary systems during the observation. The immense collecting area of FAST means that shorter observations are required to achieve a certain sensitivity, reducing the impact of binary-induced spin-period changes and the number of search trials needed to correct for it, hence opening a new parameter space with the potential to detect extremely accelerated systems.

Smits et al. (2009) estimated that ∼4000 new pulsars are expected to be discovered by FAST in the Galactic plane. Such a number is hard (if not impossible) to follow-up with a single telescope. Additional telescope facilities play an important role in helping with the follow-up observations that lead to phase-connected timing solutions, the key to extracting the scientific potential of new pulsars. Examples include the 100-m Effelsberg and 64-m Parkes radio telescopes, which despite being smaller in size, have good frequency coverage, timing stability and tracking agility, making them the ideal northern and southern counterparts to follow-up the FAST pulsar discoveries. Cameron et al. (2020) reports the Parkes follow-up of 11 pulsars, whose overall characteristics resemble the pulsars followed by Effelsberg reported in this work.

5.3.2 Effelsberg follow-up

Our follow-up observations are split into *searching mode* and *timing mode*. For both, we made use of the 7-beam receiver at a central observing frequency of 1.36 GHz. For the search observations, we have used the Pulsar Fast Fourier Transform Spectrometer (PFFTS, Barr et al., 2013). The PFFTS records data with a time resolution of 54 μs over a 300 MHz bandwidth split into 512 frequency channels. For timing, we recorded the data with the use of the high precision pulsar timing backend PSRIX (Lazarus et al., 2016). PSRIX has a bandwidth of 250 MHz into 256 channels. For the search mode, we made use of each of the beams of the 7-beam feed array, while for the timing observations only the central beam was employed.

In order to successfully confirm a candidate several considerations had to be taken into account:

Grids. Positional uncertainties were expected due to the drift scan mode and the complexity of FAST's positioning system (Nan et al., 2011). Additionally, as is shown in Figure 5.2, there is a difference in beam size, of $10'$ and $12'$ for Effelsberg and FAST respectively. To account for such offsets we have used the 7-beam receiver in such a way to construct a 3-pointing grid as displayed in Figure 5.2. With that setup, we are able to fully cover a region of $0.48^\circ \times 0.66^\circ$ around a given candidate. We rotated the 3-pointing grid along the declination axis of each candidate to maximize for declination offsets, which were the main source of error in the position. We refer to this beam set up as the *search grid*.

Telescope gain. Effelsberg gain of 1.6 K/Jy (see Cruces et al. 2020 for Effelsberg's 7-beam receiver sensitivity) versus the gain of 10.1 K/Jy of FAST's UWB receiver, implied that in order to achieve the same sensitivity an integration of $\sim$40 times longer had to be considered. However, this was analyzed on a case to case basis as some candidates where significantly bright to allow us to shorten the integrations needed.

Spectral index. All the candidates reported in this paper come from the lower part of the band of FAST's UWB receiver due to strong RFI affecting frequencies above 800 MHz. To account for the decrease of the pulsar flux density when observed at higher frequencies – such as L-band – we assumed a spectral index of -1.6 (Bates et al., 2013).

Parameter space. Our parameter space is significantly reduced when compared with blind surveys due to the prior information about the pulsar, such as position, dispersion measure (DM), and spin period. However, the long integration times for Effelsberg meant that the data needed to be searched thoroughly in the acceleration space because of the change in the spin period due to the frequency shift caused by the orbital motion of pulsars in a binary system. To that end, we made use of the pulsar search algorithms implemented for the High Time Resolution Universe (see Ng et al. 2014; Barr et al. 2013 for survey description and search methods) based on:

acceleration search, a Fourier domain periodicity search where the time series is re-sampled at different constant acceleration trials; the *Fast Folding Algorithm*, a direct folding of the data at a range of trial periods (Morello et al., 2020); and PRESTO's `singlepulse.py` (Ransom, 2011) to search for single pulses in the time series.

These considerations meant that for a given FAST candidate, the observations carried out by Effelsberg ranged between 0.5 to 2 hours per pointing. Due to the long integrations needed, we were restricted to the binary systems that we could detect through *acceleration search* according to the 10% rule (Ransom et al., 2002). This means that given a 30 minutes observation needed to reach a signal-to-noise (SNR) to allow a confirmation, we were not sensitive to detect binaries with orbital periods shorter than ∼5 hours. We observed a total of ∼40 pulsar candidates, out of which 10 were confirmed and posteriorly followed-up. The non-confirmations can be attributed to the decrease of the flux at our observing frequencies, errors in coordinates introduced by the drift-scan survey, scintillation effects, and ultimately the difference in sensitivity between FAST and Effelsberg.

After a candidate was confirmed, a second search mode observation was performed soon after to fine-tune its position through a close-packed-grid setup made only with the use of the central beam of the 7-beam receiver. This refined position allowed us to locate the pulsar somewhere closer to the center of our beam, enhancing the SNR.

We emphasize that all the considerations described above apply exclusively to the early commissioning phase with the UWB receiver. Different considerations were made after FAST was upgraded in May 2018 with the 19-beam receiver (Jiang et al., 2020). For that setup, a source passes through the $3'$ beam in ∼20 seconds, and a gain of 18.2 K/Jy at L-band was reached (Zhu et al. in prep.). A report on the Effelsberg follow-up of the new discoveries from the FAST pulsar search with the 19-beam is in preparation. We refer hereon to the pulsars discovered by FAST and followed by Effelsberg as the FAST/EFF sample, and to the FAST pulsars followed by Parkes as the FAST/PKS sample.

5.4 Method

5.4.1 Phase connected timing solutions

Despite the PFFTS data not being reliable for timing – due to the lack of precise time stamps – its filterbank format allows the observation to be easily searched for the pulsar and to measure its spin period at a given epoch in an in-coherent de-dispersion mode. Therefore, combining the information of the initial confirmation with the observations to refine its position (see Section 5.3.2), we created a folding ephemeris whose spin period and position is accurate enough for an isolated slow pulsar to start recording data in a coherent de-dispersion folding mode (hereon referred as timing data).

The created ephemerides were accurate on a days-to-weeks scale, therefore a couple of observations were planned soon after. Times of arrival (TOAs) were created with

the use of PSRCHIVE (van Straten et al., 2012). With the use of TEMPO[3] and TEMPO2 (Hobbs et al., 2006) the residuals of the timing model were minimised by fitting the spin period frequency (F0) and its derivative (F1) if they are 3σ or more significant. As the observation continued for several months we fitted as well for the position of the source. If continuous observations were not phase connected we used the "jumps" and "phase +n" method in TEMPO – where n is an integer number that accounts for the number of rotations missed – to find whether any value of n produces an unambiguous connection between TOAs. If this is not the case, we resort to the use of DRACULA[4] to systematically bridge multiple gaps between TOAs (Freire & Ridolfi, 2018).

For the binary pulsar in our sample, PSR J2337+4824, in addition to the parameters mentioned above, it was necessary to establish an orbital solution before the start of the coherent timing data recording. This solution has five Keplerian parameters: the orbital period (PB), the epoch of periastron (T0), the projected semi-major axis (A1), the longitude of the periastron (OM), and the eccentricity (ECC). These were first estimated by measuring the change of the spin period at several epochs. Once this solution is established, then using the timing data we can determine the phase connection. To do this we needed to use the DRACULA routine, because of the sparsity of detections for this pulsar.

5.4.2 Polarization calibration

We have carried out noise diode observations for several timing epochs to perform polarimetric calibration. The calibrator consists of an injected 100% linearly polarized diode signal at 1 Hz and 45° to the feeds, on a sky region 0.5^o offset from the source. Each polarimetric calibration consisted of 90–120 seconds prior to each pulsar observation. The calibration was applied through the use of PSRCHIVE's `pac` routine by creating a database of calibrators for each pulsar at each epoch. The outcome of the procedure is observed in the pulse profiles shown in Figure 5.4 and 5.5. To this end, we have combined several epochs for each pulsar to obtain a low-noise profile, whose integration times are listed in Table 5.5. The polarization properties reported in this work have adopted the instrumental convention described in van Straten et al. (2010).

After correcting for Faraday rotation (see below), we measured the fraction of linear (L/I) and circular polarization relative to the total intensity from the on-pulse region. We list these values in Table 5.5 as well. For the circular polarization, we determined the relative V/I and absolute $|V|/I$ values.

5.4.3 Rotation measure determination

After applying the polarization calibration to the data, we corrected the effect of Faraday rotation on the linear polarization. Assuming an stable RM, we report the values obtained from the combined set of observations for each pulsar (see Table 5.5).

[3] http://tempo.sourceforge.net/
[4] https://github.com/pfreire163/Dracula

We use two approaches to measure the RM value. The first is `rmfit` from PSRCHIVE, which is based on an optimization of the linear polarization fraction solely by using a range of RM trials. For comparison we also used `RMcalc.py` code implemented by Porayko et al. (2019). This approach is based on the RM synthesis method described in Brentjens & de Bruyn (2005), and reports estimates from the Bayesian Generalised Lomb-Scargle Periodogram (BGLSP) technique applied to the RM synthesis method when the RM is unambiguously determined. The RM determined trough both methods are presented in Table 5.5.

We have applied the corresponding Faraday rotation corrections to each pulsar profile only when linear polarization was measured and the RM value was above 1σ significant and was in agreement for both RM determinations.

5.4.4 Rotating vector model

We derived the geometry of the pulsars in the FAST/EFF sample whenever the results of the polarization observations led to a well-defined position angle (PA). We used the rotating vector model (RVM) described by Radhakrishnan & Cooke (1969) to relate the PA to the projection of the magnetic inclination angle α and the impact parameter β. The equation to solve is (Lorimer & Kramer, 2012):

$$\tan(\psi_{\rm o} - \psi) = \frac{\sin(\alpha)\sin(\phi_{\rm o} - \phi)}{\sin(\zeta)\cos(\alpha) - \cos(\zeta)\sin(\alpha)\cos(\phi_{\rm o} - \phi)} \tag{5.1}$$

where ϕ is the pulse phase, $\zeta = \alpha + \beta$ is the viewing angle and ϕ_o and ψ_o correspond to the pulse phase and position angle corresponding to the fiducial plane, respectively. To constrain the pulsar's viewing geometry we performed a Markov Chain Monte Carlo (MCMC) fit to the parameters in Equation 5.1.

5.5 Results

The science extracted from the FAST/EFF pulsars and following discussion on Section 5.6 is based on their timing solutions and derived parameters through the rotating dipole model, their pulse profile with polarimetric calibration, and their sky location.

The timing solutions reported in Tables 5.1, 5.2, 5.3 and 5.4 are the result of (at least) one year of timing follow-up. It is worth noting that in order to not underestimate uncertainties we have used a factor (EFAC). The EFAC multiplies the TOA uncertainties by the square of its value such as the residuals have a $\chi^2 \sim 1$.
The pulse profiles shown in Figure 5.4 and 5.5 display the integrated profile (in black) with the linearly polarized and circularly polarized flux density in red and blue, respectively. The pulse profiles are corrected for the RM values reported in Table 5.5 as measured from the RM synthesis technique described in Section 5.4.3. Above each pulse profile is displayed the observed position angle (PA). To constrain the geometry of the pulsars we fit the PAs with the standard RVM through a Monte-Carlo simulation. With the exception of PSRs J2112+4058, J2129+4119, J1951+4724, and J0402+4825, it was not possible to constrain the geometry for the rest of the sources either because

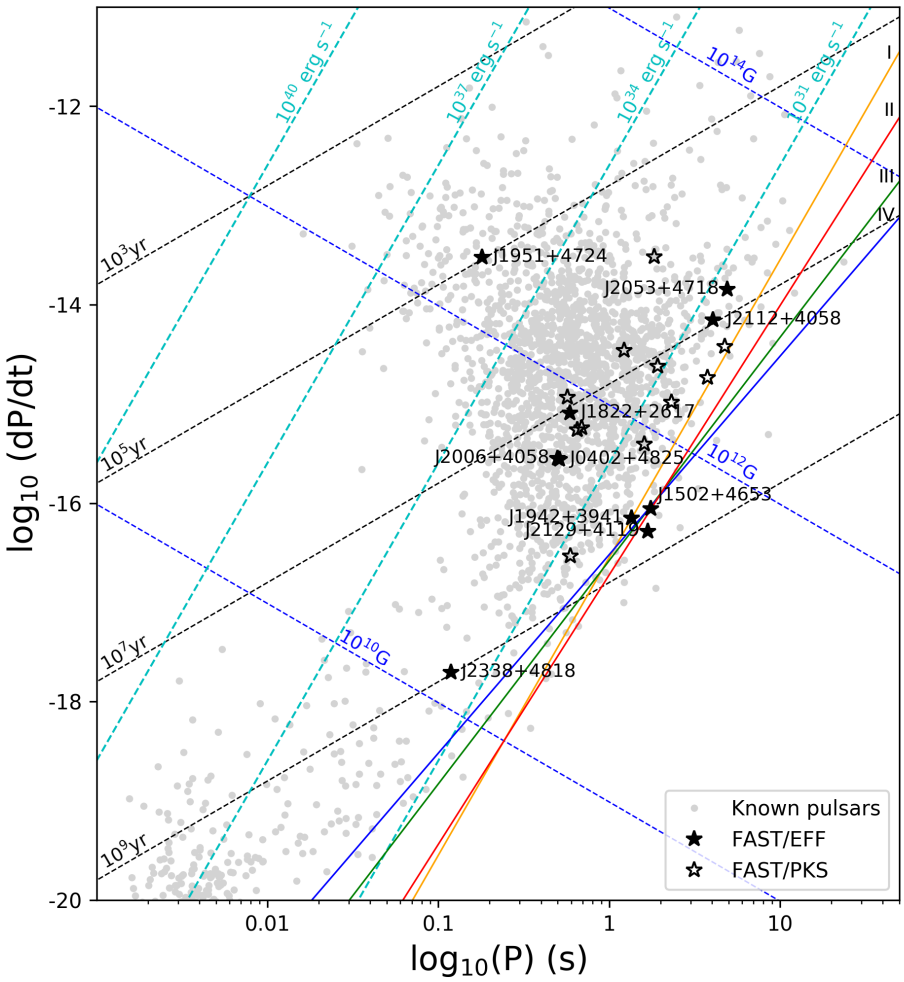

Figure 5.3: A $P - \dot{P}$ diagram. Known pulsars are shown with *grey dots*, while the new pulsar discoveries reported in this work are plotted with *filled-black stars*, and the pulsars reported by Cameron et al. (2020) with *open-black stars*. Alongside are drawn lines of constant magnetic field strength (*dark-blue dashed lines*), lines of constant spin-down age (*black dashed lines*) and lines of constant rotational energy loss (*cyan dashed lines*) as derived from the rotating dipole model. The death lines shown correspond to Bhattacharya et al. (1992) polar gap model (*orange-line*; model I), Chen & Ruderman (1993) model for a decreased polar cap area (*red-line*; model II), and Zhang et al. (2000) models for curvature radiation from the vacuum gap model (*green-line*; model III) and from the space-charged-limited flow (*blue-line*; model IV).

of the lack of observed polarization or due to insufficiently well-defined PA curves. Regarding the sky location of the FAST/EFF sources we see in Figure 5.1 that out of the 10 pulsars, 2 are located in the Galactic plane, 7 pulsars in the middle (mid) Galactic latitude region, and one at high latitude. More detailed population analysis is carried in Section 5.6. We proceed hereon with the summaries of the individual pulsars.

5.5.1 PSR J1822+2617

PSR J1822+2617 is a 0.591-s period pulsar with a dispersion measure of 64.7 $\mathrm{pc\,cm^{-3}}$. It was first confirmed by the Parkes follow-up project (Cameron et al., 2020), however, due to its high declination, it was transferred soon after to the Effelsberg campaign. As seen in the $P - \dot{P}$ diagram in Figure 5.3, it lies in the middle of the normal radio pulsar population.

It has a sharp double-peaked pulse profile, with the left component being the dominant source of emission. It is interesting that despite the integration time used to create the low-noise pulse profile, it was not possible to measure any significant trace of polarization. With the use of the cross-correlation function of the pulse dynamic spectra (Main et al., 2017) over the best observation, we estimate the diffractive scintillation timescale to be $\Delta\tau = 783\pm9$ s and the scintillation bandwidth to be $\Delta\nu = 4.9\pm0.6$ MHz. The expectation from the Cordes & Lazio (2002, hereon NE2001) free electron density model for the line-of-sight of PSR J1822+2117 are $\Delta\tau = 370\pm70$ s and $\Delta\nu = 1\pm1$ MHz.

5.5.2 PSR J1942+3941

PSR J1942+3941 is a 1.353-s pulsar with the widest pulse profile from the FAST/EFF sample given its W_{10} of 113.63 ms. With the 8500 s of integration time used to obtain the pulsar profile, a small fraction of linear and circular polarization of 7% and 9% respectively was found. Interestingly, the RM was found to be consistent with 0 $\mathrm{rad\,m^{-2}}$. Observations at lower frequencies and wide bandwidths, for instance with the Low-Frequency Array (LOFAR), could provide better constraints.

The distance inferred based on the pulsar's DM of 104.5 $\mathrm{pc\,cm^{-3}}$ is 5.4 kpc and 8.5 kpc for the NE2001 and Yao et al. (2017, hereon YMW16) models, respectively. Their disagreement is further discussed in Section 5.6.3.

5.5.3 PSR J2006+4058

PSR J2006+4058 is a 0.499-s pulsar with a DM of 259.5 $\mathrm{pc\,cm^{-3}}$, and as seen in Figure 5.3, is yet another example of a radio powered pulsar in the middle of the normal pulsar zone. Despite 14980-s of integration time, it was not possible to measure polarization. We split the observing bandwidth of 250 MHz into 10 sub-bands of 25 MHz each and explored whether the tail in the pulse profile was a consequence of scattering. We did not observe any significant frequency-dependent broadening.

Interestingly, despite its low Galactic latitude of $b = 4.73^{o}$, the NE2001 electron density model fails to estimate its distance and puts instead a lower limit of $d{>}50$ kpc.

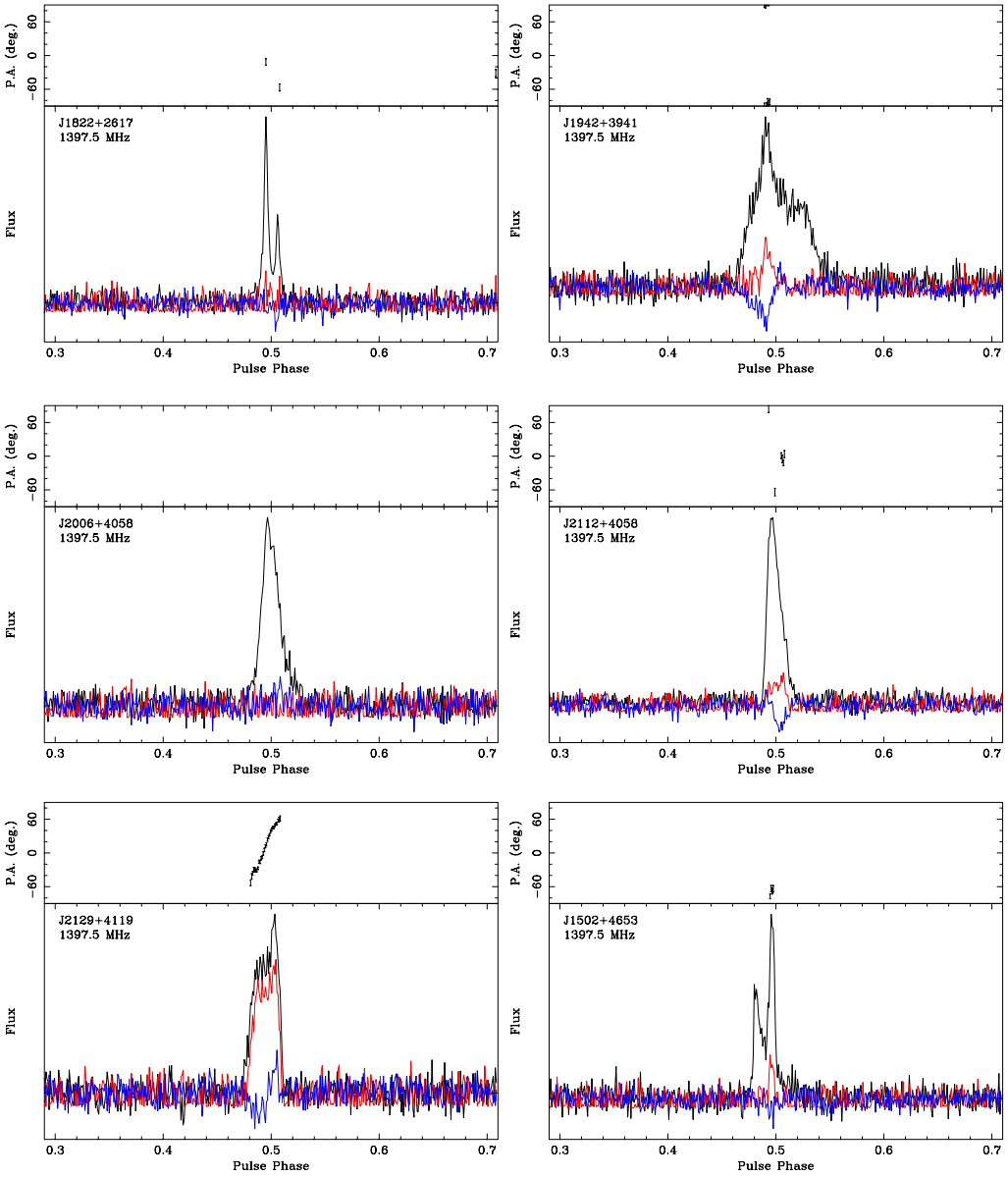

Figure 5.4: Calibrated average pulse profiles for six of the FAST/EFF pulsars: PSRs J1822+2617, J1942+3941, J2112+4058, J2129+4119, J1502+4653 and PSR J2053+4718. The polarization profiles were taken at L-band and have been corrected for Faraday rotation whenever RM was measured (see Table 5.5). The total intensity is shown in black, while linearly-polarized flux and circular-polarized flux are shown in red and blue respectively. The upper plot shows the position angle.

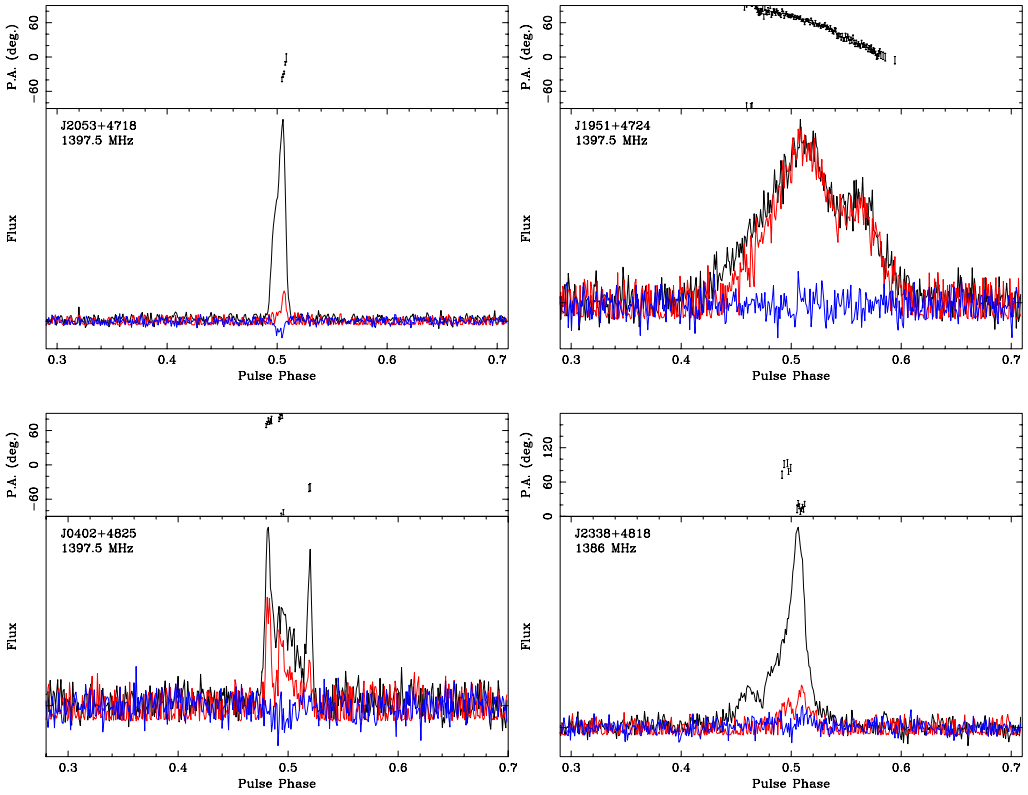

Figure 5.5: Calibrated average pulse profiles continuation: PSRs J1951+4724, J0402+4825, J2006+4058 and J2338+4818.

If this was true, the pulsar would be located outside of the Galaxy. Contrary, the YMW16 model provides better constraints on the electron density along that line-of-sight and predicts a DM distance of 12.5 kpc.

5.5.4 PSR J2112+4058

With a rotational period of 4.060 s, PSR J2112+4058 is the second slowest pulsar of the sample. Its pulsar profile displays a weak scattering tail and with no indication of RM (inferred value consistent with 0 rad m^{-2}). We measured 15% and 7% of linear and circular polarization respectively. Although there are few points in the PA swing, its inflection point (ϕ_o) is well defined and hence we are able to put constraints on the geometry of PSR J2112+4058. Through the RVM and the χ^2 minimization method described in Section 5.4.4, we estimate the magnetic inclination angle to be $\alpha = 94^{\circ}{}^{+40^{\circ}}_{-42^{\circ}}$ (1σ uncertainties). Given the large uncertainties for α (and ζ), we are unable to constrain β.

5.5.5 PSR J2129+4119

PSR J2129+4119 has a spin period of 1.687 s and a low DM of 31 pc cm^{-3}. Due to its low DM, the pulsar scintillates with a diffractive scintillation timescale $\Delta\tau = 50 \pm 7$ s over a bandwidth of $\Delta\nu = 6 \pm 0.7$ MHz, as inferred from the cross-correlation function of the pulse dynamic spectra. PSR J2129+4119 is one of the nearest pulsars from the sample, with the NE2001 model predicting a DM distance of 2.3 kpc, and the YMW16 estimating it to be 1.9 kpc.

From the pulse profile shown in Figure 5.4, we see that PSR J2129+4119 shows a high degree of linear polarization (>70%). Its PA swing is remarkably well defined over its entire pulse phase and allows the geometry to be constrained. As shown in Figure 5.7, we find $\alpha = 117^{\circ}{}^{+31^{\circ}}_{-41^{\circ}}$ and again, given the uncertainties for α and ζ we are not able to constrain β.

5.5.6 PSR J1502+4653

PSR J1502+4653 is a sharp double-peaked pulsar spinning at a period of 1.752 seconds. The right component of the pulse profile is dominant and is the only one showing traces of linear polarization. Using an integration of 53970 seconds we measured a degree of linear polarization of 8%.

With a DM of 26.6 pc cm^{-3}, the NE2001 model predicts a DM distance of 1.5 kpc while the YMW16 model puts a lower limit to the distance of 25 kpc. The disagreement between both estimations clearly shows the lack of constraints for pulsars at high Galactic latitudes due to the under-representation of sources in this area, which limits the mapping of the free electron distribution. This can be seen in Figure 5.1, where in addition to the FAST/EFF pulsars, the population of the known pulsars is shown.

5.5.7 PSR J2053+4718

With a period of 4.910 s PSR J2053+4718 is the slowest pulsar of the FAST/EFF sample. The RM deduced from RM synthesis is $-785\pm1\,\mathrm{rad\,m^{-2}}$, which is in agreement with the linear polarization optimization carried by `rmfit`. Furthermore, the Bayesian Generalized Lomb-Scargle Periodogram (BGLSP) method applied to the standard RM synthesis technique (Porayko et al., 2019) gives $-786 \pm 14\,\mathrm{rad\,m^{-2}}$. Considering that this pulsar is located close to the Galactic plane ($b = 1.6174$) and that it is in the Cygnus area, where there are a several supernova remnants and excess gas, its DM of $331.3\,\mathrm{cm^{-3}}$ pc and the high RM is perhaps expected.

Regarding the surrounding area in the Galactic plane (see Figure 5.1), we see that is not densely populated. This may be the reason why the NE2001 model fails to provide an estimation of its DM distance and instead puts an upper limit of roughly 50 kpc. Again, this would place the pulsar outside of the Galaxy. On the other hand, the YMW16 model predicts the distance to be 8.9 kpc.

5.5.8 PSR J1951+4724

PSR J1951+4724 is the youngest and most energetic pulsar of the dataset. With a spin period of 0.181 s and a spin period derivative of $3.01247(9) \times 10^{-14}$, the pulsar is located at the top left of the $P - \dot{P}$ diagram. Because of its high spin-down luminosity of 1.5×10^{35}ergs $\mathrm{s^{-1}}$, we inspected the Fermi-LAT 10-Year Point Source Catalog[5] to search for a γ-ray counterpart in the 50 MeV to 1 TeV energy range. Nonetheless, we found no counterpart within 1 degree.

From the pulse profile shown in Figure 5.4 we see that PSR J1951+4724 has a degree of linear polarization of 90%. This is the highest fraction of polarization for any FAST/EFF pulsar. The well defined PA swing across the full pulse phase provides the tightest constraints of the geometry study. We find $\alpha = 92^{\circ}{}^{+19^{\circ}}_{-14^{\circ}}$ and $\zeta = 114^{\circ}{}^{+16^{\circ}}_{-15^{\circ}}$.

We observed the J1951+4724 with the C+ receiver at Effelsberg, covering from 3 to 8 GHz continuously. Surprisingly, PSR J1951+4724 is observed up to the top of the band. Further analysis of its spectral index is left as future work. From the calibrated data we observed as well a high fraction of linear polarization. However, despite the 4 GHz bandwidth of the C+ receiver, we did not measure RM. As the pulsar is bright and its DM is not significantly high ($104.35\,\mathrm{pc\,cm^{-3}}$), observations with LOFAR could provide better constraints on its RM value.

5.5.9 PSR J0402+4825

PSR J0402+4827 is a 0.512-s period pulsar at a DM of $85.7\,\mathrm{pc\,cm^{-3}}$. It displays an interesting pulse profile consisting of two sharp peaks and an intermediate component. We find a RM of $-111(70)\,\mathrm{rad\,m^{-2}}$ and -89(9) $\mathrm{rad\,m^{-2}}$ though `rmfit` and RM synthesis respectively. Both values are consistent and when applying the corresponding Faraday rotation correction, the use of one value over the other leads to no noticeable difference in the linear polarization fraction.

[5] https://heasarc.gsfc.nasa.gov/W3Browse/fermi/fermilpsc.html

We see from the RM corrected pulse profile shown in Figure 5.5 that each of the three components shows a fraction of linear polarization, with the main contribution to it being the leading component. From the PA we determine $\alpha = 90^\circ \pm 41^\circ$, but once more, we are not able to constrain β.

5.5.10 PSR J2338+4818

PSR J2338+4818 is arguably the most interesting pulsar of the dataset. It is part of a wide binary system, it scintillates and shows evidence of long-term nulling.

5.5.10.1 Binary system

After a couple of months of follow-up, we observed a small change in the apparent spin period of the pulsar. We carried a Lomb-Scargle periodogram using the spin period measured at several epochs and found a periodicity of about 95 days. With this orbital period plus the amplitude of the oscillation in the spin period, we were able to roughly estimate the additional binary parameters; this was then used to determine the phase-coherent timing solution, using the methods described by Freire & Ridolfi (2018). Two years of observations were necessary in order to obtain enough data; this was due to the low detection rate described in Section 5.5.10.2.

The timing solution includes a highly precise estimate of the spin period (about 0.118 s), and a spin period derivative of -1.4×10^{-18}. The orbit has an eccentricity of 0.0018. The mass function of the system is 0.19263(4) and if a pulsar mass of 1.4 $M_\odot$ and an inclination angle of 90° is assumed, then the minimum mass of the companion star is 1.029 $M_\odot$. Given that minimum companion mass, the orbital parameters and the inferred age of the pulsar of ~ 0.95 Gyr, the companion is most likely a carbon-oxygen white dwarf (CO-WD) (Tauris et al., 2011a, 2012a).

5.5.10.2 Scintillation

According to the NE2001 model the estimated diffractive scintillation timescale is expected to be ∼10 minutes for an assumed 100 km/s source velocity. We investigated the timescale for the scintillation by analyzing its dynamic spectrum at 1.36 GHz. Based on three observations with high SNR, we estimated the scintillation timescale to be $\Delta\tau = 660 \pm 70$ s, over a bandwidth of $\Delta\nu = 18 \pm 3$ MHz. This is in agreement with the estimation from the NE2001 model. However, the source was detected only in 42% of the observations. Through its monitoring, the source was often observed two or more times per observing epoch, thus, we believe diffractive scintillation is not the only reason for its frequent disappearance.

5.5.10.3 Long-term nulling

Over 30 search-mode filterbank files were recorded in parallel with timing observations of PSR J2338+4818. Whenever the pulsar was not detected in the folded archives, we ran a targeted pulsar search over the filterbank files. In each case, we were also unable

to detect the pulsar in the filterbank search data. This rules out a non-detection due to poorly modeled binary parameters. Furthermore, when two or more observations were recorded within a few hours, a non-detection in one observation was also followed by a non-detection in the others. We also recorded two continuous observations of roughly four hours each on different epochs. In the first observation the source was not detected, either in the full observation length or when processing individual 30 minute chunks. During the second observation, the source was detected during the full session. This suggests that the off-mode timescale is at least a few hours, although it is likely to be considerably longer.

Table 5.1: Timing solutions part 1

Pulsar name	PSR J1822+2617	PSR J1942+3941	PSR J2006+4058
Parameters			
Right ascension, α (J2000)	18:22:44.819(2)	19:42:22.05(3)	20:06:39.098(3)
Declination, δ (J2000).....	+26:17:26.83(4)	+39:41:41.4(7)	+40:58:53.48(3)
Spin frequency, F (s^{-1}).....	1.690852663400(4)	0.73893939554(5)	2.001221096605(8)
Spin frequency derivative, $\dot{F}$ (s^{-2})..	-2.282(2)$\times10^{-15}$	-3.9(7)$\times10^{-17}$	-1.138(1)$\times10^{-15}$
Spin period, P (s).....	0.591417585722(1)	1.35329095461(9)	0.499694912119(2)
Spin period derivative, $\dot{P}$	7.983(6)$\times10^{-16}$	7(1)$\times10^{-17}$	2.843(4)$\times10^{-16}$
Dispersion measure, DM (cm^{-3} pc) .	64.7(1)	104.50	259.5(2)
Fitting parameters			
First TOA (MJD).....	58481.393	58462.761	58324.019
Last TOA (MJD).....	58895.203	58930.589	58839.727
Timing epoch (MJD).....	58688.00	58651.00	58582.00
Number of TOAs.....	132	56	79
Total integration time (s).....	49400	58080	54436
Weighted RMS residual (μs)	262.27	2881.102	469.06
EFAC	1.304	1.361	1.021
Derived parameters			
Galactic longitude, l (°).....	54.0268	73.6411	77.1185
Galactic latitude, b (°)	17.5535	8.0654	4.7313
DM distance, d (kpc)			
NE2001	3.6	5.4	50 >
YMW16	7.8	8.5	12.6
Characteristic age, τ_c (Myr).....	12.0	314.2	28.6
Surface magnetic field, B_{surf} (10^{10} G)	69.5	31.1	38.1
Spin-down luminosity, $\dot{E}$ (10^{30} erg s^{-1})	152.3	1.1	89.9

Table 5.2: Timing solutions part 2

Pulsar name	PSR J2112+4058	PSR J2129+4119	PSR J1502+4653
Parameters			
Right ascension, α (J2000)	21:12:51.76(6)	21:29:21.46(4)	15:02:19.83(1)
Declination, δ (J2000).....	+40:58:04(1)	+41:19:55(1)	+46:53:27.4(1)
Spin frequency, F (s^{-1}).....	0.24625963556(3)	0.59262128589(4)	0.57061078387(1)
Spin frequency derivative, $\dot{F}$ (s^{-2})..	-4.24(8)$\times10^{-16}$	-3(2)$\times10^{-17}$	-5.6(3)$\times10^{-17}$
Spin period, P (s).....	4.0607548114(5)	1.68741829528(1)	1.75250806373(3)
Spin period derivative, $\dot{P}$	7.0(1)$\times10^{-15}$	8(1)$\times10^{-17}$	1.7(1)$\times10^{-16}$
Dispersion measure, DM (cm^{-3} pc) .	129(8)	32(1)	26.6(5)
Fitting parameters			
First TOA (MJD).....	58522.51	58515.68	58431.88
Last TOA (MJD).....	58907.66	58839.63	58858.13
Timing epoch (MJD).....	58682.00	58695	58645.00
Number of TOAs.....	33	60	100
Total integration time (s).....	44960	74900	144100
Weighted RMS residual (μs)	1575.72	2270.86	775.61
EFAC	1.32	1.235	0.677
Derived parameters			
Galactic longitude, l (°).....	84.7385	87.1948	79.3056
Galactic latitude, b (°)	-5.1570	-7.1093	57.6263
DM distance, d (kpc)			
NE2001	5.4	2.3	1.5
YMW16	5.2	1.9	25.0
Characteristic age, τ_c (Myr).....	9.2	342.8	167.0
Surface magnetic field, B_{surf} (10^{10} G)	53.9	37.2	55.2
Spin-down luminosity, $\dot{E}$ (10^{30} erg s^{-1})	4.1	0.65	1.2

Table 5.3: Timing solutions part 3

Pulsar name	PSR J2053+4718	PSR J1951+4724	PSR J0402+4825
Parameters			
Right ascension, α (J2000)	20:53:45.49(4)	19:51:07.45(3)	04:02:40.633(9)
Declination, δ (J2000).....	+47:18:55.3(4)	+47:24:35.1(2)	+48:25:57.51(7)
Spin frequency, F (s^{-1}).....	0.20365026489(1)	5.4966921263(3)	1.95238351856(1)
Spin frequency derivative, $\dot{F}$ (s^{-2})..	-6.14(1)$\times10^{-16}$	-9.1017(3)$\times10^{-13}$	-1.050(2)$\times10^{-15}$
Spin period, P (s).....	4.9103790780(3)	0.18192759882(1)	0.512194448728(3)
Spin period derivative, $\dot{P}$	1.480(4)$\times10^{-14}$	3.01247(9)$\times10^{-14}$	2.756(5)$\times10^{-16}$
Dispersion measure, DM (cm^{-3} pc) .	331.3	104.35	85.7
Fitting parameters			
First TOA (MJD).....	58462.88	58259.105	58459.224
Last TOA (MJD).....	58956.12	58937.517	59083
Timing epoch (MJD).....	58650	58481.453266	58650.00
Number of TOAs.....	74	211	23
Total integration time (s).....	80560	59081	78679
Weighted RMS residual (μs)	2034.06	1521.69	119.79
EFAC	2.09	2.04	0.927
Derived parameters			
Galactic longitude, l (°).....	87.2061	81.1828	152.4276
Galactic latitude, b (°)	1.6174	10.3473	-3.1772
DM distance, d (kpc)			
NE2001	49.7 >	6.0	2.3
YMW16	8.9	9.0	1.8
Characteristic age, τ_c (Myr).....	5.4	0.098	30.0
Surface magnetic field, B_{surf} (10^{10} G)	862.6	236.9	38
Spin-down luminosity, $\dot{E}$ (10^{30} erg s^{-1})	4.9	$1.9 \cdot 10^5$	80.1

Table 5.4: Timing solutions part 4.

Pulsar name	PSR J2338+4818
Parameters	
Right ascension, α (J2000)	23:38:06.189(8)
Declination, δ (J2000).....	+48:18:32.19(7)
Spin frequency, F (s^{-1}).....	8.42387236305(5)
Spin frequency derivative, $\dot{F}$ (s^{-2})..	-1.40(5)$\times10^{-16}$
Spin period, P (s).....	0.1187102506901(8)
Spin period derivative, $\dot{P}$	1.98×10^{-18}
Dispersion measure, DM (cm^{-3} pc) .	35.3(7)
Orbital period (days)	95.25536(2)
Eccentricity	0.0018237(9)
Projected semi-major axis (s)	117.58572(7)
Longitude periastron (°)	99.65(2)
Epoch of periastron (MJD)	58868.444(7)
Binary model	DD
Fitting parameters	
First TOA (MJD).....	58462.941
Last TOA (MJD).....	59096.217
Timing epoch (MJD).....	58909.654
Number of TOAs.....	63
Total integration time (s).....	99263
Weighted RMS residual (μs)	111.794
EFAC	0.76
Derived parameters	
Galactic longitude, l (°).....	110.5436
Galactic latitude, b (°)	-12.7909
DM distance, d (kpc)	
NE2001	1.8
YMW16	2.0
Characteristic age, τ_c (Myr).....	950.11
Surface magnetic field, B_{surf} (10^{10} G)	1.55
Spin-down luminosity, $\dot{E}$ (10^{30} erg s^{-1})	46.7

Table 5.5: Pulse profile and polarisation properties of the FAST/EFF pulsars. The parameters listed for each pulsar from left to right are its pulse width at 50 % and 10 % of the profile peak (W_{50} and W_{10} respectively), RM is the rotation measure from `rmfit` and RM_s is the value from the RM synthesis method, fraction of linear polarization (L/I), fraction of circular polarization (V/I), absolute circular polarisation ($|V|/I$) and the total integration time ($\mathrm{T_{obs}}$) used to construct the integrated pulse profiles shown in Figures 5.4 and 5.5. 1-σ uncertainties are shown in parentheses.

PSR	W_{50} (ms)	W_{10} (ms)	RM ($\mathrm{rad\,m^{-2}}$)	RM_s ($\mathrm{rad\,m^{-2}}$)	L/I	V/I	$\lvert V\rvert/I$	$\mathrm{T_{obs}}$ (h)
J1822+2617	2.30	13.27	120(25)	67(2)	0.13(2)	-0.05(2)	0.12(2)	7200
J2006+4058	11.20	19.00	$<\lvert 200\rvert$	$<\lvert 200\rvert$	-	-	-	14980
J1942+3941	75.31	113.63	$<\lvert 110\rvert$	-7(3)	0.070(5)	-0.09(1)	0.12(1)	8500
J2112+4058	43.61	107.05	$<\lvert 160\rvert$	-7(2)	0.15(1)	-0.07(1)	0.10(1)	3650
J2129+4119	39.53	62.60	$<\lvert 300\rvert$	-30(9)	0.74(2)	-0.03(1)	0.12(1)	13740
J1502+4653	29.08	41.06	$<\lvert 120\rvert$	60(8)	0.080(2)	-0.04(1)	0.05(2)	53970
J2053+4718	57.50	86.25	-792(71)	-785(1)	0.10(1)	-0.08(2)	0.04(2)	14380
J1951+4724	48.26	72.80	$<\lvert 40\rvert$	11(5)	0.90(1)	-0.02(1)	0.06(1)	10770
J0404+4831	73.38	87.04	-111(70)	-89(9)	0.48(3)	-0.08(3)	0.11(3)	3580
J2337+4818	1.39	8.34	-	-	0.169(8)	0.051(8)	0.055(9)	14290

5.6 Discussion

5.6.1 J2338+4818

PSR J2338+4818 is located in the mildly recycled pulsar area of the $P - \dot{P}$ diagram (see Figure 5.3). The recycling scenario proposes that millisecond pulsars (MSPs) have evolved from pulsars in binary systems, where they have obtained their millisecond spin periods through the accretion of matter and angular momentum from a companion star (e.g. Bhattacharya & van den Heuvel 1991b). Somewhere within the transition to a MSP, a reduction in the magnetic field strength (B-strength) occurs (typically from 10^{12} G to 10^{8} G). However, whether the B-field is reduced as a result of age (Goldreich & Reisenegger, 1992b) or accretion (Bisnovatyi-Kogan & Komberg, 1974a) is still an open question. We describe a pulsar as mildly recycled when the accretion of matter from its companion is limited in time and did not spin the pulsar to rotational periods of the order of a few milliseconds, and its B-strength was not significantly reduced.

PSR J2338+4818 is in a wide binary of roughly 95.2 days, likely with a CO-WD companion. This conjecture is additionally supported by the pulsar's characteristic age of 0.95 Gyr, which is consistent with the time needed to evolve a main-sequence (MS) star, with a mass between 3 and 6 $M_\odot$, into a CO-WD (roughly between 0.3–0.6 Gyr, see Cruces et al. 2019); and the fact that no optical counterpart was found in the catalogues[6][7]. Considering PSR J2338+4818's distance of roughly 2 kpc, if the companion was a MS star with a mass of roughly $1M_\odot$ and an absolute magnitude of 4.8 (Sun's magnitude), the companion would have an apparent magnitude of 16 and thus likely visible by Gaia (among others).
Mildly recycled pulsars with CO-WD companions are thought to evolve from intermediate-mass ($M>3M_\odot$ for the progenitor of the companion star) X-ray binaries (IMXBs). Furthermore, because the system is in a wide binary, the accretion phase likely underwent Case C *Roche-lobe overflow* (RLO) and a common envelope phase (Tauris et al., 2011a, 2012a). In this scenario, the high B-strength is expected due to the inefficient mass transfer phase, which also leads to a not fully circularized orbit. In order to spin up a pulsar to a rotational period of 0.118 seconds, roughly $0.002M_\odot$ needs to be accreted. This value is reasonable if we consider that the accretion occurs over a few megayears and that for IMXBs system up to $10^{-8}M_\odot yr^{-1}$ can be accreted by the pulsars based on the Eddington limit.

We plot in Figure 5.10 the orbital period - eccentricity (P_b–e) relation of all the binary pulsars with either He-WD or CO-WD companions. We exclude pulsars in globular clusters since their evolution involves companion exchange, and pulsars with magnetic fields higher than $B> 10^{11}$ G, as young pulsars orbiting WDs are thought to have evolved from a different formation channel, where the close binary interaction and mass reversal led to a WD formed before the NS (Tauris & Sennels, 2000a). Thus, the systems shown in Figure 5.10 correspond to either fully or mildly recycled systems. We see that J2338+4818 follows the distribution of binaries, but most interestingly it is the

[6]SIMBAD Astronomical Database: http://simbad.u-strasbg.fr/simbad/
[7]Gaia Archive at ESA: https://gea.esac.esa.int/archive/

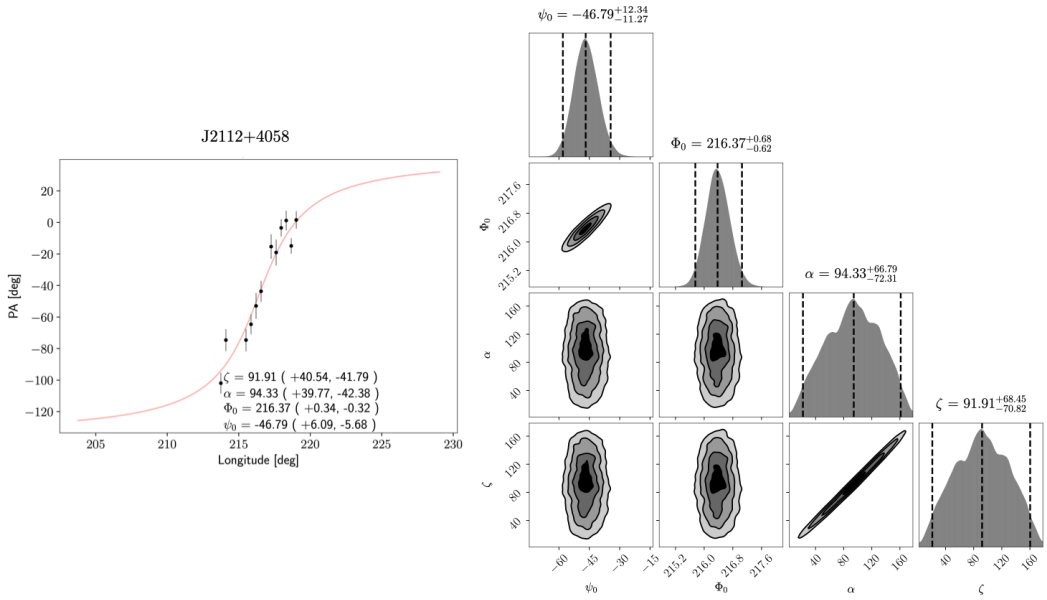

Figure 5.6: Viewing geometry of PSR J2112+4058. Left: least-squares fit to the polarization angle. Right: RVM posterior distributions to the polarization position angle (ψ_0), the rotational phase (ϕ_0), the magnetic inclination angle (α) and the viewing angle (ζ). The contours define 1σ, 2σ and 3σ confidence intervals respectively. The mean value of the distribution for each parameters is displayed with its 2σ uncertainties at the top.

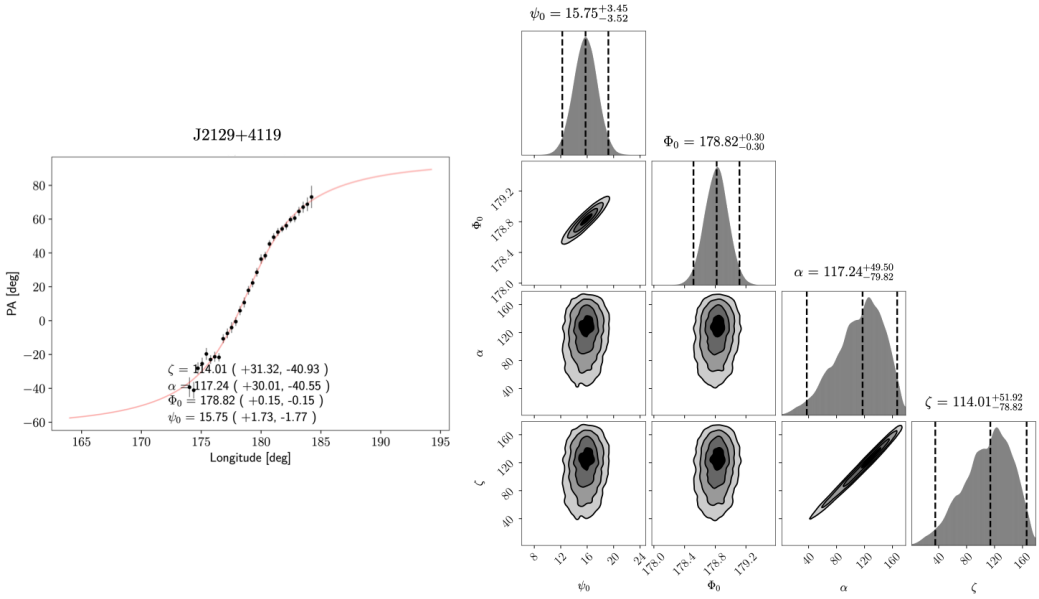

Figure 5.7: Viewing geometry of PSR J2129+4119. Details as per Figure 5.6.

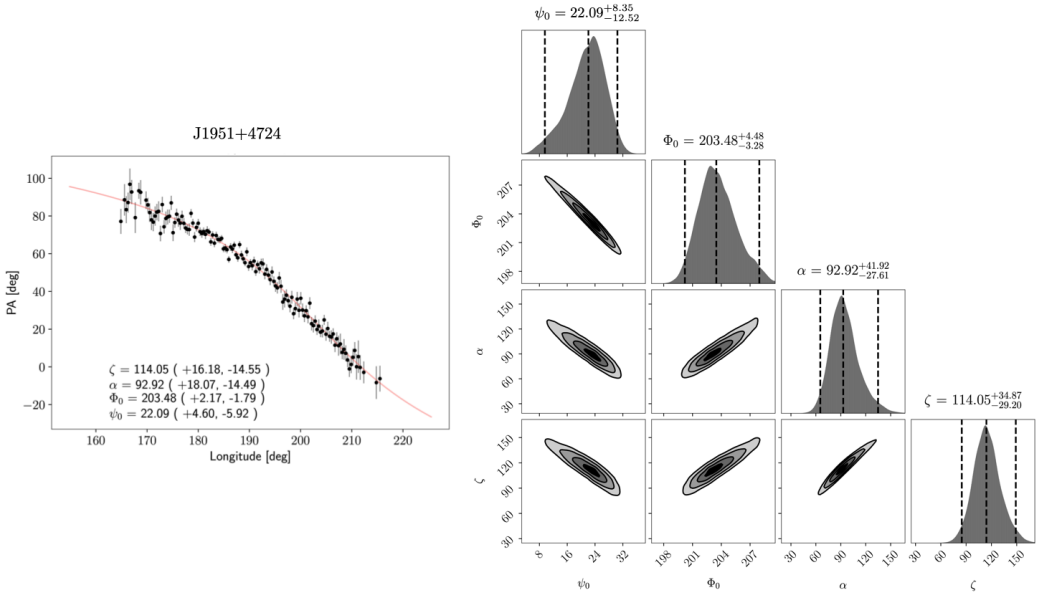

Figure 5.8: Viewing geometry of PSR J1951+4724. Details as per Figure 5.6.

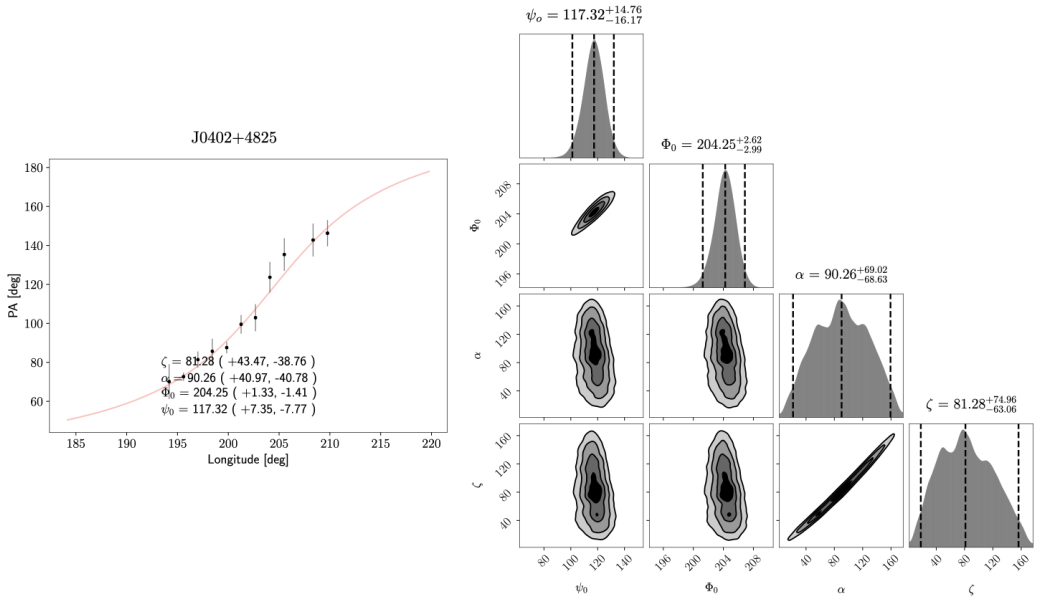

Figure 5.9: Viewing geometry of PSR J0402+4825. Details as per Figure 5.6.

widest pulsar CO-WD binary. Considering the estimated minimum mass for the CO-WD companion of 1.029 $M_\odot$, this also makes this system the widest WD binary with the most massive companion. This pulsar is also interesting because of its potential long-term nulling. Using the most densely sampled observations, where the source was observed roughly every 1-2 weeks from 2019-12-21 until 2020-03-01, we put an upper limit on its off-mode to be 20 days. With a single long observation, we put a lower limit on its off-mode to be at least a few hours. Currently, all the known long-term nulling pulsars are young sources, however, PSR J2338+4818 is an old mildly recycled pulsar. To show conclusively that PSR J2338+4818 is an long-term nuller, more observations are required. If it is indeed, then its moding could be connected with the fact that is close to the death line. The monitoring of the source with Effelsberg and FAST continues, and the results will be part of a future paper.

5.6.2 An old pulsar population

To understand the population that the pulsars studied here trace, we show a $P - \dot{P}$ diagram in Figure 5.3 with four death lines, as described below. Each death line corresponds to the point at which the radio emission of a pulsar is expected to turn off as pair production can no longer sustain radio emission, according to different pulsar models. These lines should be taken with caution as the macro parameters describing the phenomena – namely P and B – are derived from a simplistic dipole model. Higher-order magnetic fields and micro physics described by the equation-of-state (EoS) might affect the pulsar's emission, and ultimately lead to a case by case turn off based on their

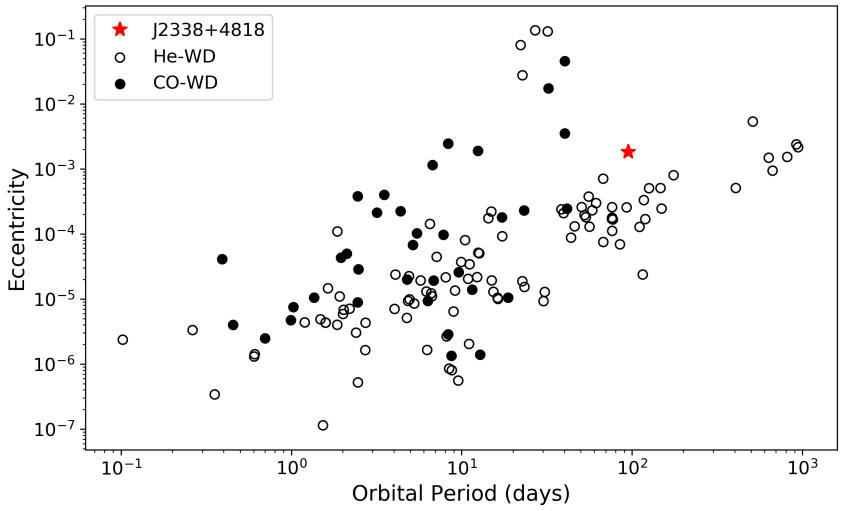

Figure 5.10: *Orbital period - eccentricity* diagram of binary pulsars with either a He (*black-open-circles*) or CO white dwarf companion (*filled-black-circles*). We have excluded pulsars in globular clusters since their evolution involves companion exchange, and pulsars with B$> 10^{11}$ G as they have evolved through a different formation channel (Tauris & Sennels, 2000a). The orbital eccentricity of PSR J2338+4818 lies in the trend observed for the other pulsar - CO WD systems.

mass. Instead, we should consider a death valley, where the likelihood of detecting a pulsar decreases further below the death line (and the further into the valley) a pulsar is.

The consideration of several death line models is motivated by the three pulsars from the FAST/EFF sample (PSRs J1942+3941, J2129+4119, and J1502+4653) that lie in the zone where only a handful of pulsars are expected. The models I, II, III, and IV shown in Figure 5.3 are:

I) Classic polar gap model, where the spin-down of the pulsar increases the thickness of the polar magnetospheric gap to a point where the minimum potential drop required for pair-production through curvature radiation is no longer supported (Bhattacharya et al., 1992; Ruderman & Sutherland, 1975). In the presence of a pure dipolar magnetic field, the death line is defined by:

$$\frac{B}{P^2} = 0.17 \times 10^{12}\,\mathrm{G/s^2} \tag{5.2}$$

II) This model considers a more complex structure for the surface magnetic field, where the field lines are considerably more curved in comparison to the dipolar case, and hence the polar cap area is reduced (Chen & Ruderman, 1993). The death line is thus described by:

$$7\,\log(B) - 13\,\log(P) = 78 \tag{5.3}$$

III) The polar gap model is corrected to account for the deviation from a flat spacetime when considering a general relativistic case (Zhang et al., 2000). This leads to a new death line described by:

$$\frac{9}{4}\log(P) - \log(\dot{P}) = 16.58 \tag{5.4}$$

IV) The space-charge-limited flow (SCLF) model is an alternative scenario to the previously mentioned vacuum gap built above the NS surface. In the SCLF model, the charged particles are not bound to the surface and can be instead easily pulled from the surface. If additionally a curved space-time is considered, the result is a smaller potential drop needed for pair production (Zhang et al., 2000). The expression for the death line is:

$$2\log(P) - \log(\dot{P}) = 16.52 \tag{5.5}$$

Regarding the position of the FAST/EFF pulsars on the $P - \dot{P}$ diagram in Figure 5.3, PSR J1942+3941 – located right at the death line from model I – and PSR J1502+4653 can be still be explained by the prediction from models II, III, and IV. However, PSR J2129+4119 is below all the death line predictions (models I, II, III, and IV). In the Figure 5.3 we also show the Parkes counterpart follow-up (*non-filled black stars*). It is interesting to note that two of those sources lie near to the line for model I (although they remain above the model I death line).

We proceed hereon with analysis of the combined sample and refer to it as the FAST-UWB pulsars. As PSR J2338+4818 is a mildly recycled pulsar area, it is thus excluded.

The first noticeable pattern is that most of the pulsars seem to be located toward the right-hand-side of the normal pulsar zone, thus implying that they correspond to an older pulsar population. We compute the Kolmogorov-Smirnov statistic (KS test) for the distribution of known pulsars (Manchester et al., 2005a) and the 21 FAST-UWB pulsars. Because MSPs are part of a different pulsar population, we exclude known pulsars with a $\dot{P} < 10^{-18}$. We test whether both samples are drawn from the same distribution, and conclude that there is evidence against with a $p - \text{value} = 0.0015$.

The population of older pulsars that FAST is finding can be attributed to its sensitivity. This is consistent with the long integrations (>30 minutes) needed by Parkes and Effelsberg to carry out the follow-up. It is worth noting that all of the FAST-UWB pulsars were discovered through integrations at FAST of less than 52 seconds with the UWB receiver. The gain of 18.2 K/Jy for the new 19-beam receiver at FAST, promises to reveal a new population of pulsars with even lower luminosities, which can play a crucial role in understanding the emission physics of pulsars and the point where their emission turns off.

5.6.3 Comparing the NE2001 and YMW16 electron density models

We saw in Section 5.5 that for three pulsars (PSRs J2006+4058, J1502+4653 and J2053+4718) either the NE2001 or the YMW16 model failed to correctly estimate the

distance from the DM of the pulsar, and instead placed a lower limit on its value that is likely far greater than the true distance. Additionally, except for PSRs J2112+4119, J2129+4119, J0402+4825, and J2338+4818, the DM distance estimates from both models are not consistent. To better illustrate these differences we show in Figure 5.11 the distance estimates derived from the NE2001 model (top) and from the YMW16 model (bottom) against the distance from the Galactic plane (z) based on each model. We include all the known pulsars and the FAST-UWB dataset.
First, we see that both models show an artifact due to the boundary of the electron density model. While for the YMW16 model the boundary appears at a value of 25 kpc independent of z, for the NE2001 model the border of the model shows a more complex structure reached at 50 kpc for $|z| < 20$ kpc and at different distances for higher $|z|$. Secondly, for the majority of the FAST-UWB pulsars the YMW16 distance estimation is larger than the NE2001 estimation for as much as a factor two. Pulsars at high b (or z) such as PSR J1502+4653 seem to be more problematic for the YMW16 model than for the NE2001 model. While the YMW16 model places a lower bound of 25 kpc on their distance, the NE2001 model locates them nearby, only within a couple of kiloparsecs. On the other hand, the NE2001 model fails to estimate a distance for three sources located near the Galactic plane. For those pulsars, the YMW16 model derives a distance well before its boundaries.

To understand the difference in the derived distance estimation by the two models and the extent of their accuracy, it is compelling to recap on their assumptions. To map the distribution of free electron in the Galaxy both models consider main large-scale components: a spiral-arm structure, the Galactic center component, an inner thin and outer thick disk component, and the local interstellar medium. The difference of both models lies in the electron densities (n_e) and extent of the before mentioned components, but most importantly how specific lines-of-sight are accounted for. For instance, the NE2001 model introduces artificial clumps and voids to account for the DM excess or lack towards the line-of-sight of particular pulsars, while the YMW16 model includes real features such as Nebulae, Local Bubble, Carina over-density, and Sagittarius under-density.

A key component to map the electron content is pulsars, due to the propagation effects that their radio pulses are subject to. Such effects are measure in the form of DM, scintillation bandwidth, and temporal and angular broadening due to scattering. These measures are only meaningful if they are accompanied by an independent distance estimation, for instance, through timing parallax or interferometric parallax, association to GCs or supernova remnants (SNR), or with HI absorption. Nonetheless, only $\sim$10% of the known pulsar have independent distance estimations. This low fraction of sources considerably limits the modeling of the free electron content.

The YMW16 is a later model of the free electron density, and made use of 189 independent pulsar distance estimations, in contrast to the 112 pulsars available at the time the NE2001 model was developed. The fact that only tens of pulsars - out of the roughly 3000 known - are located at high Galactic latitude makes their not-well-constrained DM derived distances not surprising. This is why the unconstrained DM of PSR J1502+465 according to YMW16 is expected. However, PSRs J2006+4058 and

J2053+4718, the two FAST/EFF pulsars at the boundary of the NE2001 model, are located near the Galactic plane. For those cases, it is rather their Galactic Longitude (77.1° and 87.2° respectively) what explains the unconstrained DM distances. At the time the NE2001 model was developed not many pulsars where known near the sky region between $70° < l < 100°$. The under-representation of pulsars in that region in combination with the high DMs of 259.5 $\mathrm{cm}^{-3}\,\mathrm{pc}$ and 331.3 $\mathrm{cm}^{-3}\,\mathrm{pc}$ for J2006+4058 and J2053+4718, respectively, could explain why the model fails to estimate a distance and instead places a lower limit locating the pulsars outside of the Galaxy. We test this hypothesis by trying a series of DM trials from 100 up to 400 $\mathrm{pc\,cm}^{-3}$ and coordinates in the above-mentioned region and with $|b| < 6°$. We observed that for DM$> 300\mathrm{pc\,cm}^{-3}$ (the exact value varies with b) the distance prediction was $>$50 kpc.

For future updates of the electron density models, the current FAST pulsar discoveries have the potential to contribute to mapping along their line-of-sight, upon its independent distance determination.

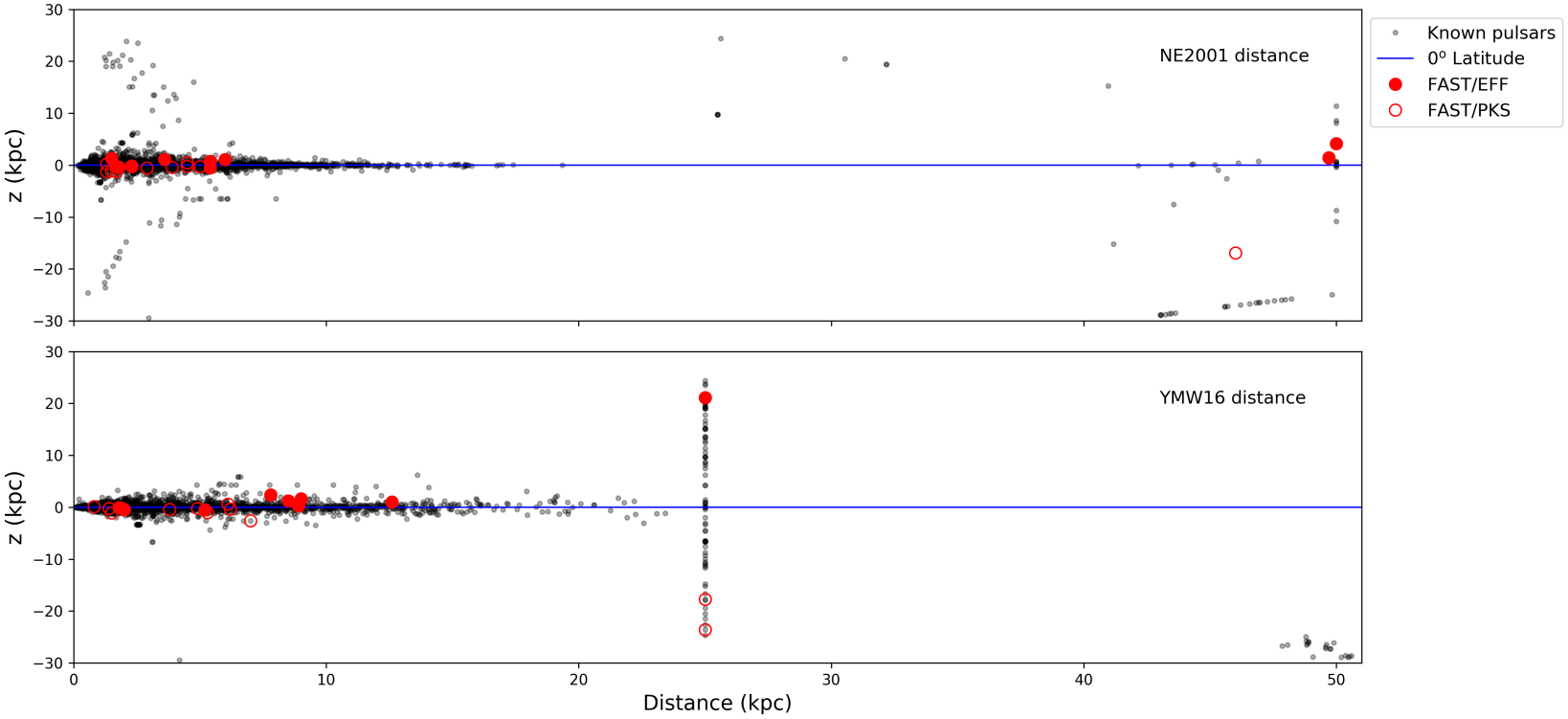

Figure 5.11: DM distance estimates based on the NE2001 (top) and YMW16 electron density model (bottom) against the distance from the Galactic plane (z) based on each model. The *red-filled-circles* correspond to the FAST's UWB-receiver discoveries that were timed by Effelsberg and the *open-red-circles* corresponds to the FAST pulsars timed by Parkes.

5.6.4 Detectability in previous surveys

The FAST-UWB pulsars were found during FAST's early commissioning phase, with the use of a single-beam receiver in drift-scan. Despite a gain of 10.1 K/Jy – in comparison with 18.2 K/Jy for the 19-beam receiver – the UWB receiver provided a sensitivity comparable to Arecibo Observatory (AO). To date roughly 70 pulsars were discovered by the UWB receiver: 11 are reported in Cameron et al. (2020), 10 in this work, and the remaining with ongoing follow-ups.

Even though the UWB receiver was equipped to cover a frequency range from 270 MHz to 1.62 GHz, the new pulsars were mostly found in the 270-500 MHz band due to the drop in efficiency for frequencies above 800 MHz. Because of this, we compare with other pulsar surveys carried out in the low-frequency regime (< 500 MHz) and explore whether the FAST-UWB pulsars could have been discovered earlier. We identify four main surveys: AO327 carried by AO at a central frequency of 327 MHz (Deneva et al., 2013); GBT350 (Hessels et al., 2008) and GBNCC (Stovall, 2013), both carried with the Green Bank Telescope (GBT) at a central frequency of 350 MHz; and LOFAR's LOTAAS survey at a central frequency of 135 MHz (Sanidas et al., 2019). We summarize in Table 5.6 the above-mentioned surveys and the main parameters used in the sensitivity comparison. We explore exclusively the detectability of the FAST-UWB sample - composed of the 11 pulsars reported by Cameron et al. (2020) and 10 from this work. For the detectability of the FAST-UWB sources with surveys carried at L-band refer to the discussion in Cameron et al. (2020).

The flux density for the FAST/PKS pulsars at 1.4 GHz (S_{1400}) ranges from roughly 0.1 to 1.0 mJy (Cameron et al., 2020). Because we have not performed flux calibration of the FAST/EFF pulsars, we restrict ourselves to the flux ranges provided by the FAST/PKS sample. As they trace the same population, this assumption is reasonable. We scale the flux density to a frequency of 300 MHz with the assumption of a spectral index $\alpha = -1.6$ (Bailes et al., 2008) and find that the flux density ranges from 1.1 to 11.7 mJy.

Considering the LOTAAS survey sensitivity to pulsars with flux densities (S) above 5 mJy for a 3600 s integration, and their visibility to declinations above 0° (see Table 5.6), the FAST/EFF pulsars as well as PSRs J1945+1211 and J1919+2621 from the FAST/PKS sample could have been detected. Furthermore, because of the long integration of 3600 s, scintillation would not prevent a detection. For the GBT350 survey, due to their northern Galactic plane restriction to declination above 38°, could have potentially detected all the FAST/EFF pulsars except for PSR J1822+2617. In contrast, the GBNCC survey carried as well by GBT, explored all their observable sky (declination above −40°). GBNCC sensitivity to pulsar with $S > 0.7$ mJy could have potentially detected all of the FAST-UWB pulsars. However, scintillation could have played a role for the low DM pulsar given the short integrations of roughly two minutes. For the pulsar with high DM, pulse broadening due to scattering is likely not the reason, due to the long spin periods of the pulsars and the expected broadening of a couple of milliseconds at 300 MHz.

AO327 survey is the most comparable survey to the FAST pulsar survey reported

Table 5.6: Pulsar surveys at low frequencies and their parameters. The first column list the survey name, the second column names the telescope (abbreviations: EFF=Effelsberg, GBT=Green Bank, AO=Arecibo observatory), f corresponds to the central observing frequency and Δf corresponds to the frequency bandwidth, T_{obs} is the observation time needed to achieved a minimum observable flux S_{min}. time.

Survey	Telescope	f (MHz)	Δf (MHz)	T_{obs} (s)	Gain (K/Jy)	S_{min} (mJy)	Visibility (Declination)
AO327	AO	327	69	60	11.0	0.3	$-1°$–$+38°$
GBT350	GBT	350	50	149	2.0	1.0	$> +38°$
GBNCC	GBT	350	100	120	2.0	0.7	$> -40°$
LOTAAS	LOFAR	135	32	3600	1.7	5.0	$> 0°$
FAST-UWB	FAST	500	530	52	9.0	0.2	$-15°$–$+62°$

here. With a sensitivity to pulsars with $S > 0.3$ mJy, and a comparable integration to FAST – at the testing phase – AO327 could have seen all the FAST/EFF pulsars and PSRs J1945+1211, J2323+1214, and J1919+2621 from the FAST/PKS sample. Again, scintillation could be invoked for the low DM pulsars, but once more, pulse broadening is likely not the reason for the high DM sources.
The determination of FAST-UWB pulsar's flux densities low frequencies (such as S_{400}) could provide insights on why these pulsars were not detected before. We suggest to explore the data of the corresponding surveys by folding the observations (if existing) with the ephemeris provided in Cameron et al. (2020) and in this work.

5.7 Conclusions

We reported the follow-up with Effelsberg of 10 new pulsars from the early FAST pulsar survey. They were the result of the commissioning phase with the UWB receiver with a gain of 10.1 K/Jy, and recording data from 270 MHz up to 1.62 GHz. However, the new pulsars were mostly discovered near the 500 MHz band. We have monitored with Effelsberg the pulsars for over one a year, until a fully connected phase solution was achieved. We analysed their scientific potential based on such timing solution and their polarimetric properties.

We measured a high degree of linear polarization – higher than 70% – in PSRs J2129+4058 and J1951+4724. Despite that for most of the FAST/EFF pulsar some fraction of linear polarization was measured, only PSRs J2112+4058, J2129+4119, J1951+4724 and J0402+4825 had their PA swing sufficiently well defined to constraint the magnetic inclination angle. We use the rotating vector model (Radhakrishnan & Cooke, 1969), and determine the best fit for the PA with an MCMC approach. We determined $\alpha = 94^{\circ}{}^{+40^{\circ}}_{-42^{\circ}}$ for PSR J2112+4058, $\alpha = 117^{\circ}{}^{+30^{\circ}}_{-41^{\circ}}$ for PSR J2129+4119, $\alpha = 93^{\circ}{}^{+19^{\circ}}_{-14^{\circ}}$ for PSR J1951+4724, and $\alpha = 90^{\circ}{}^{+41^{\circ}}_{-41^{\circ}}$ for PSR J0402+4825. However, because of the uncertainties in the measurements, we are not able to restrict β (impact parameter). Regarding circular polarization, except for PSRs J2006+4058, where no

polarization was measured, all the pulsars show an absolute circular polarization lower than 12%.

From the FAST/EFF pulsars, PSRs J2053+4718 and J0402+4825 are located at low latitudes ($b < |3.5°|$), near the Galactic plane; and PSR J1502+4653 at high Galactic latitude. The remaining pulsars are located at mid-Galactic latitude. We used the pulsar's DM to obtain an estimate of their distance through the NE2001 and the YMW16 free electron density models. We found large disagreements for PSRs J2006+4058 and J2053+4718, where the NE2001 estimates a lower limit of 50 kpc on their distance, placing the pulsars outside the Galaxy, while the YMW16 model estimates a distance of 12.6 and 8.0 kpc respectively. However, it is highly unlikely that the pulsars are extragalactic despite their relatively high DM of 259.5 and 331.3 pc cm^{-3}, respectively. We instead propose that their high estimated distance limits are due to an artifact of the NE2001 model, due to the not well-sampled electron density for longitudes between $70° < l < 100°$. On the other side, the YMW16 model fails to estimate a distance to PSR J1502+4653 despite its low DM of 26.6 pc cm^{-3} and instead yields a lower limit of 25 kpc. However, the unconstrained distance to pulsars at high latitudes is expected due to the under-representation of pulsar in that area leading to a poor mapping of the average electron density for those lines-of-sight.

From the $P - \dot{P}$ diagram analysis based on the timing solutions of the FAST/EFF pulsars, we see that except for PSR J2338+4818, all the pulsars are located in the normal pulsar zone. Highlights are PSRs J1951+4724, a young and energetic pulsar; and J2129+4119, J1942+3941, and J1502+4654 old pulsars below the classic death line model. We add to our analysis the FAST/PKS dataset counterpart, consisting of 11 FAST pulsars discovered with identical set up. We refer to this sample as the FAST-UWB pulsars, and noticed that as a whole they seem to trace an older pulsar population. We have tested this by computing the Kolmogorov–Smirnov statistic of the 21 FAST-UWB pulsars against the known population of normal radio pulsars. With a of $p-\text{value} = 0.0015$, we rejected that the two samples are drawn from the same pulsar distribution. Given FAST's sensitivity, uncovering a population of old dim pulsar is perhaps expected. If this is the case, it has the potential to play a key role in the understanding of the emission physics of pulsar and the point at which their radio emission ceases.

PSR J2338+4818 is perhaps the most interesting pulsar of the sample. It is a mildly recycled pulsar in a wide (95.2 days) binary orbit with a massive CO-WD companion. From its mass function and with the assumption of a pulsar mass of 1.4 $M_\odot$, we estimated the companion to have a minimum mass of 1.029 $M_\odot$. Systems like this, evolve from an IMXB, where the inefficient mass transfer through type C Roche-lobe overflow phase leads to a pulsar that was not fully spun-up to few milliseconds, and a not completely circularized orbit in comparison to pulsars in closer binaries and with less massive companions (Tauris et al., 2011a, 2012a).

Additional interesting aspects of PSR J2338+4818 is that it seems to be the widest binary with a massive white dwarf companion ($M>0.8\,M_\odot$), of the recycled/mildly-recycled systems. Finally, it also has a high non-detection rate. The pulsar is not detected in over half of the observations despite its diffractive scintillation timescale

being roughly 10 minutes, and the typical observations lasting at least one hour. With two continuous observation lasting roughly four hours, and several one-hour long observations spaced by 2-4 hours, we constrained the off-mode to be at least four hours. We continue the FAST and Effelsberg monitoring of PSR J2338+4818 with the aim to discern the origin of its off-mode.

Lastly, we explored whether the FAST-UWB pulsars could have been detected by previous surveys. Because the pulsars were found near the 500 MHz band, we compared with surveys carried at a central frequency below 500 MHz. To this end, we extrapolated the measured flux densities at 1.4 GHz of FAST-UWB pulsar to 300 MHz with the assumption of a spectral index of -1.6. Considering the declination range of the different surveys (see Table 5.6), we concluded that the FAST-UWB pulsars could have been potentially detected either by AO327 (Deneva et al., 2013), GBT350 (Hessels et al., 2008), GBNCC (Stovall, 2013) or the LOOTAS survey (Sanidas et al., 2019). However, this rough estimation did not consider the effect of scintillation, which could have been the ultimate reason for some of the FAST-UWB pulsars to not be detected due to the short integrations (tens of seconds) used for most of the mentioned surveys. We highlight that the FAST-UWB pulsars were discovered at the commissioning phase of FAST, with the use of the UWB receiver which was a testing instrument, not aimed to exploit FAST full sensitivity but rather to serve as a tool to work towards accurate positioning, timing clock accuracy, and data flow; while the ultimate instrument: the 19-beam receiver, was under development. Nowadays, with the use of this receiver FAST has reached a sensitivity of roughly 18.2 K/Jy, and has discovered tens of new pulsars. These discoveries and the remaining pulsars from the UWB receiver are currently under monitoring.

We stress the importance of collaboration in the era of radio astronomy with most sensitive radio telescopes such as FAST, Meerkat, and SKA. The high number of discoveries expected by each of these telescopes is hard if not impossible to follow-up by a single facility. To move the timing of the brighter sources to telescopes such as SRT, GMRT, VLA, Parkes, Lovell, GBT, and Effelsberg, can optimize the use of the most sensitive telescopes to discover the most exciting sources, and to time the pulsars that are to dim to be seen by less sensitive telescopes.

Acknowledgements

We thank Dr. N. Porayko, Dr. I Antoniadis, J. Wongphecauxon and Dr. R. Main for helpful discussions. This publication is based on observations with the 100-m telescope of the Max-Planck-Institut für Radioastronomie at Effelsberg. We thank Dr. A. Kraus for scheduling our observations.

Chapter 6

On the weak magnetic field of millisecond pulsars: does it decay before accretion?

This chapter is based on an article titled *"On the weak magnetic field of millisecond pulsars: does it decay before accretion?"*, which is published in Monthly Notices of the Royal Astronomical Society, Volume 490, Issue 2, Pages 2013–2022, 2019[1]. The manuscript remains unchanged, but is formatted to fit the template of the thesis.

The project started as part of my master thesis, where I worked on the simulation and obtained early results through its testing. During the doctoral studies I performed the analysis: I studied the properties of pulsars at birth to derive the initial conditions, I studied the coupled evolution of the physical variables and the role of superconductivity/superfluidity to understand the shortcomings of the model, and I expanded the parameter space for the magnetic field evolution through the study of different lengths of its spacial variations. Additionally, I studied the binary evolution of systems in a wide orbit with a WD component and an MSP with a high magnetic field. With the previous, I obtained the results and written the manuscript.

The full author list is **M. Cruces**, A. Reisenegger, and Thomas M. Tauris.

6.1 Abstract

Millisecond pulsars are old, fast spinning neutron stars thought to have evolved from classical pulsars in binary systems, where the rapid rotation is caused by the accretion of matter and angular momentum from their companion. During this transition between classical and millisecond pulsars, there is a magnetic field reduction of ~ 4 orders of magnitude, which is not well understood. According to the standard scenario, the magnetic field is reduced as a consequence of accretion, either through ohmic dissipation or through screening by the accreted matter. We explored an alternative hypothesis in which the magnetic field is reduced through *ambipolar diffusion* before the accretion. This is particularly effective during the long epoch in which the pulsar has cooled, but has not yet started accreting. This makes the final magnetic field dependent on the evolution time of the companion star and thus its initial mass. We use observed binary systems to constrain the time available for the magnetic field decay based on the current pulsar companion: a helium white dwarf, a carbon-oxygen white dwarf, or

[1] https://doi.org/10.1093/mnras/stz2701

another neutron star. Based on a simplified model without baryon pairing, we show that the proposed process agrees with the general distribution of observed magnetic field strengths in binaries, but is not able to explain some mildly recycled pulsars where no significant decay appears to have occurred. We discuss the possibility of other formation channels for these systems and the conditions under which the magnetic field evolution would be set by the neutron star crust rather than the core.

6.2 Introduction

Millisecond pulsars (MSPs) are old neutron stars (NSs) thought to have evolved from classical pulsars in binary systems, where they have obtained their fast rotation through the accretion of matter and angular momentum from a companion star in a close binary system (Alpar et al., 1982; Bhattacharya & van den Heuvel, 1991a; Tauris & van den Heuvel, 2006). MSPs also have substantially weaker surface dipole magnetic fields compared to the normal population of young radio pulsars, typically $B \sim 10^{8-9}$ G vs. 10^{11-13} G, respectively (Manchester et al., 2005b), which is usually also explained as a result of accretion (Bisnovatyi-Kogan & Komberg, 1974b; Bhattacharya, 2011), a hypothesis we will hereafter call "accretion scenario". One mechanism proposed for this is the enhanced resistivity of the NS crust as it is heated by the accretion (Geppert & Urpin, 1994). However, this would require the magnetic flux to go exclusively through the crust of the NS, which is implausible, unless it is somehow expelled from the core, e.g. through a strong Meissner effect or a very high resistivity. Another proposal is screening of the magnetic field by the accreted matter (Romani, 1990), which in turn has the difficulty of magneto-hydrodynamic (MHD) instabilities (Mukherjee et al., 2013a,b).

In this paper, we explore the alternative hypothesis of a magnetic field decay produced before the accretion process through *ambipolar diffusion* (Goldreich & Reisenegger, 1992a), in which the magnetic flux is transported by the charged particles (protons and electrons) in the NS core as these are pushed by the Lorentz force, making them move relative to the neutrons. Since the collision rate between charged particles and neutrons is strongly dependent on temperature, this mechanism ("diffusion scenario") becomes effective at late times ($\gtrsim 10^6$yr) for non-superfluid cores, once the NS has cooled down, but before it is reheated by accretion.

We do not attempt to construct a realistic, quantitatively reliable model, which would be highly complex, requiring 3-dimensional multi-fluid MHD simulations with largely unknown ingredients such as the impurity content of the NS crust and the mutual interactions of superfluid, superconducting, and normal particles of different kinds in the core. Instead, we present a "toy model" for the coupled evolution of a NS magnetic field, temperature, and rotation, with each of these variables represented by a single number and ignoring the presence of possible superfluid and superconducting states and a solid crust. The purpose of this model is to explore the plausibility of the diffusion hypothesis by comparing the results of this model with the observed magnetic fields of pulsars with degenerate companions, in which the main-sequence lifetime of

the companion's progenitor star determines the time available for this process. A more detailed model must be left for future work.

This paper is organized as follows. In section 6.3.1, we describe the mechanism of *ambipolar diffusion*. In section 6.3, we show the model used for the evolution of the NS's core temperature, rotation, and magnetic field strength. In section 6.4, we present the results on how this evolution proceeds and the predictions on how a NS will move on the $P - \dot{P}$ plane as first ambipolar diffusion reduces the magnetic field and then accretion increases the rotation rate. In section 6.5, we discuss the implications of our results, and the shortcomings of our model, while in section 6.6, we present the conclusions of our work.

6.3 Model

6.3.1 Ambipolar diffusion in the NS core

NS magnetic fields probably have their origin in the field of their non-degenerate progenitor stars, which is amplified by flux freezing during the collapse and further by differential rotation, instabilities, and convective motions in the proto-NS following the supernova explosion. Once these motions have settled, the magnetic field reaches an equilibrium configuration that is likely to fill the whole volume of the NS, stabilized by the composition gradient (radially decreasing proton/neutron ratio) in the NS core (Reisenegger & Goldreich, 1992; Goldreich & Reisenegger, 1992a; Reisenegger, 2009). Since the conductivity is very high (Baym et al., 1969), the magnetic field is effectively frozen into the charged particles (e. g., Spruit 2013; Thorne & Blandford 2017). Thus, for the magnetic field to evolve, the charged particles have to move, somehow overcoming the composition gradient. This can happen in two different ways, which are effective in opposite temperature regimes (Goldreich & Reisenegger 1992a; see also Hoyos et al. 2008, 2010):

(i) At *high temperatures*, charged particles and neutrons are strongly coupled to each other by collisions, but they can convert into each other by weak interactions (*Urca reactions*). Thus, the core matter can be considered as a single fluid that gradually changes its composition as it moves radially at a rate proportional to the Urca reaction rate, but much slower than the neutrino cooling time (Reisenegger 2009; Ofengeim & Gusakov 2018). This is likely to be important in the case of magnetars, where the heat generated by the dissipation of the magnetic energy might keep the NS core hot enough so a substantial decay can actually happen (Thompson & Duncan, 1996b; Reisenegger, 2009).

(ii) At *low temperatures*, Urca reactions are essentially frozen, but the collision rate between neutrons and charged particles is also strongly suppressed, therefore it becomes possible for these two components to move separately, with different velocity fields, in this way allowing the composition to adjust to its equilibrium state at any given density. This relative motion between neutrons and charged particles, known as "ambipolar diffusion", is the focus of the present work.

In the simplified model of Goldreich & Reisenegger (1992a), which takes the neutrons as a fixed background and ignores the possible presence of superfluids or superconductors, the magnetic field $\vec{B}$ is transported by the charged particles at the ambipolar diffusion velocity

$$\vec{v}_{AD} = \frac{\vec{f}_B^s}{n_c \left(m_p/\tau_{pn} + m_e^*/\tau_{en}\right)}, \tag{6.1}$$

where $\vec{f}_B^s$ is the solenoidal part of the magnetic force density (see Goldreich & Reisenegger 1992a for details), n_c is the number density of charged particles, m_p is the proton mass, m_e* is the effective electron mass, and τ_{ij} is the mean time between collisions of particles of species i against species j. Together with the advection equation for the magnetic field,

$$\frac{\partial \vec{B}}{\partial t} = \nabla \times \left(\vec{v}_{AD} \times \vec{B}\right) \tag{6.2}$$

this yields the characteristic time scale for ambipolar diffusion,

$$t_{AD} = 3 \times 10^9 \, \frac{T_4^2 L_5^2}{B_8^2} \, \mathrm{yr}, \tag{6.3}$$

(Goldreich & Reisenegger, 1992a), here normalized in convenient units whose relevance will be clear in section 6.4: T_4 is the core temperature in units of 10^4 K, $B_8 = B/(10^8\,\mathrm{G})$, and L_5 is the characteristic lengthscale of magnetic field gradients in units of 10^5 cm. The typical decay time obtained, $\sim$ Gyr, is of the order of expected evolution times of the low-mass progenitors of white dwarfs (WDs), and might thus be probed in NS-WD binary systems, where the WD acts as a clock.

6.3.2 The crust as an effective vacuum

In order to affect the surface dipole field inferred from the pulsar spin-down rate, the processes happening in the NS core must somehow be transmitted through the solid crust. If the Lorentz forces are strong enough to break the crust, they could move the crustal matter and in this way rearrange the surface field. This is plausible in the case of magnetars, but probably not in rotation-powered pulsars, much less once their magnetic field has been reduced close to MSP levels. Another possibility is a crust with a resistive (Ohmic) diffusion time shorter than the ambipolar diffusion time in the core, which will also allow a rapid rearrangement of the surface field controlled by the processes going on in the core. In order to maintain a high resistivity even at low temperatures, the crustal solid must have a high impurity content.

The timescale for Ohmic diffusion due to impurity scattering is (Cumming et al., 2004)

$$t_{Ohm} = 5.7\,\mathrm{Myr} \frac{\rho_{14}^{5/3}}{Q} \left(\frac{Z}{30}\right) \left(\frac{Y_e}{0.05}\right)^{1/3} \left(\frac{Y_n}{0.8}\right)^{10/3} \left(\frac{f}{0.5}\right)^2 \left(\frac{g_{14}}{2.45}\right)^{-2}, \tag{6.4}$$

where ρ_{14} is the crust density in units of $10^{14}\mathrm{g\,cm^{-3}}$, Z is the atomic number of the dominant nuclei, Y_e and Y_n are the electron and neutron fraction, respectively, and f

is a factor that accounts for interactions between neutrons. By far the most uncertain variable is the *impurity parameter* Q, which quantifies the root-mean-square deviations from the crust average composition. Its value has been theoretically estimated to lie anywhere between 10^{-3} (Flowers & Ruderman, 1977) for very pure crusts that have not been subject to accretion up to 100 for accreted crusts where the accreted material has replaced the original crust (Schatz et al., 1999). Recent models for the observed thermal relaxation of transient accretors after outbursts require a relatively low impurity parameter ($Q \sim 1$) at low densities ($\rho < 8 \times 10^{13}\,\mathrm{g\,cm^{-3}}$) and a substantially higher value ($Q \sim 20$) in the deepest and densest layers (Deibel et al., 2017). Although it is not clear how representative these values are for a crust that has *not* undergone accretion, this makes it plausible to have $t_{Ohm} \ll t_{AD}$. In this limit, essentially no currents flow in the crust, so the latter will act as an extension of the near-vacuum outside the star, and the surface magnetic field will be determined by the bottleneck in the core.

6.3.3 Magneto-thermo-roto-chemical evolution in the core

When analyzing the magnetic field decay in old NSs, we must take into account that the decay rate depends on the core temperature T, which itself is evolving. At early times, T decreases mainly through the emission of neutrinos produced by Urca reactions in the core, and later through the emission of thermal photons from the surface. If no reheating mechanisms were present, the temperature would decay to extremely low values within $\sim 10^7\,\mathrm{yr}$. However, several reheating mechanisms have been proposed in the literature (see Gonzalez & Reisenegger 2010 for a summary and references), and the detection of likely thermal ultraviolet emission from three pulsars in the age range $\sim 10^{7-10}\mathrm{yr}$ (Kargaltsev et al., 2004; Durant et al., 2012; Rangelov et al., 2017; Pavlov et al., 2017), indicating surface temperatures $T_s \sim 10^5\mathrm{K}$, appears to confirm this prediction. Among the mechanisms proposed, Gonzalez & Reisenegger (2010) found that two of them are most promising to explain the thermal emission of very old, low-B NSs. One of these is the friction caused by the motion of superfluid neutron vortices in the NS crust (Alpar et al., 1984), which depends on the very uncertain angular momentum excess J in the crustal superfluid. The other is "rotochemical heating": As the NS rotation slows down, the star contracts, causing chemical imbalances among the particle species present, e. g.,

$$\eta_{npe} \equiv \mu_n - \mu_p - \mu_e > 0 \quad \text{and} \quad \eta_{np\mu} \equiv \mu_n - \mu_p - \mu_\mu > 0, \tag{6.5}$$

where μ_i is the chemical potential (roughly the Fermi energy) of particle species i, and the labels n, p, e, and μ stand for neutrons, protons, electrons, and muons, although other particle species might also be present and involved in these processes. This induces non-equilibrium Urca reactions that deposit energy inside the NS, keeping it warm for as long as it keeps spinning down (Reisenegger, 1995; Fernández & Reisenegger, 2005). Similarly, various spin-down-induced nuclear reactions in the NS crust (e. g., Haensel & Zdunik 1990) also reheat the star, but only in the case of NSs whose crust

has previously been compressed by a substantial amount of accretion (Gusakov et al., 2015).

Here, we use the code of Petrovich & Reisenegger (2010) for the coupled evolution of the temperature and the chemical imbalances with neutrino and photon cooling as well as rotochemical heating, considering only modified Urca reactions without Cooper pairing gaps. To this, we add evolution equations for the magnetic field undergoing ambipolar diffusion,

$$\dot{B} \approx -\frac{B}{t_{AD}}, \tag{6.6}$$

and the decreasing rotation rate due to magnetic dipole spin-down,

$$\dot{\Omega} = -\frac{2R_c^6}{3c^3 I} B^2 \Omega^3 \tag{6.7}$$

where R_c and I are the star's core radius and moment of inertia, and c is the speed of light, as well as a magnetic dissipation term in the thermal evolution equation, with total power

$$\dot{E}_B \approx \frac{1}{3} R_c^3 B \dot{B}, \tag{6.8}$$

We note that the magnetic field evolution is treated very schematically, with a single scalar variable B representing a potentially complex vector field, and assuming that it decays on the ambipolar diffusion timescale, very similar to the approach of Xia et al. (2013). This assumption is contradicted by simulations of ambipolar diffusion in axial symmetry, which show that the magnetic field relaxes to a stable equilibrium state in which the Lorentz force is balanced by a pressure gradient in the charged particles (Castillo et al., 2017), so the dissipation stops. However, non-axisymmetric instabilities likely lead to a full decay, as observed in 3-dimensional MHD simulations (Mitchell et al., 2015).

Our code allows us to track the core temperature T_c, surface temperature T_s, chemical imbalances η_{npe} and $\eta_{np\mu}$, magnetic field strength B, spin period P and its derivative $\dot{P}$ as functions of time. The values of these outputs are governed by the initial spin-period P_0, the initial field strength B_0, the lengthscale L of spatial variations of the magnetic field, and the time available for the evolution.

6.3.4 Constraining the time available for magnetic field decay

In the proposed scenario, the magnetic field of NSs in binary systems will decay until their companion star initiates transferring mass onto their surface, increasing their core temperature to $\sim 10^8$K and thus choking the ambipolar diffusion. After accretion stops, internal reheating processes in the much faster rotating NS are expected to keep the core temperature high enough for ambipolar diffusion to remain negligible. This prevents further decay of the surface B-field below residual values of the order $\sim 10^8$ G, as observed in recycled radio MSPs with old WD companions. As a rough estimate, we assume that the accretion starts once the companion star ends its main-sequence

Table 6.1: Companion types, lower and upper boundaries of the main sequence progenitor mass range that can be confidently assumed to produce this kind of remnant (Tauris et al., 2012b), and respective main-sequence lifetime estimated from equation (6.9).

Companion type	M_{pc} $[M_\odot]$	t_{MS} [yr]
helium WD (He WD)	1	1×10^{10}
	1.6	3×10^{9}
massive WD (CO WD)	3	6×10^{8}
	6	1×10^{8}
neutron star (NS)	10	3×10^{7}
	25	3×10^{6}

lifetime, which thus sets the time available for magnetic field decay in the NS as:

$$t_{MS} \approx 10^{10}\mathrm{yr} \left(\frac{M_{MS}}{M_\odot} \right)^{-2.5} \tag{6.9}$$

(Kippenhahn & Weigert, 1990), which roughly holds for main sequence masses, M_{MS} in the range $0.1 - 50\,M_\odot$. Of course this ignores the time needed for the formation of the pulsar. In the case of a WD companion, the evolutionary time of the (more massive) NS progenitor is much shorter than that of the (less massive) WD progenitor, so the correction is negligible. This may not hold for double NS systems, where the progenitor masses might have been similar, thus leading to similar and unknown evolutionary times. In this latter case, the already very short time estimated in our approach might still be an overestimate of the actual time available. Finally, we note that for short orbital period MSPs (less than a few days), the assumption of a pre-accretion NS B-field decay timescale equal to the main-sequence lifetime of its companion star progenitor is somewhat an overestimate as the accretion is often a result of Case A Roche-lobe overflow (RLO) in low-mass X-ray binaries (LMXBs), whereas it is a slight underestimate in wider orbit MSPs where the companion star is a red giant prior to RLO (Tauris & Savonije, 1999). In any case, equation (6.9) is a reasonable approximation, within a factor of two, for the timescale in which ambipolar diffusion is active in the NS core. There are currently 286 binary radio pulsars known, of which compact object companion stars are found to include: He WDs (121), CO WDs (40) and NSs (19), according to the latest version 1.59 of the ATNF Pulsar Catalogue (Manchester et al., 2005b). Typical examples of main-sequence masses of their progenitor stars (e.g. Tauris et al., 2011b) are shown in Table 6.1. In the rest of this work, we disregard the 78 binary pulsars which are found in globular clusters, since their evolutionary history is uncertain as it might involve encounter events in such a dense stellar environment whereby the companion star is exchanged and information of the binary origin is lost.

6.4 Results

6.4.1 Coupled evolution of physical variables

In our numerical models, we consider NSs with the equation of state AV14+UVII (Wiringa et al., 1988) and central density $\rho_c = 1.2 \times 10^{15}$ g cm^{-3}, corresponding to a mass $M_{NS} = 1.4\,M_\odot$ and radius $R_{NS} = 11.4$ km, and assuming its core occupies 90 % of the total radius. Fig. 6.1 shows the evolution of two hypothetical pulsars with initial magnetic field $B_0 = 10^{12}$ G and with initial spin periods $P_0 = 15$ ms and 0.5 s. These periods were chosen based on PSR J0537-6910, the fastest spinning young pulsar known to date (Marshall et al., 1998), and on population synthesis models suggesting that many pulsars are born with much slower spins (e. g., Faucher-Giguère & Kaspi 2006). We also explore two options for the lengthscale L of the spatial variations of the magnetic field: $L = 0.1R_c$ as in Goldreich & Reisenegger (1992a), and $L = R_c$ as the maximum plausible value for an ordered magnetic field.

Fig. 6.1 shows that, for $t \lesssim 10^6$ yr, the magnetic field remains essentially constant (because the temperature is still high), the spin period increases as expected for a constant dipole, and the temperature is progressively reduced by passive cooling processes, for all combinations of P_0 and L explored. For $t \gtrsim 10^6$ yr, the NS has cooled enough for the magnetic field to start decaying substantially, at a faster rater for smaller L. Around $t = 10^7$ yr, a small bump in the temperature curve shows a reheating effect from magnetic field decay. By that time, the chemical imbalance has grown enough for rotochemical heating in the core to dominate the reheating, leading to a quasi-stationary state (Reisenegger, 1995; Fernández & Reisenegger, 2005) in which the Urca reactions compensate for the contraction of the star and their heat input compensates for the photon cooling through the NS surface, keeping both η_{npe} and T_c roughly constant. Since the model NSs with faster initial rotations build up a larger imbalance, their cores will remain warmer, leading to a slower decay of the magnetic field. However, in all four models considered, the magnetic field keeps decaying roughly as $B \propto t^{-1/2}$ for all times $t \gtrsim 10^7$ yr, as expected from equation (6.3) with constant T_c. Therefore, the final field strength will depend on the time t at which the accretion heats up the core, stopping the ambipolar diffusion.

6.4.2 Evolution on the $P\dot{P}$-diagram

Since the two observables leading to the estimation of the magnetic field strength are the spin-period P and its derivative $\dot{P}$ (see equation [6.7]), it is useful to analyze the model predictions on the so-called $P - \dot{P}$ diagram for NSs. Each panel in Fig. 6.2 is a $P - \dot{P}$ diagram containing the full sample of known pulsars in the *ATNF pulsar catalogue* (Manchester et al., 2005b)[2], except for objects located in globular clusters, where the dense environment can cause companion exchange and hence the current companion may not be suitable to infer the pulsar evolution history. Each panel highlights binary pulsars with a different companion type, showing that pulsars

[2]Version 1.54; http://www.atnf.csiro.au/people/pulsar/psrcat.

(a) Spin period evolution

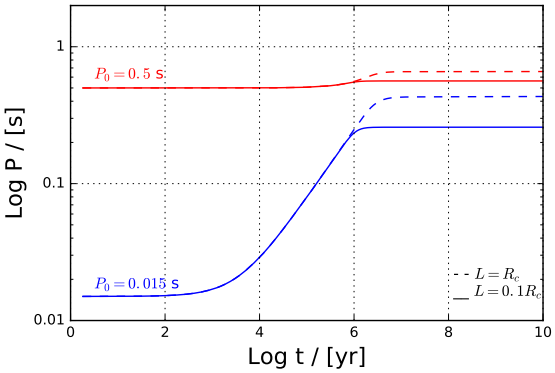

(b) Magnetic field strength evolution

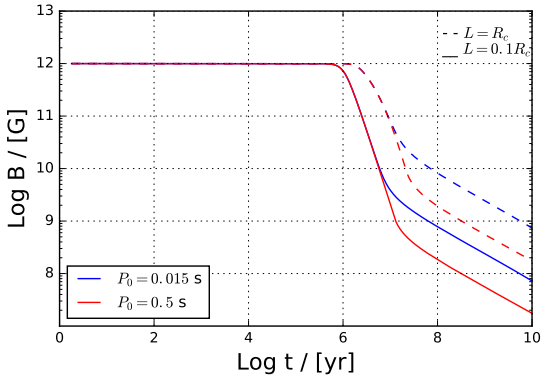

(c) Core temperature and chemical imbalance evolution

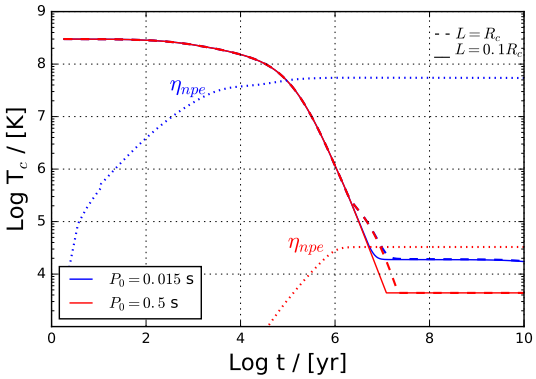

Figure 6.1: Computed evolution for pulsars with initial spin periods $P_0 = 0.015$ s (in blue) and $P_0 = 0.5$ s (in red) and characteristic lengthscales of magnetic field gradients $L = 0.1R_c$ (solid lines) and $L = R_c$ (dashed lines), with neutrino and photon cooling, rotochemical and magnetic heating, magnetic dipole spin-down, and magnetic field decay through ambipolar diffusion, assuming no accretion, superfluidity, superconductivity, or direct Urca reactions, and zero conductivity in the crust. The panels show (a) the rotation period P, (b) the magnetic field strength B, and (c) the core temperature T_c and chemical imbalance η_{npe}, (divided by Boltzmann's constant k in order to convert to temperature units; dotted lines), all as functions of time.

with less massive companions also tend to have weaker magnetic fields.

It can be seen in Fig. 6.2 that the evolution from classical pulsars to MSPs in the ambipolar diffusion scenario can be clearly divided into three successive stages:

(i) The pulsar spins down (and cools) at roughly constant magnetic field.

(ii) The magnetic field decays through ambipolar diffusion, while the rotation period approaches a constant value. During this stage, the NS crosses the "death line", at which the pulsar activity ceases. Since at this point the temperature is also extremely low, the NS should become undetectable.

(iii) Accretion from the binary companion increases the temperature, choking ambipolar diffusion and thus the field decay, and accelerates the rotation, moving the pulsar back across the death line into the MSP region of short spin periods and weak magnetic fields.

Clearly, the different times available for magnetic field decay, depending on the companion mass, produce a trend in the final magnetic fields that roughly follows that in the observed systems. This can also be seen in Fig. 6.3. Our simplified model does fairly well in reproducing the ranges of magnetic field strengths in which the bulk of pulsars of each companion class are found, although there is a number of outliers, specifically towards stronger fields than predicted, which we discuss below.

In Fig. 6.4, we explore the dependence of the evolution on the initial magnetic field B_0 of the pulsar. For large values of B_0, the pulsar spins down at roughly constant $B \approx B_0$ for $\sim 10^6$ yr, reaching longer periods for stronger B_0. At this point, the star has cooled enough for ambipolar diffusion to set in, rapidly reducing the magnetic field and thus essentially stopping the spin-down. Contrary to the final rotation period, the final value of B is essentially independent of B_0. On the other hand, for small B_0 and $L = R_c$, the ambipolar diffusion time remains long even after $t \sim 10^7$ yr, when the temperature has been strongly reduced. Therefore the spin-down continues until much later, and only then the ambipolar diffusion sets in and reduces the field.

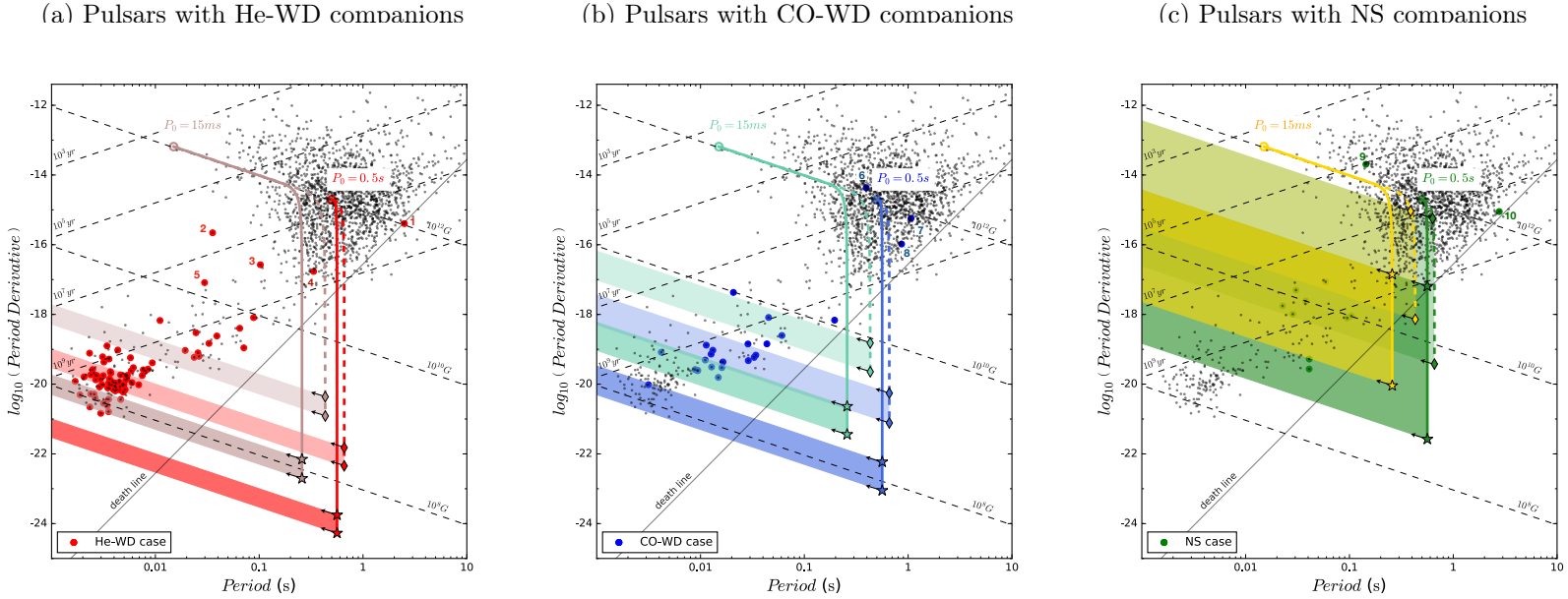

Figure 6.2: $P - \dot{P}$ diagrams for known pulsars from the *ATNF pulsar catalog* (black dots), excluding objects in globular clusters. Lines of constant magnetic field strength and of constant characteristic (spin-down) age according to the magnetic dipole model are traced with grey dashed lines. In each panel, binary pulsars with a different companion type are highlighted: (a) He-WD (red circles), (b) CO-WD (blue circles), and (c) NS companions (green circles). The tracks show the evolution of a pulsar with initial spin-period of $P_0 = 15$ ms (in peach-color for [a], aqua-color for [b], and yellow for [c]), and another one with $P_0 = 0.5$ s (in red for [a], blue for [b], and green for [c]). Solid lines are used for $L = 0.1R_c$, and dashed lines for $L = R_c$. The starting points of the tracks are marked with open circles and the end points with *star* and *diamond* symbols, based on the time available for *ambipolar diffusion* (t_{MS}) given in Table 6.1. The shaded and hatched regions represent the regions where pulsars are expected to be found once they are spun up by accretion after the magnetic field has decayed (indicated with black arrows). For all the tracks an initial magnetic field strength of $B_0 = 10^{12}$G was considered.

6.5 Discussion

6.5.1 Outliers

Fig. 6.3 shows that the actual distribution of pulsar magnetic fields for each companion class has a peak at about the expected location, but also a tail towards stronger magnetic fields that cannot be explained by a straightforward application of our model. Table 6.2 lists the problematic objects, all of which are located in the region of classical (isolated, non-recycled) pulsars with relatively strong magnetic fields ($B \sim 10^{10-12}$ G) rather than that of "recycled", weak magnetic field MSPs ($B \sim 10^{8-9}$G), as expected at least for those with WD companions (objects 1-8). Since we are not considering pulsars in globular clusters, it is very unlikely that any of these Galactic field pulsars would have exchanged their companion during their lifetime.

Disregarding object 2 (where no eccentricity has been measured, nor an upper limit estimated) and 5, a common characteristic of the problematic objects is the relatively large eccentricity of their orbits, which contradicts the highly circular ($e \lesssim 10^{-4}$) orbits expected for binary systems following mass transfer and tidal interactions (Phinney, 1992; Stovall et al., 2019). In addition, objects 1, 2, 3, 4 and 8 are wide binaries with orbital periods longer than 200 days. These systems are therefore expected to have accreted less material due to their shorter X-ray lifetime (Tauris & Savonije, 1999; Podsiadlowski et al., 2002), as is also reflected in their relatively long spin periods. All fully recycled (< 10 ms) pulsars have orbital periods below 200 days (Tauris et al., 2012b). The above characteristics are therefore well supported by the standard scenario involving accretion-induced B-field decay.

The feature regarding relatively significant eccentricity and high magnetic fields in pulsars with WD companions not only challenges the ambipolar diffusion scenario, where the weak MSP fields are a consequence of the old age of the NS, but also the standard accretion scenario for object 5 (PSR J1841+0130) which has an orbital period of only 10 days. In this system, if the NS was formed before its WD companion, the mass transfer should not only have reduced the magnetic field strength, but also have circularized the orbit (Verbunt & Phinney, 1995). NSs born after the WD companion (Dewey & Cordes, 1987), accretion-induced collapse (AIC) of a massive WD (Taam & van den Heuvel, 1986), and a merger of two WDs (Saio & Nomoto, 1985) in a triple system are among the scenarios suggested as alternatives channels for the formation of binary unusual NSs.

Tauris & Sennels (2000b) used population synthesis to analyze the evolution of interacting binaries leading to the formation of systems with a young NS member orbiting an old WD, i.e. systems where the NS was formed after the WD due to mass reversal resulting from mass transfer between the progenitor stars. It was suggested that PSR J1141−6545 and PSR B2303+46 (objects 6 and 7, respectively, in Table 6.2) are systems where the pulsar was formed after the WD. From the standard scenario, the high magnetic fields observed here is a natural consequence of the NS being non-recycled. From the ambipolar diffusion scenario, the high magnetic fields observed would be a consequence of the young age of the NS. The high magnetic field and large

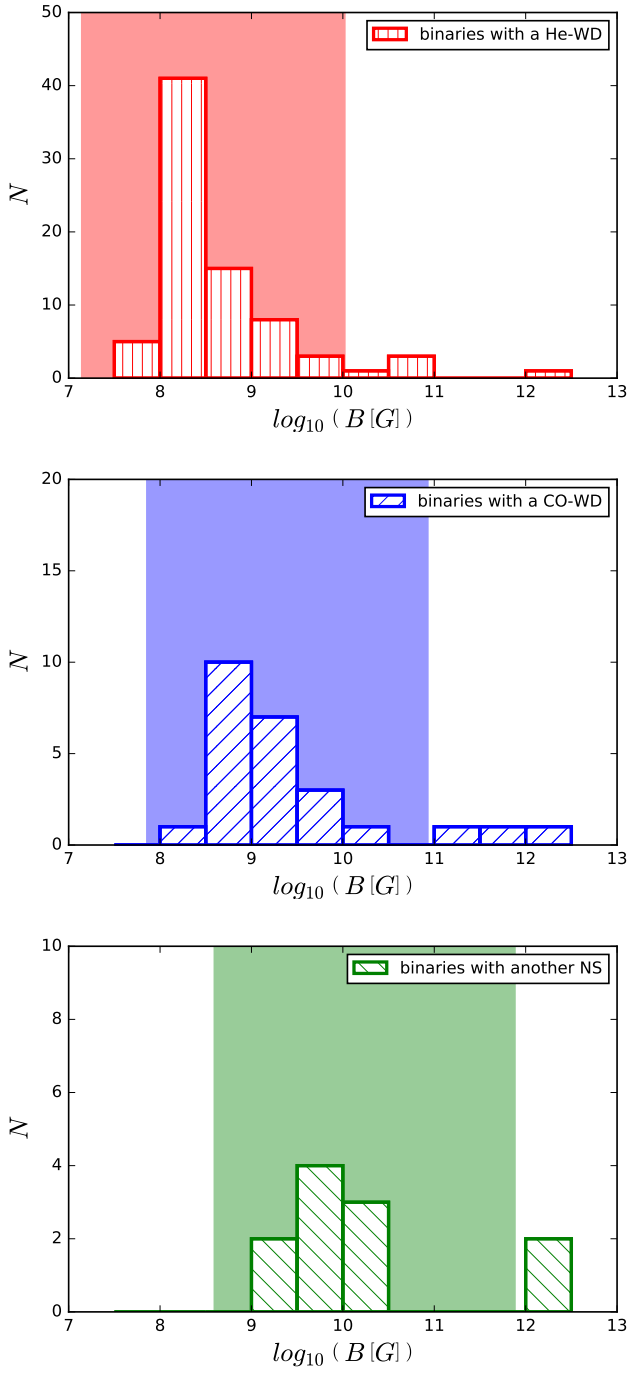

Figure 6.3: Magnetic field strength distribution for pulsars in binary systems. Red (upper plot), blue (center plot), and green (bottom) histograms show the observed distributions of pulsars with He WD, CO WD or NS companions, respectively. The shaded regions of the same colors are the predictions from the ambipolar diffusion scenario for the final B domain occupied by each type of binaries by varying all the parameters: $L \in [0.1R_c, R_c]$, $P_0 \in [0.015\text{s}, 0.5\text{s}]$, $B_0 \in \left[10^{11}, 10^{14}\ \text{G}\right]$ and the time ranges as compiled in table 6.2.

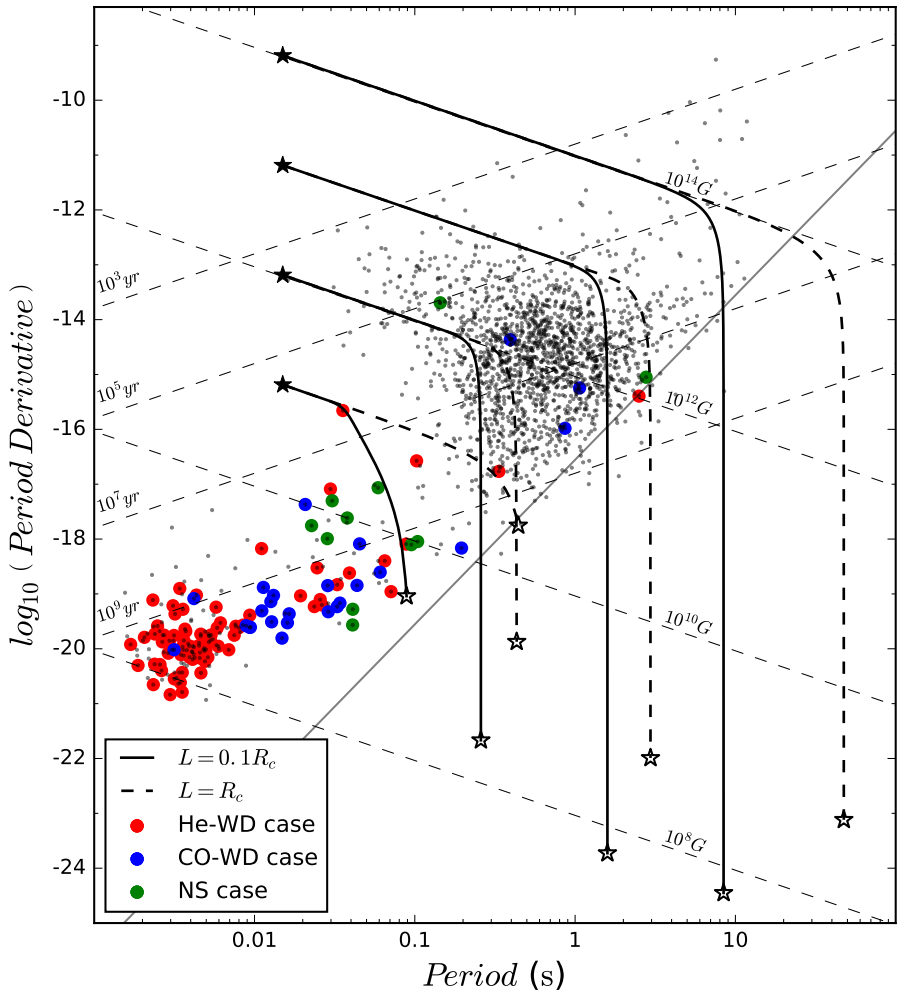

Figure 6.4: Tracks followed by a pulsar born with $P_0 = 15\,\mathrm{ms}$ for different initial magnetic field strengths $B_0 = 10^{11}, 10^{12}, 10^{13}$, and $10^{14}\,\mathrm{G}$, considering $L = 0.1R_c$ (solid lines) and $L = R_c$ (dashed lines). The starting point in each track is tagged with a filled star, while the final point reached after $10^9\,\mathrm{yr}$ is marked with an open star. Binary pulsars with a He WD companion are highlighted with red dots, pulsars with a CO WD with blue dots, and pulsars with a NS companion with green dots.

eccentricity in PSR J1822−0848 (object 1) and PSR B0820+02 (object 8) may suggest these pulsars belong to the same population. Nevertheless, Tauris et al. (2012b) argued that these eccentricities are not large enough for such wide orbits based on expectations for an unperturbed imprint of the supernova explosion if the NS formed after the WD. Instead, it was proposed that these pulsar binaries originate from very wide-orbit LMXBs resulting in CO remnants (Tauris & Savonije, 1999), and that PSR1822−0848 experienced a mild spiral-in from an almost unbound common envelope (CE).

In the AIC scenario, accretion onto a massive WD ($1.1 - 1.3 M_{\odot}$; Tauris et al. 2013 and references therein) may lead to the formation of a super-Chandrasekhar WD, which can collapse immediately or after it loses sufficient spin angular momentum after the accretion phase (Freire & Tauris, 2014). As found by Tauris et al. 2013, binary pulsars formed via AIC and which have He WD companions are expected to have orbital periods of either $10 - 60$ days or > 500 days, depending on whether these systems originated from a main-sequence or a giant-star donor. The exact orbital period boundaries are uncertain and depend on details of WD accretion physics.

For standard evolution of an X-ray binary with a NS accretor, when the donor is a giant star, the outcome is a mildly recycled NS (due to the short duration of the RLO) with a He WD or CO WD companion – depending on the initial orbital period and the mass of the donor – with orbital periods spanning between hundreds and more than a thousand days. We propose that PSR J1840−0643, PSR J1711−4322 and PSR J1803−2712 (objects 2, 3, and 4 respectively) might be formed in a similar way as PSR B0820+02 (i.e. RLO in a wide-orbit LMXB), with the difference that the initial orbital period in these systems were slightly smaller and therefore ended up as a He WD systems, given the WD mass–orbital period correlation (Tauris & Savonije, 1999). If, however, magnetic flux conservation during the AIC process applies, magnetic field strengths above 10^{10} G (as observed in all objects in Table 6.2) can be expected for the formed NS if we consider the broad range in magnetic field strengths covered by magnetic WDs. (We note that only $\sim 10^4$ G is needed for a WD progenitor to produce a post-AIC field of 10^{10} G.) Furthermore, post-AIC systems are expected to undergo additional mass transfer after formation of the NS (Tauris et al., 2013). Magnetic field strengths in WDs can be as high as 10^9 G, as revealed from Zeeman and cyclotron effect (Ferrario et al., 2015). If such WDs collapse due to AIC they might produce NS with magnetar-like magnetic fields.

Another alternative channel for the formation of NSs is through the merger of two close massive WDs. In this scenario, the evolution of two intermediate-mass close stars may lead to the formation of a double WD system in which orbital energy is released via gravitational wave radiation, leading to a merger forming the NS (Saio & Nomoto, 1985). In order to connect this formation channel with the current observed pulsars with a WD companion, a third member in a wide orbit needs to be present.

Rappaport et al. (2013) estimated that at least 20% of the close binaries in the Galactic disk contain a third member in a wide orbit. In the WD merger scenario, a high eccentricity is expected due to the release of binding energy, if the binary survives the effect of the merger. It can be speculated that this scenario might explain the high eccentricity of 0.058 seen for PSR J1822−0848 in a binary with a He WD, although

RLO from the tertiary star to the inner binary after the WD merger event would probably have circularized the orbit. The high magnetic field strength observed might be due to the young age of this pulsar or be a product of a relatively large seed magnetic field in the WDs.

Weak spiral-in due to an unbound common envelope of an asymptotic giant branch star has been claimed in order to explain pulsars with high magnetic fields in wide, eccentric binaries with $P_b < 1000$ days like PSR J1822-0848 (Tauris et al., 2012b). This post-MS phase where the RLO was not efficient would explain the almost non-recycled characteristics of some pulsars in the accretion scenario, but not in the ambipolar diffusion scenario, where magnetic field decay is still expected due to the long MS timescale of several Gyr for the WD progenitor – unless the NS formed somewhat recently through some of the alternative scenarios discussed above.

PSR J0737−3039B is the slower pulsar in the "double pulsar" binary, and thus the second NS to form in the system (Lyne et al., 2004). The same may be the case for PSR J1906+0746, in which the companion star is not detected and its properties are therefore unknown (Lorimer et al. 2006; van Leeuwen et al. 2015).

6.5.2 Crustal resistivity and impurity parameter

If the outlier objects do not have a different origin, but their NS component was formed before its WD companion, we would need to re-examine our assumptions. A possible explanation for the mismatch between the magnetic field strength predicted in the diffusion scenario and the observed magnetic field strength of pulsars in wide binaries lies in one of the strongest assumptions of the diffusion model, namely that the Ohmic dissipation of currents in the crust (equation 6.4) is much faster than the ambipolar diffusion in the cool ($T_c \sim 10^4$ K) core of an old, non-accreting NS, so the latter process controls the decay of the magnetic field. This requires the crust before accretion to have a moderately high impurity parameter, $Q \gtrsim 1$. If this is not the case, the magnetic field will remain "frozen" into the crust and will not decay on the ambipolar diffusion time.

Regardless of the actual value of Q, we do not expect strong variations from one pulsar to another, unless it is modified by accretion. If Q is very small in all pristine pulsars, our model would not be viable and some version of the accretion scenario would be favored.

6.5.3 Shortcomings of our model

We emphasize once more that the model we use is a very simplified toy model. First, instead of considering a three-dimensional vector field and the particle density perturbations caused by it (e. g., Goldreich & Reisenegger 1992a; Hoyos et al. 2008; Castillo et al. 2017), we characterized the magnetic field strength by a single number $B(t)$, whose time-variation is controlled by a characteristic time t_{AD} that depends on a constant (and somewhat arbitrary) characteristic length scale L. Current two-dimensional (axially symmetric) simulations (Castillo et al., 2017) show that the magnetic field

might reach an equilibrium configuration in which ambipolar diffusion does not lead to further decay, thus clearly invalidating our model from this moment onwards. On the other hand, such equilibria might be subject to three-dimensional instabilities (Mitchell et al., 2015), which have not yet been explored in the two-fluid model for a neutron star core. In the latter case, the magnetic field would keep decaying, and our model would be closer to the truth.

Also, the microphysics going into the estimate of t_{AD} is strongly simplified. As in previous work (Goldreich & Reisenegger, 1992a; Hoyos et al., 2008; Castillo et al., 2017), we are assuming that the neutron star core is composed exclusively of non-superfluid neutrons, non-superconducting protons, and electrons (without muons, hyperons, or other particles likely to appear at very high densities) and cools through modified Urca processes. At the very low temperatures at which the evolution occurs in this model, it is likely that at least some part of the neutron star core will be in a superfluid or superconducting state, which would affect the dynamics (particularly t_{AD}), the heat capacity, and the neutrino cooling and heating rates (e. g., Petrovich & Reisenegger 2010). However, it is not clear at present how much of the core is affected, what values are taken by the energy gaps, and whether the protons form a type-I or type-II superconductor. Furthermore, in spite of recent progress (Gusakov et al., 2017; Passamonti et al., 2017; Kantor & Gusakov, 2018; Drummond & Melatos, 2018), there is not yet a self-consistent model for the dynamics of this kind of matter in the presence of rotation (which produces quantized vortices in the neutron superfluid) and a magnetic field (which is confined into quantized flux tubes in a type-II superconductor and into more complex domains if the superconductor is of type-I). Given all these uncertainties and their complex interaction, their effect on the validity of our toy model is quite unclear at this point, possibly being quite large.

These systematic uncertainties due to missing physics cannot be quantified without actually building more sophisticated models. Therefore the (large) range of model parameters explored in this work and considered, in particular, in generating the ranges in final magnetic field strengths shown in Fig. 6.3, clearly still underestimate the true uncertainties, perhaps by a large amount. Thus, it is perhaps surprising that our very simple model produces a semi-quantitative agreement with the available data, which we tentatively take to indicate that a better model might also give a good (hopefully better) description. Of course, given the many simplifications, the agreement might just be a coincidence, and a more realistic model might not fit the data well.

Table 6.2: Summary of properties of the outlier objects labeled in Fig. 6.2, from the *ATNF pulsar catalog* (Manchester et al. 2005b; http://www.atnf.csiro.au/people/pulsar/psrcat). In the last column, we add our proposed formation scenario for each system, which might make it consistent with our model. Abbreviations: LMXB (Low mass x-ray binaries), CE (common-envelope phase), AIC (accretion-induced collapse), WDNS (white dwarf born before the neutron star) and 2nd NS (second neutron star to be formed).

Companion type	Object number	Pulsar name	Spin period P [s]	Magnetic field B [G]	Orbital period P_b [days]	Eccentricity	Proposed formation
He WD	1	J1822-0848	2.5045	1×10^{12}	286	0.058	wide-LMXB and CE
	2	J1840-0643	0.0355	9×10^{10}	937	Unknown	wide-LMXB or AIC
	3	J1711-4322	0.1026	5×10^{10}	922	0.002	wide-LMXB or AIC
	4	J1803-2712	0.3344	8×10^{10}	407	0.005	wide-LMXB or AIC
	5	J1841+0130	0.0297	2×10^{10}	10.5	8×10^{-5}	AIC
CO WD	6	J1141-6545	0.3938	1×10^{12}	0.197	0.171	WDNS
	7	B2303+46	1.0663	8×10^{11}	12.3	0.658	WDNS
	8	B0820+02	0.8648	3×10^{11}	1232	0.011	wide-LMXB
NS	9	J1906+0746	0.1440	2×10^{12}	0.165	0.085	2nd NS?
	10	J0737-3039B	2.7734	2×10^{12}	0.102	0.087	2nd NS

6.6 Conclusions

We explored a scenario in which the weak magnetic fields of MSPs are caused by ambipolar diffusion in the NS core in the non-superfluid/superconductor regime. This process is effective while the core is cool, i.e. in the time interval after the initial cooling of the NS and until its reheating by mass transfer from its companion star. The duration of this time interval is approximately set by the main-sequence lifetime of the companion star, since it most often fills its Roche lobe once it becomes a giant. For the core to drive the magnetic field decay, the currents in the crust must be dissipated by ohmic diffusion before the temperature drops and ambipolar diffusion starts playing a role. The previous condition ($t_{Ohm} \ll t_{AD}$) holds if the *impurity parameter* Q is high enough for the impurity scattering to dominate and to suppress the flow of currents in the crust. In this scenario, the crust behaves as an extension of the near-vacuum outside the star.

With a simple model, we can roughly reproduce the magnetic field strengths of the bulk of the pulsars in binary systems with He WDs, CO WDs, and NSs, given the main-sequence lifetime inferred for the progenitor of the respective companion. There are, however, a certain number of outliers that have substantially stronger magnetic fields than predicted by straightforward application of this model (and which are also problematic for the more standard, accretion-induced field decay scenario), and most of which have relatively wide orbits and moderate to large eccentricities. A possible explanation is that these belong to a different population in which the NS was formed relatively recently, through alternative channels such as: WD–NS formation reversal, accretion-induced collapse of a WD, or merger of the inner two WDs in a triple system. Otherwise, one would have to invoke a very pure crust with a high conductivity, which would not allow the magnetic field to decay unless it is somehow driven by accretion.

We motivate further analysis of the formation channels leading to wide, eccentric binary systems containing pulsars whose magnetic field has not decayed significantly, as they challenge our understanding of pulsar evolution and particularly how the recycling process to form a MSP proceeds.

Acknowledgements

We thank the referee for the helpful suggestions. We are grateful to C. Espinoza, J. Tan, and P. Freire for useful conversations about pulsar evolution. M. Cruces and A. Reisenegger acknowledge funding from FONDECYT Regular Projects 1150411 and 1171421, CONICYT Chile-Germany International Cooperation Grant DFG-06, and the Center for Astronomy & Associated Technologies (CATA; CONICYT project Basal AFB-170002). This work made extensive use of the SAO/NASA Astrophysics Data System (ADS; adsabs.harvard.edu).

Chapter 7

Repeating behaviour of FRB 121102: periodicity, waiting times and energy distribution

This chapter is based on an article titled *"Repeating behaviour of FRB 121102: periodicity, waiting times, and energy distribution"*, which is published in Monthly Notices of the Royal Astronomical Society, Volume 500, Issue 1, Pages 448–463, 2020[1].

As the lead author of this publication, I have performed the Effelsberg observations, reduced and searched the data, performed the analysis, and written the manuscript.

The full author list is **M. Cruces**, L. G. Spitler, P. Scholz, R. Lynch, A. Seymour, J. W. T. Hessels, C. Gouiffés, G. H. Hilmarsson, M. Kramer, and S. Munjal.

7.1 Abstract

Detections from the repeating fast radio burst FRB 121102 are clustered in time, noticeable even in the earliest repeat bursts. Recently, it was argued that the source activity is periodic, suggesting that the clustering reflected a not-yet-identified periodicity. We performed an extensive multi-wavelength campaign with the Effelsberg telescope, the Green Bank telescope and the Arecibo Observatory to shadow the Gran Telescope Canaria (optical), NuSTAR (X-ray) and INTEGRAL (gamma-ray). We detected 36 bursts with Effelsberg, one with a pulse width of 39 ms, the widest burst ever detected from FRB 121102. With one burst detected during simultaneous NuSTAR observations, we place a 5-σ upper limit of 5×10^{47} erg on the 3–79 keV energy of an X-ray burst counterpart. We tested the periodicity hypothesis using 165-hr of Effelsberg observations and find a periodicity of 161±5 days. We predict the source to be active from 2020-07-09 to 2020-10-14 and subsequently from 2020-12-17 to 2021-03-24. We compare the wait times between consecutive bursts within a single observation to Weibull and Poisson distributions. We conclude that the strong clustering was indeed a consequence of a periodic activity and show that if the few events with millisecond separation are excluded, the arrival times are Poisson distributed. We model the bursts' cumulative energy distribution with energies from $\sim 10^{38}$-10^{39} erg and find that it is well described by a power-law with slope of $\gamma = -1.1 \pm 0.2$. We propose that a single power-law might be a poor descriptor of the data over many orders of magnitude.

[1] https://doi.org/10.1093/mnras/staa3223

7.2 Introduction

Fast radio bursts (FRBs) are an observational phenomenon consisting of bright flashes of millisecond duration, detected so-far exclusively at radio frequencies, where detections have been made – as of now – at frequencies as low as 328 MHz (Pilia et al., 2020; Chawla et al., 2020) and as high as 8 GHz (Gajjar et al., 2018). Although the majority of the sources are seen as one-off events, there are a couple of FRBs known to show repeated bursts at a consistent sky position. Example of this is FRB 121102 (Spitler et al., 2016), the first known repeating source, which was localized by VLA observations (Chatterjee et al., 2017) and posteriorly its position pinpointed to milliarcsecond precision by VLBI (Marcote et al., 2017), and associated to a low-metallicity dwarf galaxy at redshift z=0.193 by the Gemini North observatory (Tendulkar et al., 2017).

Since the discovery of the Lorimer burst in archival pulsar data from the Parkes radio telescope (Lorimer et al., 2007), huge advances in the FRB field have been made during the last years with the discovery of over 100 FRBs (Petroff et al., 2016)[2], localizations to host galaxies (Chatterjee et al., 2017; Bannister et al., 2019; Marcote et al., 2020; Ravi et al., 2019; Macquart et al., 2020), rotation measure (RM) and polarization measurements – revealing sometimes up to 100% linearly polarized pulses with changing RM – probing the highly magnetic environment where the bursts originate (Michilli et al., 2018), and most recently the discovery of an active phase with a periodicity of 16 days in the repetition of FRB 180916.J0158+65 (The CHIME/FRB Collaboration et al., 2020), and a potential 157 days periodicity for FRB 121102 (Rajwade et al., 2020).

Nonetheless, their astrophysical origin remains a mystery. Among the most popular models we find: mergers of double neutron star (DNS) systems (Totani, 2013b; Dokuchaev & Eroshenko, 2017), young magnetars (Margalit et al., 2019), giant pulses from pulsars (Keane et al., 2012b) and highly magnetic pulsar-asteroid interactions (Bagchi, 2017) (see the FRB theory catalogue[3] for more examples). While for some progenitor scenarios the detections are restricted to the radio frequencies regime, such as giant pulses from pulsars (Cordes & Wasserman, 2016) and NS-WD mergers (Liu, 2018), other models predict counterparts at multiple wavelengths. An example of this is the young magnetar model, in which an additional X-ray afterglow and optical counterpart for its supernova remnant are expected (Margalit et al., 2019).

SGR J1935+2154 provides a particularly interesting magnetar-FRB link. This soft-gamma-ray repeater located in the Galaxy was associated with strong radio bursts (The CHIME/FRB Collaboration et al., 2020), followed by an X-ray counterpart (Mereghetti et al., 2020). For other scenarios such as the NS-NS merger scenario, in addition to optical emission from the kilonova and X-ray from an afterglow, a soft gamma-ray burst and gravitational wave counterparts are predicted (Dokuchaev & Eroshenko, 2017). Multi-wavelength campaigns have the potential to constrain the aforementioned scenarios and to provide insights on the mechanisms at work. Yet, such campaigns are not plausible for most FRBs given their positional uncertainties of several arcminutes. As

[2] http://frbcat.org/
[3] https://frbtheorycat.org

of now, few non-repeating FRBs have localization down to arcsecond precision (Bhandari et al., 2020; Prochaska et al., 2019), however, their one-off nature makes multi-wavelength observations extremely challenging. On the contrary, repeating FRBs with precise localizations allows triggering observations at other wavelengths based on activity detected in the radio frequencies. Multi-wavelength follow-up from repeating FRBs, such as FRB 121102, have been key to our current understanding of FRBs. They have provided further evidence for the extragalactic origin of FRBs, by ruling out the presence of an intervening HII region responsible for the dispersion measure (DM) excess of FRBs (Scholz et al., 2016), and have placed limits on the X-ray emission in the 0.5-10 keV to be less than 3×10^{-11} erg cm^{-2} (Scholz et al., 2017).

To understand the progenitors of FRBs, observations spanning multiple epochs allow for a long-term periodicity study, which can be indicative of the presence of rotating binary systems, and how the detected bursts distribute in energy and waiting times provide clues on the nature of the source originating such bursts. The high-energy bursts of magnetars and the giant radio pulses from pulsars have shown to have energy distributions well modeled by a power-law. For magnetars it is found a slope γ of -0.6 to -0.7 (Göğüş et al., 1999, 2000), while for giant pulses from the Crab pulsar, is observed $\gamma = -2.0$ (Popov & Stappers, 2007; Bera & Chengalur, 2019).

Motivated by these, we have performed an extended follow-up on FRB 121102 using the 100-m Effelsberg (EFF) radio telescope from September 2017 to June 2020. Some of the epochs are part of a multi-wavelength follow-up campaign to shadow higher energy telescopes such as NuSTAR, INTEGRAL, and the Gran Canaria Telescope (GTC), with radio telescopes such as Effelsberg, the 100-m Robert C. Byrd Green Bank Telescope (GBT), and the 305-m Arecibo Observatory (AO). We describe the observation setup and the algorithms employed for the data processing in Section 7.3. In Section 7.4 we report the bursts and their properties. We use the simultaneous observations with NuSTAR to place limits on the X-ray emission, and use the observed epochs with Effelsberg to test the potential 157-d periodicity reported by Rajwade et al. (2020). Additionally, we test how the bursts are distributed within an active window, and as a whole study their cumulative energy distribution. We discuss the implications of the encountered periodicity, how the time interval between bursts distributes, and the power-law fit to the energy distribution in Section 7.5. We summarize and conclude in Section 7.6.

7.3 Observations and search

Here we describe the radio observations simultaneous with three higher energy telescopes: NuSTAR, INTEGRAL, and GTC. The details of the radio observations are listed in Table 7.1 and the high energy observations in Table 7.2. The full coverage in frequency and time for FRB 121102 by the different telescopes is shown in Figure 7.1. It can be seen that in the case of the X-ray observations, EFF and AO observed simultaneously with NuSTAR (Target ID: 80301307, PI: Scholz), and EFF and GBT observed simultaneously with INTEGRAL (project ID: 1420030, PI: GOUIFFES). For

the optical observations with GTC, only EFF observed (project ID: 98-17, PI: Spitler). Such experiment had a similar approach to Hardy et al. (2017), but with the GTC instead used for optical monitoring. The Effelsberg observations between 2018-02-05 to 2018-02-11 and 2019-01-09 to 2019-02-11 were scheduled together with the GTC to search for simultaneous optical bursts using HiPERCAM (Dhillon et al., 2018). No radio bursts were detected during the simultaneous optical observations, and the results from the analysis of the optical data alone are outside the scope of this paper.

FRB 121102 had an exposure time of 128 hours with Effelsberg, 26.25 hours with GBT, 3.7 hours with AO, 25.2 hours with NuSTAR and 240 hours with INTEGRAL. The only session with radio detections at the time of a simultaneous X-ray observation was on September 06, 2017, during a NuSTAR session (see section 7.4.2). For some radio observations extended time coverage was performed. That is the case from the 24 to the 28 of September 2017 where EFF and GBT had almost full coverage, in some cases with simultaneous observing as well as one radio telescope taking over from the other. However, as seen in Figure 7.1 no radio burst was detected in those observations.

We proceed hereon with the description of the observations and the data processing.

7.3.1 Effelsberg telescope

We took data using the 7-beam feed array receiver with the Pulsar Fast Fourier Transform Spectrometer (PFFTS, Barr et al., 2013), and the high precision pulsar timing backend PSRIX (Lazarus et al., 2016). The PFFTS records data at a central frequency of 1.36 GHz with 300-MHz of bandwidth divided into 512 frequency channels and a time resolution of 54.613 μs. However, these data are not synchronized with a maser clock. To compensate, we recorded simultaneously the incoming data of the central beam with the backend used for pulsar timing, PSRIX, as it provides high precision time stamps. This backend's band is centered at 1.3589 GHz, with a bandwidth of 250 MHz divided into 256 channels and a time resolution of 51.2 μs. This allows us to obtain the precise time of arrivals (TOAs) of the detected bursts displayed in Table 7.4.

While the central beam of the 7-beam receiver was pointing at FRB 121102 with right ascension α = 05:31:58.70 and declination δ = +33:08:52.5 00 (Chatterjee et al., 2017), all the remaining beams from the feed array were simultaneously recorded with the PFFTS for the purpose of radio frequency interference (RFI) mitigation.

7.3.1.1 Single pulse search

We searched for single pulses in the time series from 500 pc cm^{-3} up to 600 pc cm^{-3}, with steps of 1 pc cm^{-3}, using a pipeline based on the *pulsar search software* PRESTO (Ransom, 2011). The timeseries were downsampled by a factor 16 to match the intra-channel dispersion delay at 1.510 GHz, corresponding to the top of the frequency band. Candidates down to a signal-to-noise (S/N) of 6 were explored leading to a total of 36 bursts detected in the PFFTS data (see Figures 7.2, 7.3 and 7.4).

To calculate the accurate topocentric TOAs, we run a similar single-pulse search

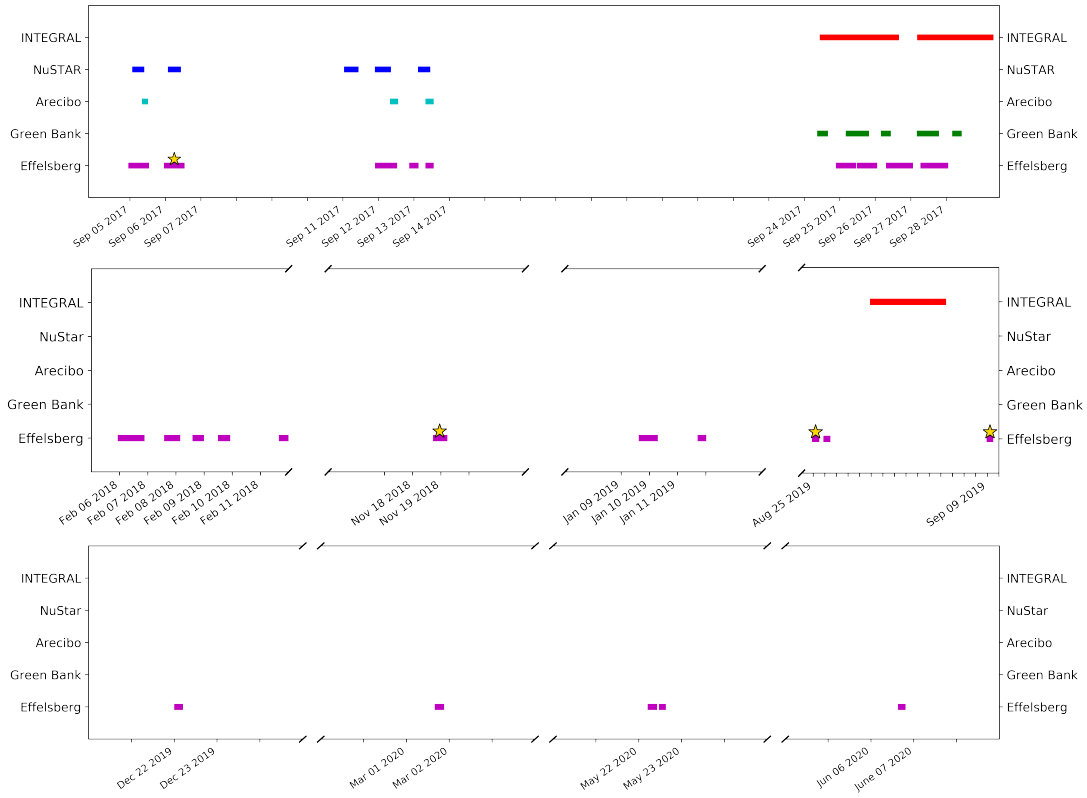

Figure 7.1: Follow-up observations for FRB 121102 with Effelsberg (magenta), Green bank (green), Arecibo (cyan), NuSTAR (blue) and INTEGRAL (red). The yellow star marker indicates an epoch where at least one burst was detected.

Table 7.1: Description of the radio follow-up observations of FRB 121102. First column names the telescope (abbreviations: EFF=Effelsberg, GBT=Green Bank, AO=Arecibo observatory), second and third column list the starting time of the observation and its duration, and the fourth column shows the number of bursts detected. The observations for EFF were carried at a central frequency of 1.36 GHz, for AO at 4.5 GHz and for GBT at 2.0 GHz.

Telescope	**Start** (UTC)	**Duration** (s)	**Events**
EFF	2017-09-05 00:55:54	36000	0
AO	2017-09-05 10:05	1009	0
EFF	2017-09-06 00:58:22	36000	7
EFF	2017-09-11 23:49:16	39600	0
AO	2017-09-12 09:49	6118	0
EFF	2017-09-12 22:53:54	8412	0
AO	2017-09-13 09:46	6166	0
EFF	2017-09-24 23:17:54	34854	0
GBT	2017-09-24 10:45	11700	0
EFF	2017-09-25 23:19:57	34992	0
GBT	2017-09-25 06:00	7200	0
GBT	2017-09-25 10:45	25200	0
EFF	2017-09-26 23:28:52	32400	0
GBT	2017-09-26 05:45	9900	0
EFF	2017-09-27 23:26:49	23580	0
GBT	2017-09-27 06:00	9000	0
GBT	2017-09-27 10:45	22500	0
GBT	2017-09-28 06:00	9000	0
EFF	2018-02-05 18:36:47	22962	0
EFF	2018-02-07 16:39:04	30018	0
EFF	2018-02-08 16:46:25	16044	0
EFF	2018-02-09 14:33:58	18000	0
EFF	2018-02-11 18:20:54	13704	0
EFF	2018-11-18 19:58:50	25200	24
EFF	2019-01-09 17:29:53	39600	0
EFF	2019-01-11 19:39:45	7590	0
EFF	2019-08-25 04:10:13	6876	2
EFF	2019-08-26 03:38:19	4975	0
EFF	2019-09-09 04:59:27	3600	3
EFF	2019-12-22 01:42:15	5400	0
EFF	2020-03-01 17:28:46	7200	0
EFF	2020-05-22 06:37:34	7200	0
EFF	2020-05-22 13:03:29	7200	0

Table 7.2: Description of the NuSTAR and INTEGRAL follow-up observations of FRB 121102. The ID for NuSTAR corresponds to the observation ID, while for INTEGRAL the ID corresponds to the revolution number.

Telescope	ID	Start time (UTC)	End time (UTC)	Exposure (s)
NuSTAR	80301307002	2017-09-05 03:31:32	2017-09-05 13:39:33	15528
NuSTAR	80301307004	2017-09-06 03:38:11	2017-09-06 13:54:41	17567
NuSTAR	80301307006	2017-09-11 02:49:08	2017-09-11 14:30:23	21177
NuSTAR	80301307008	2017-09-11 23:37:24	2017-09-12 11:48:38	20917
NuSTAR	80301307010	2017-09-13 04:53:09	2017-09-13 14:37:12	15476
INTEGRAL	1866	2017-09-24 12:22:33	2017-09-26 16:28:18	179092
INTEGRAL	1867	2017-09-27 06:20:13	2017-09-29 07:19:30	171675
INTEGRAL	2131	2019-08-30 04:07:16	2019-09-01 09:09:36	182321
INTEGRAL	2132	2019-09-01 19:28:59	2019-09-04 00:55:56	184376
INTEGRAL	2133	2019-09-04 11:16:37	2019-09-06 05:13:53	141549

on PSRIX data and cross-match with the bursts detected in the PFFTS. This is due to the lag between the recording of the backends of ∼15 seconds. Barycenter TOAs (t_{bary}) are afterwards calculated as follows:

$$t_{\rm bary} = t_{\rm topo} - \Delta D/f^2 + \Delta_{R\odot} \tag{7.1}$$

where t_{topo} is the topocentric time of arrival at the telescope, in this case Effelsberg. The second term is the delay caused by dispersion due to the interstellar medium (ISM), which depends on the observing frequency f, and $\Delta D = 4.1488008 \times 10^3$ MHz ^{2}pc^{-1} cm^3 $\times$ DM. The third and last term on equation (7.1), $\Delta_{R\odot}$, is the Römer delay, which is the light-travel time between the telescope (for Effelberg longitude = 6.882 778°, latitude =50.524 72°) and the solar system barycenter.

7.3.1.2 Intra-observation periodicity search

For completeness we processed the data of the central beam with the *acceleration search* pipeline used to search for pulsars in The High Time Resolution Universe Survey – Northern sky (HTRUN; see Barr et al. 2013 for survey description), and the *fast folding algorithm* (FFA) based on Morello et al. (2020) implementation. The DM trials ranged from 530 pc cm^{-3} to 590 pc cm^{-3} for the acceleration search, and from 0 pc cm^{-3} to 600 pc cm^{-3} for FFA search. No source was found within the candidates down to a S/N of 8.

7.3.2 Green Bank Telescope

We observed FRB 121102 with the GBT's S-Band receiver at a center frequency of 2 GHz and a total bandwidth of 800 MHz, though a notch filter between 2.3 and 2.36 GHz

removes interference from satellite radio, slightly reducing the effective bandwidth. We used the Green Bank Ultimate Pulsar Processing Instrument (GUPPI, Ransom et al., 2009) to coherently dedisperse incoming data at a DM of 560 pc/cm^{-3}, recording self and cross-polarization products with 512 frequency channels and a sampling time of 10.24 μs.

We used the PRESTO routine `rfifind` to flag samples contaminated by interference and applied this mask in subsequent processing (Ransom, 2011). We searched for bursts using the PRESTO routine `single_pulse_search.py`, similar to data from Effelsberg, but with slightly different parameters. De-dispersed time series were created at trial DMs of 527 to 587 pc/cm^{-3} with steps of 0.2 pc/cm^{-3} and downsampled to a time resolution of 81.92 μs. We searched for pulses with a maximum width of 100 ms and inspected all candidates with a S/N $\geq$ 6. Astrophysical pulses will exhibit a characteristic increase in S/N as the trial DM approaches the true DM of the source. We also created the dynamic spectrum for each promising candidate to investigate the time and frequency behavior in more detail. We determined that all high S/N bursts detected in our search were terrestrial interference and did not detect any astrophysical bursts from FRB121102.

7.3.3 Arecibo Observatory

The simultaneous observations with NuSTAR were obtained through a DDT to the Arecibo Observatory (project code P3219). Note, only half of the scheduled observations were possible due to the telescope shutdown for hurricane Irma. Similarly, simultaneous observations planned along with INTEGRAL were not possible due to the observatory shutdown after hurricane Maria.

Data were recorded with the C-lo receiver and PUPPI pulsar backend. PUPPI recorded filterbank files coherently dedispersed to DM=557 pc cm^{-3}. The recorded bandwidth at 4.1-4.9 GHz was divided into 512 channels yielding a frequency resolution of 1.56 MHz. The time resolution of the data was 10.24 μs. The raw data contain full polarization information, which can be used to obtain the rotation measure and polarization profiles in the event of a detection.
Before searching, the filterbank data were downsampled in time to 81.92 μs, the number of channels reduced to 64, and the total intensity (Stokes I) values are extracted. The data were searched with a simple PRESTO based pipeline (Ransom, 2011), downsampled in time by a factor of 16 and dedispersed with trial DMs ranging from 507 pc cm^{-3} and 606 pc cm^{-3} in steps of 1 pc cm^{-3}. In order to optimize burst detection, the dedispersed time series were convolved with a template bank of boxcar matched filters up to 49 ms. Candidate bursts were identified in the convolved, dedispersed time series by applying a S/N threshold of 6. The resulting diagnostic plots were searched by eye, and no bursts were found.

Table 7.3: Technical information of the observation setup for AO, GBT and EFF radiotelescopes listed in Table 7.1. The frequency refers to the central frequency for the bandwidth of the receiver, T_{sys} is the temperature system, S/N_{min} to the minimum detectable signal-to-noise of a single pulse and F_{min} refers to the fluence threshold for a bursts of 1 ms duration given S/N_{min}.

Telescope	Backend	Frequency (GHz)	Bandwidth (MHz)	SEFD (Jy)	S/N_{min}	F_{min} (Jy ms)
AO	PUPPI	4.5	800	3.5	10	0.03
GBT	GUPPI	2.0	740	10.0	7	0.05
EFF	PFFTS	1.36	300	17.0	7	0.15

7.3.4 NuSTAR

FRB 121102 was observed by NuSTAR (Harrison et al., 2013) between 2017 September 5 and 11 in five separate observations with their start times and durations shown in Table 7.2. The data were processed using HEASOFT[4] and the standard tools `nupipeline` and `nuproducts`. We extracted source photons from a 2′-radius circular region centered on the source position. We used a background region of identical size positioned away from the source. Photon arrival times were corrected to the Solar-System Barycenter using the source position from Chatterjee et al. (2017).

7.3.5 INTEGRAL

FRB 121102 was observed by the INTEGRAL satellite in late September 2017 in pointing mode and then in 2019 in a Target of Opportunity mode. In both cases, the goal was to search for a possible Hard X-Ray/soft gamma-ray counterpart to the radio emission. The log of the observations with start time and duration is shown in Table 7.2. The INTEGRAL data were processed using the standard INTEGRAL Offline Scientific Analysis (OSA) software[5]. No radio burst was triggered by the Effelsberg telescope during the INTEGRAL exposures, preventing a search for a coincident impulsive event. Searches for correlations before or after the radio burst and with signals from other radio facilities are currently underway (Gouiffes et al, in preparation).

7.4 Burst properties

During our follow-up observations, 36 bursts were detected with Effelsberg and none with GBT or AO. The 36 bursts are displayed in Figures 7.2, 7.3 and 7.4 and their inferred properties in Table 7.4. The figures show the dynamic spectra of the bursts

[4] `http://heasarc.gsfc.nasa.gov/ftools`
[5] `https://www.isdc.unige.ch/integral/analysis#Software`

over the 235 MHz frequency band, while the top panels show the pulse profiles after integrating the dynamic spectrum in frequency.

Our reported bursts come from four epochs (MJD 58002, 58440, 58720, and 58735) and hinting towards three different values for the dispersion measure of the bursts as a result of S/N optimization. However, given the sub-structure present in some of the bursts, such as bursts B11, B20, and B26, we do not report the dispersion value that yields the highest S/N. Furthermore, we do not attempt to optimize the dispersion value, as our incoherently dedispersed data might not be resolving sub-structure that would otherwise be evident with coherent dedispersion. Instead, we make use of values reported in the literature at epochs near our detections. For the bursts from September 2017 we use the value of 560.5 pc cm^{-3} reported by Hessels et al. (2019), while for the bursts from November 2018 we use 563.6 pc cm^{-3} (Josephy et al., 2019) and for August and September 2019 a value of 563.5 pc cm^{-3} (Oostrum et al., 2020). Such values were deduced from frequency structure optimization by finding the dispersion value that maximizes the forward derivative of the dedispersed time series (Hessels et al., 2019).

To calculate the properties of the bursts (Table 7.4), such as the S/N, flux density, fluence, and the full-width half-maximum (FWHM), we used DSPSR (van Straten & Bailes, 2011) to extract a snapshot of data from the PFFTS filterbank file and chose a time resolution that matched the intra-channel smearing time. Subsequently, we inferred the properties of each burst as implemented in Houben et al. (2019). The bursts were fit with a Gaussian-model calculated through least-squares optimization. The height and full width half maximum (FWHM) were obtained afterward from such best fit, and the S/N deduced from the peak and its associated error with the root-mean-square (rms) of the noise fluctuations. We converted these values to flux (S) by using the radiometer equation for single pulses:

$$S = \frac{(S/N) \cdot \mathrm{SEFD}}{\sqrt{n_p \cdot \mathrm{FWHM} \cdot \Delta\nu}} \tag{7.2}$$

for Effelsberg 7-beam's receiver, the system equivalent flux density ($SEFD$) has a mean value of 17 Jy for each of the two polarisations (n_p). The bandwidth ($\Delta\nu$) considered for the calculation is 235 MHz, which corresponds to the remaining of the 300 MHz bandwidth for the PFFTS data after cropping the band edges.

From Table 7.4 we see that the brightest bursts of the dataset are B6, B22, B23, B26, with flux densities of 1.56 Jy, 1.4 Jy, 1.0 Jy, and 1.2 Jy respectively, and whose emission extends across the full bandwidth. For bursts such as B10 and B11, their emission comes from the lower part of the frequency band, while B14 is an example of emission coming predominately from the upper part of the frequency band.
Six bursts show multi-component profiles: B11, B14, B20, B23, B25, and B26. The number of components ranges from two components, such as B25, to three components for B11 and B26. Particularly interesting bursts are B10 and B14, displaying a weak trailing emission tail, and B20 and B26 with a characteristic downward drifting pattern. B20 and B21 are the closest spaced bursts of our dataset with a TOA difference of ∼38 milliseconds. Although the majority of the published bursts have separations above 1

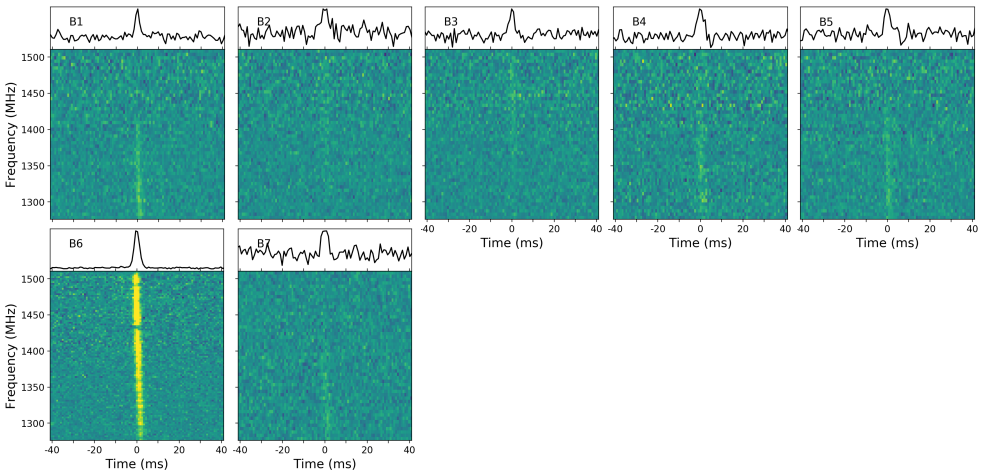

Figure 7.2: Profiles for the bursts detected on September 2017 with Effelsberg at 1.36 GHz. The top plot displays the pulse profiles obtained when integrating in frequency the dynamic spectra in the lower panel. The bursts have been incoherently de-dispersed at 560.5 pc cm^{-3} (Hessels et al., 2019). For visualisation purposes B1–B5 and B7 were frequency scrunched by a factor of 8 and B6 by a factor of 4.

second, it is known that few bursts cluster around TOA separations of 20-40 millisecond (Scholz et al., 2017; Hardy et al., 2017; Gourdji et al., 2019; Caleb et al., 2020) and potentially as low as 2.56 millisecond (see Gajjar et al. 2018). However, whether this latter case corresponds indeed to two separated events or different components of one burst is ambiguous.

B31 is arguably the most interesting burst from the sample. It has a width of 39±2 ms, and is, as of now, the broadest burst detected from FRB 121102. To determine its width we have used the FWHM of the Gaussian fit to the two main components of the pulse profile. Given that the known typical durations of the bursts from FRB 121102 are of the order of a couple of milliseconds, we wonder whether the previously mentioned events with separations 20-40 milliseconds (Scholz et al., 2017; Hardy et al., 2017; Gourdji et al., 2019; Caleb et al., 2020) correspond to single events in which only the strongest components are detected. This will be discussed further in Section 7.5.

7.4.1 Short-term TOA periodicity search

Given the high number of bursts detected within one single observation, we searched for an underlying periodicity in the arrival times of the bursts detected in the November 2018 dataset. First, we employed an algorithm commonly used to find the periods of bursts from rotating radio transients[6] (McLaughlin et al., 2009). For a range of trial

[6] `rrat_period` in PRESTO pulsar search software

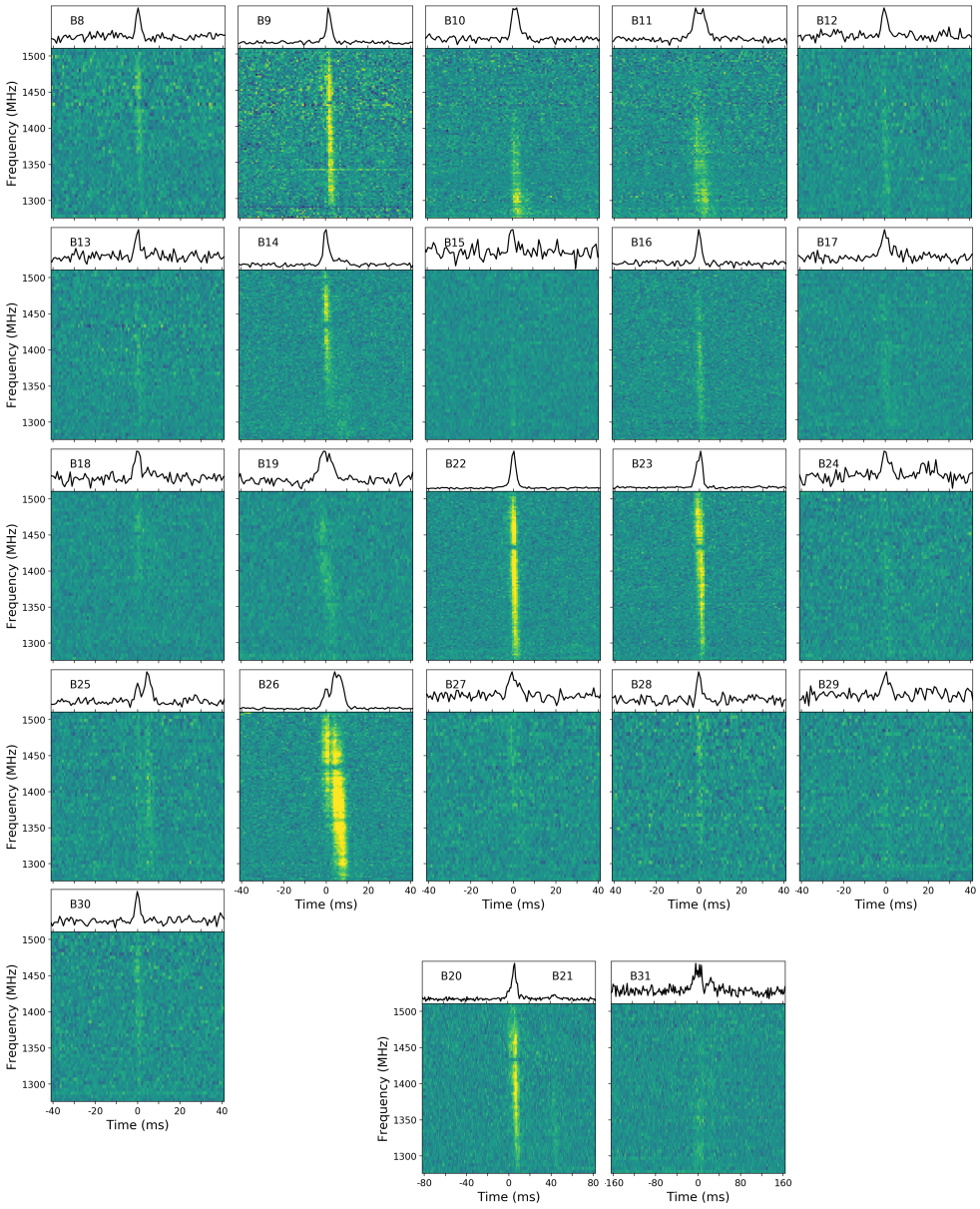

Figure 7.3: Profiles for the bursts detected on November 2018 with Effelsberg at 1.36 GHz. The top plot displays the pulse profiles obtained when integrating the dynamic spectra in the lower panel. The bursts have been incoherently de-dispersed at 563.5 pc cm^{-3} (Josephy et al., 2019). For visualisation purposes bursts B9–B11, B14, B16, B20–B23 and B26 were frequency scrunched by a factor of 4, B31 by a factor 2, and the rest of the bursts by a factor of 8.

Table 7.4: Properties of the bursts detected with Effelsberg. The TOAs are barycentred and referred to infinite frequency. All the errors displayed correspond to one standard deviation and arise from the error in the determination of the pulse widths and the rms of noise oscillations in the determination of the S/N. S/N_i is the signal-to-noise from the discovery as reported by the pipelines and S/N_f is the value obtained after manual cleaning.

Burst No	MJD	S/N_i	S/N_f	Flux density (Jy)	Fluence (Jy ms)	FWHM (ms)
B1	58002.060649899	12.6	12.1	0.19 ±0.02	0.47	2.4 ± 0.2
B2	58002.060794618	6	7.1	0.08 ± 0.01	0.36	4.3± 0.7
B3	58002.063269026	7.9	9.2	0.13 ± 0.02	0.38	2.7 ± 0.4
B4	58002.104939709	10.4	10.1	0.13 ± 0.01	0.47	3.5 ± 0.4
B5	58002.139243447	8.8	9.9	0.13 ± 0.02	0.43	3.16 ± 0.4
B6	58002.166825811	93.7	108.4	1.56 ± 0.2	4.64	2.97 ± 0.03
B7	58002.258539197	6.3	9.2	0.12 ± 0.01	0.41	3.2 ± 0.4
B8	58440.838835667	12.1	13.1	0.21 ± 0.03	0.49	2.3 ± 0.2
B9	58440.862656975	36.1	38	0.58 ± 0.08	1.51	2.57 ± 0.08
B10	58440.923733529	22	24.2	0.29 ± 0.04	1.20	4.0 ± 0.2
B11	58440.936807041	29.1	31.7	0.30 ± 0.04	2.04	6.7 ± 0.2
B12	58440.989835921	11.4	12.3	0.17 ± 0.02	0.53	3.0 ± 0.3
B13	58440.998861733	7.4	7.7	0.13 ± 0.02	0.27	2.0 ± 0.2
B14	58441.007579584	34.6	40.8	0.58 ± 0.08	1.74	2.97 ± 0.09
B15	58441.008221936	7	7.1	0.11 ± 0.01	0.26	2.4 ± 0.4
B16	58441.012582998	18.8	24.7	0.38 ± 0.05	0.96	2.5 ± 0.1
B17	58441.015540453	11.3	13.8	0.11 ± 0.01	1.00	8.6 ± 0.8
B18	58441.018047897	11.1	11.7	0.15 ± 0.02	0.54	3.5 ± 0.4
B19	58441.019135880	18.1	22.6	0.21 ± 0.03	1.46	6.8 ± 0.4
B20	58441.028824049	48.4	56.4	0.57 ± 0.08	3.38	5.8 ± 0.1
B21	58441.028824494	6.4	8.7	0.08 ± 0.01	0.54	6.3 ± 0.9
B22	58441.029775293	84.2	93.5	1.4 ± 0.2	3.84	2.73 ± 0.03
B23	58441.059832185	66.7	78.5	1.0 ± 0.1	3.57	3.35 ± 0.05
B24	58441.059991054	7.8	8.6	0.10 ± 0.01	0.43	4.1 ± 0.6
B25	58441.061410818	14.3	16.8	0.16 ± 0.02	1.07	6.6 ± 0.5
B26	58441.064588499	105.2	136.9	1.2 ± 0.1	9.38	7.6 ± 0.1
B27	58441.067400861	8.9	11.2	0.10 ± 0.01	0.70	6.4 ± 0.7
B28	58441.106370081	9.5	11.5	0.18 ± 0.02	0.42	2.2 ± 0.2
B29	58441.109293484	7.3	8.1	0.09 ± 0.01	0.41	4.2 ± 0.6
B30	58441.112477441	10.6	13.4	0.21 ± 0.03	0.51	2.4 ± 0.2
B31	58441.124609034	14.4	20.4	0.08 ± 0.01	3.14	39 ± 2
B32	58720.206275908	77.2	77.4	0.9 ± 0.1	3.13	3.20 ± 0.05
B33	58720.230616442	8.9	8.4	0.12 ± 0.01	0.34	2.7 ± 0.3
B34	58735.230804235	25.6	28.3	0.49 ± 0.07	1.00	2.04 ± 0.08
B35	58735.237756158	23.8	24.2	0.38 ± 0.05	0.94	2.4 ± 0.1
B36	58735.239630828	46.5	59.4	0.8 ± 0.1	2.61	3.13 ± 0.06

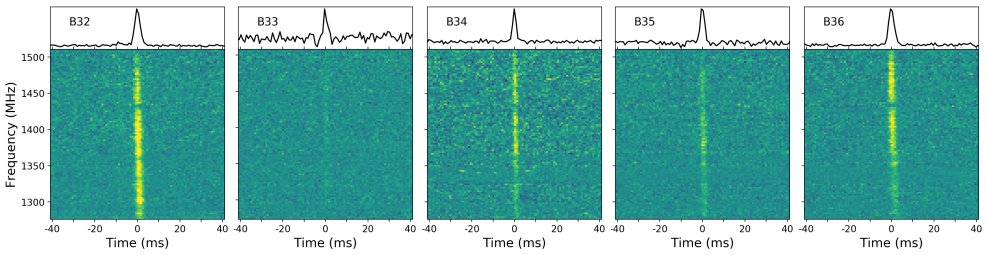

Figure 7.4: Profiles for the bursts detected on August and September 2019 with Effelsberg. The top plot displays pulse profile obtained when integrating the dynamic spectra in the lower panel. The bursts have been incoherently de-dispersed at a value of 563.6 pc cm^{-3} (Oostrum et al., 2020). For visualisation purposes all the bursts were frequency scrunched by a factor of 4.

periods, the number of rotations between consecutive bursts is calculated, and the best period is the greatest common denominator that groups the bursts into the narrowest range of pulse phase. We note that this algorithm does not work well if bursts arrive over a wide range of rotational phases or if there are multiple emission windows. B20 and B21 are only separated by ∼38 ms and might be two components of one long burst, so we excluded B21 from our analysis.

Using the remaining 23 bursts, this algorithm gave a best-fit period that grouped the bursts within a window of ∼0.6 in phase. In order to test the robustness of this finding, we repeated the search 100 times using a sub-sample of 12 randomly chosen bursts. Each trial gave a different period, so we conclude the period determined with all the bursts is not real. Furthermore, we can exclude a period longer than ∼0.1 s with a narrow emission window.

Lastly, we also carried out a periodogram search over the same 23 TOAs and found no underlying periodicity.

7.4.2 NuSTAR

The NuSTAR observations overlapped with radio observations, but only one burst was detected while NuSTAR was observing the source. We searched in time near the burst detected by Effelsberg (Burst B6) that occurred during the NuSTAR observation on 2019-09-06. The closest X-ray photon to the time of the Effelsberg burst was 15 s away. Given this separation, the false alarm probability given the 3–79 keV NuSTAR count rate of 0.03 count/s is 60%.

Using an identical method to that employed in Scholz et al. (2017), we place limits on the X-ray emission from putative models. That is, we place a count rate limit using the Bayesian method of Kraft et al. (1991), and translate that to a fluence limit using the spectral response of NuSTAR and an assumed spectrum. In Table 7.5 we show the

resulting limits.

Compared to the limits placed by Scholz et al. (2017) on X-ray emission at the time of radio bursts from FRB 121102 using *Chandra* and *XMM*, the limits placed here using NuSTAR are not as constraining for the low absorption case (10^{22} cm^{-2}), which corresponds to a typical value for a sightline out of the Milky Way and through the disk of a spiral, Milky-way-like, host galaxy. However, for the highly absorbed case (10^{24} cm^{-2}), the NuSTAR limits are about an order of magnitude lower for the hard spectral models (Blackbody and Cutoff PL) and about twice as low for the soft power-law model. These NuSTAR limits therefore further constrain the energetics of X-ray counterparts to radio bursts from FRB 121102, in the case where it is highly absorbed by material close to the source (e.g. supernova ejecta Metzger et al., 2017b).

Table 7.5: Burst limits for different X-ray spectral models. The energies are calculated assuming the measured luminosity distance to FRB 121102, 972 Mpc (Tendulkar et al., 2017). In the table Γ is the spectral index.

Model	$N_{\rm H}$ ($\rm cm^{-2}$)	kT/Γ (keV/-)	Absorbed 3–79 keV Fluence Limit (10^{-9} erg $\rm cm^{-2}$)	Unabsorbed 3–79 keV Energy Limit (10^{47} erg)	Extrapolated 0.5–10 keV Energy Limit (10^{45} erg)	Extrapolated 10 keV–1 MeV Energy Limit (10^{47} erg)
Blackbody	10^{22}	10	2	2	8	2
Blackbody	10^{24}	10	3	3	12	3
Cutoff PL	10^{22}	0.5	3	3	14	50
Cutoff PL	10^{24}	0.5	4	5	20	80
Soft PL	10^{22}	2	0.6	0.6	60	0.9
Soft PL	10^{24}	2	1.1	2	180	3

Note: 5-σ confidence upper limits.
Assumed blackbody temperature, kT, for blackbody model and power-law index for power-law models.

7.4.3 Full Effelsberg sample

In addition to the set of 36 bursts that we report in Table 7.4, we incorporate into the following analysis the published datasets from Hardy et al. (2017) and Houben et al. (2019). Such datasets were acquired with Effelsberg using the identical setup (see Section 7.3.1). In total, our sample contains 57 bursts detected in 165 hours of observations in epochs between MJD 57635 to 59006.

7.4.3.1 Long-term periodicity

We create a time series from the dates of the EFF observations and label a session with 1 when at least one event was detected and with 0 when no bursts were detected. Because the observations were not done with a regular cadence, the time series is unevenly sampled. We search for a periodic signal through a periodogram analysis.

The majority of the observations were not triggered based on known source activity, but instead, scheduled based on the availability of the higher energy telescopes. The exception is the observations in early September 2017 coordinated with *N*uSTAR, which were scheduled based on the GBT detections at C-band presented in Gajjar et al. (2018). Furthermore, we consider a periodogram search to be a valid approach, as the full sample of detections and non-detections is included. Note, our dataset, which totals 34 epochs, is composed of roughly 70% non-detections. This is often not the case, as published data is biased towards detections.

Following the formulation presented in VanderPlas (2018), we proceed with the Lomb-Scargle periodogram, which is displayed on the top of Figure 7.5. First, we subtract the mean value from the time series. This step is important as the Lomb-Scargle model assumes that the data is centered around the mean value of the signal. As seen in Figure 7.5 the periodogram peaks at a period of 161±5 days, in agreement with the postulate of Rajwade et al. (2020). The 1-σ uncertainty is not estimated from the width of the peak, as this is not optimal for time series with long baselines and few data points. Instead, we determine the uncertainty of the peak, σ_{ls}, through (VanderPlas, 2018):

$$\sigma_{ls} = \frac{\mathrm{FWHM}}{2}\sqrt{\frac{2}{\mathrm{N}\cdot \mathrm{S/N}^2}} \tag{7.3}$$

where N is the number of points in the dataset and FWHM is the full-width at half-maximum of the Gaussian fit to the peak.

Given the presence of several peaks with significant power in the Lomb-Scargle periodogram, we investigate if any are introduced from the observing function. This is plausible as the Lomb-Scargle periodogram of the data in Figure 7.5 is the result of the convolution of the true signal from FRB 121102, and a set of top-hat functions with different durations, which describe the observations (window function). We compute the Lomb-Scargle periodogram of the window function by keeping the epochs unchanged but setting all values to one (for detections and non-detections). For the window transform the data is not centered. We identify several peaks in the periodogram of the

window function that are also present in the periodogram of the data. Some peaks among the top 15 periods are marked in Figure 7.5 with the black arrows and correspond to (from right to left) 119, 75, 70, 19, 16, and 14 days roughly. More importantly, the analysis of the window function down to the top 20 periods did not show any peak at 161 days, supporting the conclusion that the 161 day period is in the data.

We further test the hypothesis of an underlying periodicity through the use of the bivariate l_1-periodogram, also referred to as the *robust*-periodogram (Li, 2010). This type of periodogram is derived from the maximum likelihood of multiple frequency estimation, and it uses the least-absolute deviations regression model – instead of the least-squares minimization as the Lomb-Scargle periodogram – which is a robust regression against heavy-tailed noise and outliers. The robust periodogram predicts a 161 days period as well, perfectly in agreement with the Lomb-Scargle prediction.

To calculate the significance of the peak, we estimate the false alarm probability using a bootstrap method with 10,000 trials. We keep the epochs unchanged and for each trial draw randomly the outcome of an observation (detection or non-detection). We record the maximum power of each generated Lomb-Scargle periodogram and calculate the probability that a given power exceeds a threshold through percentile rank. The dotted lines in the Lomb-Scargle periodogram in Figure 7.5 show the 1-σ, 2-σ, and 3-σ significance levels for the highest peak, determined by the 10,000 bootstrap resamplings. We determine a significance of roughly 2.7-σ for the 161 days peak. This approach answers the question of how likely it is that any period will have, by chance, a power above a given value. However, this is a conservative approach, and in the case of non-Gaussian noise, it underestimates the significance levels.

We ask now, specifically, how likely it is that a period of 161 days, by chance, will have a signal power above 1-σ, 2-σ and 3-σ significance levels. This is equivalent to a false-positive rate of 161 days period among 10,000 bootstrap trails. We run the simulation and keep the powers encountered at 161 days. Through this approach, the peak is found to have a significance above 4-σ level. We do not approach more sophisticated methods to estimate the false alarm rate as it is outside the scope of the paper, but we clearly show that the periodicity reported by Rajwade et al. (2020) is also seen in our dataset.

In the lower panel of Figure 7.5, we see the outcome of assigning a phase to each epoch by folding at a period of 161 days. The y-axis shows the length of each observation. We take MJD 57057 as reference for phase $\phi = 0$. From the outermost observations with detections, we infer an active window of 54%. However, we notice that while the end of the active window is densely sampled (by chance), the start of the active phase is not. Motivated by this, and in order to test how representative the Effelsberg dataset is, we add the published follow-up observations on FRB 121102 at L-band (1-2 GHz). The frequency constraint is driven by fact that simultaneous observations at radio frequencies greater than ∼GHz have mostly not led to simultaneous detections, suggesting that a given activity extends only over a couple of hundreds of Megahertz (Law et al., 2017). We extend the dataset by including the detections and non-detections reported by Spitler et al. (2014, 2016), Scholz et al. (2016, 2017), Gourdji et al. (2019) and Oostrum et al. (2020). We refer hereon to this dataset as the

L-band dataset.

The L-band dataset is composed of a total of 179 epochs from which 43 are detections and 136 non-detections. The Lomb-Scargle periodogram for this dataset infers a period of 158±3 days, which is consistent with the period deduced independently from the EFF dataset and with Rajwade et al. (2020). To define a more constraining active phase we proceed with the prediction of 161 days and fold the L-band epochs. By considering the left and right-most observations with detection in the L-band dataset we define an active phase of roughly 60%, which is shown in Figure 7.5 with the yellow-shadowed region. Based on the inferred periodicity of 161 days and the active phase of 60%, we construct the active windows. We use as reference for $\phi = 0$ the MJD 57075, and find that the epochs with detections fall into 5 activity windows: 57590-57687, 57751-57848, 57912-58009, 58395-58492 and 58717-58814.

We note that the width of the active phase is dependent on the selection of the period and on observations at the start and end of the on-phase. For periods between 156 days and 161 the active window ranges from 56% to 62%. It is worth noting that Rajwade et al. (2020) defined the period from dispersion minimization, i.e. choosing the period gives the narrowest possible active window. Naturally, more observations with detections outside of the limits defined here will broaden the active window.

7.4.3.2 Repetition pattern on active phase

In this section, we investigate the waiting time statistics between consecutive bursts on shorter time scales. Time independent Poissonian statistics as well as Weibull distribution with shape parameter $k < 1$ have been previously assumed. While $k < 1$ means that clustering is present in the data (the lower the k the higher the degree of clustering), when $k = 1$ the Poissonian case is recovered, and for $k >> 1$ we are in the presence of a constant separation, implying periodicity.

Oppermann et al. (2018) used a Weibull distribution with shape parameter k smaller than one using ∼80 hours of FRB 121102 follow-up data. In the analysis of Oppermann et al. (2018), the sample contained observations taken with Arecibo, Effelsberg, GBT, VLA, and Lovell at different observing frequencies ranging from 0.8 – 4.8 GHz. The 17 bursts contained in the data led to the conclusion that a Weibull distribution with a shape parameter of k=0.34 and a mean event rate of r=5.7 day^{-1}, is a much better descriptor for the time interval between consecutive events than Poissonian statistics. Recently, Oostrum et al. (2020) came to a similar conclusion using WSRT/Apertif data.

We would like to test whether this strong clustering observed was a consequence of the unknown periodicity of FRB 121102. However, in a different approach to the one carried in Oppermann et al. (2018) work, we do not combine bursts from different telescopes and observing frequencies, as their difference in sensitivity leads to different event rates, and this might bias the observed clustering. As mentioned in Section 7.4.3.1 our observations fall into 5 activity windows: MJD 57590-57687, 57751-57848, 57912-58009, 58395-58492 and 58717-58814. We group all the observations with and without detections falling into such windows to study the waiting time between consecutive bursts.

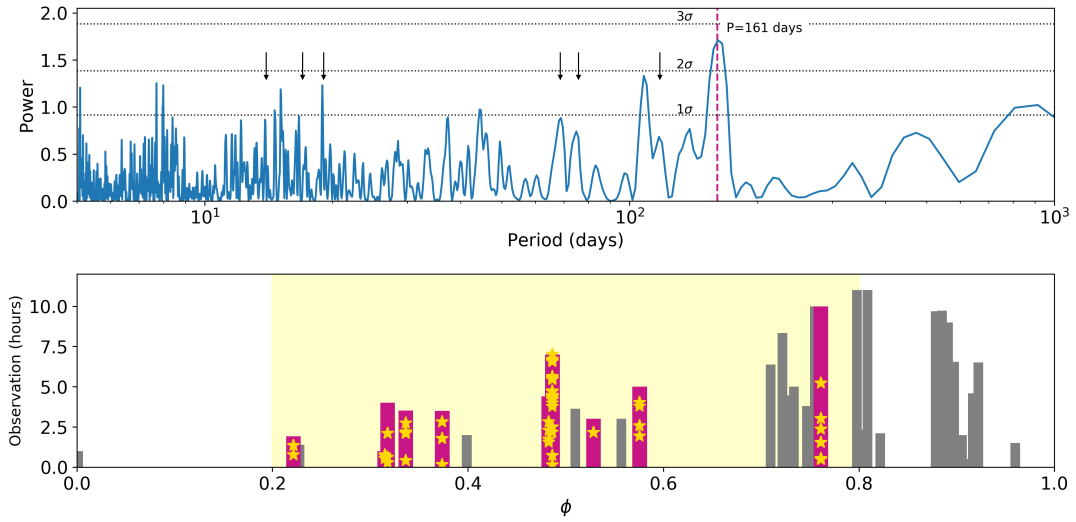

Figure 7.5: Periodicity analysis for FRB121102. Top: Lomb-Scargle periodogram for the Effelsberg dataset at 1.36 GHz composed of 34 epochs from September 2016 to June 2020. The vertical dashed line shows the best period prediction and the arrows show peaks coming from the window transform. The horizontal dotted lines show the 1-σ, 2-σ, and 3-σ significance levels deduced from 10,000 bootstrap resamplings. Bottom: phases of the observations based on a 161 days periodicity displayed against the length of its observation. In Magenta are highlighted the epochs with detections for which the yellow-*stars* indicate the time within a given observation where the bursts occurred. The bars in grey are the observations for which no bursts were detected, and the yellow-shaded region is the estimated active phase from the L-band dataset and referred to MJD 57075 as the epoch with phase $\phi = 0$.

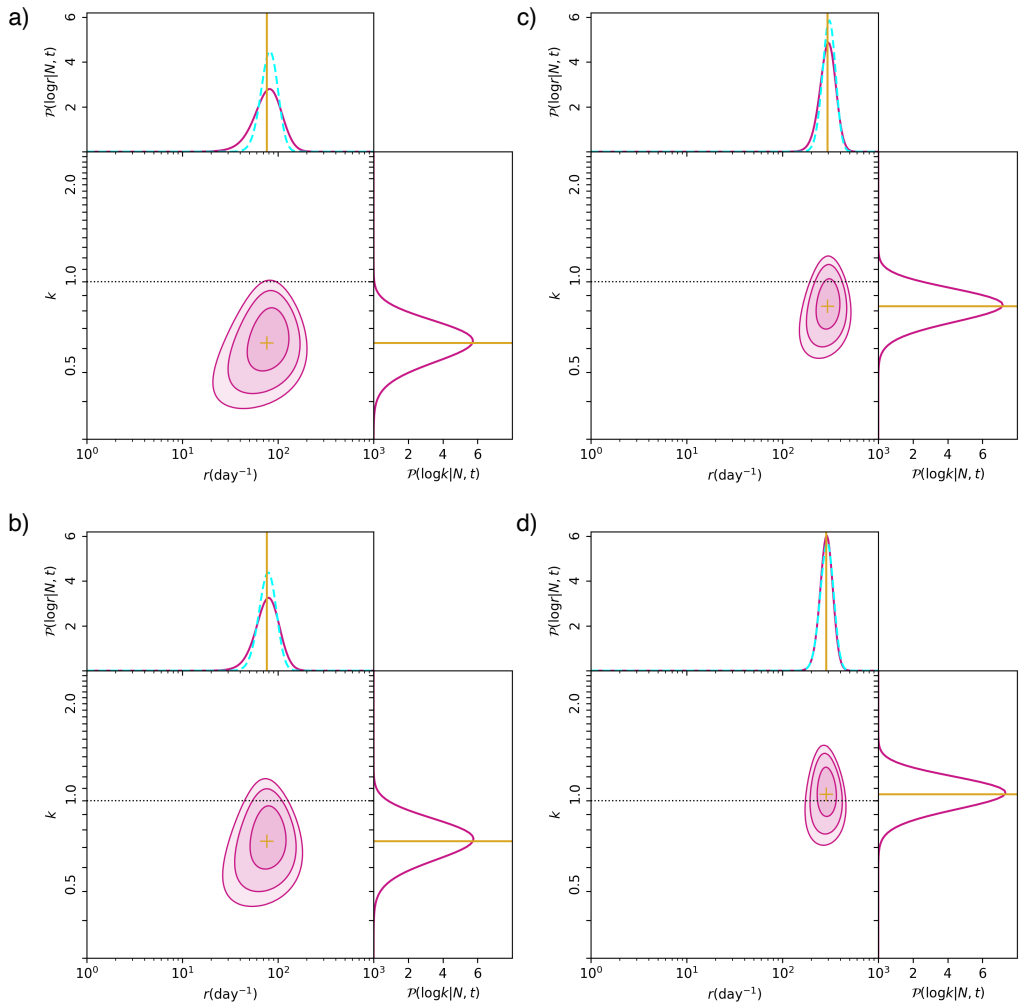

Figure 7.6: 2-dimensional posterior probability distribution for the shape parameter k and the event rate r for a Weibull distribution (magenta). The cyan-dashed curve represents the expectation for the event rate from a classic Poissonian distribution and the yellow lines indicate the mean values of the posterior distribution for k and r. The contours in the parameter space represent 65%, 95% and 99% confidence intervals, and the horizontal dotted-lines mark $k = 1$ for reference. Top: fit to all the events in November 2018 sample (panel a) and for Gourdji et al. (2019) in panel (c). Bottom: fit to November 2018 set (panel b) and Gourdji et al. (2019) (panel d) when excluding events with $\delta t < 1$ s respectively.

We use the two-dimensional posterior probability for k and r, and the one-dimensional marginal posterior for k and r formalism implemented by Oppermann et al. (2018)[7]. Our first approach is to treat each active window independently. However, this implicitly assumes that the event rate is constant across the full active phase. Clearly, this must not be the case, for instance, if the on-window has a Gaussian profile, which could lead to higher event rates at the center of the window. Nonetheless, except for the epoch of November 2018, we note that there are not sufficient bursts per active window to reduce the parameter space of the posterior probability to well-constrained values. This means that it cannot be differentiated between a Poisson and Weibull distribution. Because the November 2018 observation consists of a single 7-hour long session, we focus now on the statistics within a single, long observation.

The result for the November 2018 epoch is shown in Figure 7.6 (left) and the values for k and r presented in Table 7.6. The posterior distribution for all the bursts of November 2018 in panel a) Figure 7.6 shows that for a Weibull fit the shape parameter is $k = 0.62^{+0.1}_{-0.09}$ and the event rate is $r = 74^{+31}_{-22}$ day^{-1} (magenta curves in Figure 7.6). From a Poissonian distribution the average rate is $r_{\rm p} = 82 \pm 27$ day^{-1} (cyan curves in Figure 7.6). Both values report 1-σ intervals and consider a fluence threshold of 0.15 Jy ms for bursts of 1 ms duration which is imposed by Effelsberg's sensitivity to bursts with S/N > 7.

To perform an additional test on how well Poisson and Weibull distributions fit this set of bursts, we plot the empirical cumulative density function (ECDF) of the time interval between consecutive bursts (δt) in Figure 7.7. The cumulative density functions from Weibull ($P_{\rm w}$) and Poissonian ($P_{\rm p}$) statistics are described by (Oppermann et al., 2018):

$$P_{\rm w}\ (\delta t, k, r) = 1 - e^{-(\delta t\, r \Gamma(1+1/k))^k} \tag{7.4}$$

$$P_{\rm p}\ (\delta t, r_p) = 1 - e^{-\delta t\, r_p} \tag{7.5}$$

in the equations above r_p and r represents the event rates for Poissonian and Weibull case, respectively, k is the shape parameter and Γ is the incomplete gamma function. k and r are taken from the mean value of the two-dimensional posterior probability function.

Figure 7.7 shows the ECDF of the November 2018 dataset alongside the fit from the Weibull and Poisson models. Qualitatively, Weibull's CDF better describes the distribution. To quantify the fit we compute the Kolmogorov-Smirnov statistic (KS test) of the November 2018 sample versus its Weibull distribution fit and versus its Poisson distribution fit. We obtain a p-value of 0.84 and 0.12 for the Weibull and Poisson fit respectively, meaning that the null hypothesis – of the November sample drawn from a Weibull or Poisson distribution – cannot be rejected. Nonetheless, when considering as well the KS statistic we find that the absolute max distance between the ECDF of the sample and the CDF fits (equations 7.4 and 7.5) are 0.13 and 0.27 for the Weibull and Poisson fit respectively. Therefore, we conclude that for the full November 2018 sample the best fit is a Weibull distribution with $k = 0.62^{+0.1}_{-0.09}$ and the event rate of $r = 74^{+31}_{-22}$ day^{-1}. It is worth noting that the tail to the left of the ECDF

[7] https://github.com/nielsopp/frb_repetition

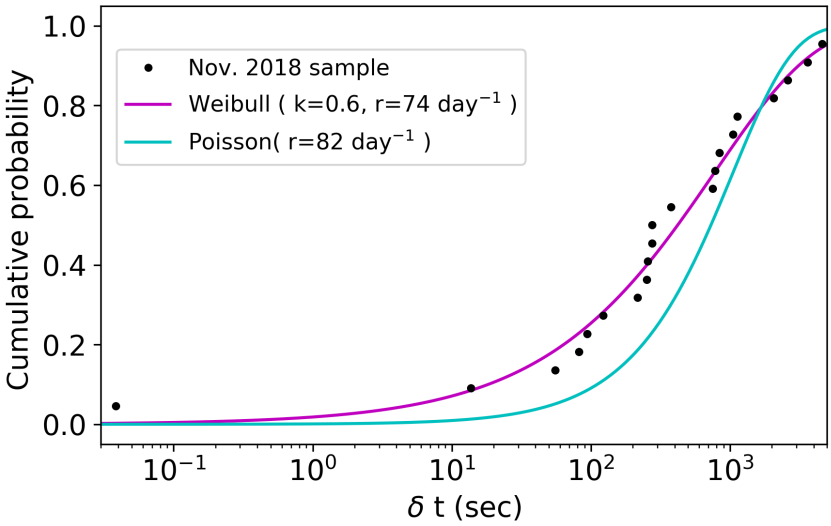

Figure 7.7: Empirical cumulative density function of the waiting time between consecutive bursts (δt) of FRB 121102 for the November 2018 dataset (bursts B8 to B31 in Table 7.4). The magenta and cyan color represent the best-fit from the Weibull and Poisson cumulative density functions, respectively.

in Figure 7.7 is fit by neither of the distributions. This single event corresponds to the separation of ∼38 ms between bursts B20 and B21, as previously discussed. From a Poisson distribution, the probability of having a waiting time of 38 milliseconds or shorter is 0.003%. We recall the previous discussion on B31 and its 39±2 ms duration, and the cluster behavior for bursts with waiting times shorter than 1 second observed by Li et al. (2019) and Gourdji et al. (2019). Therefore, we exclude events with $\delta\,t$ <1 s to explore whether this single wait time has a strong effect on the determination of the shape parameter for the Weibull distribution. We obtain $k' = 0.73^{+0.12}_{-0.10}$ and show in Figure 7.6 panel b the posterior distributions after excluding $\delta\,t$ <1 s. It is observed that removing a single wait time narrows the posterior distribution for the event rate and moves it closer to a Poissonian distribution.

To expand on this strong dependence of the shape parameter on a few clustered events, we additionally model independently the 41 bursts detected with Arecibo by Gourdji et al. (2019). We find $k = 0.82^{+0.1}_{-0.09}$ for the whole 41 bursts (panel c Figure 7.6) and $k' = 1.0^{+0.2}_{-0.1}$ for the resultant 39 bursts when excluding events with $\delta t < 1$ s (panel d Figure 7.6). For this dataset, the exclusion of 2 bursts results in a change to the Poissonian case. Interestingly the sub-set of bursts from our Effelsberg sample from Houben et al. (2019) includes two epochs separated by a couple of days before and after the Gourdji et al. (2019) detections. The posterior probability for Houben et al. (2019) subset gives a $k = 1.0^{+0.4}_{-0.2}$, which agrees with the k value that we obtained for Gourdji et al. (2019). We discuss the meaning of the exclusion of events with $\delta\,t < 1$ s

in Section 7.5.

7.4.3.3 Energy distribution

In this section, we study the isotropic energy distribution of the 57 bursts that compose the Effelsberg sample as it can provide insights on the mechanisms responsible for its emission generation. Some sources with accretion disks, such as X-ray binaries and AGNs show a log-normal relation in their flux distribution (Kunjaya et al., 2011), other sources, such as high-energy bursts of magnetars (Göğüş et al., 2000) and the X-ray flares from Sgr A* (Li et al., 2015), show a power-law in the form of $N \propto E^\gamma$, where N is the rate of events above a given energy value E. Interestingly, sources like pulsars show a bimodal relation: their regular emission is well modeled with a log-normal distribution (Burke-Spolaor et al., 2012), while giant pulses are modeled by a power-law distribution (Karuppusamy et al., 2010). Examples of sources exhibiting a power-law behaviour for their energy distribution are the Crab pulsar, whose giant pulses distribute with an index $\sim \gamma = -2$ (Popov & Stappers, 2007; Karuppusamy et al., 2010) and high energy bursts from magnetars with index γ =-0.6 – -0.7 (Göğüş et al., 1999, 2000).

Given its repeating nature, FRB 121102 allows us to study how its bursts distribute over a given energy range. This energy range is so far limited to radio frequencies. We compute the isotropic energy E for a given burst as:

$$E = \frac{1}{1+z} F(\mathrm{Jy\,s}) \times \Delta\nu(\mathrm{Hz}) \times 10^{-23} \mathrm{ergs^{-1}\,cm^{-2}Hz^{-1}} \times 4\pi\, L^2 \tag{7.6}$$

where z is the redshift, F is the fluence of the burst, $\Delta\nu$ is the bandwidth and L is the luminosity distance, whose value we take as 972 Mpc (Tendulkar et al., 2017). Figure 7.8 shows the cumulative energy distribution of all the bursts, which is calculated from the cumulative distribution of the mean burst rate. The plateau observed for energies below 10^{38} erg, is due to the reach of the completeness limit, i.e threshold where we are not sensitive enough and start missing events.

We fit a slope to the data using the Maximum-likelihood method for a power-law fit as described in James et al. (2019) and obtain a slope of $\gamma = -1.1 \pm 0.1$ when we exclude the bursts below the completeness level and above of the saturation. The saturation is caused by the down-conversion of the data from 32-bits to 8-bits.

We tested the saturation limit by analyzing single pulses from B0329+54, one of the brightest pulsars in the northern sky. We compared the SNR of the bursts in the raw 32-bit data and in the converted 8-bit data. We concluded that low-to-mid SNR bursts showed a nearly one-to-one relation, but as the S/N exceeds ∼80 the relation starts breaking leading to a drop in the SNR. We have determined the saturation limit to be affecting bursts above energies of 10^{39}ergs based on the expected energy of a burst with an SNR of 80 and FWHM of 5 ms (average duration from our sample).

On the lower end of the energy range, the completeness threshold has been defined based on the convergence of γ shown at the right of Figure 7.8. Each data point corresponds to the determination of γ from the inclusion of a successive burst. As

Table 7.6: Posterior values for the event rate (r) and shape parameter (k) from a Weibull Statistics and the event rate r_p from a Poissonian distribution. Prime values indicate the outcome of excluding bursts with waiting times shorter than 1 second ($\delta t < 1\,\mathrm{s}$). The event rates consider a fluence threshold 0.15 Jy ms for bursts with a 1 ms duration and S/N above 7, and the confidence intervals shown assume 1-σ uncertainties.

Dataset	r_p (day^{-1})	r (day^{-1})	k	r'_p (day^{-1})	r' (day^{-1})	k'
All	8 ± 3	7^{+3}_{-2}	$0.40^{+0.04}_{-0.03}$	8 ± 3	7^{+3}_{-2}	$0.43^{+0.04}_{-0.03}$
On-ϕ	18 ± 4	18^{+5}_{-4}	$0.50^{+0.05}_{-0.03}$	17 ± 4	17^{+5}_{-3}	$0.57^{+0.06}_{-0.04}$
November 2018	82 ± 9	74^{+31}_{-22}	$0.62^{+0.10}_{-0.09}$	79±9	76^{+26}_{-19}	$0.73^{+0.12}_{-0.10}$
Gourdji et al. (2019)	307±17	294^{+57}_{-52}	$0.82^{+0.12}_{-0.09}$	292±17	286^{+44}_{-44}	$1.0^{+0.2}_{-0.1}$
Houben et al. (2019)	20±4	18^{+8}_{-5}	$1.0^{+0.4}_{-0.2}$	-	-	-

the bursts are sorted from higher to lower energy the convergence of γ goes from the right to the left. We see in Figure 7.8, that if the last three bursts with energies below $10^{38}\mathrm{ergs}^{-1}$ are not considered, the slope of the power-law fit is truncated to $\gamma = -1.1 \pm 0.1$.

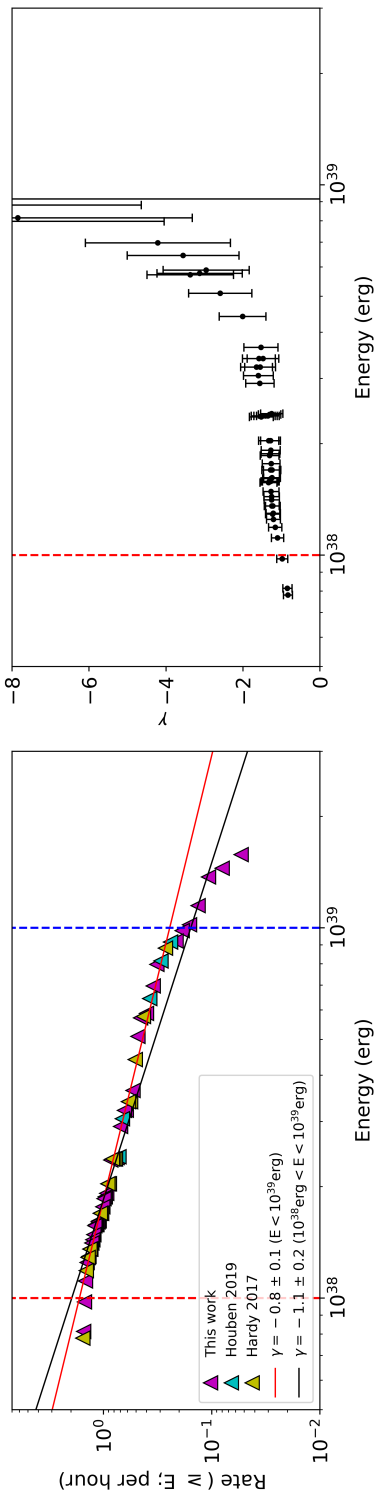

Figure 7.8: Left: cumulative energy distribution of the bursts from FRB 121102 detected by Effelsberg at 1.36 GHz, shown in magenta for the dataset presented in Table 7.4, in yellow for the detections from Hardy et al. (2017) and in cyan for Houben et al. (2019). The isotropic energy is calculated as described in equation (7.6) and the fit corresponds to a power-law of the form $N \propto E^{\gamma}$ estimated through maximum-likelihood. The red-dashed line shows the completeness limit for Effelsberg at $\sim$E$= 10^{38}$ erg and the blue-dashed line marks the bursts above the saturation limit roughly at E$= 10^{39}$ erg. Right: convergence of the power-law slope γ as determined from the Maximum-likelihood estimation. The red-dashed vertical line represents the truncated value by excluding bursts below the completeness limit.

7.5 Discussion

It is long known that detections of FRB 121102 are clustered in time. Much of this clustering likely reflected a not-yet-defined periodicity. Here we investigated whether there is still clustering within a single observation or active phase.

We defined active windows for FRB 121102 based on the 161 days period deduced from the 34 total epochs in the Effelsberg dataset but constrain the width of the active phase to be roughly 60% based on the 179 observations from the L-band band dataset. This mixed approach is motivated by the poor coverage of the phases prior to the start of the active phase as seen in Figure 7.5. This phenomenon is purely by chance as the observations were scheduled mostly based on telescope availability, which led to unevenly sampled epochs and different observation lengths. We use the MJD 57075 as a reference epoch and estimate the next active phase to be from MJD 59039 to 59136 followed by a period of inactivity until the next cycle from MJD 59200 to 59297. Our predicted active phase is shifted with respect to the prediction from Rajwade et al. (2020) by 37 days later, due to the difference in periodicity of 157 and 161 days predicted by Rajwade et al. (2020) and our work, as well as the estimated on-phase of 54% and roughly 60% respectively, and ultimately due to the difference in the reference epochs used of MJD 58200 in Rajwade et al. (2020) and MJD 57075 used by us. This is not surprising as the entire phase is not fully sampled by the existing observations. Besides observations during the predicted window, where chances to detect bursts are higher, we also recommend unbiased observations through the entire phase to better constrain the activity window.

Regarding the waiting time between consecutive bursts, we first consider all the Effelsberg data – composed of 165 hours of observations and 57 bursts – and ask how clustered the events are. From the two-dimensional posterior probability for k and r and the one-dimensional marginal posterior for k we obtain an event rate of $7^{+3}_{-1}\mathrm{day}^{-1}$ and $k{=}0.40^{0.04}_{0.03}$ for a Weibull distribution and a rate of 8 ± 3 day^{-1} from Poisson. On the other hand, if we acknowledge the presence of a periodic active phase and restrict the observations to the 5 active windows in which the Effelsberg data falls: MJD 57590-57687, 57751-57848, 57912-58009, 58395-58492, and 58717-58814 we determine $18^{+5}_{-4}\mathrm{day}^{-1}$ and $k{=}0.50^{0.05}_{0.03}$ for a Weibull distribution and a rate of 18 ± 4 day^{-1} from Poisson. For both datasets, we also calculate the values after excluding wait times with $\delta t < 1\,\mathrm{s}$. All values are listed in Table 7.6. The rates consider events above a fluence threshold of 0.15 Jy ms for bursts of 1 ms duration which is imposed by Effelsberg's sensitivity to bursts with S/N > 7.

However, the previous results for k and r when restricting the observations to the active window implicitly assume that the event rate is constant across all the active windows and across the full active phase, which may not be the case. If we restrict the analysis to each active window independently, we notice that November 2018 sample is the only one providing sufficient bursts in a single active window to reduce the parameter space of the posterior probability to well-constrained values. As the November 2018 sample is the only observation falling into the MJD 58395-58492 window, a possible change in the observed rate across the active window is not a

concern. Instead, we are exploring possible clustering on time scales of hours.

From the waiting times for the November 2018 sample shown in Figure 7.7, we see that the peak in δt is roughly at $\sim$200 seconds. This set of 24 bursts during a single continuous 7-hr observation (see Table 7.1) provides the most meaningful constraints out of the 13 observations from the Effelsberg dataset.

Something peculiar about this observation is that most of the bursts were detected in the second half of the observation. If the 7-hour session is split into two sections of 3.5 hours each, the inferred Poisson rates are 27 ± 5 day^{-1} and 137 ± 12 day^{-1} for the first and second half, respectively.

We explore first the possibility of an observational bias leading to the observed disparity. Possible reasons are a change in the sensitivity of the telescope during the session, with the sensitivity improving in the second half and more RFI during the first half. We note that the observation started at UTC 19:58:50 at nearly 30° in elevation, passed the zenith, and finished at 65° at UTC 02:58:50 on the next day.

As the observations were done at 1.4 GHz, there is no gain-elevation effect due to the deformation of the antenna. However, the system temperature, $T_{\rm sys}$, increases by roughly 5 K due to atmospheric effects (opacity $\tau = 0.01$) at an elevation of 30°. The system temperature measured at the zenith is 21 K. This change in $T_{\rm sys}$ leads to a decrease in the system equivalent flux density (SEFD) from 19.0 Jy at zenith to 15.4 Jy at 30°. This implies that a burst detected at zenith with an SNR of 8.5 could be easily missed as it would fall below detectability (SNR$<$7) at 30° elevation. We neglect bursts with SNR < 8.5 from the second half of the observation (B13, B15, and B29) and obtain a new Poissonian rate of 116 ± 11 day^{-1}, which still does not match the event rate of the first part of the observation at the 3-σ level.

Lastly, we check the influence of RFI. We inspect the mask files created by `rfifind` (Ransom, 2011) for each one-hour long scan, and conclude that there is no obvious change in the RFI situation during the session. Furthermore, the number of candidates generated during the first and the second part of the observation, and find 8873 and 15074 respectively, which is in agreement with the expectation of more RFI at the higher elevations. A change in the RFI situation during the observation does not explain the higher rate inferred in the second part. From these checks, we conclude that the higher rate toward the end of the observation in November 2018 is likely not an observational bias.

We continue to explore the event rate asymmetry beyond Poissonian statistics, and in particular, if the detections of November 2018 are better fit by a Weibull distribution with $k < 1$. As described in Section 7.4.3.2, the best fit from the two dimensional posterior distribution for k and r predicts $k = 0.62^{+0.10}_{-0.09}$, while if the one burst with $\delta t < 1$ s is excluded then $k' = 0.73^{+0.12}_{-0.10}$. This strong dependence on the estimation of k with few burst closely spaced is more evident with Gourdji et al. (2019) dataset, where the value shifts from $k = 0.82^{+0.1}_{-0.09}$ to $k' = 1.0^{+0.2}_{-0.1}$. In addition to the difference in the number of events included in the November 2018 and Gourdji et al. (2019) samples – 24 and 41 in total, respectively – the November observation was a single 7 hours long session, while the sample from Gourdji et al. (2019) comes from two sessions each of roughly 1.5 hours on consecutive days. Both observations are occurred at the center of

their respective on-phase windows, with the November 2018 events at roughly $\phi = 0.5$ (see Figure 7.5) and Gourdji et al. (2019) at $\phi = 0.55$. If we scale the Effelsberg event rate for November 2018 of 3.4 bursts/hr to AO's sensitivity we find a rate of 19 bursts/hr. The scaling considers the SEFDs described in Table 7.3 and the power low index of $\gamma = -1.1$ determined in Section 7.4.3.3. The scaled rate is in fair agreement with the rate of 14 burst/hr from Gourdji et al. (2019). Nonetheless, we cannot draw general conclusions on whether the center of the on-window leads to higher rates as we lack information on whether all the active windows have a similar activity behaviour.

Regarding the strong clustering reported by Oppermann et al. (2018) and recently by Oostrum et al. (2020), we infer this was likely a consequence of the unknown periodicity and on-phase. If the analysis is limited to the active windows, despite some indication for small clustering, it is less obvious that it indeed differs from the Poissonian case. It is interesting that the exclusion of one wait time from the November 2018 dataset and two from the Gourdji et al. (2019) dataset reduces considerably the parameter space of posterior probability for k and r as seen in the top and bottom panels in Figure 7.6, pre and post exclusion respectively. Particularly, the exclusion of two closely separated bursts from Gourdji et al. (2019) brings the distribution from a mildly clustered scenario to a distribution well described by Poisson statistics.

While excluding short waiting times allows us to investigate the change in k, their existence cannot be neglected. If the two distributions, with $\delta t < 1$ s, and δt of hundreds of seconds, are generated from different processes, the latter appears to be consistent with Poissonian process. Another possible explanation, as hinted by B31, is that events separated by a couple of tens of milliseconds are in reality the two strongest components of broad bursts. If this is the case, considering the November 2018 and Gourdji et al. (2019) sample we conclude that the waiting time is still consistent with a Poisson distribution. Telescopes such FAST and Arecibo are crucial to discern this matter.

If on the contrary, the events with $\delta t < 1$ s are indeed independent bursts generated from the same mechanism as the ones separated by tens-to-hundreds of seconds, such mechanism needs to account for the high energy generation needed on a couple of milliseconds timescale. A high number of bursts on a given on-window is the ideal scenario to test how clustered the events are. To this end, telescopes such as Arecibo and FAST are also key given their sensitivity.

We stress that the combination of detections with different instruments can be misleading as the different sensitivities influence the event rate. An interesting study is to compare datasets of different telescopes over the same active window, or for a given telescope to compare the repetition pattern at different active phases to explore whether the event rate is constant or rather higher at given phases, such as the center of the active window. From the phase plot in Figure 7.5 we see that the number of events seems to be higher towards the center of the active phase. However, given the few epochs with detections, this estimation might not be significant.

Regarding how the energy of the bursts from FRB121102 is distributed, Law et al. (2017) calculated a power-law slope of $\gamma = -0.6^{+0.2}_{-0.3}$ for nine bursts detected by the Very Large Array at 3 GHz. The bursts energies ranged from 3×10^{38} erg to 9.8×10^{39} erg. In contrast, Gourdji et al. (2019) came to a much steeper value of $\gamma = -1.8 \pm 0.3$ for

a set of 41 bursts detected with Arecibo at 1.4 GHz. These bursts have an inferred energy ranging from 2×10^{37} erg to $\sim 2 \times 10^{38}$ erg, therefore probing a lower energy regime. Recently, Oostrum et al. (2020) came to a value of -1.7±0.6 from 30 bursts detected with WSRT/Apertif with energies in the range of 7×10^{38} erg to 6×10^{39} erg.

We show in Figure 7.9 the previously reported values for γ in addition to our measurement (see Section 7.4). The y-axis errors in both panels represent the 1-σ uncertainties of γ. The x-axis bars denote the time span (left panel) and the energy range (right panel) of each dataset used for the gamma determination. Despite marginally agreeing if 3-σ intervals are considered, converging to $\gamma \sim -1$, it is worth investigating the potential reasons for the different values encountered.

First, there is a strong dependence of the γ value with the completeness limit used. Our measured value after rejecting the bursts below the completeness threshold and above the saturation limit is $\gamma = -1.1 \pm 0.2$. If the completeness threshold is not considered and the slope for all the bursts below the saturation limit is included, the slope flattens and becomes $\gamma = -0.8 \pm 0.1$. This is consistent with the $\gamma = -0.6^{+0.2}_{-0.3}$ reported by Law et al. (2017) and would misleadingly indicate a γ near to the expected values for magnetars. Gourdji et al. (2019) and Oostrum et al. (2020) took into consideration such threshold for Arecibo and WSRT/Apertif respectively when reporting γ. It would be interesting to explore whether γ changes for Law et al. (2017) dataset if the completeness limit is considered. Regarding a potential dependence on γ with time, as proposed by Oostrum et al. (2020), we see in Figure 7.9 that the bursts considered for the Effelsberg dataset span roughly 3 years. From Figure 7.8 we see that all the bursts from the dataset are well mixed and follow the same trend, with no indication for different γ with time.

The discrepancy of the values reported as of now challenge the universality of the power-law index for the cumulative energy distribution of the bursts and raises the question of whether we are in presence of a much more complex energy distribution (see right panel of Figure 7.9). Given that the energy range span of our dataset lies between the sample of low energy bursts of Gourdji et al. (2019) and the more energetic bursts reported by Law et al. (2017) and Oostrum et al. (2020), one possibility is that a single power-law does not well describe the data over many orders of magnitude. In the right side of Figure 7.9, if we exclude the value reported by Law et al. (2017) – where the completeness threshold was not considered – we see that the slope of the energy distribution is steep for energies near 10^{40}erg and 10^{38}erg, while being flatter in the intermediate energy range.

As the γ value estimated from VLA comes from bursts detected at 3 GHz - contrary to the sample from AO, WSRT, and Eff at roughly 1.4 GHz - it could be that there is a dependency arising from the observing frequency. Additionally, the sensitivity of the instrument can play a role. Lastly, it can be that the observed energy distribution does not completely trace an intrinsic mechanism, but rather affected by propagation effects and observational biases. For instance, while Gourdji et al. (2019) and Oostrum et al. (2020) bursts were coherently de-dispersed, the Law et al. 2017 and our Effelsberg sample are not. Perhaps not resolving the complex structure of some bursts leads to differences in the estimations of the widths of the bursts and therefore affecting their

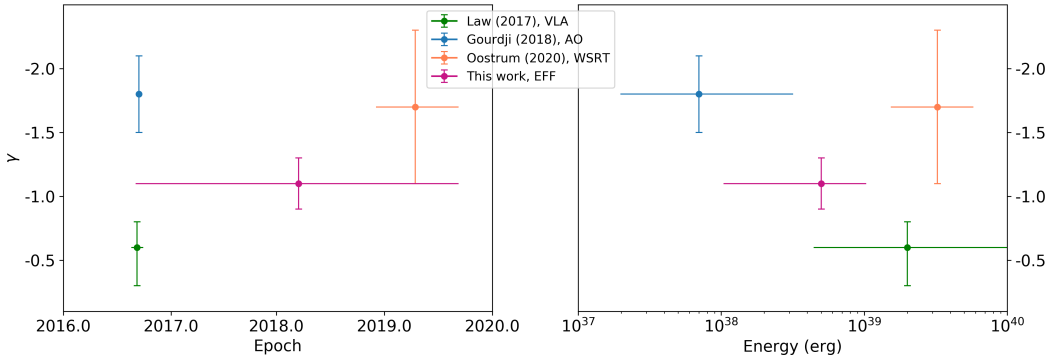

Figure 7.9: Measured values for the slope of the power-law (γ) fit to the cumulative energy distribution of bursts from FRB 121102 as a function of time (left) and energy range (right). In green, the value is shown for the 9 bursts detected with the VLA at 3 GHz (Law et al., 2017), in blue for 41 bursts detected with AO at 1.4 GHz (Gourdji et al., 2019), in orange for 30 bursts from WSRT at 1.4 GHz (Oostrum et al., 2020) and in magenta for the 57 bursts from Eff studied in this work. The error bars on the γ values indicate 1-σ uncertainties. The x-axis error bars indicate the time span of the dataset used to determine γ (left) and energy span of the dataset used to determine γ (right).

energy estimation.

We emphasize the importance of considering instrumental effects such as completeness and saturation limits, as well as the difference in sensitivities for the different telescopes when estimating the fit to the energy distribution of detected bursts.

7.6 Conclusion

We have carried out an extensive 128-hour campaign with Effelsberg on the first repeater ever detected, FRB 121102, from September 2017 to June 2020. Some epochs are part of a multi-wavelength campaign to shadow telescopes at higher frequencies such as NuSTAR, INTEGRAL, and GTC. In total Effelsberg observed for 128 hr., Green Bank telescope 26 hr. and the Arecibo observatory 3.7-hr. At the time of the NuSTAR session on 2017-09-06 one burst was detected with Effelsberg: B6 (see Figure 7.2) with flux of 1.56 ± 0.2 Jy ms. However, no X-ray photons were connected with such event. We placed upper limits on the energy of an X-ray burst counterpart to radio burst B6, which depends on the assumed spectral model (see Table 7.5). These limits are about an order of magnitude more constraining than those placed using *Chandra* and *XMM* by Scholz et al. (2017) for the case where X-ray emission is highly absorbed by material close to the source.

We combine our Effelsberg dataset with the published observations carried with identical setup by Hardy et al. (2017) and Houben et al. (2019). The extended sample

is composed of roughly 165 hours of observation from MJD 57635 to 59006 and consists of 34 epochs from which roughly 70% are non-detections. Given that the observations were mostly randomly scheduled and that the full set of detections and non-detections are known, we searched for an underlying periodicity through the Lomb-Scargle periodogram. We find a 161±5 days period and an active window of roughly 54%, which broadens to roughly 60% after considering published observations at L-band. These values agree with the finding of Rajwade et al. (2020) on the potential 157 days periodicity for FRB 121102.

We continue to investigate how the time interval for consecutive bursts is distributed within the active windows, and particularly whether a Weibull distribution with $k < 1$ (to allow clustering) describes the data better than the classic time-independent Poissonian statistics. To this end, we use the formalism implemented in Oppermann et al. (2018) over all the observations in the Effelsberg dataset lying within an active window. The November 2018 session is the only observation providing a reduced parameter space on the posterior probability for k and r, mainly due to the high event rate and observation length. We observe a mild clustering in the sample, however, we find that the Weibull fitting is highly biased towards few events with waiting times shorter than one second. We test this finding with Gourdji et al. (2019) dataset which contains a total of 41 bursts over 3.2 hours of observation. We conclude that if the few shortly spaced events are removed, then $k = 1$, meaning that the distribution is indistinguishable from a Poisson distribution. A bimodal distribution of the waiting time has been observed before by Li et al. (2019) and Gourdji et al. (2019) and could hint towards two mechanisms responsible for the events with $\delta t < 1\,\mathrm{s}$ of separation and the ones that are hundreds of seconds apart.

An alternative scenario is that the events that are tens of milliseconds apart correspond to the main components of broad bursts in which weak, intermediate components are not detectable. This hypothesis is supported by burst B31 detected in November 2018, which with an FWHM of 39±2 ms is the widest burst ever measured for this source. We conclude that the strong clustering observed by Oppermann et al. (2018) and Oostrum et al. (2020) was a consequence of the unknown periodicity for FRB 121102.

Finally, we study the cumulative energy distribution of the 57 bursts from the Effelsberg dataset. We fit a power law of the form $N \propto E^{\gamma}$ through maximum likelihood analysis and find a slope of $\gamma = -1.1 \pm 0.1$. This value lies between the $\gamma = -0.6^{+0.2}_{-0.3}$ reported by Law et al. (2017) and $\gamma = -1.8$ from Gourdji et al. (2019). Given the different energy regimes covered by the different studies, we suggest that a single power-law might not fit the data over many orders of magnitude or that the instrumental effects, such as completeness threshold and saturation, play an important role in its estimation. We find no indication for an epoch evolving γ as proposed by Oostrum et al. (2020), as the bursts from the Effelsberg dataset are well mixed and described by a single power-law over the roughly 3 years of the data span.

We finalize with key points to be considered after the results of this work:

1. Given the existence of broad bursts with durations of tens of milliseconds, it

is advised to future FRB searches to expand the parameter space of the burst widths to at least hundreds of milliseconds. For previously searched data, it is strongly encouraged to re-process the data.

2. When doing a periodogram search it is important to compute the window transform to discard fake periodicities introduced, for instance, by the observation cadence (see Section 7.4.3.1) or noise-level. In addition to reporting the uncertainty of the measured periodicity (see Equation 7.3) the false-alarm probability should be calculated as well. A conservative computational method is a bootstrap.

3. We stress the importance of reporting non-detections in follow-up campaigns for any FRB. The knowledge of the start, duration, and outcome of the observation helps to better constrain the statistics for FRBs such as an underlying periodic active window and probability for detections of events.

4. Instrumental effects such completeness limits, effects due to data conversion, and sensitivity should be taken into account when comparing energy distribution, event rates, waiting times, etc. across different telescopes.

Acknowledgements

We thank the referee for helpful and insightful comments that improved the quality of the manuscript. We thank Dr. R. Wharton, Dr. N. Porayko, and L. Houben for helpful discussions. This publication is based on observations with the 100-m telescope of the Max-Planck-Institut für Radioastronomie at Effelsberg. We thank Dr. A. Kraus for scheduling our observations. This publication has received funding from the European Union's Horizon 2020 research and innovation program under grant agreement No 730562 [RadioNet]. L.G.S. is a Lise Meitner independent research group leader and acknowledges funding from the Max Planck Society. J.W.T.H. acknowledges funding from an NWO Vici grant ("AstroFlash"). Partly based on observations with INTEGRAL, an ESA project with instruments and science data center funded by ESA member states. The Arecibo Observatory is a facility of the National Science Foundation operated under a cooperative agreement (#AST-1744119) by the University of Central Florida in alliance with Universidad Ana G. Méndez (UAGM) and Yang Enterprises (YEI), Inc.

Chapter 8

Discussion and future work

We have studied two classes of radio transient phenomena associated with NSs: pulsars and FBRs. FRBs were discovered while searching for pulsars in archival data. Although the progenitor of such fast millisecond duration radio flashes remains unknown, increasing observational evidence suggests (at least some) FRBs may also originate from NSs. In this thesis, I focused on the targeted radio searches of pulsars candidates from the FAST radio telescope and bursts from FRB 121102, and the understanding of their physical properties and evolution over a wide range of timescales. For pulsars, we studied in Chapter 5 their spin period – of a fraction of a second and more – and their orbital periods – tens of days. In Chapter 6 we simulated the long-term evolution of the spin period, temperature and magnetic field strength of pulsars over timescales of megayears up to gigayears. For FRBs, in Chapter 7 we studied their millisecond duration, a short-term – of the order of a couple of seconds – and long term periodicity – of the order of a few months. We also studied the clustering of the time of arrival of the bursts over timescales of hours. I finalize with a discussion of the main implications of this thesis in future searches of radio transients and the future work.

8.1 Searching for radio transients

8.1.1 The new era of pulsar surveys

With tens of time more sensitivity than any other radio telescope to date, the recently commissioned FAST and the coming SKA, are the most sensitive instrument to search for pulsars. They are expected to find thousands of new pulsars and to open a new parameter space for extremely accelerated binary systems and pulsars too dim to be seen in previous surveys. Following-up all the pulsar discoveries to obtain a timing solution – the key to extract the scientific potential of the discoveries – is hard (if not impossible) for a single telescope given the time span and cadence required. With the Effelsberg and Parkes monitoring of the pulsars discovered during FAST's commissioning phase, we have shown that complementing the surveys with smaller capabilities is key to reduce the observing load of the more sensitive radio telescope, thus, allowing more time to be spent on the search of new sources.

One of the main challenges of this collaborative approach is to pinpoint the pulsar's position using the smaller single-dish radio telescope. Large uncertainties are expected when the search is carried out in drift scan mode and/or with instruments with large fields of view. The reduced FoV of telescopes such as Effelsberg – due to the dish aperture and observing frequencies – require to perform a sky grid. Considering the

long integrations and several pointings needed to fully cover a sky region, the procedure is time-consuming. As we discussed in Chapter 5, using Effelsberg's 7-beam receiver to confirm a FAST candidate typically required 3 hours to pinpoint the position of a source to its beam size. Although this approach already optimized the required observing time when compared to single-beam receivers, it could be further reduced with the use of a *phased array feed* (PAF). PAFs are a type of multi-beam receivers in which the beam shapes and distribution are computer-controlled. They provide larger instantaneous FoV and precise localisations, meaning that one observation can be tuned to confirm and narrow-down the position of a pulsar. Effelsberg is currently commissioning its PAF receiver. Although the system temperature is higher in comparison with the 7-beam receiver (thus less sensitive) it is aimed to be a precursor for the cryogenically cooled PAF which is currently under development.

In the era of major radio telescopes such as FAST and SKA, smaller single-dish facilities still play an important role in confirming and monitoring part of the discoveries. Upgrading them with PAF receivers will be a game-changer due to the boost in their performance and sensitivity.

8.1.2 Monitoring of repeating FRBs

As discussed in Chapter 7, the different progenitor scenarios for FRBs predict counterparts at multiple wavelengths. For instance, the young magnetar embedded in a supernova remnant predicts an X-ray afterglow and optical emission from its supernova remnant. Multi-wavelength follow-up of repeating FRBs are key to constrain such progenitor scenarios. Because the detections are, as of now, limited to the radio frequency regime, the broadly used approach is to trigger observations at higher frequencies – such as optical and X-ray – based on activity reported in radio. Usually, the monitoring required tens of hours before a radio burst is detected at the time of simultaneous observations. This is changing with the recent discovery of periodic active phases for some FRBs, where the probability of detecting bursts are higher. However, when observing simultaneously with optical telescopes, the weather conditions (ex.: humidity and opacity) determines ultimately whether a simultaneous observation is feasible or not.

The extensive monitoring needed for single-dish radio telescopes during a multi-wavelength campaign can be mitigated with the use of PAF receivers, where beams can be arranged to observe several targets simultaneously.

Triggering multi-wavelength observations also relies on the rapid processing of radio data. For Effelsberg, the semi-real-time data processing needs significant manual intervention. However, as the number of telescopes equipped with real-time FRB searches increases, we can expect that future upgrades to Effelsberg will include a fully automated process.

8.2 Future work

8.2.1 Effelsberg follow-up of FAST discoveries

The FAST-EFF mildly recycled pulsar, PSR J2338+4818 is of particular interest given the estimated minimum mass for the CO-WD companion. This places the system as the widest binary with the most massive WD companion. Extending the timing solution of PSR J2338+4818 and improving the accuracy might allow Shapiro delay to be measured and thus the precise masses of the system. We continue the FAST and Effelsberg monitoring of PSR J2338+4818 intending to achieve such timing solution and to discern whether the frequent non-detections of the pulsar are due to long-term nulling or diffractive scintillation.

Regarding the ongoing drift-scan survey with FAST, Effelsberg has been key to the confirmation and follow-up of the discoveries. The quickly growing number of candidates require more facilities to monitor the discoveries due to limited cadence on sources due to FAST being a transit instrument – important for short-period binaries. In May 2018, FAST was upgraded with a 19-beam receiver with a gain of 18.2 K/Jy at L-band. By now, it has led to the discovery of another 100 good pulsar candidates. Effelsberg has confirmed another five pulsar candidates, among which we find two normal pulsars and three millisecond pulsars with spin periods of 21.2 ms, 4.59 ms and 3.39 ms. The first is in a close binary with an orbital period of 15.5 hours. The regular monitoring to achieve a timing solution is in progress. The new pulsars can be used to map the free electron content of the Galaxy, the most stable millisecond pulsars to be included in pulsar timing arrays to detect gravitational waves, and the pulsars in close binaries to test theories of gravity; to name just a few science cases.

Since the start of the FAST-Effelsberg collaboration, the projects have been continuously growing. For FRB searches, the 19-beam receiver and the boost in telescope sensitivity to bursts with fluences as low as 0.03 Jy ms, has led to five repeating FRB candidates that are visible to Effelsberg. We have begun the follow-up of such FRBs using Effelsberg as part of an interferometric array with the *European VLBI Network* (EVN) and using Effelsberg as a stand-alone instrument. While one of them is confirmed to be a repeating FRB, the remaining four have spectral components similar to repeating FRBs. Particularly, FRB 181123 has a complex multi-peak profile and down-drifting pattern resembling repeating FRBs such as FRB 121102. The work was published in Zhu et al. (2020). Although, as of now, no event has been detected with Effelsberg, the monitoring is ongoing. While a detection with EVN can lead to an accurate location of the FRB, bursts detected with Effelsberg alone can provide constraints on the event rate, energy distribution and their polarimetric properties.

8.2.2 $P - \dot{P}$ evolution of pulsars

The code developed to track the coupled evolution of the magnetic field strength, the temperature and spin rotation of NSs can be applied to understand the evolution in the $P - \dot{P}$ of the FAST-EFF pulsars. Figure 8.1 shows preliminary results of their expected evolutionary paths assuming a dipolar magnetic field configuration evolving

through ambipolar diffusion (see Chapter 6). For PSRs J1502+4653, J1942+3941 and J2129+4119 and PSRs J1822+2617, J2006+4058 and J0402+4825 one path is drawn for each set, as they are expected to have a very similar evolution. Interestingly, PSR J1822+2617 is expected to be a younger version of J2006+4058 and J0402+4825, as they are further below the track. For all the FAST-EFF pulsars it was considered a generic initial spin period of 15 ms and initial magnetic field strength in such a way to reproduce the observed spin-periods.

PSR J2338+4818 is once more of particular interest as it corresponds to the population of mildly recycled pulsars in long period binaries where no significant B-field decay appeared to have occurred. Such systems challenge the scenario of magnetic field decay before the accretion process as the old WD companion hints towards sufficiently long-timescales for B-field decay. However, as we see in Figure 8.1, PSR J2338+4818 is well explained by the model if a pulsar born with a low B-field strength of 5×10^{11} G is considered. Provided constraints on the mass of the CO white dwarf companion (through Shapiro delay), the time available for the magnetic field decay can be further restricted.

Given FAST sensitivity and the indications it is finding an older population of pulsars, it can be speculated that more systems like PSR J2338+4818 will be found; thus, helping to understand the long-standing question of whether the magnetic field of pulsars decay as a result of age or due to an accretion process. It is emphasised that the evolutionary paths are preliminary results, aimed to explore whether ambipolar diffusion is a viable mechanism to explain the location in the $P - \dot{P}$ diagram of the FAST-EFF pulsars. Further investigation is required to explore the suitable initial parameters and to restrict the time available for evolution. While for binary systems the companion type leads to an estimate of such timescale, for isolated pulsars the estimation comes from the characteristic age.

Additional application of the model regards FRBs. It has been suggested that FRBs can be created from giant magnetic flares of a magnetar driven by ambipolar diffusion in the NS core. By changing accordingly the initial conditions to a magnetar scenario (stronger magnetic fields and higher initial temperatures), we can track the magnetic field evolution and energy budget on short timescales.

The MRT simulation will be improved to include a continuous mapping of the parameter space of the initial conditions, rather than a specific set of parameters.

8.2.3 Repeating Fast radio bursts

The monitoring of FRB 121102 with Effelsberg continues. Additional data – detections and non-detections – will increase the accuracy of the periodicity and will further constrain the active phase. With detections over a given activity window, it can be investigated whether the event rate is constant across an active phase, or higher at particular phases. With a larger burst sample, we can better constrain the clustering of the events and disentangle whether they follow a Poisson or Weibull distribution.

An additional monitored repeating FRB is FRB 180916.J0158+65. We followed a similar approach to the simultaneous X-ray and radio Observations of FRB 121102

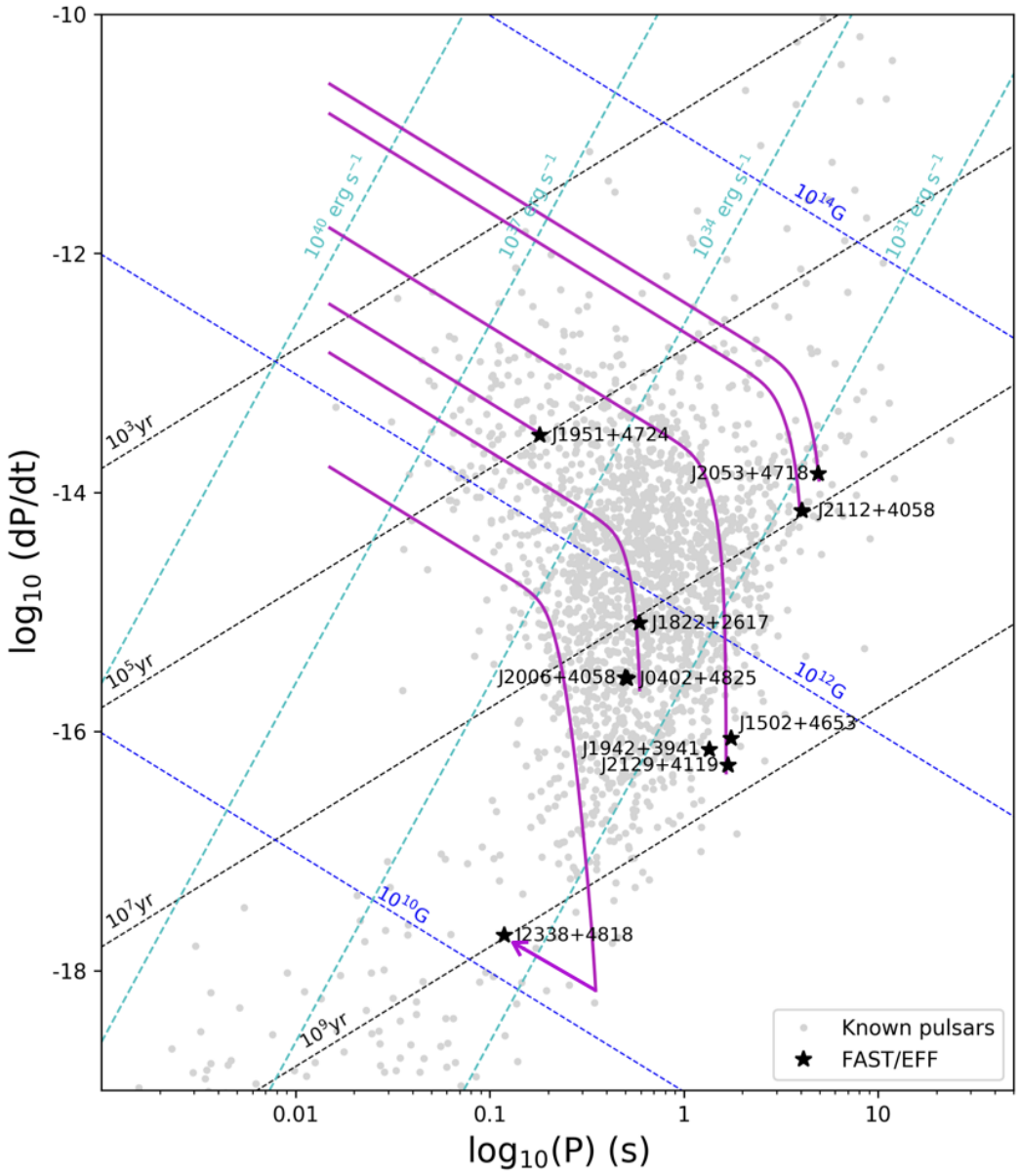

Figure 8.1: A $P-\dot{P}$ diagram. Known pulsars are shown with *grey dots*, while the FAST-EFF discoveries reported in Chapter 5 are plotted with *filled-black stars*. The *magenta curves* show their proposed evolutionary path following a magnetic field decay driven by ambipolar diffusion (see Chapter 6). For PSR J2338+4818 the arrow indicates the direction followed after the magnetic field decay, as the pulsar is spun-up by accretion. Alongside are drawn lines of constant magnetic field strength (*dark-blue dashed lines*), lines of constant spin-down age (*black dashed lines*) and lines of constant rotational energy loss (*cyan dashed lines*) as derived from the rotating dipole model.

using Effelsberg. Additional radio facilities were CHIME and Deep Space Network radio telescopes. No bursts were detected in overlapping Effelsberg-Chandra observations. However, a single radio burst was detected with CHIME during simultaneous Chandra observations. No X-ray event was associated with such event, thus placing a 5-σ upper limit of $< 1.6 \times 10^{45}$ erg on the 0.5–10 keV energy of an X-ray burst counterpart. The results were published in Scholz et al. (2020).

8.3 Closing remarks

As new major radio facilities come into play, the future of pulsar and FRB science looks bright. From the thousands of new radio transients expected to be found, we may speculate that new classes of neutron stars will be discovered, as well as exciting new systems such as double pulsar systems and the long-awaited pulsar-black-hole binary. These relativistic systems could provide superb natural laboratories to further test theories of gravity in the strong-field regime.

For FRBs, with more sources and localizations, we may soon disentangle the mystery of their progenitor source.

Nevertheless, innovation comes at a cost. In the new era of radio astronomy, the major challenges will be handling the huge data rates and mitigating the strong effect of radio frequency interference. Certainly, part of the automation will be based on machine learning techniques to identify the astrophysical signals among the millions of terrestrial candidates.

Bibliography

Abbate F., Bailes M., Buchner S. J., Camilo F., Freire P. C. C., Geyer M., Jameson A., Kramer M., Possenti A., Ridolfi A., Serylak M., Spiewak R., Stappers B. W., Venkatraman Krishnan V., 2020, MNRAS, 498, 875 (Cited on page 28.)

Abbott B. P., Abbott R., Abbott T. D., LIGO Scientific Collaboration Virgo Collaboration 2017, Phys. Rev. Lett., 119, 161101 (Cited on page 86.)

Abdo A. A., Ackermann M., Ajello M., Anderson B., Atwood W. B., Axelsson M., Baldini L., Ballet J., Barbiellini G., Baring M. G., Bastieri D., Baughman B. M., Bechtol K., Bellazzini R., Berenji B., Bignami G. F., Blandford R. D., Bloom E. D., Bonamente E., Borgland A. W., Bregeon J., Brez A., Brigida M., Bruel P., Burnett T. H., Caliandro G. A., Cameron R. A., Caraveo P. A., Casandjian J. M., Cecchi C., Çelik Ö., Chekhtman A., Fermi LAT Collaboration 2009, Science, 325, 840 (Cited on page 52.)

Alexander D. M., Hickox R. C., 2012, New A Rev., 56, 93 (Cited on page 3.)

Alpar M. A., Cheng A. F., Ruderman M. A., Shaham J., 1982, Nature, 300, 728 (Cited on pages 19 and 120.)

Alpar M. A., Pines D., Anderson P. W., Shaham J., 1984, ApJ, 276, 325 (Cited on page 123.)

Alpar M. A., Sauls J. A., 1988, ApJ, 327, 723 (Cited on page 6.)

Anderson P. W., Itoh N., 1975, Nature, 256, 25 (Cited on page 19.)

Antoniadis J., Freire P. C. C., Wex N., Tauris T. M., Lynch R. S., van Kerkwijk M. H., Kramer M., Bassa C., Dhillon V. S., Driebe T., Hessels J. W. T., Kaspi V. M., Kondratiev V. I., Langer N., Marsh T. R., McLaughlin M. A., Pennucci T. T., Ransom S. M., Stairs I. H., van Leeuwen J., Verbiest J. P. W., Whelan D. G., 2013, Science, 340, 448 (Cited on pages 6 and 23.)

Arponen J., 1972, Nucl. Phys. A, 191, 257 (Cited on page 6.)

Arzoumanian Z., Baker P. T., Blumer H., Becsy B., Brazier A., Brook P. R., Burke-Spolaor S., Chatterjee S., Chen S., Cordes J. M., Cornish N. J., Crawford F., Cromartie H. T., DeCesar M. E., Demorest P. B., Dolch T., Ellis J. A., Ferrara E. C., Fiore W., Fonseca E., Garver-Daniels N., Gentile P. A., Good D. C., Hazboun J. S., Holgado A. M., Islo K., Jennings R. J., Jones M. L., Kaiser A. R., Kaplan D. L., Kelley L. Z., Shapiro Key J., Laal N., Lam M. T., Lazio T. J. W., Lorimer D. R., Luo J., ... 2020, arXiv e-prints, p. arXiv:2009.04496 (Cited on page 22.)

Baade W., Zwicky F., 1934, Proceedings of the National Academy of Science, 20, 254 (Cited on pages 4 and 6.)

Backer D. C., 1970, Nature, 228, 42 (Cited on page 19.)

Bagchi M., 2017, ApJ, 838, L16 (Cited on pages 27 and 140.)

Bahramian A., Heinke C. O., Sivakoff G. R., Gladstone J. C., 2013, ApJ, 766, 136 (Cited on page 51.)

Bailes M., Possenti A., Johnston S., Kramer M., Burgay M., Bhat R., Keith M., Burke-Spolaor S., van Straten W., Stappers B., Bates S., , 2008, The High Time Resolution Universe, ATNF Proposal (Cited on page 115.)

Bannister K. W., Deller A. T., Phillips C., Macquart J.-P., Prochaska J. X., Tejos N., Ryder S. D., Sadler E. M., Shannon R. M., Simha S., Day C. K., McQuinn M., North-Hickey F. O., Bhandari S., Arcus W. R., Bennert V. N., Burchett J., Bouwhuis M., Dodson R., Ekers R. D., Farah W., Flynn C., James C. W., Kerr M., Lenc E., Mahony E. K., ... 2019, Science (Cited on page 140.)

Barr E. D., Champion D. J., Kramer M., Eatough R. P., Freire P. C. C., Karuppusamy R., Lee K. J., Verbiest J. P. W., Bassa C. G., Lyne A. G., Stappers B., Lorimer D. R., Klein B., 2013, MNRAS, 435, 2234 (Cited on pages 5, 44, 63, 89, 142 and 145.)

Barrau A., Rovelli C., Vidotto F., 2014, Phys. Rev. D, 90, 127503 (Cited on page 26.)

Bassa C. G., Janssen G. H., Karuppusamy R., Kramer M., Lee K. J., Liu K., McKee J., Perrodin D., Purver M., Sanidas S., Smits R., Stappers B. W., 2016, MNRAS, 456, 2196 (Cited on page 43.)

Bates S. D., Lorimer D. R., Verbiest J. P. W., 2013, MNRAS, 431, 1352 (Cited on page 89.)

Baym G., Pethick C., Pines D., 1969, Nature, 224, 673 (Cited on page 121.)

Beloborodov A. M., Li X., 2016, ApJ, 833, 261 (Cited on page 26.)

Bera A., Chengalur J. N., 2019, MNRAS, 490, L12 (Cited on page 141.)

Bhandari S., Keane E. F., Barr E. D., Jameson A., Petroff E., Johnston S., Bailes M., Bhat N. D. R., Burgay M., Burke-Spolaor S., Caleb M., Eatough R. P., Flynn C., Green J. A., Jankowski F., Kramer M., Krishnan V. V., Morello V., Possenti A., Stappers B., Tiburzi C., van Straten W., Andreoni I., Butterley T. ., 2018, MNRAS, 475, 1427 (Cited on page 27.)

Bhandari S., Sadler E. M., Prochaska J. X., Simha S., Ryder S. D., Marnoch L., Bannister K. W., Macquart J.-P., Flynn C., Shannon R. M., Tejos N., Corro-Guerra F., Day C. K., Deller A. T., Ekers R., Lopez S., Mahony E. K., Nuñez C., Phillips C., 2020, ApJ, 895, L37 (Cited on page 141.)

Bhattacharya D., 2011, in Göğüş E., Belloni T., Ertan Ü., eds, American Institute of Physics Conference Series Vol. 1379 of American Institute of Physics Conference Series, Evolutionary processes in Neutron Star Binaries. pp 31–34 (Cited on page 120.)

Bhattacharya D., van den Heuvel E. P. J., 1991a, Phys. Rep., 203, 1 (Cited on pages 19 and 120.)

Bhattacharya D., van den Heuvel E. P. J., 1991b, Phys. Rep., 203, 1 (Cited on page 106.)

Bhattacharya D., Wijers R. A. M. J., Hartman J. W., Verbunt F., 1992, A&A, 254, 198 (Cited on pages 18, 93 and 110.)

Bisnovatyi-Kogan G. S., Komberg B. V., 1974a, Soviet Ast., 18, 217 (Cited on page 106.)

Bisnovatyi-Kogan G. S., Komberg B. V., 1974b, Soviet Ast., 18, 217 (Cited on page 120.)

Bochenek C. D., Ravi V., Belov K. V., Hallinan G., Kocz J., Kulkarni S. R., McKenna D. L., 2020, arXiv e-prints, p. arXiv:2005.10828 (Cited on page 27.)

Bogdanov S., Guillot S., Ray P. S., Wolff M. T., Chakrabarty D., Ho W. C. G., Kerr M., Lamb F. K., Lommen A., Ludlam R. M., Milburn R., Montano S., Miller M. C., Bauböck M., Özel F., Psaltis D., Remillard R. A., Riley T. E., Steiner J. F., Strohmayer T. E., Watts A. L., Wood K. S., Zeldes J., Enoto T., Okajima T., Kellogg J. W., Baker C., Markwardt C. B., Arzoumanian Z., Gendreau K. C., 2019, ApJ, 887, L25 (Cited on page 22.)

Bonetti L., Ellis J., Mavromatos N. E., Sakharov A. S., Sarkisyan-Grinbaum E. K., Spallicci A. D. A. M., 2017, Physics Letters B, 768, 326 (Cited on page 29.)

Bourgois G., Guélin M., Quang Rieu N., 1969, Nature, 222, 963 (Cited on page 5.)

Brentjens M. A., de Bruyn A. G., 2005, A&A, 441, 1217 (Cited on page 92.)

Burgio G. F., Schulze H. J., Weber F., 2003, A&A, 408, 675 (Cited on page 6.)

Burke-Spolaor S., Bannister K. W., 2014, ApJ, 792, 19 (Cited on page 24.)

Burke-Spolaor S., Johnston S., Bailes M., Bates S. D., Bhat N. D. R., Burgay M., Champion D. J., D'Amico N., Keith M. J., Kramer M., Levin L., Milia S., Possenti A., Stappers B., van Straten W., 2012, MNRAS, 423, 1351 (Cited on page 162.)

Caleb M., Stappers B. W., Abbott T. D., Barr E. D., Bezuidenhout M. C., Buchner S. J., Burgay M., Chen W., Cognard I., Driessen L. N., Fender R., Hilmarsson G. H., Hoang J., Horn D. M., Jankowski F., Kramer M., Lorimer D. R., Malenta M., Morello V., Pilia M., Platts E., Possenti A., Rajwade K. M., Ridolfi A., Rhodes L., Sanidas S., Serylak M., Spitler L. G., Townsend L. J., Weltman A., Woudt P. A., Wu J., 2020, arXiv e-prints, p. arXiv:2006.08662 (Cited on page 149.)

Cameron A. D., Barr E. D., Champion D. J., Kramer M., Zhu W. W., 2017, MNRAS, 468, 1994 (Cited on page 56.)

Cameron A. D., Champion D. J., Kramer M., Bailes M., Barr E. D., Bassa C. G., Bhandari S., Bhat N. D. R., Burgay M., Burke-Spolaor S., Eatough R. P., Flynn C. M. L., Freire P. C. C., Jameson A., Johnston S., Karuppusamy R., Keith M. J., Levin L., Lorimer D. R., Lyne A. G., McLaughlin M. A., Ng C., Petroff E., Possenti A., Ridolfi A., Stappers B. W., van Straten W., Tauris T. M., Tiburzi C., Wex N., 2018, MNRAS, 475, L57 (Cited on page 21.)

Cameron A. D., Li D., Hobbs G., Zhang L., Miao C. C., Wang J. B., Yuan M., Wang S., Jacobs Corban G., Cruces M., Dai S., Feng Y., Han J., Kaczmarek J. F., Niu J. R., Pan Z. C., Qian L., Tao Z. Z., Wang P., Wang S. Q., Xu H., Xu R. X., Yue Y. L., Zhang S. B., Zhi Q. J., Zhu W. W., Champion D. J., Kramer M., Zhou S. Q., Qiu K. P., Zhu M., 2020, MNRAS, 495, 3515 (Cited on pages 86, 88, 93, 94, 115 and 116.)

Camilo F., Ransom S. M., Halpern J. P., Reynolds J., 2007, ApJ, 666, L93 (Cited on page 20.)

Camilo F., Ransom S. M., Halpern J. P., Reynolds J., Helfand D. J., Zimmerman N., Sarkissian J., 2006, Nature, 442, 892 (Cited on pages 5 and 20.)

Castillo F., Reisenegger A., Valdivia J. A., 2017, MNRAS, 471, 507 (Cited on pages 124, 134 and 135.)

Champion D. J., Petroff E., Kramer M., Keith M. J., Bailes M., Barr E. D., Bates S. D., Bhat N. D. R., Burgay M., Burke-Spolaor S., Flynn C. M. L., Jameson A., Johnston S., Ng C., Levin L., Possenti A., Stappers B. W., van Straten W., Thornton D., Tiburzi C., Lyne A. G., 2016, MNRAS, 460, L30 (Cited on pages 24 and 27.)

Chatterjee S., Law C. J., Wharton R. S., Burke-Spolaor S., Hessels J. W. T., Bower G. C., Cordes J. M., Tendulkar S. P., Bassa C. G., Demorest P., Butler B. J., Seymour A., Scholz P., Abruzzo M. W., Bogdanov S., Kaspi V. M., Keimpema A., Lazio T. J. W., Marcote B., McLaughlin M. A., Paragi Z., Ransom S. M., Rupen M., Spitler L. G., van Langevelde H. J., 2017, Nature, 541, 58 (Cited on pages 5, 25, 140, 142 and 147.)

Chawla P., Andersen B. C., Bhardwaj M., Fonseca E., Josephy A., Kaspi V. M., Michilli D., Pleunis Z., Bandura K. M., Bassa C. G., Boyle P. J., Brar C., Cassanelli T., Cubranic D., Dobbs M., Dong F. Q., Gaensler B. M., Good D. C., Hessels J. W. T., Landecker T. L., Leung C., Li D. Z., Lin H.-. H., Masui K., Mckinven R., Mena-Parra J., Merryfield M., Meyers B. W., Naidu A., Ng C., Patel C., Rafiei-Ravandi M., Rahman M., Sanghavi P., Scholz P., Shin K., Smith K. M., Stairs I. H., Tendulkar S. P., Vanderlinde K., 2020, The Astrophysical Journal, 896, L41 (Cited on pages 27 and 140.)

Chen K., Ruderman M., 1993, ApJ, 402, 264 (Cited on pages 93 and 110.)

CHIME/FRB Collaboration Andersen B. C., Bandura K., Bhardwaj M., Boubel P., Boyce M. M., Boyle P. J., Brar C., Cassanelli T., Chawla P., Cubranic D., Deng M.,

Dobbs M., Fandino M., Fonseca E., Gaensler B. M., Gilbert A. J., Giri U., Good D. C., Halpern M., Hill A. S., Hinshaw G., Höfer C., Josephy A., Kaspi V. M., Kothes R., 2019, ApJ, 885, L24 (Cited on pages 24 and 25.)

Connor L., Miller M. C., Gardenier D. W., 2020, MNRAS, 497, 3076 (Cited on page 28.)

Cordes J. M., 2002, in Stanimirovic S., Altschuler D., Goldsmith P., Salter C., eds, Single-Dish Radio Astronomy: Techniques and Applications Vol. 278 of Astronomical Society of the Pacific Conference Series, Pulsar Observations I. – Propagation Effects, Searching Distance Estimates, Scintillations and VLBI. pp 227–250 (Cited on page 11.)

Cordes J. M., Freire P. C. C., Lorimer D. R., Camilo F., Champion D. J., Nice D. J., Ramachand ran R., Hessels J. W. T., Vlemmings W., van Leeuwen J., Ransom S. M., Bhat N. D. R., Arzoumanian Z., McLaughlin M. A., Kaspi V. M., Kasian L., Deneva J. S., Reid B., Chatterjee S., Han J. L., Backer D. C., Stairs I. H., Deshpand e A. A., Faucher-Giguère C. A., 2006, ApJ, 637, 446 (Cited on page 5.)

Cordes J. M., Lazio T. J. W., 2002, arXiv e-prints, pp astro–ph/0207156 (Cited on pages 13, 51, 86 and 94.)

Cordes J. M., Wasserman I., 2016, MNRAS, 457, 232 (Cited on page 140.)

Cordes J. M., Wasserman I., Hessels J. W. T., Lazio T. J. W., Chatterjee S., Wharton R. S., 2017, ApJ, 842, 35 (Cited on page 27.)

Counselman Charles C. I., Shapiro I. I., 1968, Science, 162, 352 (Cited on page 5.)

Craft H. D., Sutton J. M., Comella J. M., 1968, Nature, 219, 1237 (Cited on page 5.)

Cromartie H. T., Fonseca E., Ransom S. M., Demorest P. B., Arzoumanian Z., Blumer H., Brook P. R., DeCesar M. E., Dolch T., Ellis J. A., Ferdman R. D., Ferrara E. C., Garver-Daniels N., Gentile P. A., Jones M. L., Lam M. T., Lorimer D. R., Lynch R. S., McLaughlin M. A., Ng C., Nice D. J., Pennucci T. T., Spiewak R., Stairs I. H., Stovall K., Swiggum J. K., Zhu W. W., 2020, Nature Astronomy, 4, 72 (Cited on page 23.)

Cruces M., Reisenegger A., Tauris T. M., 2019, MNRAS, 490, 2013 (Cited on page 106.)

Cruces M., Spitler L. G., Scholz P., Lynch R., Seymour A., Hessels J. W. T., Gouiffès C., Hilmarsson G. H., Kramer M., Munjal S., 2020, arXiv e-prints, p. arXiv:2008.03461 (Cited on page 89.)

Cumming A., Arras P., Zweibel E., 2004, ApJ, 609, 999 (Cited on page 122.)

Dai S., Johnston S., Bell M. E., Coles W. A., Hobbs G., Ekers R. D., Lenc E., 2016, MNRAS, 462, 3115 (Cited on page 17.)

Damour T., Deruelle N., 1985, Ann. Inst. Henri Poincaré Phys. Théor, 43, 107 (Cited on page 80.)

Damour T., Deruelle N., 1986, Ann. Inst. Henri Poincaré Phys. Théor, 44, 263 (Cited on page 80.)

Davies J. G., Large M. I., 1970, MNRAS, 149, 301 (Cited on page 5.)

Davis M. M., Taylor J. H., Weisberg J. M., Backer D. C., 1985, Nature, 315, 547 (Cited on page 19.)

Deibel A., Cumming A., Brown E. F., Reddy S., 2017, ApJ, 839, 95 (Cited on page 123.)

Dellinger J. H., 1937, Terrestrial Magnetism and Atmospheric Electricity (Journal of Geophysical Research), 42, 49 (Cited on page 3.)

Demorest P. B., Pennucci T., Ransom S. M., Roberts M. S. E., Hessels J. W. T., 2010, Nature, 467, 1081 (Cited on page 23.)

Deneva J. S., Stovall K., McLaughlin M. A., Bates S. D., Freire P. C. C., Martinez J. G., Jenet F., Bagchi M., 2013, ApJ, 775, 51 (Cited on pages 115 and 118.)

Detweiler S., 1979, ApJ, 234, 1100 (Cited on page 22.)

Dewey R. J., Cordes J. M., 1987, ApJ, 321, 780 (Cited on page 130.)

Dhillon V., Dixon S., Gamble T., Kerry P., Littlefair S., Parsons S., Marsh T., Bezawada N., Black M., Gao X., Henry D., Lunney D., Miller C., Dubbeldam M., Morris T., Osborn J., Wilson R., Casares J., Muñoz-Darias T., Pallé E., Rodriguez-Gil P., Shahbaz T., de Ugarte Postigo A., 2018, in Proc. SPIEVol. 10702 of Society of Photo-Optical Instrumentation Engineers (SPIE) Conference Series, First light with HiPERCAM on the GTC. p. 107020L (Cited on page 142.)

Dokuchaev V. I., Eroshenko Y. N., 2017, arXiv e-prints, p. arXiv:1701.02492 (Cited on page 140.)

Drummond L. V., Melatos A., 2018, MNRAS, 475, 910 (Cited on page 135.)

Duan X., J. M., Zhao Z., 2016, MDPI and ACS Style, pp 4,20 (Cited on page 47.)

Durant M., Kargaltsev O., Pavlov G. G., Kowalski P. M., Posselt B., van Kerkwijk M. H., Kaplan D. L., 2012, ApJ, 746, 6 (Cited on page 123.)

Eatough R. P., Keane E. F., Lyne A. G., 2009, MNRAS, 395, 410 (Cited on pages 69 and 70.)

Eatough R. P., Kramer M., Lyne A. G., Keith M. J., 2013, MNRAS, 431, 292 (Cited on page 55.)

Eatough R. P., Molkenthin N., Kramer M., Noutsos A., Keith M. J., Stappers B. W., Lyne A. G., 2010, MNRAS, 407, 2443 (Cited on page 62.)

Espinoza C. M., 2018, in Weltevrede P., Perera B. B. P., Preston L. L., Sanidas S., eds, Pulsar Astrophysics the Next Fifty Years Vol. 337, Braking indices and spin evolution: something is loose inside neutron stars. pp 221–224 (Cited on page 10.)

Espinoza C. M., Lyne A. G., Stappers B. W., 2017, MNRAS, 466, 147 (Cited on page 10.)

Falcke H., Rezzolla L., 2014, A&A, 562, A137 (Cited on page 26.)

Faucher-Giguère C.-A., Kaspi V. M., 2006, ApJ, 643, 332 (Cited on page 126.)

Fernández R., Reisenegger A., 2005, ApJ, 625, 291 (Cited on pages 123 and 126.)

Ferrario L., de Martino D., Gänsicke B. T., 2015, Space Sci. Rev., 191, 111 (Cited on page 133.)

Flowers E., Ruderman M. A., 1977, ApJ, 215, 302 (Cited on page 123.)

Fonseca E., Andersen B. C., Bhardwaj M., Chawla P., Good D. C., Josephy A., Kaspi V. M., Masui K. W., Mckinven R., Michilli D., Pleunis Z., Shin K., Tendulkar S. P., Bandura K. M., Boyle P. J., Brar C., Cassanelli T., Cubranic D., Dobbs M., Dong F. Q., Gaensler B. M., Hinshaw G., Land ecker T. L., Leung C., Li D. Z., Lin H. H., Mena-Parra J., Merryfield M., Naidu A., Ng C., Patel C., Pen U., Rafiei-Ravandi M., Rahman M., Ransom S. M., Scholz P., Smith K. M., Stairs I. H., Vanderlinde K., Yadav P., Zwaniga A. V., 2020, ApJ, 891, L6 (Cited on page 25.)

Franklin K. L., Burke B. F., 1956, AJ, 61, 177 (Cited on page 3.)

Freire P. C., Kramer M., Lyne A. G., 2001, MNRAS, 322, 885 (Cited on pages 78 and 82.)

Freire P. C. C., Bassa C. G., Wex N., Stairs I. H., Champion D. J., Ransom S. M., Lazarus P., Kaspi V. M., Hessels J. W. T., Kramer M., Cordes J. M., Verbiest J. P. W., Podsiadlowski P., Nice D. J., Deneva J. S., Lorimer D. R., Stappers B. W., McLaughlin M. A., Camilo F., 2011, MNRAS, 412, 2763 (Cited on page 23.)

Freire P. C. C., Ridolfi A., 2018, MNRAS, 476, 4794 (Cited on pages 91 and 99.)

Freire P. C. C., Tauris T. M., 2014, MNRAS, 438, L86 (Cited on page 133.)

Gajjar V., Siemion A. P. V., Price D. C., Law C. J., Michilli D., Hessels J. W. T., Chatterjee S., Archibald A. M., Bower G. C., Brinkman C., Burke-Spolaor S., Cordes J. M., Croft S., Enriquez J. E., Foster G., Gizani N., Hellbourg G., Isaacson H., Kaspi V. M., Lazio T. J. W., Lebofsky M., Lynch R. S., MacMahon D., McLaughlin M. A., Ransom S. M., Scholz P., Seymour A., Spitler L. G., Tendulkar S. P., Werthimer D., Zhang Y. G., 2018, ApJ, 863, 2 (Cited on pages 140, 149 and 155.)

Galt J., Lyne A. G., 1972, MNRAS, 158, 281 (Cited on page 16.)

Gamow G., 1939, Physical Review, 55, 718 (Cited on page 6.)

Gendreau K. C., Arzoumanian Z., Okajima T., 2012, in Space Telescopes and Instrumentation 2012: Ultraviolet to Gamma Ray Vol. 8443 of Society of Photo-Optical Instrumentation Engineers (SPIE) Conference Series, The Neutron star Interior Composition ExploreR (NICER): an Explorer mission of opportunity for soft x-ray timing spectroscopy. p. 844313 (Cited on page 22.)

Geppert U., Urpin V., 1994, MNRAS, 271 (Cited on page 120.)

Goldreich P., Reisenegger A., 1992a, ApJ, 395, 250 (Cited on pages 10, 120, 121, 122, 126, 134 and 135.)

Goldreich P., Reisenegger A., 1992b, ApJ, 395, 250 (Cited on page 106.)

Gonzalez D., Reisenegger A., 2010, A&A, 522, A16 (Cited on page 123.)

Gourdji K., Michilli D., Spitler L. G., Hessels J. W. T., Seymour A., Cordes J. M., Chatterjee S., 2019, ApJ, 877, L19 (Cited on pages 149, 156, 159, 161, 163, 166, 167, 168, 169 and 170.)

Göğüş E., Woods P. M., Kouveliotou C., van Paradijs J., Briggs M. S., Duncan R. C., Thompson C., 1999, ApJ, 526, L93 (Cited on pages 141 and 162.)

Göğüş E., Woods P. M., Kouveliotou C., van Paradijs J., Briggs M. S., Duncan R. C., Thompson C., 2000, ApJ, 532, L121 (Cited on pages 28, 141 and 162.)

Gullahorn G. E., Rankin J. M., 1978, ApJ, 225, 963 (Cited on page 13.)

Gusakov M. E., Kantor E. M., Ofengeim D. D., 2017, Phys. Rev. D, 96, 103012 (Cited on page 135.)

Gusakov M. E., Kantor E. M., Reisenegger A., 2015, MNRAS, 453, L36 (Cited on page 124.)

Haensel P., Zdunik J. L., 1990, A&A, 227, 431 (Cited on page 123.)

Hankins T. H., Rickett B. J., 1975, in Methods in Computational Physics. Volume 14 - Radio astronomy Vol. 14, Pulsar signal processing. pp 55–129 (Cited on page 35.)

Harding A. K., Contopoulos I., Kazanas D., 1999, ApJ, 525, L125 (Cited on page 10.)

Hardy L. K., Dhillon V. S., Spitler L. G., Littlefair S. P., Ashley R. P., De Cia A., Green M. J., Jaroenjittichai P., Keane E. F., Kerry P., Kramer M., Malesani D., Marsh T. R., Parsons S. G., Possenti A., Rattanasoon S., Sahman D. I., 2017, MNRAS, 472, 2800 (Cited on pages 142, 149, 155, 164 and 169.)

Harrison F. A., Craig W. W., Christensen F. E., Hailey C. J., Zhang W. W., Boggs S. E., Stern D., Cook W. R., Forster K., Giommi P., Grefenstette B. W., Kim Y., Kitaguchi T., Koglin J. E., Madsen K. K., Mao P. H., Miyasaka H., Mori K., Perri M., Pivovaroff M. J., Puccetti S., Rana V. R., Westergaard N. J., Willis J., Zoglauer A., An H., Bachetti M., Barrière N. M., Bellm E. C., Bhalerao V., Brejnholt N. F., Fuerst F., Liebe C. C., ... 2013, ApJ, 770, 103 (Cited on page 147.)

Heintz K. E., Prochaska J. X., Simha S., Platts E., Fong W.-f., Tejos N., Ryder S. D., Aggarwal K., Bhandari S., Day C. K., Deller A. T., Kilpatrick C. D., Law C. J., Macquart J.-P., Mannings A., Marnoch L. J., Sadler E. M., Shannon R. M., 2020, arXiv e-prints, p. arXiv:2009.10747 (Cited on page 24.)

Herbst E., 1995, Annual Review of Physical Chemistry, 46, 27 (Cited on page 11.)

Hessels J. W. T., Ransom S. M., Kaspi V. M., Roberts M. S. E., Champion D. J., Stappers B. W., 2008, in Bassa C., Wang Z., Cumming A., Kaspi V. M., eds, 40 Years of Pulsars: Millisecond Pulsars, Magnetars and More Vol. 983 of American Institute of Physics Conference Series, The GBT350 Survey of the Northern Galactic Plane for Radio Pulsars and Transients. pp 613–615 (Cited on pages 115 and 118.)

Hessels J. W. T., Ransom S. M., Stairs I. H., Freire P. C. C., Kaspi V. M., Camilo F., 2006, Science, 311, 1901 (Cited on page 38.)

Hessels J. W. T., Spitler L. G., Seymour A. D., Cordes J. M., Michilli D., Lynch R. S., Gourdji K., Archibald A. M., Bassa C. G., Bower G. C., Chatterjee S., Connor L., Crawford F., Deneva J. S., Gajjar V., Kaspi V. M., Keimpema A., Law C. J., Marcote B., McLaughlin M. A., Paragi Z., Petroff E., Ransom S. M., Scholz P., Stappers B. W., Tendulkar S. P., 2019, ApJ, 876, L23 (Cited on pages 25, 148 and 149.)

Hewish A., Bell S. J., Pilkington J. D. H., Scott P. F., Collins R. A., 1968, Nature, 217, 709 (Cited on pages 3 and 4.)

Hilmarsson G. H., Michilli D., Spitler L. G., Wharton R. S., Demorest P., Desvigfnes G., Gourdji K., Hackstein S., Hessels J. W. T., Nimmo K., Seymour A. D., Kramer M., McKinven R., 2020, arXiv e-prints, p. arXiv:2009.12135 (Cited on page 25.)

Hilmarsson G. H., Spitler L. G., Keane E. F., Athanasiadis T. M., Barr E., Cruces M., Deng X., Heyminck S., Karuppusamy R., Kramer M., Sathyanarayanan S. P., Ventakraman Krishnan V., Wieching G., Wu J., Wucknitz O., 2020, arXiv e-prints, p. arXiv:2009.14042 (Cited on page 51.)

Hobbs G., 2005, PASA, 22, 179 (Cited on page 22.)

Hobbs G., 2012, arXiv e-prints, p. arXiv:1205.6273 (Cited on pages 80 and 83.)

Hobbs G., Archibald A., Arzoumanian Z., Backer D., Bailes M., Bhat N. D. R., Burgay M., Burke-Spolaor S., Champion D., Cognard I., et al. 2010, Classical and Quantum Gravity, 27, 084013 (Cited on pages 22 and 86.)

Hobbs G., Dai S., Manchester R. N., Shannon R. M., Kerr M., Lee K.-J., Xu R.-X., 2019, Research in Astronomy and Astrophysics, 19, 020 (Cited on page 50.)

Hobbs G. B., Edwards R. T., Manchester R. N., 2006, MNRAS, 369, 655 (Cited on page 91.)

Houben L. J. M., Spitler L. G., ter Veen S., Rachen J. P., Falcke H., Kramer M., 2019, A&A, 623, A42 (Cited on pages 148, 155, 161, 163, 164 and 169.)

Hoyos J., Reisenegger A., Valdivia J. A., 2008, A&A, 487, 789 (Cited on pages 121, 134 and 135.)

Hoyos J. H., Reisenegger A., Valdivia J. A., 2010, MNRAS, 408, 1730 (Cited on page 121.)

Igoshev A. P., Popov S. B., 2013, MNRAS, 432, 967 (Cited on page 19.)

Jackson J. D., 1975, Classical electrodynamics; 2nd ed.. Wiley, New York, NY (Cited on page 7.)

James C. W., Ekers R. D., Macquart J. P., Bannister K. W., Shannon R. M., 2019, MNRAS, 483, 1342 (Cited on page 162.)

Jansky K. G., 1933, Nature, 132, 66 (Cited on page 3.)

Jenet F., Finn L. S., Lazio J., Lommen A., McLaughlin M., Stairs I., Stinebring D., Verbiest J., Archibald A., Arzoumanian Z., Backer D., Cordes J., Demorest P., Ferdman R., Freire P., Gonzalez M., Kaspi V., Kondratiev V., Lorimer D., Lynch R., Nice D., Ransom S., Shannon R., Siemens X., 2009a, arXiv e-prints, p. arXiv:0909.1058 (Cited on page 22.)

Jenet F., Finn L. S., Lazio J., Lommen A., McLaughlin M., Stairs I., Stinebring D., Verbiest J., Archibald A., Arzoumanian Z., Backer D., Cordes J., Demorest P., Ferdman R., Freire P., Gonzalez M., Kaspi V., Kondratiev V., Lorimer D., Lynch R., Nice D., Ransom S., Shannon R., Siemens X., 2009b, arXiv e-prints, p. arXiv:0909.1058 (Cited on page 86.)

Jiang P., Tang N.-Y., Hou L.-G., Liu M.-T., Krčo M., Qian L., Sun J.-H., Ching T.-C., Liu B., Duan Y., Yue Y.-L., Gan H.-Q., Yao R., Li H., Pan G.-F., Yu D.-J., Liu H.-F., Li D., Peng B., Yan J., FAST Collaboration 2020, Research in Astronomy and Astrophysics, 20, 064 (Cited on pages 48, 49 and 90.)

Jiang P., Yue Y., Gan H., Yao R., Li H., Pan G., Sun J., Yu D., Liu H., Tang N., Qian L., Lu J., Yan J., Peng B., Zhang S., Wang Q., Li Q., Li D., 2019, Science China Physics, Mechanics, and Astronomy, 62, 959502 (Cited on page 48.)

Josephy A., Chawla P., Fonseca E., Ng C., Patel C., Pleunis Z., Scholz P., Andersen B. C., Bandura K., Bhardwaj M., Boyce M. M., Boyle P. J., Brar C., Cubranic D., Dobbs M., Gaensler B. M., Gill A., Giri U., Good D. C., Halpern M., Hinshaw G., Kaspi V. M., Landecker T. L., Lang D. A., Lin H. H., Masui K. W., Mckinven R., Mena-Parra J., Merryfield M., Michilli D., Milutinovic N., Naidu A., Pen U., ... 2019, ApJ, 882, L18 (Cited on pages 148 and 150.)

Kantor E. M., Gusakov M. E., 2018, MNRAS, 473, 4272 (Cited on page 135.)

Kargaltsev O., Pavlov G. G., Romani R. W., 2004, ApJ, 602, 327 (Cited on page 123.)

Karuppusamy R., Stappers B. W., van Straten W., 2010, A&A, 515, A36 (Cited on pages 28 and 162.)

Kashiyama K., Ioka K., Mészáros P., 2013, ApJ, 776, L39 (Cited on page 26.)

Kaspi V. M., Taylor J. H., Ryba M. F., 1994, ApJ, 428, 713 (Cited on page 23.)

Keane E. F., Stappers B. W., Kramer M., Lyne A. G., 2012a, MNRAS, 425, L71 (Cited on page 24.)

Keane E. F., Stappers B. W., Kramer M., Lyne A. G., 2012b, MNRAS, 425, L71 (Cited on page 140.)

Keith M. J., Jameson A., van Straten W., Bailes M., Johnston S., Kramer M., Possenti A., Bates S. D., Bhat N. D. R., Burgay M., Burke-Spolaor S., D'Amico N., Levin L., McMahon P. L., Milia S., Stappers B. W., 2010, MNRAS, 409, 619 (Cited on page 5.)

Kippenhahn R., Weigert A., 1990, Stellar Structure and Evolution (Cited on page 125.)

Kraft R. P., Burrows D. N., Nousek J. A., 1991, ApJ, 374, 344 (Cited on page 152.)

Kramer M., Champion D. J., 2013, Classical and Quantum Gravity, 30, 224009 (Cited on pages 22, 43 and 86.)

Kramer M., Jessner A., Doroshenko O., Wielebinski R., 1997, ApJ, 488, 364 (Cited on page 44.)

Kramer M., Lyne A. G., O'Brien J. T., Jordan C. A., Lorimer D. R., 2006, Science, 312, 549 (Cited on pages 5 and 11.)

Kramer M., Stairs I. H., Manchester R. N., McLaughlin M. A., Lyne A. G., Ferdman R. D., Burgay M., Lorimer D. R., Possenti A., D'Amico N., Sarkissian J. M., Hobbs G. B., Reynolds J. E., Freire P. C. C., Camilo F., 2006, Science, 314, 97 (Cited on pages 5, 21 and 86.)

Kramer M., Stappers B., 2015, in Advancing Astrophysics with the Square Kilometre Array (AASKA14) Pulsar Science with the SKA. p. 36 (Cited on page 4.)

Kraus A., Holst C., Nothnagel A., Bach U., 2015, in 2015 1st URSI Atlantic Radio Science Conference (URSI AT-RASC) Measuring the surface accuracy of the effelsberg 100-m radio telescope. pp 1–1 (Cited on page 43.)

Kumar P., Shannon R. M., Osłowski S., Qiu H., Bhandari S., Farah W., Flynn C., Kerr M., Lorimer D. R., Macquart J. P., Ng C., Phillips C. J., Price D. C., Spiewak R., 2019, ApJ, 887, L30 (Cited on pages 24 and 25.)

Kunjaya C., Mahasena P., Vierdayanti K., Herlie S., 2011, Astrophysics and Space Science - ASTROPHYS SPACE SCI, 336 (Cited on pages 28 and 162.)

Lai D., Bildsten L., Kaspi V. M., 1995, ApJ, 452, 819 (Cited on page 19.)

Lattimer J. M., Prakash M., 2001, ApJ, 550, 426 (Cited on page 86.)

Law C. J., Abruzzo M. W., Bassa C. G., Bower G. C., Burke-Spolaor S., Butler B. J., Cantwell T., Carey S. H., Chatterjee S., Cordes J. M., Demorest P., Dowell J., Fender R., Gourdji K., Grainge K., Hessels J. W. T., Hickish J., Kaspi V. M., Lazio T. J. W., McLaughlin M. A., Michilli D., Mooley K., Perrott Y. C., Ransom S. M., Razavi-Ghods N., Rupen M., Scaife A., Scott P., Scholz P., Seymour A., Spitler L. G., Stovall K., Tendulkar S. P., Titterington D., Wharton R. S., Williams P. K. G., 2017, ApJ, 850, 76 (Cited on pages 26, 156, 167, 168, 169 and 170.)

Lazarus P., Karuppusamy R., Graikou E., Caballero R. N., Champion D. J., Lee K. J., Verbiest J. P. W., Kramer M., 2016, MNRAS, 458, 868 (Cited on pages 46, 89 and 142.)

Lentati L., Taylor S. R., Mingarelli C. M. F., Sesana A., Sanidas S. A., Vecchio A., Caballero R. N., Lee K. J., van Haasteren R., Babak S., Bassa C. G., Brem P., Burgay M., Champion D. J., Cognard I., Desvignes G., Gair J. R., Guillemot L., Hessels J. W. T., Janssen G. H., Karuppusamy R., Kramer M., Lassus A., Lazarus P., Liu K., Osłowski S., Perrodin D., Petiteau A., Possenti A., Purver M. B., Rosado P. A., Smits R., Stappers B., Theureau G., Tiburzi C., Verbiest J. P. W., 2015, MNRAS, 453, 2576 (Cited on page 22.)

Li B., Li L.-B., Zhang Z.-B., Geng J.-J., Song L.-M., Huang Y.-F., Yang Y.-P., 2019, arXiv e-prints, p. arXiv:1901.03484 (Cited on pages 161 and 170.)

Li D., Pan Z., 2016, Radio Science, 51, 1060 (Cited on page 87.)

Li L.-B., Huang Y.-F., Zhang Z.-B., Li D., Li B., 2017, Research in Astronomy and Astrophysics, 17, 6 (Cited on page 50.)

Li T.-H., 2010, Signal Processing, 90, 2133 (Cited on page 156.)

Li Y.-P., Yuan F., Yuan Q., Wang Q. D., Chen P. F., Neilsen J., Fang T., Zhang S., Dexter J., 2015, ApJ, 810, 19 (Cited on pages 28 and 162.)

Liao K., Zhang S. B., Li Z., Gao H., 2020, ApJ, 896, L11 (Cited on page 29.)

Liu X., 2018, Ap&SS, 363, 242 (Cited on page 140.)

Lorimer D. R., 1998, Living Reviews in Relativity, 1, 10 (Cited on page 21.)

Lorimer D. R., Bailes M., McLaughlin M. A., Narkevic D. J., Crawford F., 2007, Science, 318, 777 (Cited on pages 5, 23, 24 and 140.)

Lorimer D. R., Faulkner A. J., Lyne A. G., Manchester R. N., Kramer M., McLaughlin M. A., Hobbs G., Possenti A., Stairs I. H., Camilo F., Burgay M., D'Amico N., Corongiu A., Crawford F., 2006, MNRAS, 372, 777 (Cited on page 134.)

Lorimer D. R., Kramer M., 2012, Handbook of Pulsar Astronomy (Cited on pages 10, 14, 15, 16, 17, 39, 41, 54, 58, 60, 75, 82, 84 and 92.)

Lorimer D. R., Lyne A. G., McLaughlin M. A., Kramer M., Pavlov G. G., Chang C., 2012, ApJ, 758, 141 (Cited on page 11.)

Lovelace R. V. E., Tyler G. L., 2012, The Observatory, 132, 186 (Cited on page 4.)

Luo R., Men Y., Lee K., Wang W., Lorimer D. R., Zhang B., 2020, MNRAS, 494, 665 (Cited on page 28.)

Lyne A. G., 2009, Intermittent Pulsars. Springer Berlin Heidelberg, Berlin, Heidelberg, pp 67–72 (Cited on page 19.)

Lyne A. G., Burgay M., Kramer M., Possenti A., Manchester R. N., Camilo F., McLaughlin M. A., Lorimer D. R., D'Amico N., Joshi B. C., Reynolds J., Freire P. C. C., 2004, Science, 303, 1153 (Cited on page 134.)

Lyne A. G., Jordan C. A., Graham-Smith F., Espinoza C. M., Stappers B. W., Weltevrede P., 2015, MNRAS, 446, 857 (Cited on page 19.)

Lyne A. G., Lorimer D. R., 1994, Nature, 369, 127 (Cited on page 19.)

Lyutikov M., 2014, Astronomische Nachrichten, 335, 227 (Cited on page 26.)

Macquart J.-P., Kanekar N., 2015, ApJ, 805, 172 (Cited on page 16.)

Macquart J. P., Prochaska J. X., McQuinn M., Bannister K. W., Bhandari S., Day C. K., Deller A. T., Ekers R. D., James C. W., Marnoch L., Osłowski S., Phillips C., Ryder S. D., Scott D. R., Shannon R. M., Tejos N., 2020, Nature, 581, 391 (Cited on pages 24 and 140.)

Main R., Lin R., van Kerkwijk M. H., Pen U.-L., Rudnitskii A. G., Popov M. V., Soglasnov V. A., Lyutikov M., , 2017, Resolving the emission regions of the Crab pulsar's giant pulses (Cited on page 94.)

Manchester R. N., Hobbs G. B., Teoh A., Hobbs M., 2005a, AJ, 129, 1993 (Cited on page 111.)

Manchester R. N., Hobbs G. B., Teoh A., Hobbs M., 2005b, AJ, 129, 1993 (Cited on pages 120, 125, 126 and 136.)

Manchester R. N., Lyne A. G., Camilo F., Bell J. F., Kaspi V. M., D'Amico N., McKay N. P. F., Crawford F., Stairs I. H., Possenti A., Kramer M., Sheppard D. C., 2001, MNRAS, 328, 17 (Cited on page 5.)

Marcote B., Nimmo K., Hessels J. W. T., Tendulkar S. P., Bassa C. G., Paragi Z., Keimpema A., Bhardwaj M., Karuppusamy R., Kaspi V. M., Law C. J., Michilli D., Aggarwal K., Andersen B., Archibald A. M., Bandura K., Bower G. C., Boyle P. J., Brar C., Burke-Spolaor S., Butler B. J., Cassanelli T., Chawla P., Demorest P., Dobbs M., Fonseca E., Giri U., Good D. C., Gourdji K., Josephy A., Kirichenko A. Y., Kirsten F., Landecker T. L., ... 2020, Nature, 577, 190 (Cited on page 140.)

Marcote B., Nimmo K., Hessels J. W. T., Tendulkar S. P., Bassa C. G., Paragi Z., Keimpema A., Bhardwaj M., Karuppusamy R., Kaspi V. M., Law C. J., Michilli D., Aggarwal K., Andersen B., Archibald A. M., Bandura K., Bower G. C., Boyle P. J., Brar C., Burke-Spolaor S., Butler B. J., Cassanelli T., Chawla P., Demorest P., Dobbs M., Fonseca E., Giri U., Good D. C., Gourdji K., Josephy A., Kirichenko A. Y., Kirsten F., Landecker T. L., Lang D., Lazio T. J. W., Li D. Z., Lin H. H., Linford J. D., Masui K., Mena-Parra J., Naidu A., ... 2020, Nature, 577, 190 (Cited on page 25.)

Marcote B., Paragi Z., Hessels J. W. T., Keimpema A., van Langevelde H. J., Huang Y., Bassa C. G., Bogdanov S., Bower G. C., Burke-Spolaor S., Butler B. J., Campbell R. M., Chatterjee S., Cordes J. M., Demorest P., Garrett M. A., Ghosh T., Kaspi V. M., Law C. J., Lazio T. J. W., McLaughlin M. A., Ransom S. M., Salter C. J., Scholz P., Seymour A., Siemion A., Spitler L. G., Tendulkar S. P., Wharton R. S., 2017, ApJ, 834, L8 (Cited on pages 25 and 140.)

Margalit B., Berger E., Metzger B. D., 2019, ApJ, 886, 110 (Cited on page 140.)

Marshall F. E., Gotthelf E. V., Zhang W., Middleditch J., Wang Q. D., 1998, ApJ, 499, L179 (Cited on page 126.)

Mazets E. P., Golenetskij S. V., Guryan Y. A., 1979, Soviet Astronomy Letters, 5, 343 (Cited on page 20.)

McLaughlin M. A., Lyne A. G., Keane E. F., Kramer M., Miller J. J., Lorimer D. R., Manchester R. N., Camilo F., Stairs I. H., 2009, MNRAS, 400, 1431 (Cited on pages 20 and 149.)

McLaughlin M. A., Lyne A. G., Lorimer D. R., Kramer M., Faulkner A. J., Manchester R. N., Cordes J. M., Camilo F., Possenti A., Stairs I. H., Hobbs G., D'Amico N., Burgay M., O'Brien J. T., 2006, Nature, 439, 817 (Cited on page 5.)

Mereghetti S., Savchenko V., Ferrigno C., Götz D., Rigoselli M., Tiengo A., Bazzano A., Bozzo E., Coleiro A., Courvoisier T. J. L., Doyle M., Goldwurm A., Hanlon L., Jourdain E., von Kienlin A., Lutovinov A., Martin-Carrillo A., Molkov S., Natalucci L., Onori F., Panessa F., Rodi J., Rodriguez J., Sánchez-Fernández C., Sunyaev R., Ubertini P., 2020, ApJ, 898, L29 (Cited on pages 27 and 140.)

Metzger B. D., Berger E., Margalit B., 2017a, ApJ, 841, 14 (Cited on page 26.)

Metzger B. D., Berger E., Margalit B., 2017b, ApJ, 841, 14 (Cited on page 153.)

Michilli D., Seymour A., Hessels J. W. T., Spitler L. G., Gajjar V., Archibald A. M., Bower G. C., Chatterjee S., Cordes J. M., Gourdji K., Heald G. H., Kaspi V. M., Law C. J., Sobey C., Adams E. A. K., Bassa C. G., Bogdanov S., Brinkman C., Demorest P., Fernandez F., Hellbourg G., Lazio T. J. W., Lynch R. S., Maddox N., Marcote B., McLaughlin M. A., Paragi Z., Ransom S. M., Scholz P., Siemion A. P. V., Tendulkar S. P., van Rooy P., Wharton R. S., Whitlow D., 2018, Nature, 553, 182 (Cited on pages 25, 26 and 140.)

Mitchell J. P., Braithwaite J., Reisenegger A., Spruit H., Valdivia J. A., Langer N., 2015, MNRAS, 447, 1213 (Cited on pages 124 and 135.)

Morello V., Barr E. D., Bailes M., Flynn C. M., Keane E. F., van Straten W., 2014, MNRAS, 443, 1651 (Cited on page 62.)

Morello V., Barr E. D., Stappers B. W., Keane E. F., Lyne A. G., 2020, MNRAS, 497, 4654 (Cited on pages 56, 57, 90 and 145.)

Mukherjee D., Bhattacharya D., Mignone A., 2013a, MNRAS, 430, 1976 (Cited on page 120.)

Mukherjee D., Bhattacharya D., Mignone A., 2013b, MNRAS, 435, 718 (Cited on page 120.)

Muslimov A., Page D., 1996, ApJ, 458, 347 (Cited on page 19.)

Nan R., Li D., Jin C., Wang Q., Zhu L., Zhu W., Zhang H., Yue Y., Qian L., 2011, International Journal of Modern Physics D, 20, 989 (Cited on pages 50, 86 and 89.)

Narayan R., 1992, Philosophical Transactions of the Royal Society of London Series A, 341, 151 (Cited on pages 3 and 16.)

Ng C., Bailes M., Bates S. D., Bhat N. D. R., Burgay M., Burke-Spolaor S., Champion D. J., Coster P., Johnston S., Keith M. J., Kramer M., Levin L., Petroff E., Possenti A., Stappers B. W., van Straten W., Thornton D., Tiburzi C., Bassa C. G., Freire P. C. C., Guillemot L., Lyne A. G., Tauris T. M., Shannon R. M., Wex N., 2014, MNRAS, 439, 1865 (Cited on page 89.)

Ng C., Champion D. J., Bailes M., Barr E. D., Bates S. D., Bhat N. D. R., Burgay M., Burke-Spolaor S., Flynn C. M. L., Jameson A., Johnston S., Keith M. J., Kramer M., Levin L., Petroff E., Possenti A., Stappers B. W., van Straten W., Tiburzi C., Eatough R. P., Lyne A. G., 2015, MNRAS, 450, 2922 (Cited on page 55.)

Noutsos A., Kramer M., Carr P., Johnston S., 2012, MNRAS, 423, 2736 (Cited on page 19.)

Ofek E. O., 2017, ApJ, 846, 44 (Cited on page 51.)

Ofengeim D. D., Gusakov M. E., 2018, Phys. Rev. D, 98, 043007 (Cited on page 121.)

Oostrum L. C., Maan Y., van Leeuwen J., Connor L., Petroff E., Attema J. J., Bast J. E., Gardenier D. W., Hargreaves J. E., Kooistra E., van der Schuur D., Sclocco A., Smits R., Straal S. M., ter Veen S., Vohl D., Adams E. A. K., Adebahr B., de Blok W. J. G., van den Brink R. H., van Cappellen W. A., Coolen A. H. W. M., Damstra S., van Diepen G. N. J., ... 2020, A&A, 635, A61 (Cited on pages 148, 152, 156, 157, 167, 168, 169 and 170.)

Oppenheimer J. R., Volkoff G. M., 1939, Physical Review, 55, 374 (Cited on page 4.)

Oppermann N., Yu H.-R., Pen U.-L., 2018, MNRAS, 475, 5109 (Cited on pages 28, 157, 160, 167 and 170.)

Özel F., Freire P., 2016, ARA&A, 54, 401 (Cited on pages 22 and 86.)

Palliyaguru N., Stinebring D., McLaughlin M., Demorest P., Jones G., 2015, ApJ, 815, 89 (Cited on page 16.)

Palliyaguru N. T., Agarwal D., Golpayegani G., Lynch R., Lorimer D. R., Nguyen B., Corsi A., Burke-Spolaor S., 2020, arXiv e-prints, p. arXiv:2007.13246 (Cited on page 51.)

Passamonti A., Akgün T., Pons J. A., Miralles J. A., 2017, MNRAS, 469, 4979 (Cited on page 135.)

Pavlov G. G., Rangelov B., Kargaltsev O., Reisenegger A., Guillot S., Reyes C., 2017, ApJ, 850, 79 (Cited on page 123.)

Perna R., Soria R., Pooley D., Stella L., 2008, Monthly Notices of the Royal Astronomical Society, 384, 1638 (Cited on page 19.)

Petroff E., Barr E. D., Jameson A., Keane E. F., Bailes M., Kramer M., Morello V., Tabbara D., van Straten W., 2016, PASA, 33, e045 (Cited on page 140.)

Petroff E., Hessels J. W. T., Lorimer D. R., 2019, A&A Rev., 27, 4 (Cited on page 28.)

Petroff E., Keane E. F., Barr E. D., Reynolds J. E., Sarkissian J., Edwards P. G., Stevens J., Brem C., Jameson A., Burke-Spolaor S., Johnston S., Bhat N. D. R., Kudale P. C. S., Bhand ari S., 2015, MNRAS, 451, 3933 (Cited on page 24.)

Petrovich C., Reisenegger A., 2010, A&A, 521, A77 (Cited on pages 124 and 135.)

Phinney E. S., 1992, Philosophical Transactions of the Royal Society of London Series A, 341, 39 (Cited on page 130.)

Pilia M., Burgay M., Possenti A., Ridolfi A., Gajjar V., Corongiu A., Perrodin D., Bernardi G., Naldi G., Pupillo G., Ambrosino F., Bianchi G., Burtovoi A., Casella P., Casentini C., Cecconi M., Ferrigno C., Fiori M., Gendreau K. C., Ghedina A., Naletto G., Nicastro L., Ochner P., Palazzi E., Panessa F., Papitto A., Pittori C., Rea N., Rodriguez Castillo G. A., Savchenko V., Setti G., Tavani M., Trois A.,

Trudu M., Turatto M., Ursi A., Verrecchia F., Zampieri L., 2020, arXiv e-prints, p. arXiv:2003.12748 (Cited on pages 27 and 140.)

Podsiadlowski P., Rappaport S., Pfahl E. D., 2002, ApJ, 565, 1107 (Cited on page 130.)

Popov M. V., Stappers B., 2007, A&A, 470, 1003 (Cited on pages 141 and 162.)

Porayko N. K., Noutsos A., Tiburzi C., Verbiest J. P. W., Horneffer A., Künsemöller J., Osłowski S., Kramer M., Schnitzeler D. H. F. M., Anderson J. M., Brüggen M., Grießmeier J. M., Hoeft M., Schwarz D. J., Serylak M., Wucknitz O., 2019, MNRAS, 483, 4100 (Cited on pages 92 and 98.)

Potekhin A. Y., Pons J. A., Page D., 2015, Space Science Reviews, 191, 239–291 (Cited on page 19.)

Price D. C., 2016, arXiv e-prints, p. arXiv:1607.03579 (Cited on page 35.)

Prochaska J. X., Macquart J.-P., McQuinn M., Simha S., Shannon R. M., Day C. K., Marnoch L., Ryder S., Deller A., Bannister K. W., Bhandari S., Bordoloi R., Bunton J., Cho H., Flynn C., Mahony E. K., Phillips C., Qiu H., Tejos N., 2019, Science, 366, 231 (Cited on page 141.)

Qiang D.-C., Deng H.-K., Wei H., 2020, Classical and Quantum Gravity, 37, 185022 (Cited on page 29.)

Radhakrishnan V., Cooke D. J., 1969, Astrophys. Lett., 3, 225 (Cited on pages 14, 92 and 116.)

Rajwade K. M., Mickaliger M. B., Stappers B. W., Morello V., Agarwal D., Bassa C. G., Breton R. P., Caleb M., Karastergiou A., Keane E. F., Lorimer D. R., 2020, MNRAS, 495, 3551 (Cited on pages 27, 140, 141, 155, 156, 157, 165 and 170.)

Rangelov B., Pavlov G. G., Kargaltsev O., Reisenegger A., Guillot S., van Kerkwijk M. H., Reyes C., 2017, ApJ, 835, 264 (Cited on page 123.)

Ransom S., , 2011, PRESTO: PulsaR Exploration and Search TOolkit (Cited on pages 55, 69, 70, 90, 142, 146 and 166.)

Ransom S. M., Demorest P., Ford J., McCullough R., Ray J., DuPlain R., Brandt P., 2009, in American Astronomical Society Meeting Abstracts #214 Vol. 214 of American Astronomical Society Meeting Abstracts, GUPPI: Green Bank Ultimate Pulsar Processing Instrument. p. 605.08 (Cited on page 146.)

Ransom S. M., Eikenberry S. S., Middleditch J., 2002, AJ, 124, 1788 (Cited on pages 55 and 90.)

Rappaport S., Deck K., Levine A., Borkovits T., Carter J., El Mellah I., Sanchis-Ojeda R., Kalomeni B., 2013, ApJ, 768, 33 (Cited on page 133.)

Ravi V., Catha M., D'Addario L., Djorgovski S. G., Hallinan G., Hobbs R., Kocz J., Kulkarni S. R., Shi J., Vedantham H. K., Weinreb S., Woody D. P., 2019, Nature, 572, 352 (Cited on page 140.)

Reifenstein E. C. I., Brundage W. D., Staelin D. H., 1969, ApJ, 156, L125 (Cited on page 5.)

Reisenegger A., 1995, ApJ, 442, 749 (Cited on pages 123 and 126.)

Reisenegger A., 2009, A&A, 499, 557 (Cited on page 121.)

Reisenegger A., Goldreich P., 1992, ApJ, 395, 240 (Cited on page 121.)

Rickett B. J., Coles W. A., Bourgois G., 1984, A&A, 134, 390 (Cited on page 16.)

Riley T. E., Watts A. L., Bogdanov S., Ray P. S., Ludlam R. M., Guillot S., Arzoumanian Z., Baker C. L., Bilous A. V., Chakrabarty D., Gendreau K. C., Harding A. K., Ho W. C. G., Lattimer J. M., Morsink S. M., Strohmayer T. E., 2019, ApJ, 887, L21 (Cited on page 22.)

Romani R. W., 1990, Nature, 347, 741 (Cited on page 120.)

Ruderman M. A., Sutherland P. G., 1975, ApJ, 196, 51 (Cited on page 110.)

Saio H., Nomoto K., 1985, A&A, 150, L21 (Cited on pages 130 and 133.)

Sanidas S., Cooper S., Bassa C. G., Hessels J. W. T., Kondratiev V. I., Michilli D., Stappers B. W., Tan C. M., van Leeuwen J., Cerrigone L., Fallows R. A., Iacobelli M., Orrú E., Pizzo R. F., Shulevski A., Toribio M. C., ter Veen S., Zucca P., Bondonneau L., Grießmeier J. M., Karastergiou A., Kramer M., Sobey C., 2019, A&A, 626, A104 (Cited on pages 115 and 118.)

Schatz H., Bildsten L., Cumming A., Wiescher M., 1999, ApJ, 524, 1014 (Cited on page 123.)

Scholz P., Bogdanov S., Hessels J. W. T., Lynch R. S., Spitler L. G., Bassa C. G., Bower G. C., Burke-Spolaor S., Butler B. J., Chatterjee S., Cordes J. M., Gourdji K., Kaspi V. M., Law C. J., Marcote B., McLaughlin M. A., Michilli D., Paragi Z., Ransom S. M., Seymour A., Tendulkar S. P., Wharton R. S., 2017, ApJ, 846, 80 (Cited on pages 25, 141, 149, 152, 153, 156 and 169.)

Scholz P., Cook A., Cruces M., Hessels J. W. T., Kaspi V. M., Majid W. A., Naidu A., Pearlman A. B., Spitler L. G., Bandura K. M., Bhardwaj M., Cassanelli T., Chawla P., Gaensler B. M., Good D. C., Josephy A., Karuppusamy R., Keimpema A., Kirichenko A. Y., Kirsten F., Kocz J., Leung C., Marcote B., Masui K., Mena-Parra J., Merryfield M., Michilli D., Naudet C. J., Nimmo K., Pleunis Z., Prince T. A., Rafiei-Ravandi M., Rahman M., Shin K., Smith K. M., Stairs I. H., Tendulkar S. P., Vanderlinde K., 2020, ApJ, 901, 165 (Cited on page 178.)

Scholz P., Spitler L. G., Hessels J. W. T., Chatterjee S., Cordes J. M., Kaspi V. M., Wharton R. S., Bassa C. G., Bogdanov S., Camilo F., Crawford F., Deneva J., van Leeuwen J., Lynch R., Madsen E. C., McLaughlin M. A., Mickaliger M., Parent E., Patel C., Ransom S. M., Seymour A., Stairs I. H., Stappers B. W., Tendulkar S. P., 2016, ApJ, 833, 177 (Cited on pages 141 and 156.)

Schuh H., Behrend D., 2012, Journal of Geodynamics, 61, 68 (Cited on page 43.)

Shand Z., Ouyed A., Koning N., Ouyed R., 2016, Research in Astronomy and Astrophysics, 16, 80 (Cited on page 26.)

Shannon R. M., Ravi V., Coles W. A., Hobbs G., Keith M. J., Manchester R. N., Wyithe J. S. B., Bailes M., Bhat N. D. R., Burke-Spolaor S., Khoo J., Levin Y., Oslowski S., Sarkissian J. M., van Straten W., Verbiest J. P. W., Wang J. B., 2013, Science, 342, 334 (Cited on page 22.)

Shannon R. M., Ravi V., Lentati L. T., Lasky P. D., Hobbs G., Kerr M., Manchester R. N., Coles W. A., Levin Y., Bailes M., Bhat N. D. R., Burke-Spolaor S., Dai S., Keith M. J., Osłowski S., Reardon D. J., van Straten W., Toomey L., Wang J. B., Wen L., Wyithe J. S. B., Zhu X. J., 2015, Science, 349, 1522 (Cited on page 75.)

Shapiro I. I., 1964, Phys. Rev. Lett., 13, 789 (Cited on page 81.)

Shrauner J. A., 1997, PhD thesis, PRINCETON UNIVERSITY (Cited on page 37.)

Smits R., Lorimer D. R., Kramer M., Manchester R., Stappers B., Jin C. J., Nan R. D., Li D., 2009, A&A, 505, 919 (Cited on pages 50 and 88.)

Snell R. L., 2011, Interstellar Medium. Springer Berlin Heidelberg, Berlin, Heidelberg, pp 837–843 (Cited on page 11.)

Spitler L. G., Cordes J. M., Hessels J. W. T., Lorimer D. R., McLaughlin M. A., Chatterjee S., Crawford F., Deneva J. S., Kaspi V. M., Wharton R. S., Allen B., Bogdanov S., Brazier A., Camilo F., Freire P. C. C., Jenet F. A., Karako-Argaman C., Knispel B., Lazarus P., Lee K. J., van Leeuwen J., Lynch R., Ransom S. M., Scholz P., Siemens X., Stairs I. H., Stovall K., Swiggum J. K., Venkataraman A., Zhu W. W., Aulbert C., Fehrmann H., 2014, ApJ, 790, 101 (Cited on pages 24 and 156.)

Spitler L. G., Scholz P., Hessels J. W. T., Bogdanov S., Brazier A., Camilo F., Chatterjee S., Cordes J. M., Crawford F., Deneva J., Ferdman R. D., Freire P. C. C., Kaspi V. M., Lazarus P., Lynch R., Madsen E. C., McLaughlin M. A., Patel C., Ransom S. M., Seymour A., Stairs I. H., Stappers B. W., van Leeuwen J., Zhu W. W., 2016, Nature, 531, 202 (Cited on pages 5, 24, 140 and 156.)

Spruit H., Phinney E. S., 1998, Nature, 393, 139 (Cited on page 19.)

Spruit H. C., 2008, in Bassa C., Wang Z., Cumming A., Kaspi V. M., eds, 40 Years of Pulsars: Millisecond Pulsars, Magnetars and More Vol. 983 of American Institute of Physics Conference Series, Origin of neutron star magnetic fields. pp 391–398 (Cited on page 6.)

Spruit H. C., 2013, ArXiv e-prints (Cited on page 121.)

Staelin D. H., Reifenstein Edward C. I., 1968, Science, 162, 1481 (Cited on page 4.)

Stairs I. H., 2003, Living Reviews in Relativity, 6, 5 (Cited on page 76.)

Stairs I. H., Splaver E. M., Thorsett S. E., Nice D. J., Taylor J. H., 2000, MNRAS, 314, 459 (Cited on page 35.)

Stovall K., 2013, PhD thesis, The University of Texas at San Antonio (Cited on pages 115 and 118.)

Stovall K., Freire P. C. C., Antoniadis J., Bagchi M., Deneva J. S., Garver-Daniels N., Martinez J. G., McLaughlin M. A., Arzoumanian Z., Blumer H., Brook P. R., Cromartie H. T., Demorest P. B., DeCesar M. E., Dolch T., Ellis J. A., Ferdman R. D., Ferrara E. C., Fonseca E., Gentile P. A., Jones M. L., Lam M. T., Lorimer D. R., Lynch R. S., Ng C., Nice D. J., Pennucci T. T., Ransom S. M., Spiewak R., Stairs I. H., Swiggum J. K., Vigeland S. J., Zhu W. W., 2019, ApJ, 870, 74 (Cited on page 130.)

Sturrock P. A., 1971, ApJ, 164, 529 (Cited on page 7.)

Taam R. E., van den Heuvel E. P. J., 1986, ApJ, 305, 235 (Cited on page 130.)

Tan C. M., Bassa C. G., Cooper S., Dijkema T. J., Esposito P., Hessels J. W. T., Kondratiev V. I., Kramer M., Michilli D., Sanidas S., Shimwell T. W., Stappers B. W., van Leeuwen J., Cognard I., Grießmeier J. M., Karastergiou A., Keane E. F., Sobey C., Weltevrede P., 2018, ApJ, 866, 54 (Cited on page 17.)

Tauris T. M., Kramer M., Freire P. C. C., Wex N., Janka H. T., Langer N., Podsiadlowski P., Bozzo E., Chaty S., Kruckow M. U., van den Heuvel E. P. J., Antoniadis J., Breton R. P., Champion D. J., 2017, ApJ, 846, 170 (Cited on page 86.)

Tauris T. M., Kramer M., Langer N., 2013, in van Leeuwen J., ed., Neutron Stars and Pulsars: Challenges and Opportunities after 80 years Vol. 291 of IAU Symposium, Recycling Pulsars: spins, masses and ages. pp 137–140 (Cited on page 133.)

Tauris T. M., Langer N., Kramer M., 2011a, MNRAS, 416, 2130 (Cited on pages 20, 99, 106 and 117.)

Tauris T. M., Langer N., Kramer M., 2011b, MNRAS, 416, 2130 (Cited on page 125.)

Tauris T. M., Langer N., Kramer M., 2012a, MNRAS, 425, 1601 (Cited on pages 20, 99, 106 and 117.)

Tauris T. M., Langer N., Kramer M., 2012b, MNRAS, 425, 1601 (Cited on pages 125, 130, 133 and 134.)

Tauris T. M., Savonije G. J., 1999, A&A, 350, 928 (Cited on pages 125, 130 and 133.)

Tauris T. M., Sennels T., 2000a, A&A, 355, 236 (Cited on pages 106 and 110.)

Tauris T. M., Sennels T., 2000b, A&A, 355, 236 (Cited on page 130.)

Tauris T. M., van den Heuvel E. P. J., 2006, Formation and evolution of compact stellar X-ray sources. pp 623–665 (Cited on page 120.)

Taylor J. H., 1975, in Bergman P. G., Fenyves E. J., Motz L., eds, Seventh Texas Symposium on Relativistic Astrophysics Vol. 262, Discovery of a pulsar in a binary system.. pp 490–492 (Cited on page 21.)

Taylor J. H., 1992, Philosophical Transactions of the Royal Society of London Series A, 341, 117 (Cited on page 74.)

Taylor J. H., Huguenin G. R., 1969, Nature, 221, 816 (Cited on pages 5 and 54.)

Taylor J. H., Hulse R. A., Margon B., Davidsen A., Mason K., Sanford P., Liller W., Bernacca P. L., Ciatti F., John R. S., Regener V. H., Papaliolios C., Pennypacker C., Canizares C., McClintock J., Jones B., Graham D., Wielebinski R., 1974, IAU Circ., 2704, 1 (Cited on page 5.)

Tendulkar S. P., Bassa C. G., Cordes J. M., Bower G. C., Law C. J., Chatterjee S., Adams E. A. K., Bogdanov S., Burke-Spolaor S., Butler B. J., Demorest P., Hessels J. W. T., Kaspi V. M., Lazio T. J. W., Maddox N., Marcote B., McLaughlin M. A., Paragi Z., Ransom S. M., Scholz P., Seymour A., Spitler L. G., van Langevelde H. J., Wharton R. S., 2017, ApJ, 834, L7 (Cited on pages 25, 140, 154 and 162.)

The CHIME/FRB Collaboration : Andersen B. C., Band ura K. M., Bhardwaj M., Bij A., Boyce M. M., Boyle P. J., Brar C., Cassanelli T., Chawla P., Chen T., Cliche J. F., Cook A., Cubranic D., Curtin A. P., Denman N. T., Dobbs M., Dong F. Q., Fandino M., Fonseca E., Gaensler B. M., Giri U., Good D. C., Halpern M., Hill A. S., Hinshaw G. F., Höfer C., Josephy A., Kania J. W., Kaspi V. M., Landecker T. L., Leung C., Li D. Z., ... 2020, arXiv e-prints, p. arXiv:2005.10324 (Cited on pages 27 and 140.)

The CHIME/FRB Collaboration Amiri M., Andersen B. C., Bandura K. M., Bhardwaj M., Boyle P. J., Brar C., Chawla P., Chen T., Cliche J. F., Cubranic D., Deng M., Denman N. T., Dobbs M., Dong F. Q., Fand ino M., Fonseca E., Gaensler B. M., Giri U., Good D. C., Halpern M., Hessels J. W. T., ... 2020, arXiv e-prints, p. arXiv:2001.10275 (Cited on pages 27 and 140.)

Thompson C., Duncan R. C., 1995, MNRAS, 275, 255 (Cited on page 20.)

Thompson C., Duncan R. C., 1996a, ApJ, 473, 322 (Cited on page 20.)

Thompson C., Duncan R. C., 1996b, ApJ, 473, 322 (Cited on page 121.)

Thorne K. S., Blandford R. D., 2017, Modern Classical Physics: Optics, Fluids, Plasmas, Elasticity, Relativity, and Statistical Physics. Princeton NJ: Princeton University Press (Cited on page 121.)

Thornton D., Stappers B., Bailes M., Barsdell B., Bates S., Bhat N. D. R., Burgay M., Burke-Spolaor S., Champion D. J., Coster P., D'Amico N., Jameson A., Johnston S., Keith M., Kramer M., Levin L., Milia S., Ng C., Possenti A., van Straten W., 2013, Science, 341, 53 (Cited on page 24.)

Tolman R. C., 1939, Physical Review, 55, 364 (Cited on page 4.)

Totani T., 2013a, PASJ, 65, L12 (Cited on page 26.)

Totani T., 2013b, PASJ, 65, L12 (Cited on page 140.)

Trigilio C., Leto P., Leone F., Umana G., Buemi C., 2000, A&A, 362, 281 (Cited on page 3.)

Turtle A. J., Vaughan A. E., 1968, Nature, 219, 689 (Cited on page 5.)

Uson J. M., Cotton W. D., 2008, A&A, 486, 647 (Cited on page 32.)

van Leeuwen J., Kasian L., Stairs I. H., Lorimer D. R., Camilo F., Chatterjee S., Cognard I., Desvignes G., Freire P. C. C., Janssen G. H., Kramer M., Lyne A. G., Nice D. J., Ransom S. M., Stappers B. W., Weisberg J. M., 2015, ApJ, 798, 118 (Cited on page 134.)

van Straten W., Bailes M., 2011, PASA, 28, 1 (Cited on page 148.)

van Straten W., Demorest P., Oslowski S., 2012, Astronomical Research and Technology, 9, 237 (Cited on pages 71, 72 and 91.)

van Straten W., Manchester R. N., Johnston S., Reynolds J. E., 2010, PASA, 27, 104 (Cited on page 91.)

VanderPlas J. T., 2018, ApJS, 236, 16 (Cited on page 155.)

Vaughan A. E., Large M. I., Wielebinski R., 1969, Nature, 222, 963 (Cited on page 5.)

Verbiest J. P. W., Lentati L., Hobbs G., van Haasteren R., Demorest P. B., Janssen G. H., Wang J. B., Desvignes G., Caballero R. N., Keith M. J., Champion D. J., Arzoumanian Z., Babak S., Bassa C. G., Bhat N. D. R., Brazier A., Brem P., Burgay M., Burke-Spolaor S., Chamberlin S. J., Chatterjee S., Christy B., Cognard I., Cordes J. M., Dai S., Dolch T., Ellis J. A., Ferdman R. D., Fonseca E., Gair J. R., Garver-Daniels N. E., Gentile P., Gonzalez M. E., Graikou E., Guillemot L., Hessels J. W. T., Jones G., Karuppusamy R., ... 2016, MNRAS, 458, 1267 (Cited on pages 22 and 74.)

Verbunt F., Phinney E. S., 1995, A&A, 296, 709 (Cited on page 130.)

Wang D., Li Z., Zhang J., 2020, Physics of the Dark Universe, 29, 100571 (Cited on page 29.)

Wei J.-J., Gao H., Wu X.-F., Mészáros P., 2015, Phys. Rev. Lett., 115, 261101 (Cited on page 29.)

Weisberg J. M., Huang Y., 2016, ApJ, 829, 55 (Cited on page 21.)

Weisberg J. M., Taylor J. H., 2005, in Rasio F. A., Stairs I. H., eds, Binary Radio Pulsars Vol. 328 of Astronomical Society of the Pacific Conference Series, The Relativistic Binary Pulsar B1913+16: Thirty Years of Observations and Analysis. p. 25 (Cited on page 21.)

Wex N., 2014, arXiv e-prints, p. arXiv:1402.5594 (Cited on pages 5 and 86.)

Williamson I. P., 1972, MNRAS, 157, 55 (Cited on page 14.)

Wiringa R. B., Fiks V., Fabrocini A., 1988, Phys. Rev. C, 38, 1010 (Cited on page 126.)

Wolszczan A., Frail D. A., 1992, Nature, 355, 145 (Cited on page 5.)

Wu X.-F., Zhang S.-B., Gao H., Wei J.-J., Zou Y.-C., Lei W.-H., Zhang B., Dai Z.-G., Mészáros P., 2016, ApJ, 822, L15 (Cited on page 29.)

Xia Z., Miao K., Na W., 2013, Chinese Physics C, 37, 085102 (Cited on page 124.)

Yao J. M., Manchester R. N., Wang N., 2017, ApJ, 835, 29 (Cited on pages 13, 51, 86 and 94.)

Zhang B., 2016, ApJ, 827, L31 (Cited on page 26.)

Zhang B., Harding A. K., Muslimov A. G., 2000, ApJ, 531, L135 (Cited on pages 93 and 111.)

Zheng Z., Ofek E. O., Kulkarni S. R., Neill J. D., Juric M., 2014, ApJ, 797, 71 (Cited on page 29.)

Zhu W., Li D., Luo R., Miao C., Zhang B., Spitler L., Lorimer D., Kramer M., Champion D., Yue Y., Cameron A., Cruces M., ... 2020, The Astrophysical Journal, 895, L6 (Cited on pages 50 and 175.)

Zhu W. W., Berndsen A., Madsen E. C., Tan M., Stairs I. H., Brazier A., Lazarus P., Lynch R., Scholz P., Stovall K., et al. 2014, The Astrophysical Journal, 781, 117 (Cited on page 62.)